

# Structural flexibility and chirality of polar molecules elucidated with broadband rotational spectroscopy

Dissertation

zur Erlangung des Doktorgrades

des Department Physik

der Universität Hamburg

vorgelegt von

**David Schmitz**

aus Mainz

Hamburg

2015

**Gutachter der Dissertation:**

PD Dr. Melanie Schnell

Prof. Dr. R. J. Dwayne Miller

**Gutachter der Disputation:**

PD Dr. Melanie Schnell

Prof. Dr. Nils Huse

**Datum der Disputation:**

28.07.2015

**Vorsitzender des Prüfungsausschusses:**

Prof. Dr. Michael Rübhausen

**Vorsitzender des Promotionsausschusses:**

Prof. Dr. Jan Louis

**Leiter des Fachbereichs Physik:**

Prof. Dr. Peter Hauschildt

**Dekan der Fakultät für Mathematik,  
Informatik und Naturwissenschaften:**

Prof. Dr. Heinrich Graener

# Abstract

An in-depth knowledge of the structure and internal dynamics of molecules and molecular complexes is key for understanding their physical, chemical, and biological properties. Due to the strong relationship between molecular structure, intra- and intermolecular forces, and molecular function, structural information is helpful for the prediction of reaction pathways or possible binding. Rotational spectroscopy is well suited to shed light on the conformational flexibility and chirality of small and medium-sized molecules of biological relevance. Besides its exceptional accuracy in structure determination of gas phase molecules, rotational spectroscopy also provides information about the intramolecular forces and even the electronic structure.

Recent developments in microelectronics now allow broadband microwave spectrometers to record wide portions of the rotational spectrum in a very time efficient way. However, analyzing the spectra of larger molecules is challenging due to close lying transitions or overlapping spectra of different structural isomers. These challenges are tackled in this thesis by the development of a computer-based routine to automate the assignment and double-resonance experiments that provide information about the connectivity of the energy levels involved.

In the framework of this thesis, a broadband chirped-pulse Fourier transform microwave spectrometer was designed, constructed and evaluated. Using this spectrometer, different organic molecules are studied with increasing structural complexity and flexibility. Starting with the family of the rather rigid *p*-halotoluenes (*p*-chloro-, *p*-bromo- and *p*-iodotoluene), their methyl internal rotation and quadrupole coupling is examined. Thereafter, the microwave spectra of the aromatic monoterpenoids thymol and carvacrol are used to determine the barrier of the methyl internal rotation. Two other monoterpenoids are studied afterwards: menthol and its ketone equivalent menthone. Due to the cyclohexane ring, their structural flexibility is increased compared to their aromatic counterpart thymol. Using the dense and overlapping spectrum of a mixture of menthone isomers, a computer program is described that automatically assigns and fits the rotational transitions based on calculated rotational constants from structural predictions.

Beyond traditional microwave spectroscopy, the chirped pulse method is extended by a polarization sensitive double-resonance scheme to differentiate between enantiomers of chiral molecules. Enantiomer differentiation and enantiomeric excess determination are presented for the molecule carvone. Furthermore, the phases of the molecular signals in double-resonance experiments are examined and compared to theoretical predictions. A strong phase change of the signal transition is observed at molecular resonance that can be exploited to yield information about the energy level arrangement and facilitate spectral assignment.

# Zusammenfassung

Die tiefergehende Kenntnis der Struktur und internen Dynamik von Molekülen und Molekülkomplexen ist entscheidend für das Verständnis ihrer physikalischen, chemischen und biologischen Eigenschaften. Da die Molekülstruktur mit den Kräften innerhalb eines Moleküls und letztendlich mit seiner Funktionalität verknüpft ist, können Strukturinformationen bei der Vorhersage von Reaktionswegen und möglichen chemischen Verbindungen helfen. Die Rotationsspektroskopie bietet nahezu ideale Voraussetzungen für die Untersuchung der strukturellen Flexibilität und Chiralität kleiner und mittelgroßer Biomoleküle. Neben der hohen Genauigkeit bei der Strukturbestimmung von Molekülen in der Gasphase liefert die Rotationsspektroskopie auch Informationen über intramolekulare Kräfte und die Ladungsverteilung.

Die schnellen Entwicklungen im Bereich der Mikroelektronik haben die technologischen Grundlagen für die Breitbandspektroskopie im Mikrowellenbereich geschaffen, die große Bereiche des Rotationsspektrums gleichzeitig erfassen kann. Die Analyse der Spektren größerer Moleküle wird allerdings durch dicht beieinander liegende Rotationsübergänge oder durch überlappende Spektren verschiedener Strukturisomere erschwert. Diesen Herausforderungen wird in dieser Arbeit mit der Entwicklung einer computergestützten Routine zur automatisierten Linienzuordnung begegnet. Des Weiteren werden Doppelresonanzexperimente vorgestellt, die Informationen über die Konnektivität der beteiligten Energieniveaus liefern.

Im Rahmen dieser Arbeit wird ein breitbandiges *Chirp*-Puls Fouriertransformations-Mikrowellenspektrometer entworfen, gebaut und evaluiert. Mithilfe dieses Spektrometers werden diverse organische Moleküle mit ansteigender Strukturkomplexität und -flexibilität untersucht. Anhand der Familie der eher starren *p*-Halogentoluole (*p*-Chlor-, *p*-Brom- und *p*-Iodtoluol) wird die interne Rotation der Methylgruppe und die Quadrupolkopplung untersucht. Danach wird mithilfe der Mikrowellenspektren der aromatischen Monoterpenoide Thymol und Carvacrol die Barriere der internen Rotation der Methylgruppe bestimmt. Zwei weitere Monoterpenoide werden anschließend untersucht: Menthol und sein Ketonäquivalent Menthon. Aufgrund des Cyclohexanringes zeigen sie eine höhere Strukturflexibilität im Vergleich zu ihrem aromatischen Pendant Thymol. Am Beispiel der dichten, sich überlappenden Spektren der Isomerenmischung von Menthon wird ein Computerprogramm getestet, das basierend auf berechneten Rotationskonstanten automatisch die verschiedenen Rotationsübergänge zuordnet.

Über die traditionelle Mikrowellenspektroskopie hinaus wird die *Chirp*-Puls Methode durch ein polarisationsempfindliches Doppelresonanzverfahren erweitert, mit dem Ziel, die Enantiomere chiraler Moleküle zu unterscheiden. Die eindeutige Unterscheidung der Enantiomere sowie die Bestimmung des Enantiomerenüberschusses wird für das Molekül Carvon vorgestellt. Weiterhin wird die Phase des molekularen Signals im Rahmen verschiedener Doppelresonanzexperimente untersucht und mit theoretischen Vorhersagen verglichen. Bei resonanter Anregung wird ein starker Phasensprung beobachtet, der genutzt werden kann, um Informationen über die Anordnung der Energieniveaus zu erhalten und um so die Spektrenzuordnung zu erleichtern.



# Publications

1. D. Schmitz, V. A. Shubert, T. Betz, and M. Schnell, *Multi-resonance effects within a single chirp in broadband rotational spectroscopy: The rapid adiabatic passage regime for benzonitrile*, J. Mol. Spec. **280**, 77-84 (2012).
2. V. A. Shubert, D. Schmitz, and M. Schnell, *Communication through the phenyl ring: internal rotation and nuclear quadrupole splitting in p-halotoluenes*, Mol. Phys. **111**, 2189-97 (2013).
3. D. Schmitz, V. A. Shubert, B. M. Giuliano, and M. Schnell, *The broadband microwave spectra of the monoterpenoids thymol and carvacrol: Conformational landscape and internal dynamics*, J. Chem. Phys. **141**, 034304 (2014).
4. V. A. Shubert, D. Schmitz, D. Patterson, J. M. Doyle and M. Schnell, *Identifying Enantiomers in Mixtures of Chiral Molecules with Broadband Microwave Spectroscopy*, Angew. Chem. Int. Ed. **52**, 1-5 (2013).
5. V. A. Shubert, D. Schmitz, and M. Schnell, *Enantiomer-sensitive spectroscopy and mixture analysis of chiral molecules containing two stereogenic centers – Microwave three-wave mixing of menthone*, J. Mol. Spec. **52**, 31-6 (2014).
6. D. Schmitz, V. A. Shubert, T. Betz, and M. Schnell, *Exploring the conformational landscape of menthol, menthone, and isomenthone: A microwave study*, Front. Chem. **3**, 15 (2015).
7. D. Schmitz, V. A. Shubert, D. Patterson, A. Krin, and M. Schnell, *Phase Dependence of Double-Resonance Experiments in Rotational Spectroscopy*, J. Phys. Chem. Lett. **6**, 1493-98 (2015).
8. V. A. Shubert, D. Schmitz, C. Medcraft, A. Krin, D. Patterson, J. M. Doyle and M. Schnell, *Rotational spectroscopy and three-wave mixing of 4-carvomenthenol: A technical guide to measuring chirality in the microwave regime*, accepted at J. Chem. Phys.

# Contents

<b>1</b>	<b>Motivation</b>	<b>1</b>
<b>2</b>	<b>Theoretical background</b>	<b>6</b>
2.1	Rotational Hamiltonian . . . . .	8
2.2	Hyperfine splitting: Nuclear quadrupole coupling . . . . .	16
2.3	Internal rotation . . . . .	22
2.4	Bloch equations . . . . .	26
2.5	Spectral fitting . . . . .	32
2.6	Quantum chemical calculations . . . . .	33
<b>3</b>	<b>Experimental details</b>	<b>41</b>
3.1	Chirped-pulse microwave spectrometer . . . . .	41
3.2	Molecular beam technique . . . . .	47
3.3	Commissioning and performance . . . . .	54
<b>4</b>	<b>Communication through the phenyl ring: internal rotation and nuclear quadrupole splitting in p-halotoluenes</b>	<b>59</b>
4.1	Introduction . . . . .	59
4.2	Experimental . . . . .	62
4.3	Computational Methods . . . . .	62
4.4	Spectral details and fitting . . . . .	62
4.5	Results and discussion . . . . .	65
4.6	Summary and conclusions . . . . .	72

---

<b>5</b>	<b>The broadband microwave spectra of the monoterpenoids thymol and carvacrol: Conformational landscape and internal dynamics</b>	<b>73</b>
5.1	Introduction . . . . .	73
5.2	Experimental and computational methods . . . . .	75
5.3	Results . . . . .	76
5.4	Discussion . . . . .	86
5.5	Conclusion and outlook . . . . .	87
<b>6</b>	<b>Exploring the conformational landscape of menthol, menthone, and isomenthone: A microwave study</b>	<b>89</b>
6.1	Introduction . . . . .	89
6.2	Experimental and computational methods . . . . .	91
6.3	Results and discussion . . . . .	93
6.4	Conclusions . . . . .	107
<b>7</b>	<b>Enantiomer differentiation by microwave three-wave mixing experiments</b>	<b>109</b>
7.1	Introduction . . . . .	109
7.2	Theoretical background . . . . .	110
7.3	Experimental details . . . . .	113
7.4	Double-resonance experiments . . . . .	114
7.5	Enantiomer differentiation . . . . .	120
7.6	Enantiomeric excess measurement . . . . .	124
7.7	Conclusion and outlook . . . . .	127
<b>8</b>	<b>Summary and outlook</b>	<b>128</b>
	<b>Bibliography</b>	<b>145</b>
<b>A</b>	<b>Three-level optical Bloch equations</b>	<b>148</b>
<b>B</b>	<b>Fourier series</b>	<b>150</b>

# Chapter 1

## Motivation

An in-depth knowledge of the structure and internal dynamics of molecules and molecular complexes is key for the understanding of their physical, chemical, and biological properties. Due to the strong relationship between the molecular structure, the intra- and intermolecular forces at play, and molecular function, structural information is helpful for the prediction of reaction pathways or possible binding. The lively interplay between structure determination and method development enabled various scientific breakthroughs, honored by several Nobel prizes (Yonath 2009 [1], Wüthrich 2002 [2], Ernst 1991 [3], Deisendorf/Huber/Michel 1988 [4, 5], Hauptmann/Karle 1985 [6, 7], Klug 1982 [8], Hodgkin 1964 [9]) in the last century. Even though biologically relevant molecules such as proteins, ribonucleic acids (RNA), or deoxyribonucleic acid (DNA) are huge, their functionality is often dominated by comparably small active sites. The understanding of the chemistry on these active sites is fundamental for drug development. However, this guest-host binding is a complex procedure depending upon conformational changes during the molecular recognition process and the chirality of the binding partners.

Rotational spectroscopy is well suited to shed light on the conformational flexibility and chirality of small and medium-sized molecules of biological relevance. Rotational spectroscopy is known for its exceptional accuracy in structure determination, but it also provides information about the intramolecular forces and even the electronic structure. The former is accessible via the effects on the of molecular vibrations, internal rotation, and centrifugal forces on the Hamiltonian, the latter by quadrupole coupling and dipole moments. Pure rotational spectroscopy is only applicable to gas-phase samples of molecules with a permanent dipole moment. However, the permanent dipole moment requirement is not a strong limitation for medium-sized biomolecules because their high asymmetry gives rise to nonzero permanent dipole moment. In contrast, the gas-phase requirement sets a challenging restriction to the maximum size of the molecule and removes the molecules from the more natural solution-phase environment, which has a direct impact on the studied conformational preferences. The size limitation is weakened by implementing advanced molecular beam sources e.g. laser ablation sources [10] and by forming molecular clusters with a solvent, the solution effect is mimicked [11–15]. Owing to recent development in the design of molecular sources and the broadband

capabilities of next generation microwave spectrometers, various building block molecules (e. g. monosaccharides [16], amino acids [17–19], nucleobases [20, 21], neurotransmitters [22]), drugs [23–27] and higher order clusters [15, 28–30] have been studied. Besides pure structure determination, complex inter- and intramolecular dynamics have also been analyzed using microwave spectroscopy [26, 31, 32].

Microwave spectroscopy also contributes significantly to the research area of astrochemistry. The molecular signals from dense gas clouds provide information how molecules are formed in space. New and powerful radio telescopes, e.g. Atacama Large Millimeter Array (ALMA) [33] and the Herschel space telescope [34], can provide multispectral images containing the signatures of several molecules and their isotopologues, molecular ions, and radicals [35–37]. However, the analysis of the spectral data bears several challenges. The molecules in outer space are far from thermal equilibrium and their internal energies are spread over several vibrational states [38, 39]. Furthermore, the harsh environmental conditions in space promoting the generation of unstable molecular ions and radicals are not easily reproduced in the laboratory. However, a discharge source is a promising approach to produce radicals with an adequate efficiency [40].

The application of microwave spectroscopy to study molecular properties is an active area of research for now almost 70 years. Microwave spectrometry emerged after World War II supported by the increased development activities of radio detection and ranging (RADAR) equipment during the war. The first microwave spectrometers measured the absorption of monochromatic microwave radiation in a gas cell or waveguide. The microwave radiation was produced by klystrons, magnetrons, or traveling-wave tubes and detected by semiconductor crystals [41, Chap. 14, Chap. 15]. Lock-in amplifiers were used to enhance the sensitivity, while modulating the excitation intensity, the excitation frequency, or the absorption frequency by means of the Stark or Zeeman effects [41, Chap. 10, Chap. 11]. The first molecule investigated extensively by microwave spectroscopy was ammonia [42–44]. This relatively simple symmetric-top molecule already exhibits two challenging spectroscopic effects, namely the inversion splitting [42, 43] and the hyperfine structure due to the nitrogen quadrupole moment [44]. The concentrated research on ammonia led to the development of the MASER (microwave amplification by stimulated emission of radiation) [45, 46], the direct predecessor of the LASER (light amplification by stimulated emission of radiation) and the first experimental demonstration of stimulated emission.

While subsequent microwave investigations focused on molecules with increasing complexity, Kraitchman laid the theoretical foundation for determining molecular structure via isotopic substitution [47]. The invention of the time-domain emission spectrometers using pulsed microwave sources significantly enhanced the sensitivity and the molecular linewidth compared to absorption spectrometers [48–50]. To overcome the drawbacks of pressure broadening and low population densities in gas-cell spectroscopy at room temperatures, Balle and Flygare combined time-domain spectroscopy with a Fabry-Perot resonator and a supersonic expansion, one of the milestones in the history of microwave spectroscopy [51]. Grabow et al. improved the experimental setup by a coaxial arrangement of the molecular beam and the microwave field

[52]. The fast scan submillimeter/millimeter spectroscopic technique (FASSST), an absorption spectroscopy technique based on voltage tunable backward wave oscillators (BWO), provided broadband capabilities in the millimeter wave spectral region [53, 54]. Two-dimensional microwave spectroscopy was used in combination with different spectrometer designs to unravel coherence pathways, population transfer, and the connectivity of rotational energy levels [55–57].

The invention of the chirped-pulse Fourier transform microwave (CP-FTMW) spectrometer by Pate and coworkers in 2008 was a huge breakthrough in terms of bandwidth, measurement time, and flexibility [58]. Since then several CP-FTMW spectrometers have been constructed in different frequency ranges [29, 59–74] and novel applications of microwave spectroscopy demonstrated, including investigation of isomerization dynamics [75, 76], two-dimensional broadband microwave spectroscopy [77], and, within the framework of this dissertation, the differentiation of enantiomers [78, 79]. One of the current development trends are low-cost high bandwidth CP-FTMW spectrometers for commercial trace gas analysis [80–82]. A CP-FTMW spectrometer has also been used to examine high Rydberg states in Sodium atoms [65]. Employing high gain frequency multiplier chains or frequency mixing CP-FTMW spectrometry can be extended to the mm-wave region [67, 70, 74, 80, 81].

Even though microwave spectroscopy is well-known for its outstanding accuracy in determining the molecular structure of gas-phase molecules, rotationally resolved UV or IR spectroscopy may complement the structural information for electronically or vibrationally excited states [83–85]. Another advantage of IR or UV spectroscopy over microwave spectroscopy is their higher time resolution that grants access to ultrafast phenomena via pump-probe experiments [86]. Rotational coherence spectroscopy (RCS), a new time-domain technique, circumvents the limitation of traditional rotational spectroscopy to polar molecules and simplifies the spectral assignment dramatically. RCS is a pump-probe approach, where the pump laser pulse creates a coherent superposition of rotational states and their evolution (dephasing and rephasing) is probed with a second laser pulse [87]. When combined with mass-spectrometry, the different isotopologues are disentangled to determine the substitution structure [88]. However, the complicated and expensive experimental setup of RCS currently outweighs its benefits by far.

Despite its exceptional structural resolution, microwave spectroscopy faces significant obstacles when it comes to structure determination of larger (bio)molecules (e.g. proteins or DNA), solution or solid-phase samples, or ultrafast phenomena (femtosecond timescale). These challenges are addressed by different, partially complementary techniques, e.g. nuclear magnetic resonance (NMR), X-ray, and electron diffraction. NMR provides excellent solution-phase structures of proteins, but each step from the sample preparation to the measurement and the final data analysis can be very tedious and time consuming [2, 89, 90]. X-ray diffraction is another more widespread method for structure determination (according to the published protein structures on the protein data base [91]), but their samples usually exist under unnatural conditions, e.g. molecular crystals or single, isolated molecules/particles, and are exposed to a harsh environment (ultrahigh vacuum). An exception to these conditions is small angle

X-ray scattering (SAXS), a low resolution technique, providing a rough estimate of the overall shape of the system under study [92–94]. High-resolution X-ray diffraction studies depend on a high quality crystalline sample, which cannot always be produced [1]. This requirement is about to change with the new, bright free-electron laser light sources. Their high photon flux allows the use of nanoprotein crystals [95–97], a single virus [98, 99], or even isolated gas-phase molecules [100]. On the other hand, the short pulse length of the X-ray laser must yield an unperturbed diffraction image before the sample transforms into a plasma (diffraction before destruction) [101–103]. To enhance the intensity and reduce the measurement time, alignment methods are applied in single molecule imaging [100].

Electron diffraction shares various properties with X-ray diffraction, but the main difference is in the interaction principle. Electrons interact with the electron cloud and the cores, while X-rays are scattered off by the electron cloud. This difference leads to about  $10^6$  higher cross sections for electron diffraction. Consequently, the samples the electrons are interacting with must be very thin (typically less than 100 nm for biological samples) and resistant to the high vacuum conditions. The structural collapse upon dehydration is prevented by the use of negative stains or flash freezing the sample [104]. However, recent developments in nanofabrication enable the development of nanofluidic cells to image biological samples in solution [105]. Another advantage of electron diffraction over X-ray diffraction is the smaller wavelength of about 2 pm (compared to 150 pm for X-ray diffraction experiments at the Linac Coherent Light Source) resulting in higher resolution images. Recent sources for X-ray and electron diffraction provide a time resolution in the femtosecond regime, which enables the observation of chemically relevant processes [106–109].

The work described herein comprises different objectives, namely the construction of a CP-FTMW spectrometer, the measurement and analysis of the rotational spectra of different organic molecules with increasing structural complexity, and the extension of the CP-FTMW technique to differentiate between enantiomers of chiral molecules. However, the central achievement is the design, construction, and evaluation of a chirped-pulse microwave spectrometer described in Chapter 3. Using this spectrometer different organic molecules are studied with increasing structural complexity and flexibility. Starting with the family of the rather rigid *p*-halotoluenes (*p*-chloro-, *p*-bromo-, and *p*-iodotoluene), their methyl internal rotation and quadrupole coupling is examined (Chap. 4). Thereafter, the microwave spectra of the aromatic monoterpenoids thymol and carvacrol are used to determine the barrier of the methyl internal rotation. Subsequently the results are presented and discussed in an extensive comparison with similar molecules (Chap. 5). Due to the cyclohexane ring, the monoterpenoids menthol and its ketone equivalent menthone are more flexible than their aromatic counterpart thymol. Consequently their conformational landscape involves more minimum structures. In Chapter 6, the rotational spectra of menthol, menthone, and isomenthone are presented together with the assignment of the rotational constants to the calculated minimum structures.

Beyond traditional microwave spectroscopy, the chirped-pulse method is extended by a polarization sensitive double-resonance scheme to differentiate between enantiomers of chiral

molecules. Enantiomer differentiation as well as enantiomeric excess determination are presented in Chapter 7. In addition, the phase of the molecular signal in double-resonance experiments is examined and compared to theoretical prediction based on the dressed-state picture. The challenging assignment of dense rotational spectra containing several species (e.g. conformers, isotopologues) is tackled in this work with the development of an automatic assignment program (Sec. 6.3) and the microwave signal phase in double-resonance experiments is exploited to gain information about the energy level arrangement (Sec. 7.4). The next chapter gives an overview of the theoretical methods employed in this work including a description of the rotational Hamiltonian, the two-level Bloch equations, and a short glance into quantum chemical methods.



## Chapter 2

# Theoretical background

Spectroscopy is a probe of the energy eigenvalues of a quantum system employing static or dynamic electromagnetic fields. For a molecule of  $N$  atoms and  $M$  electrons, the time-independent Schrödinger equation is:

$$\hat{H}\psi_n(\mathbf{Q}_1, \dots, \mathbf{Q}_N, \mathbf{q}_1, \dots, \mathbf{q}_M) = E_n\psi_n(\mathbf{Q}_1, \dots, \mathbf{Q}_N, \mathbf{q}_1, \dots, \mathbf{q}_M) \quad (2.1)$$

where  $\mathbf{Q}_i$  and  $\mathbf{q}_j$  are vectors describing the position of the  $i$ -th nuclei and the  $j$ -th electron, respectively.  $\psi_n$  represent the eigenfunctions of the Hamiltonian operator  $\hat{H}$  with their corresponding eigenvalues  $E_n$ . The Hamiltonian operator can be divided into a kinetic energy term  $\hat{T}$  and a potential energy term  $\hat{V}$  [110]:

$$\hat{H} = \hat{T} + \hat{V} = \sum_{i=1}^N \frac{\hat{\mathbf{P}}_i^2}{2m_i} + \sum_{j=1}^M \frac{\hat{\mathbf{p}}_j^2}{2m_e} + \hat{V}(\mathbf{Q}_1, \dots, \mathbf{Q}_N, \mathbf{q}_1, \dots, \mathbf{q}_M) \quad (2.2)$$

where  $\hat{\mathbf{P}}_i$  and  $\hat{\mathbf{p}}_j$  are the momentum operators of the atoms and electrons, respectively. The molecular dynamics and hence the molecular energy eigenvalues are mainly influenced by the electronic motions and the molecular vibrations and rotations. These different motions take place on different timescales. Electrons orbiting the nucleus need about a 1 fs for a revolution, much faster than the typical vibrational period of 10 – 100 fs. The rotation of the entire molecule occurs on even slower timescales of 0.1 – 10 ps. These differences in the time frames enable the separation of the distinct motions employing the central approximation in molecular spectroscopy: the Born-Oppenheimer approximation.

Within the Born-Oppenheimer approximation, the separation of the electronic and nuclear degrees of freedom becomes possible, exploiting the fact that the nuclei barely move during a period of the electronic movement [111]. Hence, the Hamiltonian can be evaluated in a two step procedure. Firstly, the electronic part of the Hamiltonian is solved with the nuclei at fixed positions  $\mathbf{Q}_a$ , and secondly the motion of the nuclei is evaluated using the averaged electric potential from step one.

Employing a similar strategy, the vibrational and the rotational motion can be separated.

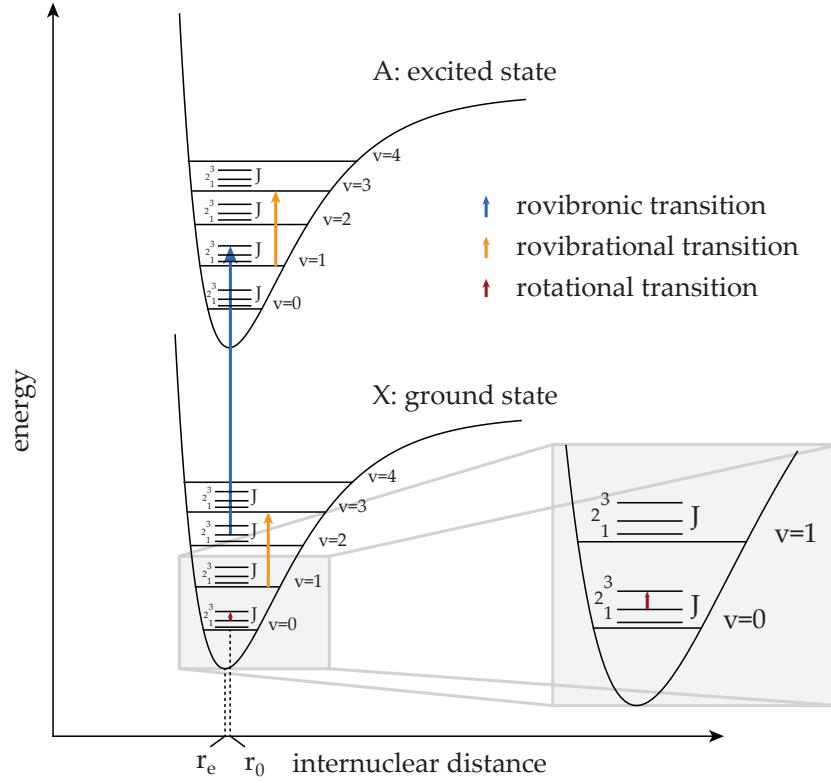


**Figure 2.1:** Potential energy curves of two electronic states of a diatomic molecule. Each electronic state is subdivided into several vibrational states, which are again subdivided into rotational states. The x-axis represents the internuclear distance. The typical energy interval of rovibronic transitions are greater than  $5000 \text{ cm}^{-1}$  ( $> 0.6 \text{ eV}$ ). The energy interval of rovibrational transitions is between  $300 - 15000 \text{ cm}^{-1}$  ( $30 - 0.7 \text{ }\mu\text{m}$ ) and rotational transitions can be found in the spectral region of  $0.03 - 300 \text{ cm}^{-1}$  ( $1 - 10000 \text{ GHz}$ ). The value  $r_e$  describes the equilibrium internuclear distance and  $r_0$  is the expectation value of the internuclear distance in the lowest vibrational state ( $v = 0$ ).

The average contribution of the fast vibrational motions are included parametrically into the rotational part of the Hamiltonian. Hence, the total molecular Hamiltonian is represented as a sum of an electronic part  $\hat{H}_{el}$ , a vibrational part  $\hat{H}_{vib}$ , a rotational part  $\hat{H}_{rot}$ , a translational part  $\hat{H}_{trans}$  and a part depending on the nuclear spin  $\hat{H}_{ns}$ :

$$\hat{H} = \hat{H}_{el}(\mathbf{q}_j, \mathbf{Q}_a) + \hat{H}_{vib}(\mathbf{Q}_i) + \hat{H}_{rot}(\theta, \phi, \chi) + \hat{H}_{trans}(X, Y, Z) + \hat{H}_{ns} \quad (2.3)$$

where  $\theta, \phi, \chi$  are the Euler angles describing the orientation of the molecule in a laboratory-fixed frame ( $X, Y, Z$ ), while  $\mathbf{q}_j$  and  $\mathbf{Q}_i$  are internal coordinates describing the position of electrons and nuclei in the molecular fixed coordinate system. The molecular energy levels and the total molecular wave function follow [110]:

$$E_n = E_{el,n} + E_{vib,n} + E_{rot,n} + E_{trans,n} + E_{ns,n} \quad (2.4)$$

$$\psi_n = \varphi_{el,n}(\mathbf{q}_j, \mathbf{Q}_a) \varphi_{vib,n}(\mathbf{Q}_i) \varphi_{rot,n}(\theta, \phi, \chi) \varphi_{trans,n}(X, Y, Z) \varphi_{ns,n} \quad (2.5)$$

**Table 2.1:** Possible identification of  $a, b, c$  with  $x, y, z$  leading to six different representations. The  $I^r$  representation is best suited to describe a prolate symmetric top or a slightly asymmetric prolate top. Whereas the  $III^r$  representation is suitable for the description of oblate symmetric top or slightly asymmetric oblate tops.

	$I^r$	$I^l$	$II^r$	$II^l$	$III^r$	$III^l$
$x$	$b$	$c$	$c$	$a$	$a$	$b$
$y$	$c$	$b$	$a$	$c$	$b$	$a$
$z$	$a$	$a$	$b$	$b$	$c$	$c$

The potential energy curves of two electronic states and the corresponding vibrational and rotational energy levels of a diatomic molecule are depicted in Figure 2.1. Microwave spectroscopy as employed in the present work probes the rotational part of the Hamiltonian. Hence, the rotational Hamiltonian and the corresponding time-independent Schrödinger equation

$$\hat{H}_{rot}\varphi_{rot} = E_{rot}\varphi_{rot} \quad (2.6)$$

are discussed in detail in the following section.

## 2.1 Rotational Hamiltonian

From classical mechanics, the rotational energy of a rigid body is given by:

$$E_{rot} = \frac{1}{2}\boldsymbol{\omega}^T \mathbf{I} \boldsymbol{\omega} = \frac{\mathbf{L}^2}{2\mathbf{I}} \quad (2.7)$$

with the inertia tensor  $\mathbf{I}$ , the angular velocity  $\boldsymbol{\omega}$ , and the angular momentum  $\mathbf{L}$ . In a rigid molecule, only the nuclei contribute significantly to the inertia tensor due to their much larger masses compared to the electrons. The nuclei of a molecule can be treated as point particles with masses  $m_i$  at coordinates  $\mathbf{Q}_i (x_i, y_i, z_i)$  in a molecule-fixed coordinate system. Hence, the inertia tensor can be written as:

$$\mathbf{I} = \sum_{i=0}^N m_i \begin{pmatrix} y_i^2 + z_i^2 & -x_i y_i & -x_i z_i \\ -y_i x_i & x_i^2 + z_i^2 & -y_i z_i \\ -z_i x_i & -z_i y_i & x_i^2 + y_i^2 \end{pmatrix} \quad (2.8)$$

Upon diagonalization, the inertia tensor is transformed to the molecule-fixed principal axis system. The principal moments of inertia are defined by the diagonal elements of the inertia tensor with increasing size  $I_a \leq I_b \leq I_c$ . Within the principle axis system the rotational energy becomes:

$$E_{rot} = \frac{L_a^2}{2I_a} + \frac{L_b^2}{2I_b} + \frac{L_c^2}{2I_c} \quad (2.9)$$

where  $L_g$  ( $g = a, b, c$ ) is the component of the angular momentum along the respective principal axis. The molecular fixed axes  $(x, y, z)$  can be assigned to the principal axes  $(a, b, c)$

in six different ways, which are summarized in Table 2.1. Those assignments or representations will become important hereinafter for the evaluation of the rotational Hamiltonian. The transformation from the classical rotational energy to the quantum mechanical rigid rotor Hamiltonian is straightforward by introducing the angular momentum operator  $\hat{\mathbf{J}}$ :

$$\hat{H}_{rid} = \frac{\hat{\mathbf{J}}^2}{2\mathbf{I}} = \frac{\hat{J}_a^2}{2I_a} + \frac{\hat{J}_b^2}{2I_b} + \frac{\hat{J}_c^2}{2I_c} \quad (2.10)$$

with

$$\hat{\mathbf{J}} = \hat{\mathbf{r}} \times \hat{\mathbf{p}} = -i\hbar (\hat{\mathbf{r}} \times \nabla) \quad (2.11)$$

where  $\hat{\mathbf{r}}$  is the position operator.

Due to the symmetry of the molecule, one of its moments of inertia might vanish or some of its moments of inertia might be equal. Hence four different classifications are established to classify molecules in rotational spectroscopy:

**Linear molecules:** Molecules with  $I_a = 0$  and  $I_b = I_c$  are called linear molecules. They belong to the point groups  $C_{\infty v}$  or  $D_{\infty h}$ . Typical examples are: hydrogen cyanide ( $HCN$ ), carbonyl sulfide ( $OCS$ ).

**Spherical-top molecules:** Spherical tops are molecules with  $I_a = I_b = I_c$  and  $T_d$ ,  $O_h$  or  $I_h$  symmetry. Typical examples are: sulfur hexafluoride ( $SF_6$ ), methane ( $CH_4$ ).

**Symmetric-top molecules:** Two moments of inertia are equal for symmetric-top molecules. If  $I_a = I_b < I_c$ , the molecule is an oblate symmetric top (disc-shaped). For prolate symmetric-top molecules (cigar shaped),  $I_a < I_b = I_c$ . A symmetric-top molecule has  $C_n$  symmetry ( $n > 2$ ) or a  $S_4$ -axis of symmetry. Examples for symmetric tops include: ammonia ( $NH_3$ , oblate), iodomethane ( $ICH_3$ , prolate), benzene ( $C_6H_6$ , oblate), propadiene ( $C_3H_4$ , prolate).

**Asymmetric-top molecules:** Asymmetric-top molecules are the largest class and as the name indicates, all moments of inertia are different:  $I_a \neq I_b \neq I_c$ . Planar molecules are an important subgroup, where  $I_c - I_b - I_a = 0$ . Examples of asymmetric-top molecules are water ( $H_2O$ ), phenol ( $C_6H_6O$ , planar), all amino acids.

The rigid rotor Hamiltonian (Eqn. 2.10) solely depends on angular momentum operators, which are defined in the molecular axis system. Even though the molecular axis system is well suited to describe the internal movements of the electrons and the nuclei, the molecular coordinate system  $(x, y, z)$  needs to be related to the laboratory-fixed coordinate system  $(X, Y, Z)$  for determining the rotational energy of a molecule. Because only the rotation and not the translational motion of the molecule is of importance for the rotational Hamiltonian, both coordinate systems coincide at the center of mass of the molecule, thus canceling out the center of mass motion. The orientation of both coordinate systems to each other is described by the three Euler angles  $\theta$ ,  $\phi$ , and  $\chi$  depicted in Figure 2.2, and the transformation

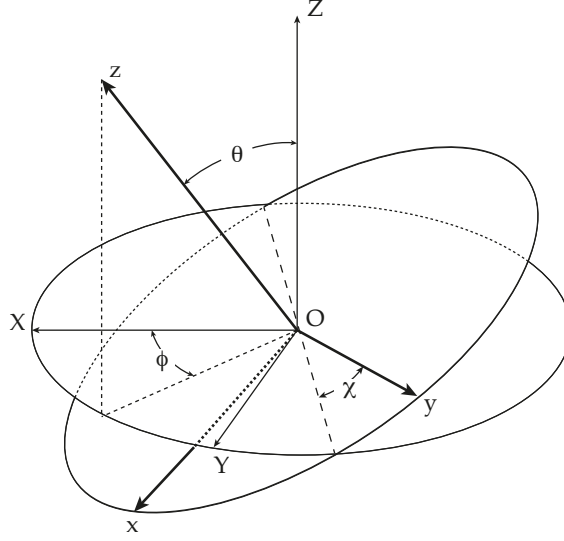


**Figure 2.2:** Illustration of the Euler angles  $\theta$ ,  $\phi$ , and  $\chi$  which define the orientation of a molecule  $(x, y, z)$  in the laboratory frame  $(X, Y, Z)$ .

is expressed by three consecutive rotations about the axes (the explicit rotation matrices are stated in [112]):

1. Rotate  $X$  and  $Y$  by an angle  $\phi$  about  $Z$  into  $X'$  and  $Y'$ .
2. Rotate  $X'$  and  $Z$  by an angle  $\theta$  about  $Y'$  into  $X''$  and  $z$ .
3. Rotate  $X''$  and  $Y'$  by an angle  $\chi$  about  $z$  into  $x$  and  $y$ .

Now, the different Cartesian components of the angular momentum operator (Eqn. 2.10) can be expressed in terms of Eulerian angles in the molecule-fixed axis system [112]:

$$\hat{J}_x = i\hbar \left[ \frac{-\cos\chi}{\sin\theta} \frac{\partial}{\partial\phi} + \frac{\cos\chi \cos\theta}{\sin\theta} \frac{\partial}{\partial\chi} + \sin\chi \frac{\partial}{\partial\theta} \right] \quad (2.12)$$

$$\hat{J}_y = i\hbar \left[ \frac{\sin\chi}{\sin\theta} \frac{\partial}{\partial\phi} - \frac{\sin\chi \cos\theta}{\sin\theta} \frac{\partial}{\partial\chi} + \cos\chi \frac{\partial}{\partial\theta} \right] \quad (2.13)$$

$$\hat{J}_z = i\hbar \frac{\partial}{\partial\chi} \quad (2.14)$$

as well as in the laboratory-fixed coordinate system:

$$\hat{J}_X = i\hbar \left[ \frac{-\cos\phi \cos\theta}{\sin\theta} \frac{\partial}{\partial\phi} + \frac{\cos\phi}{\sin\theta} \frac{\partial}{\partial\chi} - \sin\phi \frac{\partial}{\partial\theta} \right] \quad (2.15)$$

$$\hat{J}_Y = i\hbar \left[ \frac{-\sin\phi \cos\theta}{\sin\theta} \frac{\partial}{\partial\phi} + \frac{\sin\phi}{\sin\theta} \frac{\partial}{\partial\chi} + \cos\phi \frac{\partial}{\partial\theta} \right] \quad (2.16)$$

$$\hat{J}_Z = i\hbar \frac{\partial}{\partial\phi} \quad (2.17)$$

The angular momentum operators satisfy the following commutation relations [113, 114]:

$$[\hat{J}_x, \hat{J}_y] = -i\hbar\hat{J}_z, \quad [\hat{J}_z, \hat{J}_x] = -i\hbar\hat{J}_y, \quad [\hat{J}_y, \hat{J}_z] = -i\hbar\hat{J}_x \quad (2.18)$$

$$[\hat{J}_X, \hat{J}_Y] = i\hbar\hat{J}_Z, \quad [\hat{J}_Z, \hat{J}_X] = i\hbar\hat{J}_Y, \quad [\hat{J}_Y, \hat{J}_Z] = i\hbar\hat{J}_X \quad (2.19)$$

$$[\hat{\mathbf{J}}^2, \hat{J}_g] = 0, \quad g = x, y, z \quad (2.20)$$

$$[\hat{\mathbf{J}}^2, \hat{J}_G] = 0, \quad G = X, Y, Z \quad (2.21)$$

$$[\hat{J}_g, \hat{J}_G] = 0 \quad g = x, y, z \quad G = X, Y, Z \quad (2.22)$$

According to the Heisenberg uncertainty principle, only the operator  $\hat{\mathbf{J}}^2$ , one of the operators  $\hat{J}_g$  and one of the operators  $\hat{J}_G$  can be measured simultaneously. In accordance with the spectroscopic literature, the components of the angular momentum  $\hat{J}_z$  and  $\hat{J}_Z$  are chosen, the projections of the total angular momentum on the  $z$ -axis and  $Z$ -axis, respectively. The  $z$ -axis is assigned to the principal axis with the highest symmetry making use of the appropriate representation in Table 2.1. Hence a complete set of eigenfunctions  $|JKM\rangle$  can be found for the operators  $\hat{\mathbf{J}}^2$ ,  $\hat{J}_z$  and  $\hat{J}_Z$ . With the help of the ladder operator  $\hat{J}_\pm = \hat{J}_x \pm i\hat{J}_y$  and the commutation relations, the following eigenvalues can be derived [113, 115]:

$$\hat{\mathbf{J}}^2 |JKM\rangle = J(J+1)\hbar |JKM\rangle \quad (2.23)$$

$$\hat{J}_Z |JKM\rangle = M\hbar |JKM\rangle \quad (2.24)$$

$$\hat{J}_z |JKM\rangle = K\hbar |JKM\rangle \quad (2.25)$$

with quantum numbers:

$$J = 0, 1, 2, \dots$$

$$K = -J, -J+1, \dots, J-1, J$$

$$M = -J, -J+1, \dots, J-1, J$$

The quantum number  $J$  is a measure of the total angular momentum, the quantum numbers  $K$  and  $M$  describe the projections of the total angular momentum onto the  $z$ -axis and  $Z$ -axis, respectively. The derivation of explicit wave functions  $|JKM\rangle$  is rather lengthy, but they can be stated in a closed form [116, p. 241]:

$$\begin{aligned} |JKM\rangle &= \sqrt{\frac{2J+1}{8\pi^2}} e^{iM\phi} d_{MK}^{(J)}(\theta) e^{iK\chi} \\ &= \sqrt{\frac{2J+1}{8\pi^2}} X_{JKM} e^{iM\phi} e^{iK\chi} \\ &\quad \times \left\{ \sum_{\sigma} (-1)^{\sigma} \frac{(\cos \frac{1}{2}\theta)^{2J+K-M-2\sigma} (-\sin \frac{1}{2}\theta)^{M-K+2\sigma}}{\sigma! (J-M-\sigma)! (M-K+\sigma)! (J+K-\sigma)!} \right\} \end{aligned} \quad (2.26)$$

with:

$$X_{JKM} = \sqrt{(J+M)!(J-M)!(J+K)!(2J+1)}$$

The index  $\sigma$  in the sum runs from 0 or  $K - M$ , whichever is larger, up to  $J - M$  or  $J + K$ , whichever is smaller.

With the knowledge of the angular momentum operator properties and their eigenstates and eigenfunctions, it is possible to solve the rotational Hamiltonian for the different classes of molecules. Because rotational transitions and the corresponding energy levels are mostly in the frequency ranges of MHz and GHz, the rotational Hamiltonian is usually expressed in units of frequency rather than units of energy in rotational spectroscopy. The rotational constants  $A$ ,  $B$ , and  $C$  in units of frequency and with  $A \geq B \geq C$  are:

$$A = \frac{\hbar}{2I_a}, \quad B = \frac{\hbar}{2I_b}, \quad C = \frac{\hbar}{2I_c} \quad (2.27)$$

The rotational Hamiltonian  $\hat{H}_{rid}$  is redefined to have units of frequency:

$$\hat{\mathcal{H}}_{rid} = A\hat{\mathcal{J}}_a^2 + B\hat{\mathcal{J}}_b^2 + C\hat{\mathcal{J}}_c^2 \quad (2.28)$$

where the angular momentum operators are now unitless quantities with  $\hat{\mathcal{J}}_g = \hat{\mathbf{J}}_g/\hbar$  ( $g = x, y, z, X, Y, Z$ ) and  $\hat{\mathcal{J}} = \hat{\mathbf{J}}/\hbar$ . The rotational Hamiltonian of a prolate symmetric-top molecule employing the  $I^r$  representation (for  $B = C$  and with the principal axis  $a$  being the highest symmetry axis) is given by:

$$\begin{aligned} \hat{\mathcal{H}}_{rid} &= A\hat{\mathcal{J}}_a^2 + B(\hat{\mathcal{J}}_b^2 + \hat{\mathcal{J}}_c^2) \\ &= B\hat{\mathcal{J}}^2 + (A - B)\hat{\mathcal{J}}_z^2 \end{aligned} \quad (2.29)$$

Note that the choice of the representation has no effect on the eigenstates and the eigenfunctions, but assigning the  $z$ -axis to the principal axis with the highest symmetry eases the computation of the Hamiltonian dramatically. The symmetric-top Hamiltonian is a function of the operators  $\hat{\mathcal{J}}^2$  and  $\hat{\mathcal{J}}_z^2$ . Thus, the angular momentum eigenfunctions  $|JKM\rangle$  are also eigenfunctions of the symmetric-top Hamiltonian. In the absence of any electromagnetic field, the corresponding energy levels  $\mathcal{E}_{JKM}$  are  $2J + 1$  times degenerate in  $M$  and twofold degenerate in  $K$  with  $\mathcal{E}_{JKM} = \mathcal{E}_{J-KM}$ . The matrix representation of  $\hat{\mathcal{H}}_{rid}$  is diagonal, and the eigenvalues are independent of  $M$ :

$$\mathcal{E}_{rid} = BJ(J+1) + (A - B)K^2 \quad (2.30)$$

The evaluation of the transition dipole moments of symmetric-top molecules leads to the selection rules for pure rotational spectra:  $\Delta J = 0, \pm 1$ ,  $\Delta M = 0$ ,  $\Delta K = 0$  [115]. The selection rule  $\Delta K = 0$  implies that the transition frequency only depends on  $J$ . However, centrifugal distortion splits out the transitions with different  $K$  for a given  $J \rightarrow J+1$  transition, which will be explained later in this section.

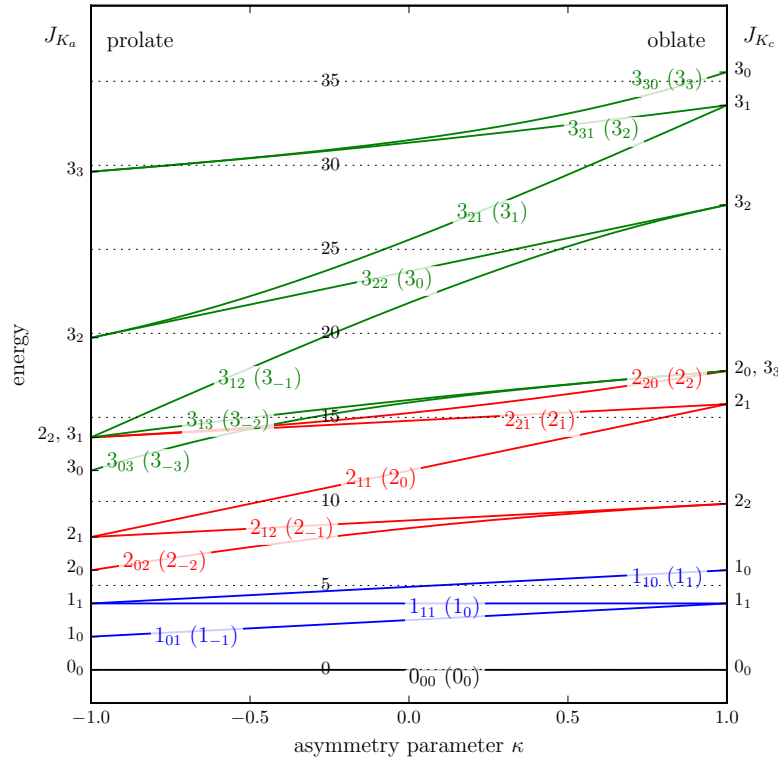


**Figure 2.3:** Rotational energy levels of an asymmetric-top molecule as a function of the asymmetry parameter  $\kappa$ . On the left the quantum numbers for the limiting prolate symmetric top are given and the right y-axis shows the quantum numbers for the limiting oblate top. The asymmetric-top energy levels are labeled by two different schemes: the King-Hainer-Cross notation  $J_{K_a K_c}$  and the energy ordering labeling  $J_\tau$ , where  $\tau$  ranges between  $-K$  and  $K$  and represents the energy ordering of a certain energy level within a  $J$ -stack. The energies are calculated for rotational constants of  $A = 3$ ,  $C = 1$  and a varying  $B$  rotational constant.

A special case of a symmetric-top molecule is the linear molecule with  $A = 0$  and  $C = B$ . For the rotational Hamiltonian in the  $I^r$  representation follows:

$$\hat{\mathcal{H}}_{rid} = B\hat{\mathcal{J}}^2 \quad (2.31)$$

Because  $\hat{\mathcal{J}}_z$  is zero for a linear molecule, the wavefunctions for a linear molecule  $|JM\rangle$  are a subset of the symmetric-top eigenfunctions, independent of the quantum number  $K$  and the Euler angle  $\chi$ . It can be shown that the spherical harmonics  $Y_{JM}(\theta, \phi)$  are simultaneously eigenfunctions of the operators  $\hat{\mathcal{J}}^2$  and  $\hat{\mathcal{J}}_Z$  [112, 115]:

$$|JM\rangle = \sqrt{\frac{1}{2\pi}} Y_{JM}(\theta, \phi) \quad (2.32)$$

The asymmetric-top Hamiltonian (Eqn. 2.28) with  $A \neq B \neq C > 0$  can not be solved analytically anymore. The choice of the representation is in principle arbitrary for an asymmetric



top, but the stability of the numerical methods employed for solving the asymmetric rotor Hamiltonian are greatly enhanced by using the appropriate representation for slightly asymmetric molecules ( $I^r$  representation for a slightly asymmetric prolate top with  $A \gg B > C$  and  $III^r$  representation for a slightly asymmetric oblate top with  $A > B \gg C$ ). Here the Hamiltonian is set up in terms of  $\hat{J}^2$ ,  $\hat{J}_z^2$  and  $\hat{J}_x^2 - \hat{J}_y^2$  employing the  $I^r$  representation:

$$\hat{\mathcal{H}}_{rid} = \frac{1}{2}(A + C)\hat{J}^2 + \left[A - \frac{1}{2}(B + C)\right]\hat{J}_z^2 + \frac{1}{2}(B - C)(\hat{J}_x^2 - \hat{J}_y^2) \quad (2.33)$$

The asymmetric-top Hamiltonian  $\hat{\mathcal{H}}_{rot}$  does not commute with  $\hat{J}_z$  any more, which means that the projection of the total angular momentum on any of the molecule-fixed axes is not constant. Nevertheless, the basis set of the asymmetric-top Hamiltonian can be set up by linear combinations of the angular momentum basis set  $|JKM\rangle$  [117, Chap. 7]. The matrix representation of the rotational Hamiltonian in Equation 2.33 is block diagonal in  $J$  and  $M$  and has only off-diagonal elements in  $K$ . The non-vanishing elements are given by [115]:

$$\langle JKM|\hat{\mathcal{H}}_{rid}|JKM\rangle = \frac{1}{2}(B+C)(J(J+1)-K^2)+AK^2 \quad (2.34)$$

$$\langle JKM|\hat{\mathcal{H}}_{rid}|JK\pm 2M\rangle = \frac{1}{4}(B-C)[(J(J+1)-K(K\pm 1))(J(J+1)-(K\pm 1)(K\pm 2))]^{\frac{1}{2}} \quad (2.35)$$

Each  $J$ -level can be evaluated individually, because the energy matrix is diagonal in  $J$ . Hence, for a specific  $J$ -level the matrix is quadratic with  $2J + 1$  rows and columns, both representing  $K$ -values ranging from  $-J$  to  $+J$ . In comparison to the symmetric-top eigenvalues, the  $\mathcal{E}_{JKM} = \mathcal{E}_{J-KM}$  degeneracy is lifted, but the  $2J + 1$  degeneracy in  $M$  remains in the absence of an electric field.

The asymmetry parameter  $\kappa$  is used to describe the asymmetry of a molecule [41, Chap. 4]:

$$\kappa = \frac{2B - A - C}{A - C} \quad (2.36)$$

For prolate symmetric tops,  $\kappa$  equals  $-1$  and in the oblate symmetric-top limit  $\kappa$  is  $1$  (compare Fig. 2.3). For asymmetric-top molecules, the expectation value of the operator  $\hat{J}_z$  is not constant and the symmetric-top quantum number  $K$  is not suited for labeling the energy levels. Therefore, the energy levels of an asymmetric top are labeled using the King-Hainer-Cross notation with the pseudo quantum numbers  $K_a$  and  $K_c$  indicating the  $K$ -values for the limiting cases of a prolate and oblate symmetric-top molecule, respectively (compare Fig. 2.3) [118]. Also the energy ordering of the levels can be extracted from the  $K_a$  and  $K_c$  values: the difference  $K_a - K_c$  gives the position in the energy level ordering ranging from  $-J$  to  $+J$ . The energy level scheme of an asymmetric-top molecule is illustrated in Figure 2.3 for different values of  $\kappa$ .

The selection rules for an asymmetric top are more complicated than for a symmetric-top molecule because all three dipole moment components along the principle axes can be non-vanishing. Each dipole moment component enables a set of transitions with different selection rules for the pseudo quantum numbers  $K_a$  and  $K_c$ . They are summarized in Table 2.2.

**Table 2.2:** Summary of the different types of possible transitions in an asymmetric-top molecule and the corresponding selection rules for the pseudo quantum numbers  $K_a$  and  $K_c$ .

	dipole	$\Delta K_a$	$\Delta K_c$
<i>a</i> -type	$\mu_a$	$0, \pm 2, \dots$	$\pm 1, \pm 3, \dots$
<i>b</i> -type	$\mu_b$	$\pm 1, \pm 3, \dots$	$\pm 1, \pm 3, \dots$
<i>c</i> -type	$\mu_c$	$\pm 1, \pm 3, \dots$	$0, \pm 2, \dots$

The selection rules for  $J$  and  $M$  are  $\Delta J = 0, \pm 1$  and  $\Delta M = 0$ . Transitions with  $\Delta J = -1$  constitute the *P*-branch and transitions with  $\Delta J = +1$  the *R*-branch. In contrast to symmetric-top molecules, also transitions with  $\Delta J = 0$  appear in the spectrum: the *Q*-branch. In emission spectroscopy only *P*- and *Q*-branch transitions are observed. A permanent dipole moment is a strict requirement for observing pure rotational spectra of any kind of molecule.

In the preceding paragraph, it was assumed for simplicity that molecules are rigid rotors, but real molecules are flexible. Molecular vibrations, internal rotations, and centrifugal forces can distort the geometry of a molecule from its equilibrium. Because vibrations happen on a much faster timescale than the rotation of a molecule, they can be included parametrically into the Hamiltonian. Thus in practice, a different set of rotational constants is used for each normal vibrational mode. Internal rotation and centrifugal distortion can not be treated in an effective manner because they alter or contribute to the angular momenta. Whereas the theory of internal rotation is covered in Section 2.3, the effects of centrifugal distortion are shortly reviewed in the following. In order to correct for centrifugal stretching of the molecule due to its rotation, higher order terms of the angular momenta need to be included into the Hamiltonian. Because of time-reversal symmetry, the odd-order terms vanish and only the even order terms need to be considered [119]:

$$\hat{\mathcal{H}}_{cd} = \hat{\mathcal{H}}_{rid} + \frac{\hbar^4}{4} \sum_{\alpha\beta\gamma\delta} \tau_{\alpha\beta\gamma\delta} \hat{\mathcal{J}}_\alpha \hat{\mathcal{J}}_\beta \hat{\mathcal{J}}_\gamma \hat{\mathcal{J}}_\delta + O(6) + \dots \quad (2.37)$$

$\alpha, \beta, \gamma$  and  $\delta$  can take any value of  $x, y$  and  $z$ . The parameters  $\tau_{\alpha\beta\gamma\delta}$  are related to the force constants within a molecule. In principle the sum in Equation 2.37 has  $3^4 = 81$  components, but Watson demonstrated, that due to symmetry properties and commutation relations, the number of components can be reduced to five determinable linear combinations of fourth-order corrections [119, 120]. Two different reduction schemes have been established in rotational spectroscopy: the A- and the S-reduction. The first one is best suited for most asymmetric-top molecules, the latter one, as the name indicates, is designed for symmetric and slightly asymmetric-top molecules. In the A-reduction, the rotational Hamiltonian including the five

quartic centrifugal distortion constants  $\Delta_J$ ,  $\Delta_{JK}$ ,  $\Delta_K$ ,  $\delta_J$  and  $\delta_K$  is given by [117, Chap. 8]:

$$\begin{aligned}\mathcal{H}_{cd}^{(A)} = & \frac{1}{2}(B^{(A)} + C^{(A)})\hat{\mathcal{J}} + \left[ A^{(A)} - \frac{1}{2}(B^{(A)} + C^{(A)}) \right] \hat{\mathcal{J}}_z^2 \\ & + \frac{1}{2}(B^{(A)} - C^{(A)})(\hat{\mathcal{J}}_x^2 - \hat{\mathcal{J}}_y^2) - \Delta_J \hat{\mathcal{J}}^4 - \Delta_{JK} \hat{\mathcal{J}}^2 \hat{\mathcal{J}}_z^2 - \Delta_K \hat{\mathcal{J}}_z^4 \\ & - 2\delta_J \hat{\mathcal{J}}^2(\hat{\mathcal{J}}_x^2 - \hat{\mathcal{J}}_y^2) + \delta_K \left[ \hat{\mathcal{J}}_z^2(\hat{\mathcal{J}}_x^2 - \hat{\mathcal{J}}_y^2) + (\hat{\mathcal{J}}_x^2 - \hat{\mathcal{J}}_y^2)\hat{\mathcal{J}}_z^2 \right] \\ & + O(6) + \dots\end{aligned}\quad (2.38)$$

For a linear molecule,  $\Delta_J$  is the only non-vanishing distortion constant and directly linked to the interatomic forces. Also for some symmetric-top molecules, the distortion constants can be related to the internuclear forces [121]. But for most asymmetric-top molecules, the distortional constants cannot provide any detailed information of the forces at play inside a molecule because of the number of different force constants involved. Even though the information is limited for this class of molecules, the distortion constants provide an idea of the stiffness of the molecule, especially when compared to other, similar molecules. Quartic distortional constants are usually much smaller than the rotational constants by three to six orders of magnitude, but they are gaining importance for high-resolution measurements and rotational spectra including high  $J$  and/or high  $K$  states. However, the main benefit of the centrifugal distortion terms is the more accurate description of the rotational Hamiltonian, rather than a direct correlation to molecular properties. The rotational constants depend on the order of the correction and the type of reduction employed, which is indicated by the superscript in the Hamiltonian 2.38. The zero-order or 'rigid' rotational constants can be extracted from the 'nonrigid' rotational constants and the centrifugal distortion constants [117]. This becomes crucial when 'rigid' rotational constants are required for structure determination or for comparison with rotational constants calculated by quantum chemistry programs. The matrix representation of the nonrigid Hamiltonian is still diagonal in  $J$  and  $M$  with the following elements [117, Chap. 8]:

$$\begin{aligned}\langle JKM | \hat{\mathcal{H}}_{cd}^{(A)} | JKM \rangle = & \frac{1}{2}(B^{(A)} + C^{(A)})(J(J+1) - K^2) + A^{(A)}K^2 - \Delta_J J^2(J+1)^2 \\ & - \Delta_{JK} J(J+1)K^2 - \Delta_K K^4 + O(6) + \dots\end{aligned}\quad (2.39)$$

$$\begin{aligned}\langle JKM | \hat{\mathcal{H}}_{cd}^{(A)} | JK \pm 2M \rangle = & \left\{ \frac{1}{4}(B^{(A)} - C^{(A)}) + \delta_J J(J+1) + \frac{1}{2}\delta_{JK} [K^2 + (K \pm 2)^2] \right\} \\ & \times [(J(J+1) - K(K \pm 1))(J(J+1) - (K \pm 1)(K \pm 2))]^{\frac{1}{2}} \\ & + O(6) + \dots\end{aligned}\quad (2.40)$$

## 2.2 Hyperfine splitting: Nuclear quadrupole coupling

Most concepts for fine and hyperfine splittings in molecular spectra can be adapted from atoms. For atoms, spin-orbit coupling of the electrons and the interaction of the magnetic nuclear moment with the magnetic fields of the electrons are the main source of fine and hyperfine splittings. However, the ground state of the molecules investigated herein is a

$^1\Sigma$  state with no electronic angular momentum and a vanishing electronic spin, because all electrons are paired in a closed-shell configuration. As a consequence, the main contribution to the fine and hyperfine splitting in atomic spectra are negligible for most ground-state molecules. Of course, excited electronic states or the corresponding molecular ions may still account for nonzero electronic angular momenta or electronic spin. Hence, the more important hyperfine interaction within these ground-state molecules is the coupling of the nuclear charge density  $\rho(\mathbf{r})$  with the electric potential  $V(\mathbf{r})$  generated by the electrons and the other nuclei:

$$E_Q = \int \rho(\mathbf{r}) V(\mathbf{r}) d\mathbf{r} \quad (2.41)$$

with the integral evaluated over the whole nuclear volume. The potential produced by the extranuclear charges can be expressed in a multipole expansion and the interaction is thus given by:

$$E_Q = \underbrace{V(0) \int \rho d\mathbf{r}}_{\text{monopole term}} + \underbrace{\sum_{i=0}^3 \frac{\partial V}{\partial x_i} \Big|_{\mathbf{r}=0} \int x_i \rho d\mathbf{r}}_{\text{dipole term}} + \underbrace{\frac{1}{2} \sum_{i=0}^3 \sum_{j=0}^3 \frac{\partial^2 V}{\partial x_i \partial x_j} \Big|_{\mathbf{r}=0} \int x_i x_j \rho d\mathbf{r}}_{\text{quadrupole term}} + \dots \quad (2.42)$$

where the  $x_i$  are the Cartesian coordinates  $x, y, z$ . The integration of the monopole term gives the constant  $ZeV(0)$ , where  $Z$  is the atomic number of the nucleus. For symmetry reasons, the dipole moment of the nuclear charge distribution vanishes for all nuclei [41, Chap. 5]. Hence, the nuclear quadrupole moment is the first nonzero and non-constant term in the series accessible by spectroscopic measurements. The motion and the nuclear charge distribution is dependent on the nuclear spin angular momentum operator  $\hat{\mathbf{I}}$ . The eigenvalues of the total nuclear spin operator  $\hat{\mathbf{I}}^2$  in the nuclear spin basis  $|IM_I\rangle$  are:

$$\hat{\mathbf{I}}^2 |IM_I\rangle = \hbar^2 I(I+1) \quad (2.43)$$

It can be shown that the quadrupole moment vanishes for nuclei with a spin smaller than one [115]. However, many atoms have at least one isotope with a nuclear spin equal or larger than one, but often this isotope is not the most abundant one or is unstable. Prominent examples of stable quadrupolar nuclei are nitrogen  $^{14}\text{N}$  with  $I = 1$ , chlorine  $^{35}\text{Cl}$  and  $^{37}\text{Cl}$  with  $I = 3/2$ , bromine  $^{81}\text{Br}$  and  $^{79}\text{Br}$  with  $I = 3/2$  and iodine  $^{127}\text{I}$  with  $I = 5/2$ . Also metals have significant nuclear quadrupole moments, and some have been studied employing microwave spectroscopy in the recent past [122–124]. A compilation of nuclear spins and quadrupole moments of most isotopes is provided by the International Union of Pure and Applied Chemistry (IUPAC) [125].

Because the electric potential  $V$  must satisfy the Laplace equation, the quadrupole term in Equation 2.41 can be expressed as a quantum-mechanical Hamiltonian with the tensors of second rank  $\hat{Q}_{ij}$  and  $\hat{V}_{ij}$  [115]:

$$\hat{H}_Q = \frac{1}{6} \hat{Q}_{ij} \cdot \hat{V}_{ij} = \frac{1}{6} \sum_i \sum_j \hat{Q}_{ij} \hat{V}_{ij} \quad (2.44)$$

with

$$\hat{V}_{ij} = \left. \frac{\partial^2 V}{\partial x_i \partial x_j} \right|_{\mathbf{r}=0} \quad (2.45)$$

and

$$\hat{Q}_{ij} = \int (3x_i x_j - \delta_{ij} \mathbf{r}^2) \rho d\mathbf{r} \quad (2.46)$$

For an atomic nucleus, the operator  $\hat{Q}_{ij}$  can be rewritten in terms of the nuclear spin operator  $\hat{\mathbf{I}}$ . The non-trivial derivation includes irreducible tensor methods, Glebsch-Gordan coefficients, and the Wigner-Eckart theorem. Charles Slichter provides a good review in his book [126]. Here only the final result is stated:

$$\hat{H}_Q = \frac{eQ}{6I(2I-1)} \sum_i \sum_j \hat{V}_{ij} \left[ \frac{3}{2} (\hat{I}_i \hat{I}_j + \hat{I}_j \hat{I}_i) - \delta_{ij} \hat{\mathbf{I}}^2 \right] \quad (2.47)$$

The quantity  $Q$  represents the quadrupolar moment of the nucleus (as tabulated in Ref. [125]), and  $e$  is the elementary charge. Its product is given by the matrix element of the operator component  $\hat{Q}_{zz}$ , where  $z$  is pointing along the direction of the nuclear spin:

$$eQ = \langle IM_I = I | \hat{Q}_{zz} | IM_I = I \rangle \quad (2.48)$$

Note that  $\hat{Q}_{zz}$  is the only relevant component of the tensor operator  $\hat{Q}_{ij}$  for deriving the quadrupolar moment. This result is due to the fact that the nuclear charges are moving rapidly along the  $z$ -axis and consequently the charge distribution appears cylindrically symmetric. Therefore the quadrupolar moment is a measure of the deviation of the nuclear charge distribution from spherical symmetry. For a positive  $Q$ , the charge distribution is elongated along  $z$ .  $Q$  has negative values for a flattened charge distribution [41, Chap. 5].

The general Hamiltonian in Equation 2.47 holds for all kinds of substances with quadrupolar nuclei: solids, liquids and gases. For rotational spectroscopy, the molecules under study need to be in the gas phase and thus the nuclear spin  $\hat{\mathbf{I}}$  and the angular momentum of the molecule  $\hat{\mathbf{J}}$  couple to the total angular momentum  $\hat{\mathbf{F}}$  with  $\hat{\mathbf{F}} = \hat{\mathbf{J}} + \hat{\mathbf{I}}$ . The angular momenta  $\hat{\mathbf{J}}$  and  $\hat{\mathbf{I}}$  are precessing about  $\hat{\mathbf{F}}$ , while  $\hat{\mathbf{F}}$  is precessing about a space-fixed axis and only the absolute value of the total angular momentum  $\hat{\mathbf{F}}^2$  and one of its components  $\hat{F}_Z$  can be measured simultaneously. The corresponding eigenvalues in the product basis of the angular momentum eigenfunctions  $|JKM\rangle$  and the nuclear spin eigenfunctions  $|IM_I\rangle$  are:

$$\hat{\mathbf{F}}^2 |JKIM_F\rangle = \hbar^2 F(F+1) \quad (2.49)$$

$$\hat{F}_Z |JKIM_F\rangle = M_F \hbar \quad (2.50)$$

$$\hat{\mathbf{I}}^2 |JKIM_F\rangle = \hbar^2 I(I+1) \quad (2.51)$$

with

$$\begin{aligned} F &= J+I, J+I-1, \dots, |J-I| \\ M_F &= F, F-1, \dots, -F \end{aligned}$$

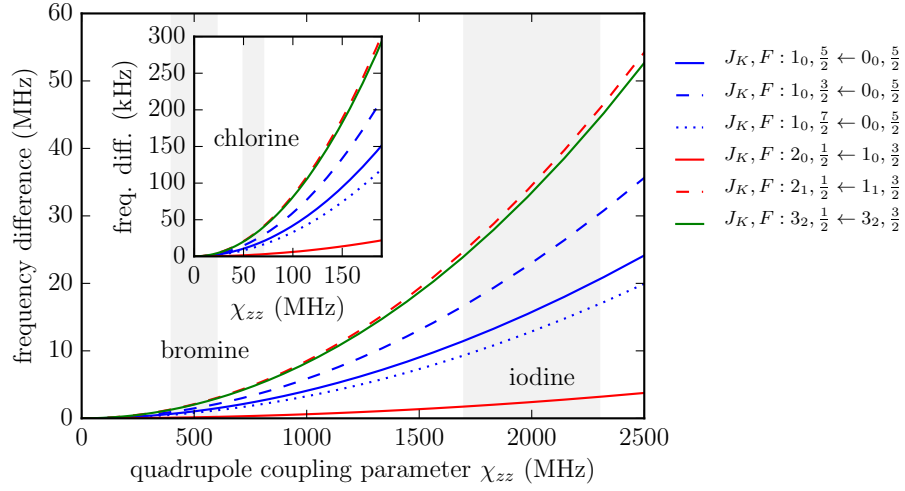


**Figure 2.4:** The frequency differences for two implementations of the quadrupole coupling Hamiltonian for different values of the quadrupole coupling constant  $\chi_{zz}$ . Various transitions of a symmetric-top molecule ( $B = 890$  MHz) are used to compare the prediction of the program XIAM neglecting terms in the Hamiltonian that are off-diagonal in  $J$  and the prediction of the program SPCAT that considers all relevant terms of the Hamiltonian. The difference between the two implementations depends heavily on the quantum numbers  $J$ ,  $K$  and  $F$  involved in the transition. The values of the quadrupole coupling constant  $\chi_{zz}$  of the halogens chlorine ( $\chi_{zz} \approx 50 - 70$  MHz), bromine ( $\chi_{zz} \approx 400 - 600$  MHz), and iodine ( $\chi_{zz} \approx 1700 - 2300$  MHz) suggest that already for the description of the quadrupole coupling of chlorine, the use of the full Hamiltonian is recommended in high-resolution microwave spectroscopy.

The quadrupolar moment operator  $\hat{Q}_{ij}$  in the Hamiltonian (Eqn. 2.44) is set up in the nuclear spin axis system with the  $z$ -axis pointing along the nuclear spin. Hence the electric field gradient operator  $\hat{V}_{ij}$  needs to be expressed in the same space-fixed axis system. Thus for a rotating molecule the electric field gradient operator becomes dependent on the angular momentum operator  $\hat{\mathbf{J}}$  describing the rotation of the molecule. Averaged over the molecular rotation, the charge distribution is cylindrically symmetric along an axis  $z_J$  parallel to  $\hat{\mathbf{J}}$ . Employing the Laplace equation it can be shown that the Hamiltonian is only dependent on  $\frac{\partial^2 V}{\partial z_J^2}$ .

In general, the matrix representation of the Hamiltonian  $\hat{H}_Q$  is not diagonal in  $J$ , because the quadrupole coupling alters the rotational wavefunctions.  $J$  is therefore not a 'good' quantum number anymore. Benz et al. derived the matrix elements of  $\hat{H}_Q$  using irreducible tensor operator methods [127]. However, for small quadrupolar moments the off-diagonal terms are negligible, because  $\hat{\mathbf{J}}$  almost coincides with  $\hat{\mathbf{F}}$ . In this case,  $\hat{H}_Q$  can be expressed in terms of nuclear spin and angular momentum operators [117, Chap. 9]:

$$\hat{H}_Q = \frac{eQq_J}{2(2J-1)I(2I-1)} \left[ 3(\hat{I} \cdot \hat{J})^2 + \frac{3}{2}\hat{I} \cdot \hat{J} - \hat{I}^2 \hat{J}^2 \right] \quad (2.52)$$

where  $q_J$  describes the expectation value of the electric field gradient at the position of the nucleus along  $z_J$ :

$$q_J = \left\langle JKM = J \left| \frac{\partial^2 V}{\partial z_J^2} \right| JKM = J \right\rangle \quad (2.53)$$

The corresponding energies are given by [117, Chap. 9]:

$$\begin{aligned} E_Q &= \frac{eQq_J}{J} \frac{\frac{3}{4}C(C+1) - I(I+1)J(J+1)}{2(2J-1)I(2I-1)} \\ C &= F(F+1) - I(I+1) - J(J+1) \end{aligned} \quad (2.54)$$

Whether the simplified Hamiltonian in Equation 2.52 can be used or not is firstly a question of the magnitude of the quadrupolar moment and secondly dependent on the spectral resolution of the experiment. In Figure 2.4, the difference for various transition frequencies obtained by including off-diagonal elements on one hand and by neglecting the off diagonal elements on the other hand are plotted for a symmetric-top molecule ( $B = 890$  MHz) against the magnitude of a virtual quadrupolar moment. The graph shows that for chlorine, bromine, and iodine the off-diagonal terms are not negligible in state-of-the-art microwave spectrometers.

The scalar molecular property  $eQq_J$  is usually expressed in the principal axis system of the molecule, because these quantities are determined experimentally:

$$\chi^{(2)} = eQq^{(2)} = \begin{pmatrix} \chi_{aa} & \chi_{ab} & \chi_{ac} \\ \chi_{ba} & \chi_{bb} & \chi_{bc} \\ \chi_{ca} & \chi_{cb} & \chi_{cc} \end{pmatrix} \quad (2.55)$$

with the elements of the second-order tensor  $q^{(2)}$ :  $q_{\alpha\beta} = \frac{\partial^2 V}{\partial \alpha \partial \beta}$ , where  $\alpha$  and  $\beta$  can take any of the values  $a$ ,  $b$  and  $c$ . For weakly coupling nuclei, such as nitrogen and chlorine, only the diagonal elements of  $\chi^{(2)}$  are experimentally accessible. Furthermore,  $\chi^{(2)}$  is symmetric and traceless ( $\chi_{aa} + \chi_{bb} + \chi_{cc} = 0$ ).

Upon diagonalization  $\chi^{(2)}$  is rotated into the principal axis system of the field gradient, with the diagonal elements  $\chi_{xx}$ ,  $\chi_{yy}$  and  $\chi_{zz}$ . For diagonalizing  $\chi^{(2)}$ , the off-diagonal elements are also needed, but they are usually not determined by experiments and, if so, they usually bear large errors (besides strongly coupling nuclei, such as iodine or rhenium). They are usually taken from quantum chemical calculations, which are capable of predicting the elements of  $\chi^{(2)}$  to an acceptable accuracy, depending on the quadrupolar nuclei. The largest component is assigned to  $\chi_{zz}$ , which points along the bond direction.

The field gradient provides valuable information about the charge distribution in the vicinity of the quadrupolar nucleus. This information is linked to the character of the chemical bond in which the quadrupolar atom is involved, assuming that the atom is only bound to one other atom. For axially symmetric bonds (such as  $\sigma$ -bonds) the following relation holds:  $\chi_{xx} = \chi_{yy} = -\frac{1}{2}\chi_{zz}$ . Any deviation from axial symmetry reflects itself in the asymmetry

**Table 2.3:** Compilation of the atomic spin  $I$ , its quadrupole moment  $Q$ , and the value of the atomic quadrupole coupling constant  $eQq_{n10}$ , where the subscript  $n10$  labels a  $p$ -state with the atomic main quantum number  $n$ .

		$I$	$Q$ (fm <sup>2</sup> ) <sup>1</sup>	$eQq_{n10}$ (MHz) <sup>2</sup>
deuterium	<sup>2</sup> H	1	+0.286 (2)	-
nitrogen	<sup>14</sup> N	1	+2.001 (10)	-10 ( $n = 2$ )
chlorine	<sup>35</sup> Cl	3/2	8.50 (11)	+109.74 ( $n = 3$ )
	<sup>37</sup> Cl	3/2	-6.44 (7)	+86.51 ( $n = 3$ )
bromine	<sup>79</sup> Br	3/2	31.8 (5)	-769.76 ( $n = 4$ )
	<sup>81</sup> Br	3/2	+26.6 (4)	-643.03 ( $n = 4$ )
iodine	<sup>127</sup> I	5/2	72.0 (20)	+2292.71 ( $n = 5$ )

<sup>1</sup> all values from Reference [125]

<sup>2</sup> all values from Reference [117, Chap. 14]

parameter  $\eta$  [117, Chap. 14]:

$$\eta = \frac{\chi_{xx} - \chi_{yy}}{\chi_{zz}} \quad (2.56)$$

For example, a double bond is expected to give rise to a nonzero asymmetry parameter. In planar molecules a good measure for the  $\pi$ -bonding nature is the Goldstein parameter  $\delta$  [128]:

$$\delta = \frac{2}{3} \frac{\chi_{xx} - \chi_{yy}}{eQq_{n10}} \quad (2.57)$$

The parameter  $q_{n10}$  is the field gradient produced by the  $p$ -electrons of the atoms. Hence, it is an atomic quantity, which can be measured precisely by atomic beam resonance experiments. There is evidence that  $d$ -electrons are more effectively screened from the nucleus than  $p$ -electrons, which contribute most to the electric field gradient at the nuclear position [117, Chap. 14]. The values of  $Q$  and  $eQq_{n10}$  for various elements are listed in Table 2.3.

Maybe the most general information deduced from the nuclear quadrupole coupling hyperfine splitting is  $i_c$ , a parameter describing the ionic character of the bond [117, Chap. 14]:

$$i_c = 1 + \frac{\chi_{zz}}{eQq_{n10}} \quad (2.58)$$

$i_c$  is zero for completely covalently bound atoms with quadrupolar nuclei and one for totally ionic bonds.

Other approaches have been derived in the past to extract more information about the bond nature from the nuclear quadrupole coupling constants. Townes and Schawlow present a theory to exploit the quadrupole coupling constant for the determination of the electronic structure. But their theory depends on assumptions that make them applicable only to



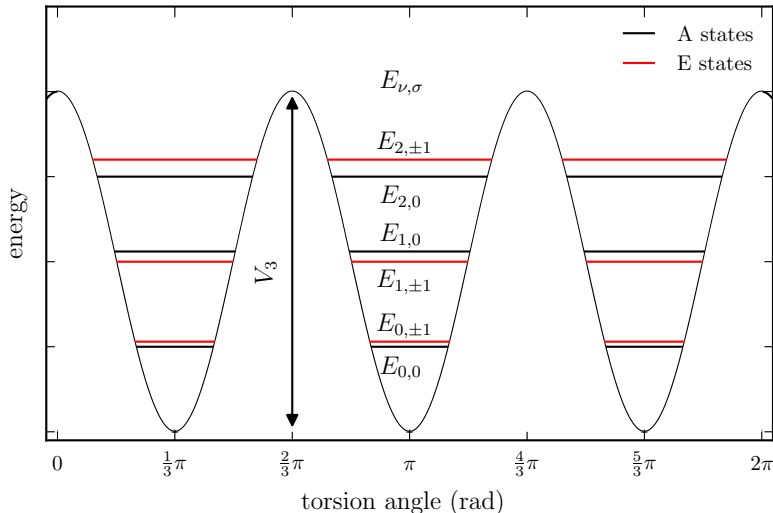


**Figure 2.5:** Three fold barrier of an internal rotor with  $C_{3V}$ -symmetry, i.e. methyl group. The horizontal lines represent the energy levels of the internal rotor and they are marked with the harmonic oscillator quantum number  $\nu$  and the symmetry label  $\sigma$ .

specific classes of molecules [129, Chap. 9].

The selection rules for  $J$  and  $K$  (or  $K_a$  and  $K_c$ ) of symmetric or asymmetric-top molecules are still valid. In addition the selection rules for the quantum number  $F$  and  $M_F$  are given by [115]:

$$\Delta F = 0, \pm 1 \quad (2.59)$$

$$\Delta M_F = 0, \pm 1 \quad (2.60)$$

Because the rotational energy levels split up into various  $F$ -sublevels (compare Eqn. 2.54), the rotational transitions exhibit a hyperfine structure. For example for a molecule containing one atom with a nuclear spin of  $I = 3/2$ , nine hyperfine components are present for transitions involving  $J', J'' > 2$ . In symmetric-top molecules the  $K$ -degeneracy of the transitions is lifted. The hyperfine pattern collapses quickly with increasing  $J$ , so that low  $J$  transitions are best suited to study nuclear quadrupole coupling.

### 2.3 Internal rotation

Internal rotation is an important example of intramolecular large amplitude motion. Large amplitude motion refers to internal movement with amplitudes on the order of the molecular bond length, which may alter the molecular structure significantly or convert the molecule from one equivalent structure to another one via tunneling. Large amplitude motions are usually the result of shallow double or even multi-well potentials, where the conventionally

isolated rotational and vibrational degrees of freedom are coupled. Depending on the temperature of the molecular sample, large amplitude motion includes large librational oscillations in a shallow potential (mostly observed in molecular clusters), soft internal rotations (like methyl group internal rotation), inversion motions (e.g. inversion of an amino group), proton tunneling, ring puckering, and structural isomerizations.

For this work, only the internal rotation of the methyl group, a symmetric rotor with  $C_{3V}$ -symmetry, is of interest. The one-dimensional rotation of a bound methyl group in the molecular potential  $V(\alpha)$  is described by the following Schrödinger equation:

$$\hat{H}\varphi(\alpha) = \left[ -F \frac{\partial^2}{\partial \alpha^2} + V(\alpha) \right] \varphi(\alpha) = E\varphi(\alpha) \quad (2.61)$$

where  $\alpha$  is the rotation angle and  $F$  is the reduced rotational constant for the motion of the methyl rotor relative to the remaining molecular framework (defined in Eqn. 2.69). Because of the symmetry properties of the methyl top, the potential  $V(\alpha)$  can be expanded in the following manner:

$$V(\alpha) = \frac{V_3}{2} (1 - \cos 3\alpha) + \frac{V_6}{2} (1 - \cos 6\alpha) + O(9) + \dots \quad (2.62)$$

For most molecules, the expansion can be truncated after the first term, but for some molecules with certain symmetry properties higher order terms gain importance. The  $V_3$  part of the potential even vanishes for toluene or *p*-substituted halotoluenes (see Chap. 4).

For simplicity only three-fold barriers are considered here, where all but the  $V_3$  coefficient vanish in the expansion. The shape of such a potential is illustrated in Figure 2.5. The solutions for the Hamiltonian in Equation 2.61 are easily obtained for the two limiting cases  $V_3 \rightarrow 0$  and  $V_3 \rightarrow \infty$ . For the free rotor case ( $V_3 = 0$ ) the eigenfunctions  $\varphi^{(0)}(\alpha)$  and the energy eigenvalues  $E^{(0)}$  have the form [117, Chap. 12]:

$$\varphi^{(0)}(\alpha) = Ae^{im\alpha} \quad (2.63)$$

$$E^{(0)} = Fm^2 \quad (2.64)$$

The values for the quantum number  $m = 0, \pm 1, \pm 2, \dots$  are obtained by applying the boundary conditions  $\varphi^{(0)}(\alpha) = \varphi^{(0)}(\alpha + 2\pi)$ . Each level is twofold degenerate, which corresponds to the different directions of the rotation in a classical picture. For high barriers,  $V_3 \rightarrow \infty$ , the potential can be expanded in  $\cos 3\alpha$  around small values of  $\alpha$  in a Taylor series:

$$\cos 3\alpha = 1 - \frac{9}{2}\alpha^2 + \frac{27}{8}\alpha^4 + \dots \quad (2.65)$$

If the expansion is truncated after the quadratic term, the well known harmonic oscillator wavefunctions are solutions for the Hamiltonian with the energies [117, Chap. 12]:

$$E^{(\infty)} = \sqrt{3V_3F} \left( \nu + \frac{1}{2} \right) \quad (2.66)$$

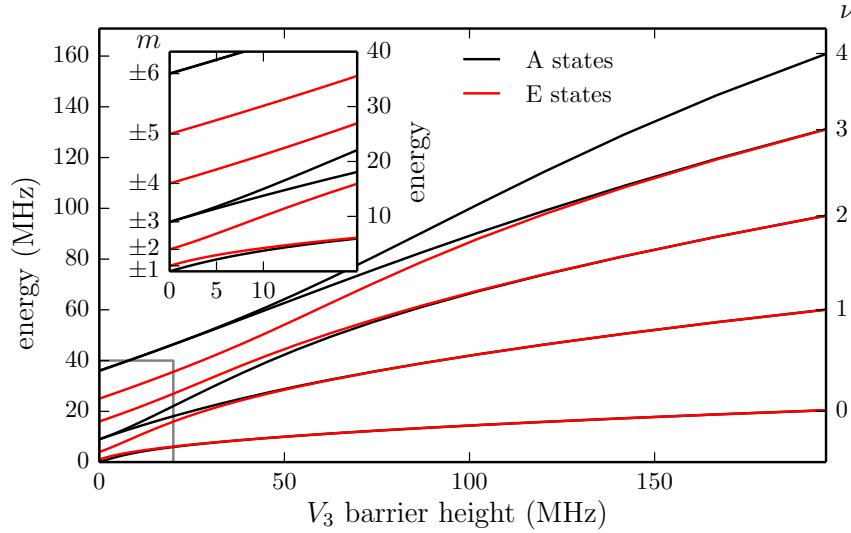


**Figure 2.6:** Energy levels of an internal rotor as a function of the barrier height of a three-fold potential. The reduced rotation constant  $F$  was set to 1 MHz. In the limit  $V_3 \rightarrow 0$ , the energies are twofold degenerate and coincide with the free rotor energies (quantum number  $m$ ) as can be seen in the inset. For  $V_3 \rightarrow \infty$  the energies are threefold degenerate and converge to the harmonic oscillator energies (quantum number  $\nu$ ).

The quantum number  $\nu$  can take the integer values  $0, 1, 2, \dots$  and each of the vibrational sublevels is triply degenerate, which corresponds to a vibration in every well of the potential. If the barrier has finite height, tunneling through the barrier can occur and the formerly triply degenerate vibrational sublevels split into two degenerate levels designated with the symmetry label E (and the quantum number  $\sigma = \pm 1$ ) and one nondegenerate level A (and the quantum number  $\sigma = 0$ ). Hence, the newly introduced quantum number  $\sigma$  defines the symmetry of the corresponding torsional wavefunction. For the general problem with a finite value of  $V_3$ , the Schrödinger equation can be rewritten as a Mathieu equation [130]. The solutions are given by the following Fourier series:

$$\varphi_{\nu\sigma}(\alpha) = |\nu\sigma\rangle = \sum_{k=-\infty}^{\infty} A_k^{(\nu)} e^{i(3k+\sigma)\alpha} \quad (2.67)$$

The calculation of the eigenvalues and the  $A_k^{(\nu)}$  coefficients is described in Reference [117, Chap. 12]. In Figure 2.6 the energies of the internal rotor are plotted versus the potential height. For  $V_3 \rightarrow 0$  the energies are twofold degenerate and coincide with the free rotor energies and for  $V_3 \rightarrow \infty$  the energies are threefold degenerate and coalesce with the harmonic oscillator energies.

For deriving the Hamiltonian, which includes both the overall and the internal rotations, one needs to consider the coupling of these two motions. Neglecting any distortional effects, the rotational Hamiltonian of a molecule with one internal rotor is expressed in the principal axis

system (PAS) [117, Chap. 12]:

$$\hat{\mathcal{H}}_{int} = A\hat{\mathcal{J}}_a^2 + B\hat{\mathcal{J}}_b^2 + C\hat{\mathcal{J}}_c^2 + F\left(\hat{\mathbf{j}}_\alpha - \rho_a\hat{\mathcal{J}}_a - \rho_b\hat{\mathcal{J}}_b - \rho_c\hat{\mathcal{J}}_c\right)^2 + V(\alpha) \quad (2.68)$$

with

$$\hat{j}_\alpha = -i\frac{\partial}{\partial\alpha}, \quad \rho_g = \frac{\lambda_g I_\alpha}{I_g}, \quad g = a, b, c$$

and

$$F = \frac{\hbar}{2rI_\alpha}, \quad r = 1 - \sum_{g=a,b,c} \lambda_g^2 \frac{I_\alpha}{I_g} \quad (2.69)$$

The angular momentum operator of the internal rotor  $\hat{\mathbf{j}}_\alpha$  is expressed in the principle axis system and  $I_\alpha$  represents the moment of inertia of the internal rotor. The orientation of the internal rotor in the principle axis system is defined by the direction cosines  $\lambda_a$ ,  $\lambda_b$ , and  $\lambda_c$ . The cross terms  $-2\hat{\mathbf{j}}_\alpha\rho_g\hat{\mathcal{J}}_g$  impede a separation of the Hamiltonian because they depend on both the asymmetric rotor basis  $|JKM\rangle$  and the torsional wavefunctions  $|\nu\sigma\rangle$ . If the barrier is high, the separation of the torsional energy levels of different  $\nu$  is large compared with the rotational levels. Hence, the internal motion can be included parametrically into the Hamiltonian as perturbations. Applying a Van Fleck transformation, the Hamiltonian can be rewritten for a specific torsional state  $|\nu\sigma\rangle$  [130]:

$$\hat{\mathcal{H}}_{int,\nu\sigma} = A\hat{\mathcal{J}}_a^2 + B\hat{\mathcal{J}}_b^2 + C\hat{\mathcal{J}}_c^2 + F \sum_n W_{\nu\sigma}^{(n)} \left(\rho_a\hat{\mathcal{J}}_a + \rho_b\hat{\mathcal{J}}_b + \rho_c\hat{\mathcal{J}}_c\right)^n \quad (2.70)$$

with the first three perturbation coefficients:

$$W_{\nu\sigma}^{(0)} = E_{\nu\sigma} \quad (2.71)$$

$$W_{\nu\sigma}^{(1)} = -2 \left\langle \nu\sigma \left| \hat{j} \right| \nu\sigma \right\rangle \quad (2.72)$$

$$W_{\nu\sigma}^{(2)} = 1 + 4F \sum_{\nu'} \frac{\left| \left\langle \nu\sigma \left| \hat{j} \right| \nu'\sigma \right\rangle \right|^2}{E_{\nu\sigma} - E_{\nu'\sigma}} \quad (2.73)$$

For a small reduced barrier  $s = \frac{4V_3}{9F}$  or when  $\rho$  and  $K$  are both large, many terms of the perturbation series must be taken into account. This effect limits the procedure to high barrier cases where a rapid convergence of the perturbation series allows most of the higher order terms to be ignored. Note, odd perturbation terms vanish for A states ( $\sigma = 0$ ). This implementation of the internal motion is called the principal axis method (PAM) and was successfully applied by Gerhard and coworkers on *o*-chlorotoluene [131]. They also provide a detailed description of the fitting procedure using the SPFIT program.

To overcome the drawbacks of not including the terms  $-2\hat{\mathbf{j}}_\alpha\rho_g\hat{\mathcal{J}}_g$  directly in the PAM Hamiltonian, two other methods have been proposed: the rho axis method (RAM) and the internal axis method (IAM). In the RAM, the coordinate system is rotated such that the  $z$  axis is parallel to  $\boldsymbol{\rho}$ , which implies that  $\rho_x$  and  $\rho_y$  are zero. Then only the term  $-2\hat{\mathbf{j}}_\alpha\rho_z\hat{\mathcal{J}}_z$  is non-vanishing and is also diagonal in the quantum number  $K$ . This approach enables the

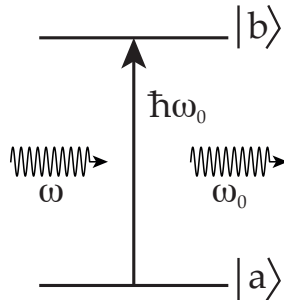


**Figure 2.7:** Two-level system with a ground state  $|a\rangle$  and an excited state  $|b\rangle$ . A photon with the energy  $\hbar\omega$  can transfer the system from the ground state to the excited state. The system decays after some time by stimulated or spontaneous emission. The photon emitted is resonant to the transition with the energy  $\omega_0 = (E_b - E_a)/\hbar$ .

separation of the torsional and rotational parts of the Hamiltonian, but the torsional part remains  $K$  dependent. The RAM Hamiltonian can be expressed as periodic solutions to the Mathieu equation, but the definition differs for the different programs employing this method: Belgi [132], ERHAM [133], the SPFIT front-end IAMCALC [134], and RAM36 [135]. For obvious reasons, the RAM is not applicable for molecules with more than one internal rotor. However, Woods proposed to use a combination of the RAM and the PAM, the combined axis method (CAM) [136, 137]. Hartwig et al. developed the program XIAM, which employs the CAM and is capable of handling molecules with up to three internal rotors [138]. In the XIAM program, the torsional states are evaluated in their individual rho-axis system and rotated to the principal axis system afterwards. In the IAM the term  $-2\hat{\mathbf{j}}_\alpha \rho_z \hat{\mathcal{J}}_z$  is eliminated by a second rotation, but the mathematical description of the Hamiltonian becomes complicated [139]. Thus, no program was developed employing this method up to now.

## 2.4 Bloch equations

In the proceeding sections, the unperturbed rotational Hamiltonian was derived. However to spectroscopically obtain information about the different energy levels of the molecule, the interaction with electromagnetic fields needs to be considered. To account for the interaction, the unperturbed rotational Hamiltonian  $\hat{\mathcal{H}}_0$  is extended by a time dependent interaction term  $\hat{V}(t)$ . Usually  $\hat{\mathcal{H}}_0$  is expressed as diagonal matrix with the unperturbed energy eigenvalues on the main diagonal and  $\hat{V}(t)$  adds off-diagonal elements describing the coupling of the different states via the electromagnetic radiation [140]. For simplicity, the following discussion is limited to two coupling states. In the case of an isolated system of two non-degenerate eigenstates  $|a\rangle$  and  $|b\rangle$  (compare Fig. 2.7), the unperturbed Hamiltonian  $\hat{\mathcal{H}}_0$  can be written:

$$\hat{\mathcal{H}}_0 = \begin{pmatrix} E_a & 0 \\ 0 & E_b \end{pmatrix} \quad (2.74)$$

The interaction is induced by a linearly polarized electromagnetic wave  $\mathbf{F}$  propagating along the  $y$ -axis with the field amplitude  $\mathcal{E}(\mathbf{r}, t)$ :

$$\mathbf{F} = \left( \frac{1}{2} \mathcal{E}(\mathbf{r}, t) \mathbf{e}_z e^{i(ky - \omega t)} + \frac{1}{2} \mathcal{E}^*(\mathbf{r}, t) \mathbf{e}_z e^{-i(ky - \omega t)} \right) \quad (2.75)$$

where  $\omega$  is the angular frequency and  $k$  is the wave vector along the  $y$ -axis. For this example the field amplitude  $\mathcal{E}$  is chosen such that it is a real quantity and constant in space and time. Furthermore, the propagation term  $ky$  is neglected, because the interaction volume is assumed to be much smaller than the wavelength of the radiation (electric dipole approximation). The electromagnetic radiation  $\mathbf{F}$  is then:

$$\mathbf{F} = \frac{1}{2} \mathcal{E} \mathbf{e}_z (e^{i\omega t} + e^{-i\omega t}) \quad (2.76)$$

The interaction Hamiltonian  $\hat{V}$  is given by the product of the space-fixed dipole moment operator  $\hat{\mu}$  and the electromagnetic field  $\mathbf{F}$ :

$$\hat{V}(t) = \hat{\mu} \cdot \mathbf{F} = \begin{pmatrix} 0 & \mu_{ab} \\ \mu_{ba} & 0 \end{pmatrix} \cdot \mathbf{F} = \begin{pmatrix} 0 & \mu \\ \mu & 0 \end{pmatrix} \cdot \mathbf{F} \quad (2.77)$$

The transition dipole moment  $\mu_{ab}$  is the complex conjugate of the transition dipole moment  $\mu_{ba}$ . If  $\mu_{ab}$  is a real quantity ( $\mu_{ab} = \mu_{ba}^* = \mu_{ba} \equiv \mu$ ) and the quantization axis of the molecule is chosen to be parallel to the electromagnetic radiation (in this case along the  $z$ -axis), the Hamiltonian of the system  $\hat{\mathcal{H}}$  can be expressed by:

$$\hat{\mathcal{H}} = \hat{\mathcal{H}}_0 - \hat{V} = \begin{pmatrix} E_a & -\frac{1}{2} \mu \mathcal{E} (e^{i\omega t} + e^{-i\omega t}) \\ -\frac{1}{2} \mu \mathcal{E} (e^{i\omega t} + e^{-i\omega t}) & E_b \end{pmatrix} \quad (2.78)$$

In rotational spectroscopy, a single molecule in a specific quantum state is not probed, but rather many molecules in a statistical ensemble of quantum states. These mixed states are best described by the density matrix formalism introduced by von Neumann [141]. Mixed quantum states and the density matrix formalism are explained in detail elsewhere [142], so that here only the important results and properties are stated. The density operator is defined by:

$$\hat{\rho} = \sum_n p_n |\psi_n\rangle \langle \psi_n| \quad (2.79)$$

where  $p_n$  is the probability to encounter a single quantum system of the mixture in the state  $|\psi_n\rangle$ . The density operator can be expressed in a matrix representation using a convenient set of  $N$  basis states [142, Chap. 2]. The corresponding density matrix is a Hermitian  $N \times N$  matrix with a trace of one. The diagonal elements represent the population of the different states, and the off-diagonal elements characterize the coherences between the different states. The density matrix contains the whole information of the statistical ensemble and especially

the expectation value of any observable  $\hat{A}$  is given by:

$$\langle \hat{A} \rangle = \text{Tr} (\hat{\rho} \hat{A}) \quad (2.80)$$

The time evolution of the density matrix is predicted by the Liouville equation:

$$i\hbar \frac{\partial \hat{\rho}(t)}{\partial t} = [\hat{\mathcal{H}}(t), \hat{\rho}(t)] \quad (2.81)$$

The density matrix for the two-level system discussed previously and illustrated in Figure 2.7 is defined by:

$$\hat{\rho} = \begin{pmatrix} \rho_{aa} & \rho_{ab} \\ \rho_{ba} & \rho_{bb} \end{pmatrix} \quad (2.82)$$

Before the time evolution of the density matrix elements is derived, the Hamiltonian can be simplified by applying the rotating wave approximation (RWA), which is conveniently done in the interaction picture. After transforming the Hamiltonian back to the Schrödinger picture, the evaluation of the Liouville equation yields:

$$\frac{\partial \rho_{aa}}{\partial t} = \dot{\rho}_{aa} = -i\frac{\Omega}{2} (\rho_{ab}e^{-i\omega t} - \rho_{ba}e^{i\omega t}) \quad (2.83)$$

$$\dot{\rho}_{bb} = i\frac{\Omega}{2} (\rho_{ab}e^{-i\omega t} - \rho_{ba}e^{i\omega t}) \quad (2.84)$$

$$\dot{\rho}_{ab} = i\omega_0\rho_{ab} - i\frac{\Omega}{2} (\rho_{aa}e^{-i\omega t} - \rho_{bb}e^{i\omega t}) \quad (2.85)$$

$$\dot{\rho}_{ba} = -i\omega_0\rho_{ba} + i\frac{\Omega}{2} (\rho_{aa}e^{-i\omega t} - \rho_{bb}e^{i\omega t}) \quad (2.86)$$

with the Rabi frequency  $\Omega = \frac{\mathcal{E}\mu}{\hbar}$  and the resonance frequency  $\omega_0 = (E_b - E_a)/\hbar$ . The rapid oscillation at the optical frequency  $\omega$  can be eliminated by transforming to a rotating frame:

$$\begin{aligned} \varrho_{aa} &= \rho_{aa}, & \varrho_{bb} &= \rho_{bb} \\ \varrho_{ab} &= \rho_{ab}e^{i\omega t}, & \varrho_{ba} &= \rho_{ba}e^{-i\omega t} \end{aligned}$$

The resulting equations are the so-called optical Bloch equations:

$$\dot{\varrho}_{aa} = -i\frac{\Omega}{2} (\varrho_{ab} - \varrho_{ba}) \quad (2.87)$$

$$\dot{\varrho}_{bb} = i\frac{\Omega}{2} (\varrho_{ab} - \varrho_{ba}) \quad (2.88)$$

$$\dot{\varrho}_{ab} = -i\delta\varrho_{ab} - i\frac{\Omega}{2} (\varrho_{aa} - \varrho_{bb}) \quad (2.89)$$

$$\dot{\varrho}_{ba} = i\delta\varrho_{ba} + i\frac{\Omega}{2} (\varrho_{aa} - \varrho_{bb}) \quad (2.90)$$

where  $\delta = \omega - \omega_0$  is the detuning of the incoming radiation from resonance. The time dependence of the density matrix elements of a two-level system can be illustrated by the

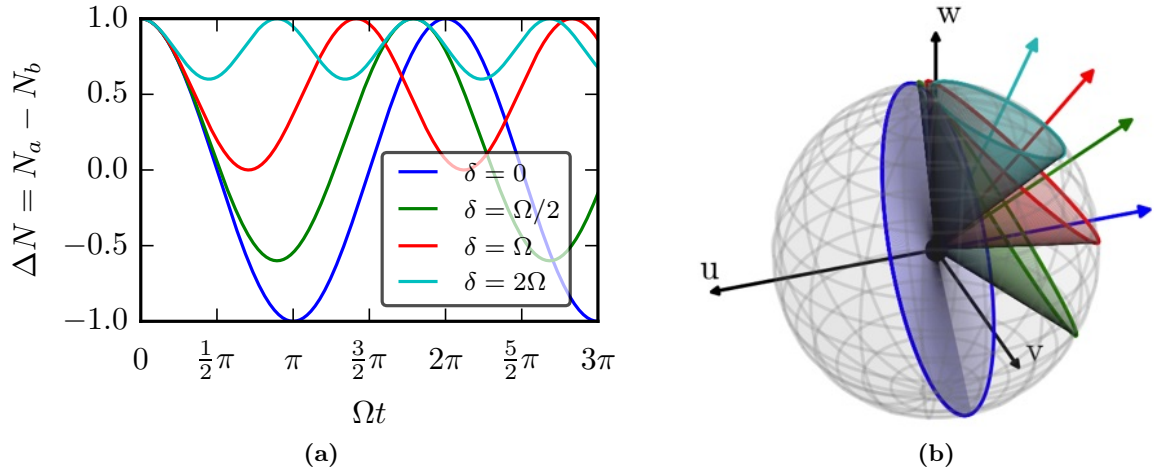


**Figure 2.8:** (a) Rabi oscillations of the population difference  $\Delta N$  for different values of the detuning neglecting all damping terms. Note, only on resonance can a complete population inversion be achieved. (b) The same values for the detuning as in (a) were used to mark the trace of the Bloch vector on the Bloch sphere. The Bloch vector itself moves on a cone with different opening angles depending on the detuning. The direction of the driving vector is indicated by arrows of different colors. In this example, the Bloch vector always has length one, because damping of the population or the coherences is neglected.

Bloch vector  $\Theta$  precessing about the effective field vector  $\Lambda$  [143]:

$$\frac{\partial \Theta}{\partial t} = \Lambda \times \Theta \quad \text{with} \quad \Theta = \begin{pmatrix} u \\ v \\ w \end{pmatrix} = \begin{pmatrix} \varrho_{ab} + \varrho_{ba} \\ i[\varrho_{ab} - \varrho_{ba}] \\ \varrho_{aa} - \varrho_{bb} \end{pmatrix} = \begin{pmatrix} 2 \cdot \text{Re}(\varrho_{ab}) \\ 2 \cdot \text{Im}(\varrho_{ab}) \\ \Delta N \end{pmatrix} \quad (2.91)$$

and

$$\Lambda = \begin{pmatrix} -\Omega \\ 0 \\ \delta \end{pmatrix}$$

For a pure state two-level system, which can be described by a single state vector  $|\psi\rangle$ , the Bloch vector has unit length and the corresponding Hilbert space is the unit sphere, the so-called Bloch sphere. If the system is isolated the system will stay in a pure state. However, interaction with the environment usually introduces damping of the population and the coherences, and the system cannot be described by pure states any more, but instead by mixed states which lie within the Bloch sphere. Spontaneous emission or inelastic collisions are damping mechanisms, which act on both the populations and the coherences. They are phenomenologically included into the Bloch equations by the damping constant  $\gamma_1$  [144]. In addition the coherence terms might be perturbed by phase changes due to elastic collisions. Hence, a second damping constant  $\Gamma$  accounts for this process. Finally, the two damping terms for the coherences are combined in the damping constant  $\gamma_2 = \frac{\gamma_1}{2} + \Gamma$  and the Bloch



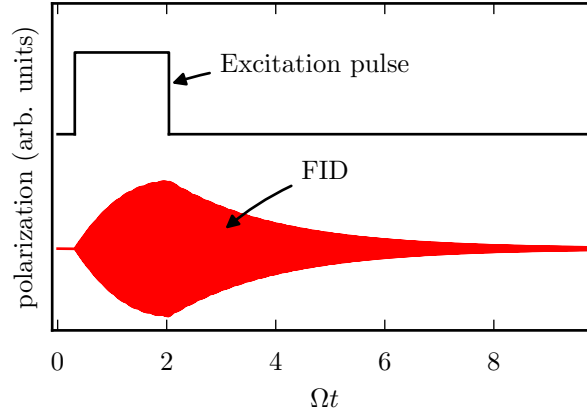


**Figure 2.9:** Scheme of transient emission spectroscopy. The polarization of the molecular ensemble builds up during the excitation pulse. When the polarization is maximized ( $\frac{\pi}{2}$ -conditions), the radiation is switched off the polarization starts to decay due to damping processes. The resulting free induction decay (FID) is recorded and the transition frequency is obtained via Fourier transformation.

equations for a two-level system with damping terms yield:

$$\dot{\varrho}_{aa} = -i\frac{\Omega}{2}(\varrho_{ab} - \varrho_{ba}) + \gamma_1\varrho_{bb} \quad (2.92)$$

$$\dot{\varrho}_{bb} = i\frac{\Omega}{2}(\varrho_{ab} - \varrho_{ba}) - \gamma_1\varrho_{bb} \quad (2.93)$$

$$\dot{\varrho}_{ab} = -(i\delta + \gamma_2)\varrho_{ab} - i\frac{\Omega}{2}(\varrho_{aa} - \varrho_{bb}) \quad (2.94)$$

$$\dot{\varrho}_{ba} = (i\delta - \gamma_2)\varrho_{ba} + i\frac{\Omega}{2}(\varrho_{aa} - \varrho_{bb}) \quad (2.95)$$

The probed observable in a spectroscopic experiment is the polarization  $\hat{P}$  with the expectation value [143]:

$$\langle \hat{P} \rangle = N \cdot \text{Tr}(\hat{\rho}\hat{\mu}) \quad (2.96)$$

where  $N$  is the number of molecules in the ensemble.

Different experimental techniques to probe molecular transitions are discussed in the following: transient absorption, transient emission, and fast passage excitation. As the name suggests, transient absorption refers to an absorption measurement while the molecules under study are exposed to a monochromatic light field. If the time resolution permits, Rabi oscillations (or optical nutation) can be observed as depicted in Figure 2.8, otherwise only a depletion of the incoming light field is observed.

In the transient emission technique, the molecules are excited by a monochromatic pulse which is short compared to the damping time constants. Afterwards the damped emission signal, the so-called free induction decay (FID), is measured in the time domain. Maximum coherence leading to a maximum emission signal is achieved by applying a  $\frac{\pi}{2}$ -pulse, where the length of the pulse is chosen such that  $\Omega \cdot t = \frac{\pi}{2}$ . In contrast a  $\pi$ -pulse leads to population inversion and a vanishing emission signal. A perfect  $\pi$ -pulse can only be realized for zero

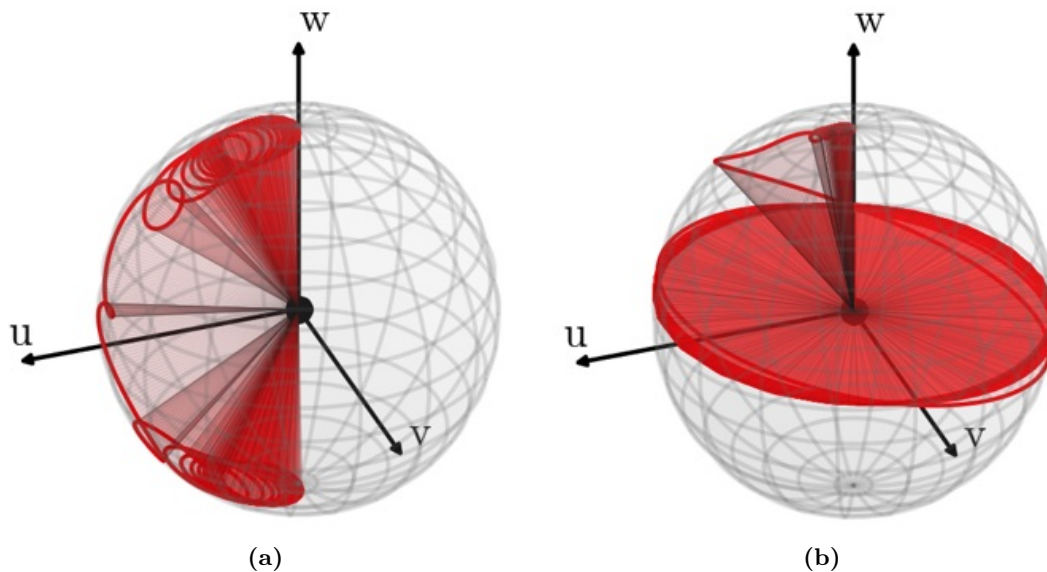


**Figure 2.10:** (a) Bloch sphere representations of a chirped pulse excitation in the rapid adiabatic passage (RAP) regime in the rotating frame. While the chirped pulse goes through resonance, the Bloch vector can follow the driving vector smoothly, which leads to complete population inversion. Far off resonance the Bloch vector rotates rapidly around the poles of the Bloch sphere. (b) Bloch sphere representations of a chirped pulse excitation in the linear fast passage (LFP) regime. In this case, the coupling is much weaker and the Bloch vector cannot follow the driving vector adiabatically anymore. This regime is best suited for maximizing the polarization of the molecular ensemble.

detuning and vanishing damping mechanisms. The pulse scheme for the transient emission technique is depicted in Figure 2.9.

In fast passage excitation, the frequency of the excitation radiation is swept through the molecular resonance in a short time. Hence, the effective field vector is no longer constant during the pulse. Two different regimes are commonly distinguished: the rapid adiabatic passage (RAP) and the linear fast passage (LFP) [143]. In the RAP regime, the Rabi frequency is large so that the coupling is strong and the Bloch vector can smoothly follow the effective field vector. Depending on the bandwidth of the pulse, this can lead to a  $\pi$ -pulse or population inversion. In the LFP regime, the coupling is weaker so that the Bloch vector cannot follow the effective field vector adiabatically. In this regime, no  $\pi$ -pulse can be achieved. The motion of the Bloch vector for the two different regimes for the same driving pulse bandwidth is illustrated in Figure 2.10a and 2.10b. Fast passage excitation is used throughout this thesis and the different regimes are evaluated using the molecule benzonitrile in Section 3.3.

The derivation of the Bloch equations for a two-level system can be applied to more complex energy level schemes. The application of the rotating wave approximation and the transformation to a rotating frame is straightforward, but the number and complexity of the equations increases rapidly, especially when multicolor experiments, pulse-sequences, or complicated level schemes are simulated. In Chapter 7, three-level Bloch equations for the three-wave

mixing experiment will be examined.

## 2.5 Spectral fitting

Key to any successful analysis of molecular spectra is the use of the appropriate Hamiltonian, which considers the quantum mechanical effects accessible with the applied experimental method. As mentioned in the beginning of this chapter, the type of observables influencing the spectrum are dependent on the time and frequency resolution of the experiment. For example, the fast motion of the electrons does not affect the pure microwave spectrum directly, but indeed the averaged molecular charge distribution influences the structure of the molecule and thus the experimentally determined rotational constants. The same is true for vibrational motions, so that a different set of rotational constants can be used for different vibrational or electronic states. However in the case of large amplitude motion, Coriolis coupling, or Fermi resonances, the coupling of the vibrational and rotational states requires an explicit consideration of the vibrational motion in the Hamiltonian. Hence, for any spectroscopic problem the question arises: What are the physical quantities affecting the spectrum at a specific experimental resolution? Sometimes, both a global approach, which aims to describe more states within the same Hamiltonian, and a local or effective approach, which splits the problem into subsets, can reproduce the experimental data with the same accuracy. Here the choice is usually a tradeoff between the complexity of the Hamiltonian and the direct access to the spectroscopic quantities of interest.

After assigning the experimentally obtained transitions to theoretically predicted ones using the corresponding quantum numbers, a least square method is used for parameter optimization. The Hamiltonian should be truncated to a minimum set of parameters, that can reproduce the spectrum to experimental accuracy [119]. The errors of the fitted parameters are then dependent on the experimental accuracy and the choice of the Hamiltonian. Different programs have been developed to match a specific class of problems. A good overview of many programs concerning microwave spectroscopy is provided by the PROSPE website, which is maintained by Z. Kisiel [145]. In the following, the fitting programs used in this dissertation are shortly discussed together with their main benefits. Detailed information about the programs are given in the chapters, where they are applied to specific problems.

**SPFIT/SPCAT:** The SPFIT/SPCAT suite of programs is one of the most prominent programs for fitting rotational spectra and was developed by H. Pickett [134, 146]. His implementation of the rotational Hamiltonian includes centrifugal distortion, quadrupole coupling of up to three nuclei, spin-rotation coupling, Coriolis coupling, and Fermi resonances. As mentioned earlier in this chapter, SPFIT can be used to treat internal rotation splitting in different ways.

**XIAM:** The program XIAM was developed by Hartwig et al. mainly to fit spectra of molecules with internal rotors [138]. The program implements first-order quadrupole

coupling, which is appropriate for weak coupling nuclei i.e. nitrogen or chlorine, but fails predicting the spectrum of larger coupling atoms i.e. bromine or iodine. Its ease of use, its speed, and its ability to fit up to three internal rotors makes XIAM widely used in the rotational spectroscopy community.

**RAM36:** Most programs aiming to predict the spectra by molecules with an internal rotor are limited to  $V_3$ -type potentials. The program RAM36 was recently designed to also fit  $V_6$ -type potentials. It was successfully tested on toluene [135].

## 2.6 Quantum chemical calculations

Quantum chemical methods have developed concurrently with the advances in computation capacities to become a powerful tool for solving the molecular Hamiltonian to determine molecular parameters. For small and medium size molecules (up to 20 heavy atoms or so), which are of relevance for microwave spectroscopy, these methods have proven to provide good results for the molecular charge distribution. In this section, the molecular Hamiltonian and the common principles of most algorithms are introduced. Afterwards different methods are presented and their possible benefits for rotational spectroscopy are discussed.

Including only the internal degrees of freedom and ignoring the nuclear spin interaction, the molecular Hamiltonian in Equation 2.2 can be rewritten to:

$$\hat{H} = \underbrace{-\sum_{i=1}^N \frac{\hbar^2}{2m_i} \nabla_i^2}_{\text{kinetic energy of the nuclei}} - \underbrace{\sum_{j=1}^M \frac{\hbar^2}{2m_e} \nabla_j^2}_{\text{kinetic energy of the electrons}} - \underbrace{\sum_{i=1}^N \sum_{j=1}^M \frac{Z_i e^2}{r_{ij}}}_{\text{nuclei-electron interaction}} + \underbrace{\sum_{j<k}^N \frac{e^2}{r_{jk}}}_{\text{electron-electron interaction}} + \underbrace{\sum_{i<l}^N \frac{Z_i Z_l e^2}{r_{il}}}_{\text{nuclei-nuclei interaction}} \quad (2.97)$$

By applying the Born-Oppenheimer approximation, the electronic wavefunctions are separated from the nuclei motions and hence the single electron Hamiltonian is given by [147, Chap. 4]:

$$\hat{h}_j = -\frac{\hbar^2}{2m_e} \nabla_j^2 - \sum_{i=1}^N \frac{Z_i e^2}{r_{ij}} + \sum_{k \neq j}^N \int \frac{e^2 |\varphi_j|}{r_{jk}} d\mathbf{r} \quad (2.98)$$

The Hamiltonian describing all electrons in a molecule is just the sum over all single electron Hamilton operators  $\hat{h}_j$ . Unfortunately, the product of the single electron waveforms is not suitable to describe the electronic waveform of the molecule because electrons are fermions and thus subject to the Pauli exclusion principle. Hence, the resulting all electron waveform of the molecule needs to be antisymmetric. John Slater proposed in 1929 to use the nowadays called Slater determinate, which results not only in an antisymmetric waveform, but also

**Table 2.4:** Compilation of the scaling behavior of different computational methods in dependence on the number of basis functions  $N$ . Note that scaling refers to how time increases with the molecular size, but says nothing about the absolute amount of time required for a given molecule.

method	Scaling behavior
DFT	$< N^3$ [147, p. 273]
HF	$N^4$ [147, p. 273]
hybrid DFT	$\approx N^4$ [147, p. 273]
MP2	$N^5$ [147, p. 237]
CCSD	$N^6$ [147, p. 237]
CCSD(T)	$N^7$ [147, p. 237]

considers the electronic spin [148]:

$$\psi(\mathbf{q}_1, \mathbf{q}_2, \dots, \mathbf{q}_M) = \frac{1}{\sqrt{M!}} \begin{vmatrix} \chi_1(\mathbf{q}_1) & \chi_2(\mathbf{q}_1) & \cdots & \chi_M(\mathbf{q}_1) \\ \chi_1(\mathbf{q}_2) & \chi_2(\mathbf{q}_2) & \cdots & \chi_M(\mathbf{q}_2) \\ \vdots & \vdots & \ddots & \vdots \\ \chi_1(\mathbf{q}_M) & \chi_2(\mathbf{q}_M) & \cdots & \chi_M(\mathbf{q}_M) \end{vmatrix} \quad (2.99)$$

As already defined,  $M$  is the total number of electrons and  $\chi$  is the product of the spatial orbital and a spin wavefunction. In order to solve the one electron Hamiltonian in Equation 2.98, the wavefunction of all other electrons  $\varphi_j$  needs to be known. However, the wavefunctions  $\varphi_j$  are initially not known because they would result from solving the  $M$  single electron Hamiltonians. A method to determine the single electron wavefunctions without the exact knowledge of the electron-electron interaction was introduced by Douglas Hartree for atoms and was improved by Wladimir Fock [149–151]. Based on their work, Hartree-Fock (HF) theory evolved and employs a self-consistent field approach [147, Chap. 4]. HF theory is an ab initio method and independent of any empirical parameters. Electron exchange correlation is considered in the HF method via the Slater determinant, but completely neglects electron-electron correlation. Hence, for most applications in rotational spectroscopy the HF method lacks accuracy.

Various theories have been developed to include electronic correlation in HF theory. One of the more relevant post-HF methods is Møller-Plesset perturbation theory of  $n$ th order (MP $n$ ) [152] and coupled cluster theory (CC) [153]. Both methods are based on an HF approach. But whereas MP $n$  theory adds the electronic correlation in a perturbative manner directly to the HF Hamiltonian, coupled cluster theory incorporates the electron-electron correlation into the molecular wavefunctions. The scaling behavior is worse for both methods compared to the HF method and increases rapidly when higher order terms are included (compare Table 2.4).

Another theoretical approach to obtain information about the electron distribution is density functional theory (DFT), where the charge density  $\rho(\mathbf{q})$  is the fundamental quantity [154].

The charge density is defined as followed:

$$\rho(\mathbf{q}) = M \int \dots \int |\psi(\mathbf{q}_1, \mathbf{q}_2, \dots, \mathbf{q}_M)|^2 d\mathbf{q}_1 d\mathbf{q}_2 \dots d\mathbf{q}_M \quad (2.100)$$

where the electronic wavefunctions with their dependence on  $M$  position vectors ( $\mathbf{q}_1, \mathbf{q}_2, \dots, \mathbf{q}_M$ ) are mapped onto the charge density, which is only dependent on a single position vector  $\mathbf{q}$ . Hohenberg and Kohn proved that the charge density specifies all molecular properties [155]. Hence, a functional  $E[\rho(\mathbf{q})]$  must exist that gives the exact ground state energy for the exact ground state density [156]:

$$E[\rho(\mathbf{q})] = E_{Ne}[\rho(\mathbf{q})] + T[\rho(\mathbf{q})] + E_{ee}[\rho(\mathbf{q})] \quad (2.101)$$

with

$$E_{Ne}[\rho(\mathbf{q})] = \int \rho(\mathbf{q}) V_{Ne}(\mathbf{q}) d\mathbf{q} \quad (2.102)$$

The total functional  $E[\rho(\mathbf{q})]$  can be expressed as a sum of a functional describing the interaction of the electrons with the external potential  $E_{Ne}[\rho(\mathbf{q})]$ , a functional describing the kinetic energy of the electrons  $T[\rho(\mathbf{q})]$  and a functional determining the electronic interaction  $E_{ee}[\rho(\mathbf{q})]$ . The choice of the functional  $E_{Ne}[\rho(\mathbf{q})]$  is straightforward, whereas the mathematical expression of the other two functionals is subject to ongoing research. Not surprisingly, the functionals are usually similar to the ones used in the HF Hamiltonian, but augmented with semi-empirical expressions for the electron correlation. If the exact functional is used, the energy is minimized for the exact charge density. These semi-empirical functionals are optimized using experimental results or benchmarked with higher level calculations. Axel Becke introduced the hybrid functional approach, which involves the exact HF exchange correlation energy and improved many molecular parameters [157]. Prominent hybrid functionals are the B3LYP (Becke, three parameter, Lee-Yang-Parr) functional [158] and the M06 series of the Minnesota functionals, which also takes dispersion interactions into account [159]. The huge advantage of the DFT methods is the low computational cost compared to post-HF ab initio methods (compare Table 2.4).

For describing the molecular wavefunction, all quantum chemical methods require a mathematical framework termed the basis set. Most methods employ the linear combination of atomic orbitals (LCAO) to form the molecular wavefunction. The atomic waveforms can be approximated by Slater type orbitals (STO), which have a radial part proportional to  $r^l e^{-\zeta r}$  ( $l$  is the angular quantum number) [160]. Spherical harmonics are used to describe the angular distribution of the orbital similar to the hydrogen atom. Unfortunately the radial part of the Slater type orbitals are difficult to handle mathematically. However, the radial part of the STOs can be approximated with a linear combination of Gaussian type orbitals (GTO) of the form  $r^l e^{-\alpha r^2}$ , which are much easier to handle computationally [161]. Figure 2.11 shows the approximation of the s-orbital of the hydrogen by one, two and three contracted Gaussian-Type Orbitals.

If only one STO is used to describe a single atomic orbital in a molecule, the basis set is

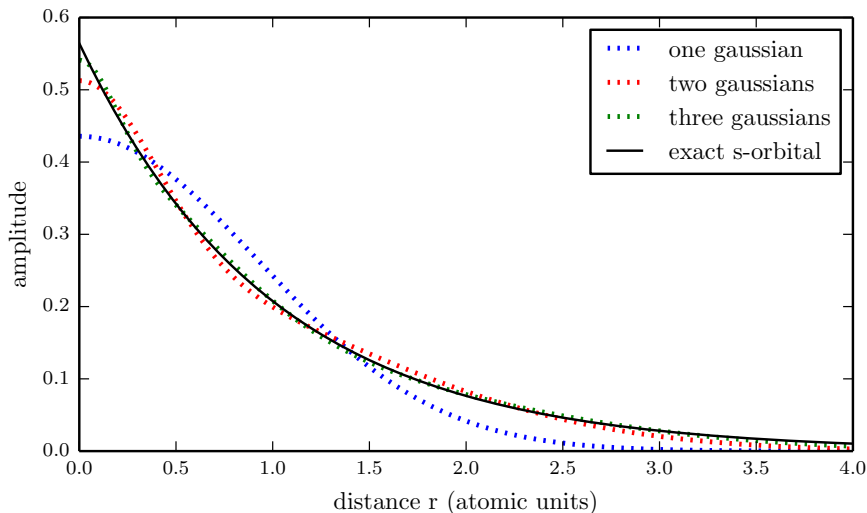


**Figure 2.11:** Approximation of the exact Slater type radial dependence of the  $s$ -orbital of hydrogen with a superposition of  $N$  Gaussian functions ( $N = 1, 2, 3$ ). Three Gaussian functions already lead to a good approximation of the Slater type radial dependence.

said to be minimal. The STO-nG series of basis sets is an example for minimal basis sets, where the STO is approximated by  $n$  GTOs [162]. Multiple-zeta basis sets use more than one STO to describe the atomic orbitals, which increases the flexibility of LCAO to mimic the molecular orbitals. Normally, the core electrons are more strongly localized around the nuclei than the valence electrons of the atoms. These differences are considered in a split-valence basis set, where only one STO is used to describe the core electrons, but the basis of the valence electrons is built upon more STOs. Polarization functions are sometimes necessary to describe the polarization of an atomic orbital due to the molecular charge distribution. They consist of STOs with the angular quantum number larger than the highest occupied atomic orbital. For loosely bound electrons in anions, Rydberg states, or van der Waals complexes, diffuse functions are useful to map the electron density correctly. They describe the long range characteristics of the electronic wavefunction and they are recognized by their small  $\zeta$  exponent.

Two classes of basis sets are widely used: Pople-type [163, 164] and Dunning-type basis sets [165]. Both are split-valence basis sets, but the Pople-type basis sets (e.g. 6-311++G\*\*)¶ provide many options to adjust the basis set to a specific problem (number of valence STOs, type and number of polarization functions and diffuse functions). The Dunning-type basis sets (e.g. aug-cc-pVTZ) provide less options for customization, but they are especially designed for

¶The nomenclature is as follows: The number before the dash indicates the numbers of Gaussians used to approximate the wavefunction of the core electrons. The numbers after the dash specify the numbers of Gaussians employed for the different STOs approximating the wavefunction of the valence electrons. In this example, three STOs are used to approximate the wavefunction of the valence electron. The first STO is approximated by three GTOs, the second and the third STOs are fitted by one GTO. The '+' is used to enable diffuse functions and the '\*\*' implements standard polarization functions. Higher order polarization functions can be activated by letters indicating the angular momentum of the polarization function i.e. (d,p).



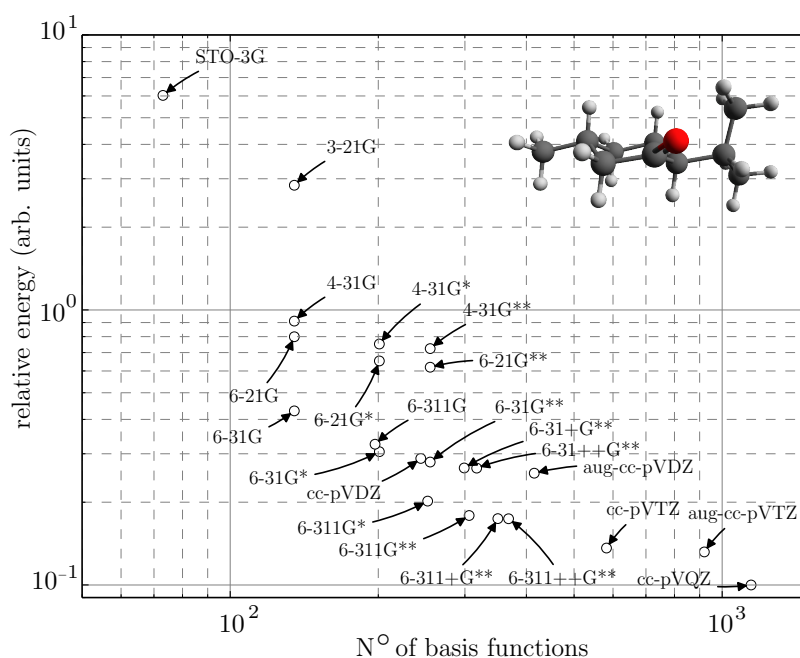


**Figure 2.12:** Relative energy of optimization calculations for menthone using the B3LYP functional and various basis sets. As expected the energy decreases with the number of basis functions included in the calculation. In the example of menthone, the use of diffuse functions did not reduce the energy significantly. In contrast the use of polarization functions has a large impact on the energy.

correlation corrected methods. The choice of the basis set depends on the molecular system under study and the available computing power. The computation time of different methods scale differently. Various scaling factors are summarized in Table 2.4. The energy converges towards a limit for the HF, post-HF and the DFT methods for an increasing number of wavefunctions. In Figure 2.12, the calculated energies for the optimized structure of menthone is shown using the B3LYP functional and different basis sets. It can be seen that diffuse functions have only a small impact on the energy, whereas the influence of the polarization functions on the energy is significant. If the calculation includes atoms with a high number of electrons, electron core potential ECP can facilitate the calculations. ECPs integrate and combine the potential produced by both the inner-shell electrons and the nucleus, which reduces the basis set for heavy atoms tremendously. A collection of many basis sets and electron core potentials in different formats are published online on the Basis Set Exchange website [166].

The interplay between theoretical investigations and rotational spectroscopy is manifold. Not only do experiments provide a high standard to benchmark quantum-chemical approaches, but theoretical results are also utilized to interpret and complement experimental outcomes. This interplay is illustrated with the example of the rotational constants, maybe the most important quantity obtained experimentally by rotational spectroscopy. The rotational constants of a calculated structure can be used to predict the rotational spectrum, thus facilitating the



spectral assignment. And the comparison of the experimentally obtained rotational constants with the calculated ones provides evidence of structural properties of the molecule under study. However, the outcome of all quantum chemical calculations should be handled with care and different methods and basis sets should be used to confirm theoretical results.

Puzzarini published an extensive review and a perspective article describing the role of theory in supporting rotational spectroscopy [167, 168]. The following discussion highlights a few topics important for this dissertation.

**Molecular structure:** In principle one of the outstanding features of rotational spectroscopy is the determination of the effective molecular structure via isotopic substitution. However, the analysis of the rotational spectra of all singly substituted species is rather tedious and the natural abundance of some isotopologues is so small that they need to be artificially enhanced in order to obtain a detectable signal. As mentioned above, information about the structure might be obtained by simply comparing the experimentally obtained rotational constants with the calculated ones. For small molecules (up to six heavy atoms) Puzzarini et al. showed excellent agreement for experimentally obtained bond length and bond angles and their calculated analogues employing high level ab initio methods (e.g. CCSD(T)) and large basis sets (e.g. cc-pVQZ) [167]. They also employed extrapolation techniques to estimate the structural parameters in the complete basis set limit [169]. Using high level calculations and extrapolation techniques, the deviation of the calculated and experimentally obtained structural parameter is on the order of a few per mille. However, computation time is usually limited and therefore the calculations for larger molecules are always a compromise between speed and accuracy. In this work, the MP2 ab initio method and DFT, employing the B3LYP and M06-2X functionals are used with different basis set. If the highest order calculation is not a feasible option, different low-level calculations employing different methods and basis sets provide a good cross-check of the results in a decent time [170]. Using the MP2 method and DFT a good overlap of the experimental and the calculated rotational constants are demonstrated in Chapter 4, Chapter 5, and Chapter 6.

**Dipole moments:** Microwave spectroscopy can provide precise values of dipole moment components via Stark effect measurements, but in the spectrometer setup presented herein this feature is not yet implemented. Even though the dipole moment components cannot be determined exactly, they are linked to the line strengths of different types of transitions (compare Table 2.2) in asymmetric-top spectra. By evaluating the intensity of the different types of transitions, the relative dipole moment components can be estimated. A comparison of this estimation to the calculated dipole moment components is helpful for the assignment of a measured spectrum to a calculated structure. Another use of the calculated dipole moment components is three-wave mixing, where the sign of the product of the dipole moment components determines the enantiomer (compare Chap. 7). When calculated dipole moments are compared with those obtained by microwave spectroscopy, they need to be expressed in the principal axis

system. Benchmark calculation for different ab initio methods and basis sets were performed by Bak et al. for a set of small molecules [171]. Their main conclusion was that the electron correlation treatment of the basis set is more important for the accuracy of the calculation than the pure size of the basis set.

**Nuclear quadrupole moment coupling:** Most quantum chemical calculations provide an estimate of the charge distributions inside a molecule. With knowledge of the charge distribution, the calculation of the nuclear quadrupole moments is straightforward by applying Equation 2.42. Mostly only the off-diagonal elements of the calculated quadrupole tensor are combined with the experimentally obtained diagonal elements to rotate the quadrupole tensor to the principal axis system of the field gradient (compare Sec. 2.2 of this chapter). Relativistic corrections must be taken into account for molecules with larger atoms (e.g. halogens) when calculating the nuclear quadrupole moment or the dipole moment, both of which depend on the charge distribution [172]. W. Bailey provides a good overview of benchmark calculations for the very common nitrogen quadrupole coupling in different molecules [173].

**Force fields:** The calculation of the harmonic and anharmonic force field of a molecule provides various benefits for microwave spectroscopy. The force field is necessary to calculate the rotational constants of vibrationally excited states. But also if the molecule is in the lowest vibrational state, its zero-point vibrations alter the ground state energy, influence the potential energy surface, and might even change the energy ordering of the non-rigid structural isomers. If a substitution structure is obtained by employing Kraitchman's equations [47], the harmonic and anharmonic part of the force field can be used to account for the change of the rotational constants due to the molecular vibrations. The resulting structure is called semi-experimental equilibrium structure and provides the best estimate for the molecular equilibrium structure from microwave spectroscopy up to now [174].

**Potential energy surface:** The complexity of the potential energy surface goes along with the flexibility of a molecule. Large and complex molecules can exhibit many conformers and even at the low temperatures of a molecular beam various conformers might remain significantly populated (compare Chap. 5 and Chap. 6). To estimate which conformers exist and their energies, a conformation search or a scan of the potential energy surface provides in-depth information. Most conformation search routines populate the conformational space manually or artificially, optimize the resulting structures and compare the structures and energies of the conformations. If the molecular flexibility is already restricted to a few coordinates, potential energy surfaces can be calculated by scanning along these coordinates. This method is applied in Chapter 5 and Chapter 6 for the rotation of the isopropyl or the hydroxyl group of the molecules carvacrol, thymol, menthol, and menthone. In molecular beam microwave spectroscopy, not only are the relative energies of the different conformers of interest, but also the barriers between them, because they might provide insight if the molecule can cool down from one local

minimum to another one during supersonic expansion [175].

## Chapter 3

# Experimental details

The experiments were performed with a molecular beam equipped chirped-pulse microwave spectrometer that was newly constructed within the framework of this thesis. The experimental techniques, spectrometer, and molecular beam are detailed in this chapter. This chapter closes with an evaluation of the experimental performance.

### 3.1 Chirped-pulse microwave spectrometer

Chirped-pulse Fourier transform microwave spectrometry (CP-FTMW) is a fast passage excitation technique pioneered by Pate et al. [58]. Fast passage excitation can be realized in two different ways: sweeping the excitation radiation through the molecular resonance or sweeping the molecular resonance through the fixed frequency of the excitation radiation. Both sweeping processes need to be fast compared to the relaxation time. McGurk et al. introduced this technique by irradiating a molecular ensemble with a fixed microwave frequency and quickly sweeping the molecular transition using the molecular Stark effect [49]. With advances in microelectronics, the digital synthesis of a microwave chirp became feasible and Pate et al. were the first to apply CP-FTMW in the cm-wavelength region [58]. The waveform of a linear chirp can be described by the following formula of the electric field:

$$\mathcal{E}(t) = \mathcal{E}_0 e^{i\left(\omega_s t + \frac{\alpha t^2}{2}\right)} \quad (3.1)$$

where  $\alpha$  is the chirp rate, defined by start and end frequency of the chirp  $\omega_s$  and  $\omega_e$ , respectively, and the pulse length  $\tau_{pul}$ :

$$\alpha = \frac{\omega_e - \omega_s}{\tau_{pul}} \quad (3.2)$$

The instantaneous frequency of the chirped microwave pulse is then given by:

$$\omega = \omega_s + \alpha t \quad (3.3)$$

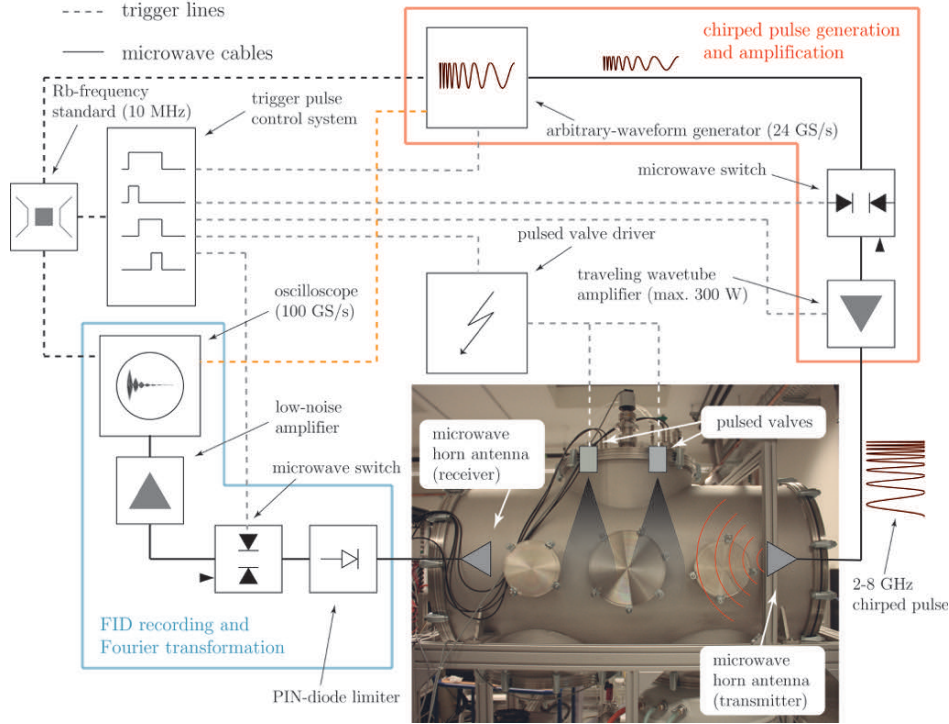


**Figure 3.1:** Experimental setup of the COMPACT microwave spectrometer. The dashed lines are trigger or synchronization lines. Solid lines represent microwave cables. The chirp is generated in the AWG, amplified by the TWA, and transmitted into the vacuum chamber via a microwave horn. The FID is received with another microwave horn, amplified with a low-noise amplifier, and finally recorded by an oscilloscope. The trigger pulse control system, the oscilloscope, and the AWG are phase locked to a Rb-frequency standard. To ensure absolute phase stability, the oscilloscope is directly triggered by the AWG by one of its marker channels.

The intensity of the emitted molecular signal is proportional to the number of molecules  $N$ , the transitions frequency  $\omega$ , the square of the transition dipole moment  $\mu^2$ , the amplitude of the excitation radiation  $\mathcal{E}_0$ , the population difference of the two states involved in the transition  $\Delta N_0$ , and the inverse square root of the chirp rate  $\alpha$  [58]:

$$S \propto N \cdot \omega \cdot \mu^2 \cdot \mathcal{E}_0 \cdot \Delta N_0 \cdot \sqrt{\frac{\pi}{\alpha}} \quad (3.4)$$

One of the objectives of this thesis was the construction of a new chirped-pulse Fourier transform microwave spectrometer, COMPACT (compact-passage acquired coherence technique). It is a combination of the designs presented by Pate et al. [58] and of that proposed by Grabow [143]. Figure 3.1 shows a scheme of the spectrometer together with a photo of the vacuum chamber. The spectrometer covers the frequency region of 2 – 8.5 GHz and was intentionally chosen to investigate complex molecules with large moments of inertia and thus small rotational constants, leading to low transition frequencies.

The heart of the spectrometer is a 24 GS/s arbitrary waveform generator (Tektronix AWG 7122A) that creates the microwave chirps. The synthesized chirps have a bandwidth of

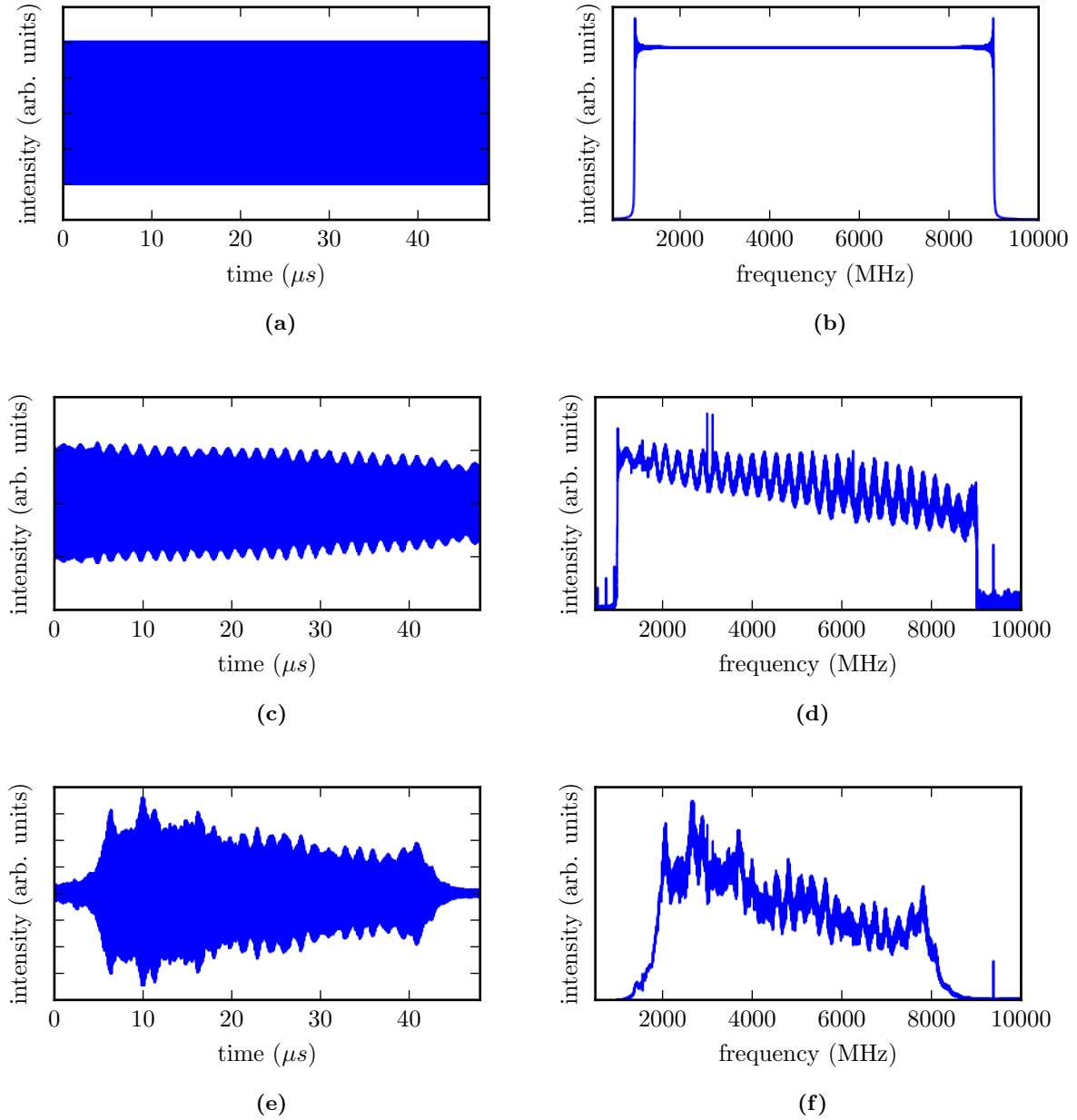


**Figure 3.2:** Evaluation of the microwave chirp (1 – 9 GHz, 48  $\mu$ s) at different stages of the experiment. (a) Waveform of the chirped pulse synthesized at 24 GS/s. (b) The spectrum of the waveform in (a). All frequency components between 1 and 9 GHz are equally abundant. (c) Waveform emitted by the AWG and directly recorded by the scope. The periodic structure upon the waveform and the corresponding spectrum (d) is most likely due to internal back reflections. (e) Waveform recorded after passing the TWTA. The corresponding spectrum (f) reveals the frequency dependence of the TWTA and the sharp cutoffs at 2 and 8 GHz.

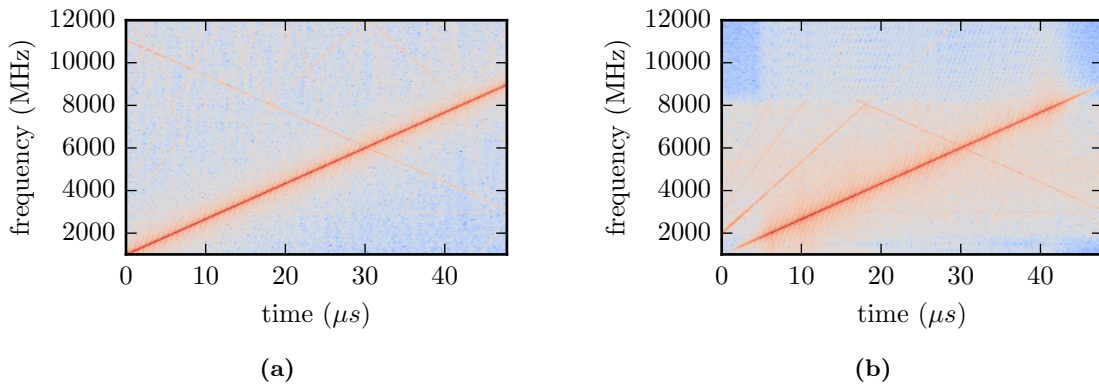


**Figure 3.3:** Spectrographs of the microwave chirp (1 – 9 GHz, 48  $\mu$ s) of the waveforms recorded directly after the AWG (a) and after passing the TWTA (b). The main microwave chirp is easily identified as straight line with a positive slope. The line with a negative slope results from mixing with internal clock of the AWG. The spectrograph in (b) also exhibits higher harmonics of the chirps introduced by the TWTA, but with a much reduced intensity. Also remarkable is the noise the TWTA adds to the spectrum in the 2 – 8 GHz bandwidth. The color scale is logarithmic for both spectrographs.

2 – 8.5 GHz and are swept linearly within a short time (typically 1  $\mu$ s to 4  $\mu$ s). The microwave excitation chirp is amplified by an adjustable traveling wave tube amplifier (Amplifier Research 300T2G8) with up to 300 W output power. All microwave components (cables, connections, microwave horns, switches etc.) bear a frequency dependent performance, but ultimately the spectrometer is governed and limited by the frequency dependence of the traveling wavetube amplifier (TWTA). Figure 3.2 illustrates the evolution of a linear 1 – 9 GHz and 48  $\mu$ s long microwave chirp at different stages of the experiment. The waveform and the Fourier transform of the chirp generated by a computer program and sampled at 24 GS/s are presented in Figures 3.2a and 3.2b. As expected, the waveform and the corresponding spectrum are perfectly flat, because the sampling theorem is fulfilled. Figure 3.2c shows the waveform emitted by the arbitrary waveform generator (AWG) and directly recorded by the oscilloscope (Tektronix DPO 71254A) at 100 GS/s. The intensity of the waveform drops slowly with increasing frequency and it exhibits a periodic structure, which might be due to internal back reflections. Some sharp intensity peaks are apparent in the spectrum at different frequencies i.e. 3000 MHz, 3125 MHz, 6250 MHz, etc. (compare Fig. 3.2d). The origin of these lines is most likely due to the channel bandwidth of 12.5 GHz of the oscilloscope. The last subset in Figure 3.2 shows the microwave chirp recorded after the TWTA. The gain of the TWTA was set to 6 %, the highest possible value before the oscilloscope was overdriven, which would result in a clipped waveform. The intensity reduction with increasing frequency seems to be enhanced compared with the waveform measured directly after the AWG. But more importantly are the abrupt intensity cutoffs at 2000 MHz and 8000 MHz, which limits the frequency bandwidth of the spectrometer. The frequency dependent performance of the TWTA needs to be kept in mind when the intensities of rotational spectra are compared with theory.



Two spectrographs are performed to reveal the time-dependence of different frequency components of the waveform after the AWG and after the TWTA. A chirp should produce a line in a spectrograph with a positive or negative slope depending on the chirp direction. The spectrograph of the waveform taken directly from the AWG shows a very intense line for the main chirp with a positive slope (Fig. 3.3a). However, there is also a trace with a negative slope, which crosses the line of the main chirp at 6 GHz. Neill et al. observed a similar behavior that they explained with frequency mixing of the chirp with the internal clock of the AWG at 10 GHz [64]. In the spectrograph generated from the waveform taken after the TWTA (Fig. 3.3b), both the strong trace with a positive slope and the weaker trace with a negative slope are still apparent. In addition, the amplifier introduces harmonics of the chirp up to the fourth order. These sidebands are so weak relative to the primary chirp that in most cases they should not significantly influence the relative intensity accuracy of the observed molecular transitions.

Hence, the frequency range is mainly defined by the TWTA and was intentionally chosen for the investigation of large and complex molecules with large moments of inertia and thus small rotational constants, leading to low transition frequencies. Furthermore, many molecular features, such as the  $K$  manifolds for asymmetric-top molecules, become more complicated with increasing rotational quantum number  $J$ , so having access to low  $J$  transitions is very valuable. In cavity-based FTMW spectroscopy, the physical size of the microwave cavity becomes an important aspect at low frequencies. Microwave reflectors as large as 48 inches (about 122 cm) are used to access the low frequency range down to 1 GHz [176]. Physical size is less of a problem with chirped-pulse spectroscopy using horn antennas.

After amplification, the excitation chirp is transmitted into the vacuum chamber using horn antennas (Advanced Technical Materials 250-441EM-NF). The distance between the emitting and the receiving horn antennas is approximately 21 cm. The molecules are seeded into a rare gas mixture and supersonically expanded into the vacuum chamber using a pulsed nozzle (Parker General Valve, Series 9). The valves are mounted on the top of the vacuum chamber about 10 cm above the microwave horns. Usually, neon is used as backing gas at stagnation pressures of 1 – 5 bar, but also helium and argon are available for this purpose. The molecule’s internal degrees of freedom are cooled efficiently in a supersonic expansion. A thermodynamical and hydrodynamical evaluation of the supersonic expansion, including the influence of different backing gases, is detailed in the next section. Depending on the molecule under study, a gas mixture can be prepared, but for larger molecules the sample needs to be heated in order to bring enough molecules into the gas phase. For those molecules, the sample container can be placed directly prior to the nozzle and both the container as well as the nozzle can be heated using a heater rope to a maximum temperature of approximately 200 °C. To avoid condensation, the tubing connecting the container and the nozzle is also heated with a heater rope.

Subsequently, the internally cold molecules interact with the microwave radiation emitted by the horn antennas. If a frequency within the chirp is resonant with a molecular transition, the molecular sample is polarized, i.e., a macroscopic dipole moment is formed (compare Sec. 2.4).



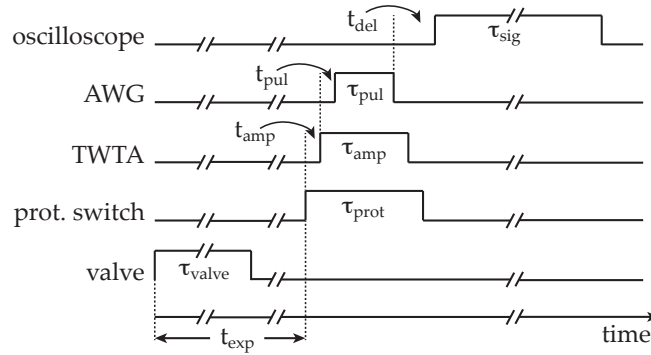


**Figure 3.4:** Trigger scheme of the experiment. An experimental sequence starts with a gas pulse. Hence, the valve is opened for a time  $\tau_{\text{valve}}$ . After a time  $t_{\text{exp}}$ , the expansion reaches the interaction region and the excitation sequence starts with opening the protection switch for a time  $\tau_{\text{prot}}$ . After a short delay  $t_{\text{amp}}$ , the TWTA is turned on and again after a short delay  $t_{\text{pul}}$  the excitation pulse is emitted. The delay  $t_{\text{del}}$  for the FID recording is set such that the excitation pulse does not interfere with the recorded signal.

The free-induction decay (FID) of the polarization is received by the second horn antenna and amplified with a low-noise microwave amplifier (Miteq Amplifier AMF-5F-0200080-15-10P). The AWG and the oscilloscope (Tektronix DPO 71254A) are phase-locked to a 10 MHz Rb-disciplined quartz oscillator (Stanford Research FS 725) to ensure phase stability. On the receiver end, a high-power diode limiter (Aeroflex ACLM-4535) and a solid-state, single-pole single-throw switch (SPST, Advanced Technical Materials S1517D) are integrated to protect the sensitive receiver electronics from the high-power excitation pulse (compare Fig. 3.1). In the current setup, the resolution is mainly determined by the length of the recorded FID (typically 10 – 50  $\mu\text{s}$ ) resulting in a linewidth as small as 20 kHz at 50  $\mu\text{s}$ .

The photon energy in the microwave spectral region is rather small compared to other spectroscopic techniques and thus the molecular signal is more difficult to detect. Hence, depending on the molecular density and the strength of the dipole moment, between hundreds and several million averages are often necessary to obtain a reasonable signal-to-noise ratio. Ensuring phase stability of the AWG and the oscilloscope during the measurement period is crucial for the performance of the experiment. Therefore, the oscilloscope is directly triggered by a marker channel of the AWG. For all other components of the experiment, a highly accurate phase stability is not mandatory and would eventually introduce unwanted signal lines in the spectrum if phase stable triggers from microwave switches couple to the microwave signal lines.

The experiment sequence is depicted in Figure 3.4. The valve is triggered at time zero and the valve driver holds it open for a time  $\tau_{\text{valve}}$ . The valve opening time was usually set to 380  $\mu\text{s}$ . Afterwards the molecules expand freely into the vacuum for a time  $t_{\text{exp}} = 600 - 900 \mu\text{s}$ . Then the actual excitation process starts with opening of the protection switch, which protects the sensitive detection electronics from the strong excitation pulse. Hence, the protection switch stays open for the time the TWTA operates and the microwave chirp is emitted. After a delay

of  $t_{amp}$ , the amplifier is turned on for a time period of  $\tau_{amp}$ . The TWTA amplifies only for the time the chirp is emitted, usually with a pre-buffer of 500 ns to account for the ramp up time of the TWTA. Finally, the AWG is triggered to fire the microwave pulse and to trigger the oscilloscope to record the FID for a time  $\tau_{sig}$ . For generating the trigger pulses, a National Instruments PXI system (PXIe-1065) is employed. The PXI system has a 100 MHz internal clock, 18 free module slots and a high speed backbone bus connecting all installed modules. A multifunction DAQ unit (NI PXI-6221 M Series) and a timing I/O module (NI PXI-6602) are used to generate and emit the trigger pulses via two front ends, which were designed and manufactured by the Leibniz-Universität Hannover. The program FTMW++ of Jens-Uwe Grabow (Leibniz-Universität Hannover) is employed as a soft panel to control the trigger sequence. The program runs in a Windows 7 environment on an embedded computer module (PXIe-8108). The program FTMW++ is complemented with self-written LabView scripts to automate different sets of experiments. The experimental repetition rate is ultimately limited by the pumping speed of the vacuum system, but in practice the FID recording by the oscilloscope already sets an upper limit for the repetition rate. Depending on the length of the recorded FID signal, the maximum repetition rate of the experiment ranges between 1 – 10 Hz.

The vacuum chamber is a 1280 mm long cylinder with a diameter of 640 mm and a total volume of 1647 l. Both ends are sealed with ISO-K 630 reducer flanges to an ISO-K 200 flange. The horns are mounted to the smaller center flanges on both sides and N-type microwave feedthroughs are used to couple the microwave excitation chirp into and the molecular signal out of the chamber. The vacuum chamber has two ISO-K 160 flanges and one ISO-K 200 flange on both sides for the adjustment of the nozzle and the microwave horns. The chamber has a ISO-K 500 flange on the top, with various adapters for different nozzles and a vacuum gauge, and two ISO-K 500 flanges on the bottom. The diffusion pump (Leybold DIP 12000) is connected to one of the flanges on the bottom, the other one is blind flanged. The diffusion pump has a pumping speed of 12000 l/s and is backed by a double stage rotary vane pump (Leybold Trivac D 40 B ATEX) with a pumping speed of 11 l/s. The pressure inside the chamber is controlled by a combined Pirani/cold cathode vacuum gauge (Pfeiffer Compact FullRange Gauge PKR 261), while a Pirani vacuum gauge (Pfeiffer TPR 280) is used to measure the pressure in the pre-vacuum line.

### 3.2 Molecular beam technique

Atomic and molecular beams are a powerful tool in many fields of physics and physical chemistry. Particularly, high precision experiments and high-resolution spectroscopy benefited tremendously from these techniques. Otto Stern pioneered the atomic and molecular beam technique and received the Nobel prize in 1943 for his contribution in this field. Rabi, Ramsey, and Herschbach advanced the beam technique or adapted it to other scientific areas. They were also awarded by the Nobel prize for their contributions on atomic and molecular beam techniques (Rabi 1944, Herschbach/Lee/Polanyi 1986, Ramsey/Paul/Dehmelt 1989). The

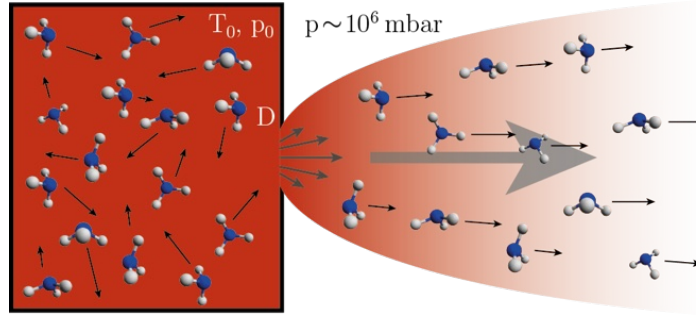


**Figure 3.5:** Graphical illustration of a beam of ammonia molecules seeded into a backing gas. The change in the density and the temperature of the beam is depicted by the red shaded color.

advantages are manifold and the most important ones for this work will be highlighted here. First of all, the internal and external degrees of freedom of the system under study can be cooled very efficiently within atomic and molecular beams. The low translational temperature (i.e. the velocity distribution within the beam is small) leads to a narrow spectral line-shape in spectroscopic techniques, whereas low rotational and vibrational temperatures limit the number of significantly populated levels, which increases the signal intensity for these populated transitions. Furthermore, low internal temperatures greatly facilitate the understanding of the molecular spectrum, because only a small subset of the molecular energy levels contribute to it. Another advantage arises when the atomic or molecular beam is so dilute that the molecules and atoms are noninteracting and the intrinsic atomic or molecular properties can be studied. Then, the collisional broadening decreases drastically and the transient time broadening dominates the line widths.

In principle, any atomic or molecular beam is a gas expansion from a high pressure area into vacuum (compare Fig. 3.5). In other words, it is an intended and very well controlled leak in the vacuum chamber [177, 178]. In the following, the focus is set on atomic beams, because the molecular beams used in this work are atomic beams seeded with a small fraction of molecules as explained later in this section. For ideal monoatomic gases, the velocity distribution  $P(v)$  inside the high pressure container follows the Maxwell-Boltzmann distribution:

$$P(v) = 4\pi \left( \frac{m}{2\pi k_B T} \right)^{3/2} v^2 e^{-\frac{mv^2}{2k_B T}} \quad (3.5)$$

Hence, the distribution depends only on the atomic mass  $m$  and the temperature  $T$  inside the container. Figure 3.6a and Figure 3.6b illustrate the effect of different atomic masses and different sample temperatures on the velocity distribution, respectively.

Depending on the pressure inside the container  $p_0$  and the diameter of the container opening  $D$  (compare Fig. 3.5), the atomic beam can be classified to be effusive or supersonic. An effusive beam is formed when the mean free path length  $\lambda$  of the atoms is much larger than the container opening. Then the atom encounters no collisions with other atoms during the expansion through the pinhole and consequently no energy is transferred. The velocity distribution

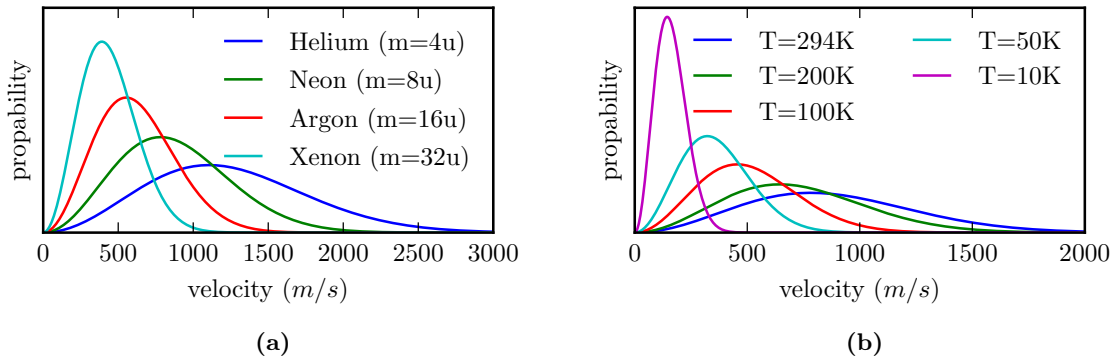


**Figure 3.6:** (a) Maxwell-Boltzmann velocity distributions of different noble gases at room temperature (294 K) and (b) Maxwell-Boltzmann velocity distributions of neon at different temperatures.

of an effusive beam follows the Maxwell-Boltzmann distribution multiplied by the velocity  $v$ , because the probability that the atom leaves the container through the orifice is proportional to its absolute velocity [179]. Even though the effusive beam cannot cool the atoms in the expansion, it still provides a noninteracting environment, which enabled many important experiments (e.g. Stern-Gerlach experiment of atomic spins interacting with magnetic fields [180, 181]). Furthermore, the velocity spread of an effusive atomic beam perpendicular to the traveling direction can be confined with the use of pinholes or skimmers. This approach is a tradeoff between velocity spread and particle density, but it allows ultimately Doppler-free spectroscopic experiments. Many atomic beam experiments rely on effusive techniques, especially when the cooling behavior is less of an issue. Moreover, effusive beams are less demanding on the pumping requirements than supersonic beam techniques.

In contrast to the effusive beam, the supersonic beam can cool the external and internal degrees of freedom of atoms and molecules very efficiently. A pinhole diameter much larger than the mean free path length  $\lambda$  enables many collisions during the expansion. Due to the collisional energy transfer, the beam is more confined and the velocity distribution is much narrower compared to the Maxwell-Boltzmann velocity distribution at the container temperature, even though the mean velocity is higher. Figure 3.7 illustrates the velocity distribution inside the container and in the atomic beam. Under the assumption that the expansion is isentropic and adiabatic, thermodynamics can be employed to determine the terminal velocity of the beam. In an isentropic and adiabatic expansion the sum of the enthalpy  $H$  and the kinetic energy of the directed mass flow is conserved (both the enthalpy and the directed mass are dependent on the distance  $x$  to the starting point of the expansion):

$$H(x) + \frac{1}{2}mv(x)^2 = \text{const.} \quad (3.6)$$

If the enthalpy is completely converted into a directed mass flow, the terminal velocity  $v_{max}$  of the atoms for an ideal gas is only dependent on the container temperature and the mass of

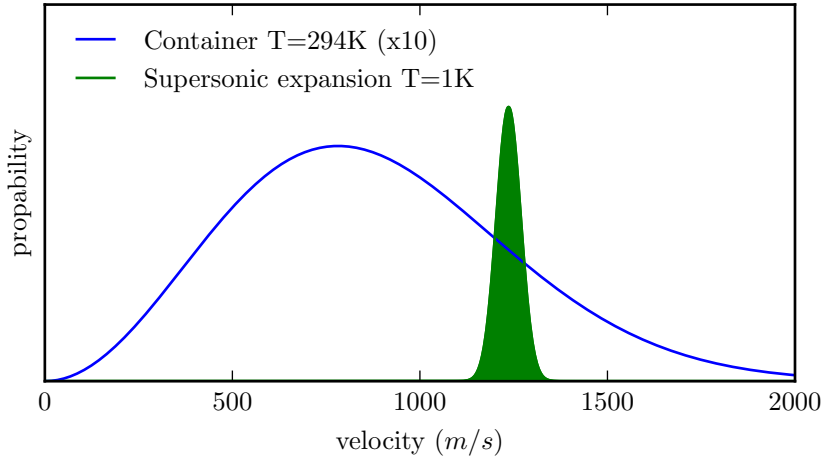


**Figure 3.7:** Comparison of the velocity distribution of neon atoms at room temperature and after supersonic expansion in an atomic beam reaching  $T = 1$  K. The velocity distribution of the supersonic expansion is shifted to the terminal velocity  $v_{max}$ . Both distributions are normalized to one.

the atoms [182]:

$$v_{max} = \sqrt{\frac{5k_B T_0}{m}} \quad (3.7)$$

where  $T_0$  is the temperature inside the container and  $m$  is the mass of the atom. In reality the expansion is not perfectly isentropic or adiabatic and the mean velocity of the ensemble of atoms will never reach the terminal velocity. However, simulations and experiments show that the mean velocity is increasing quickly with a fast convergence towards the terminal velocity in the first fraction of the expansion [183]. Hence, the terminal velocity provides already a good estimate for the mean downstream velocity of the beam [182].

Because the supersonic expansion is a very dynamic process depending on various parameters like collision rate, collision cross-section etc., the thermodynamic properties like pressure, temperature or particle density cannot be stated in a closed form for all positions in the beam. Nevertheless, the mean velocity, the pressure, the temperature, and the particle density on the centerline of the beam are dependent on only two quantities: the ratio of specific heats and the local Mach number, both of which are position dependent [182]. The local Mach number describes the ratio of the particle velocity and the local speed of sound and can be modeled using hydrodynamics. Different mathematical formulas exist to fit the results of the hydrodynamic simulations for the Mach number within distinct regions of the beam [183].

Herein the dynamics will be explained qualitatively using Figure 3.8. Within the container, the atoms collide frequently, therefore the speed of sound is much faster than the mean particle velocity, leading to a small Mach number. Inside the expansion, the situation is reversed because the temperature, the pressure, and the particle density decrease rapidly, while the mean velocity increases even faster. Hence, Mach numbers much larger than one

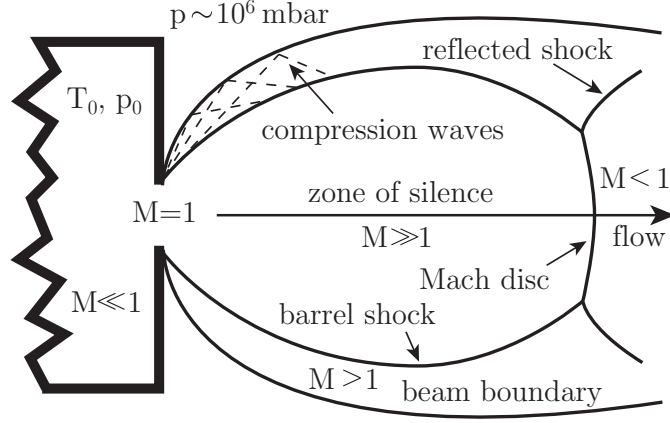


**Figure 3.8:** Scheme of the different regions in a supersonic expansion and their corresponding Mach numbers. For gas expanding from a round pinhole, a barrel shock wave is formed, where the expanding atoms collide with the background gas. The barrel shock wave together with the central shock wave, the so called Mach disc, limits the supersonic expansion with its intrinsic cooling properties. Ideally the spectroscopic measurement takes place in the zone of silence, where the low particle density leads to effectively no interactions between atoms and the temperature of the expansion has reached its stagnation value.

can be achieved in the atomic beam, which makes the expansion supersonic. For a point source, the expansion has a barrel shape and shock waves are formed at the boundaries due to the collision with the background gas. The central shock wave is called Mach disc, a phenomenon known from other supersonic processes (e.g. supersonic aircrafts or bullets). These shock waves are important for the expansion, because they protect the atoms in the so-called zone of silence from stochastic collisions with the warm background gas. The density in the zone of silence becomes so dilute that effectively no collisions take place any more. Hence, the cooling stagnates and the temperature characterizing the velocity spread drops out of equilibrium. The description of the velocity distribution with a single temperature model only makes sense when the system is in thermal equilibrium and the velocity spread follows a Gaussian distribution. Even though the conditions in a supersonic expansion are far from thermal equilibrium, the velocity distribution can be approximated by two Gaussians and two corresponding temperatures, one describing the velocity distribution longitudinal to the beam  $P_{\parallel}$ , the other one transversal to the beam  $P_{\perp}$ :

$$P_{\parallel}(v_{\parallel}) = \sqrt{\frac{m}{2\pi k_B T_{\parallel}}} e^{-\frac{m(v_{\parallel} - v_{max})^2}{2k_B T_{\parallel}}} \quad (3.8)$$

$$P_{\perp}(v_{\perp}) = \frac{m}{2\pi k_B T_{\perp}} e^{-\frac{mv_{\perp}^2}{2k_B T_{\perp}}} \quad (3.9)$$

The velocity distribution parallel to the beam  $P_{\parallel}$  is illustrated in Figure 3.7. Note, that the reliability of the simple two temperature model heavily depends on the experimental setup (e.g. if pinholes, skimmers, etc. are used to confine the beam).

The stagnation temperature decreases while the extent of the zone of silence increases with an increasing orifice diameter  $D$  or an increasing pressure inside the container  $P_0$  [182]. Both possibilities to enhance the cooling behavior have severe implications on the pumping requirements. Another effect which must be considered is the formation of clusters in a supersonic expansion. Many van der Waals complexes form easily in the cold conditions of an atomic beam. To avoid clustering, rare gas atoms are used in atomic and molecular beams. In addition, clustering requires three body collisions, that scale as  $p_0^2 D$  while two body collisions scale as  $p_0 D$  [182]. Consequently, low pressure and large diameter orifices reduce clustering.

In scientific literature, a molecular beam is often a rare gas beam doped with a small fraction of molecules. In principle a pure molecular beam can be formed, but the cooling behavior is worse than in a doped atomic beam, and the formation of dimers, trimers and higher order molecular clusters is promoted. If the fraction of molecules seeded into an atomic beam is small, the molecules thermalize with the surrounding atoms and exhibit similar thermodynamic properties. The main application of molecular beams in spectroscopy is the efficient cooling of the internal degrees of freedom, mainly the rotational and vibrational ones [184]. Within the expansion, the internal energy of the molecule is transferred to the translational energy of the surrounding atoms via inelastic binary collisions. The cooling efficiency of the internal degrees of freedom is dependent on the position in the expansion and the energy level structure of the molecule. If the energy differences of the internal degrees of freedom are small, the transfer to translational energy is more efficient, because less collisions are required to overcome the energy gap. The cooling of electronic excited states is almost impossible, but this is usually not necessary, because only the electronic ground state of most molecules is populated at room temperature. The cooling of the vibrations in a supersonic expansion heavily depends on the vibrational mode structure. In a diatomic molecule, only one vibrational mode exists and the spacing between the different vibrational energy levels is comparably large. Whereas polyatomic molecule exhibits more low lying vibrational modes, making the collisional cooling more efficient. However, the rotational internal degrees of freedom are most efficiently cooled because of their small energy differences. In the course of the expansion, the collision rate decreases and at some point this number is so small that the degrees of freedom are frozen, which means that the internal energy distribution is no longer changing. As a result, the vibrational energy distribution is frozen in first, followed by the rotational energy distribution. Because a single collision is sufficient to transfer translational energy from one particle to another, the temperatures describing the internal degrees of freedom are always larger or equal to the stagnation translational temperature. This behavior would suggest that the best internal cooling is achieved with heavy backing gases, resulting in a low stagnation translational temperature. However, the formation of clusters is enhanced for rare gas atoms with increasing size. Hence, the choice of the backing gas providing the best internal cooling is a tradeoff between a small terminal velocity distribution and cluster formation.

Figure 3.9a shows the predicted spectrum of the monoterpene carvone ( $C_{10}H_{14}O$ ) at different rotational temperatures illustrating the benefits of low rotational temperatures for mi-

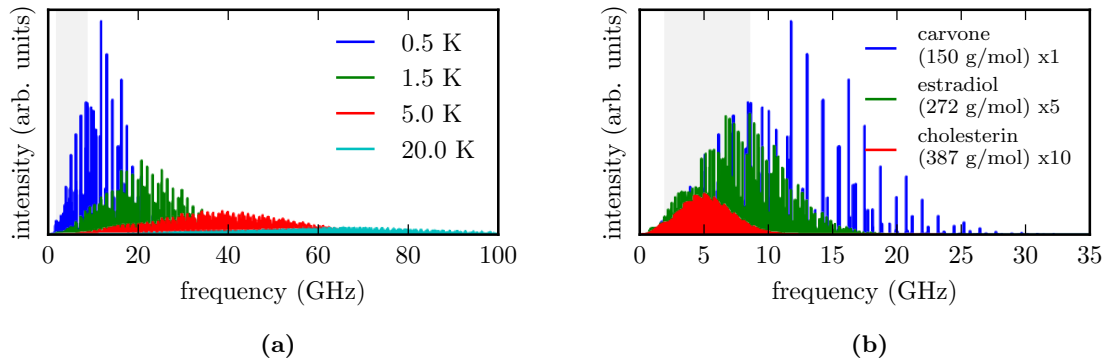


**Figure 3.9:** (a) Simulated rotational spectra of the monoterpene carvone ( $C_{10}H_{14}O$ ) at different rotational temperatures in thermal equilibrium. (b) Simulated rotational spectra of carvone, the female sex hormone estradiol ( $C_{18}H_{24}O_2$ ), and the important sterol cholesterol ( $C_{27}H_{46}O$ ) at a rotational temperature of 0.5 K illustrating the impact of the size of a molecule on the density and intensity of the rotational transitions. The rotational constants of estradiol and cholesterol were estimated via force field calculations. The grey shaded area marks the frequency range of the COMPACT spectrometer.

microwave spectroscopy. The transition intensities at lower temperatures are greatly enhanced due to the population of only a few rotational states. The probability for the population of a rotational state  $P_j$  in thermal equilibrium is given by the Boltzmann distribution:

$$P_j = \frac{N_j}{N} = \frac{g_j e^{-\frac{E_j}{k_B T_R}}}{Q_R} \quad (3.10)$$

where  $N_j$  is the number of molecules in the rotational state with the energy  $E_j$ ,  $T_R$  is the rotational temperature and  $g_j$  is the quantum state degeneracy.  $Q_R$  is the rotational partition function, where the sum goes over all rotational states:

$$Q_R = \sum_i g_i e^{-\frac{E_i}{k_B T_R}} \quad (3.11)$$

The impact of the size of the molecule on the intensity profile is illustrated in Figure 3.9b. The transitions of larger molecules like the female sex hormone estradiol ( $C_{18}H_{24}O_2$ ) or the important sterol cholesterol ( $C_{27}H_{46}O$ ) are shifted to the low frequency end of the spectrum and their intensities drop dramatically due to their high state density. As described earlier, the molecules in a supersonic expansion are not in thermal equilibrium. Usually, the intensity profile of the rotational transitions cannot be modeled exactly using a single temperature distribution. In some cases, stacks of close lying states provide more effective cooling than other pathways leading to non-equilibrium conditions [185].



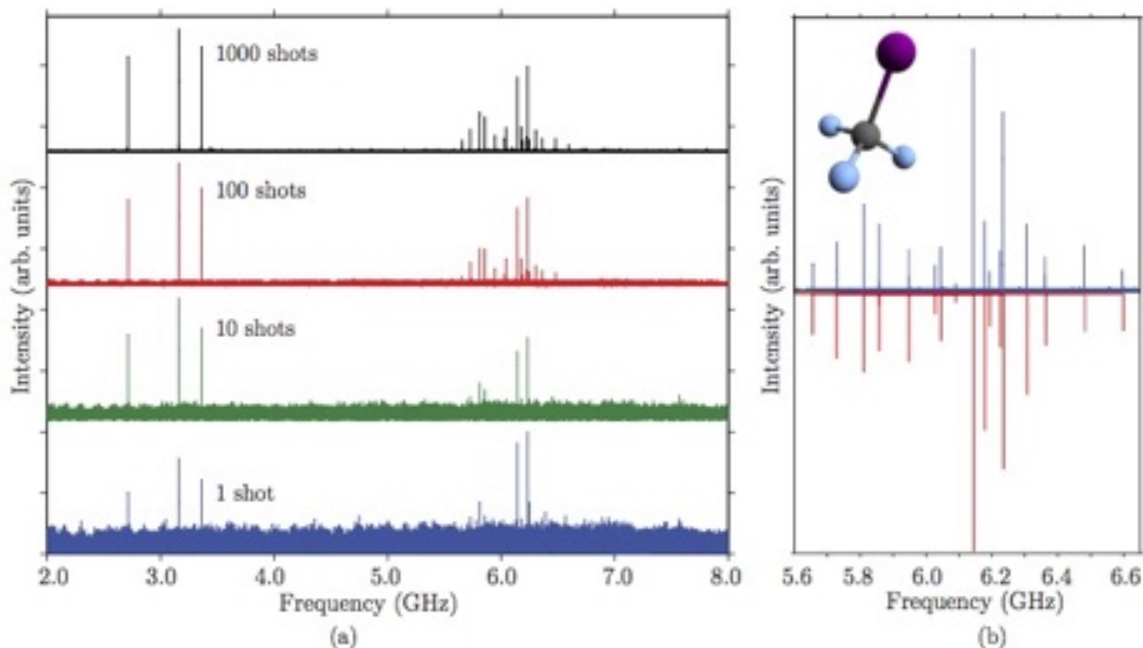


**Figure 3.10:** (a) Rotational spectrum of trifluoroiodo methane ( $\text{CF}_3\text{I}$ ) obtained with the Hamburg COMPACT spectrometer after 1, 10, 100 and 1000 acquisitions using two valves simultaneously and neon as carrier gas. The  $J \rightarrow J+1 : 0 \rightarrow 1$  (around 3 GHz) and the  $J \rightarrow J+1 : 1 \rightarrow 2$  (around 6 GHz) rotational transitions are displayed. Both transitions are split due to nuclear quadrupole coupling arising from the iodine nucleus. (b) Comparison of the experimental spectrum ( $J \rightarrow J+1 : 1 \rightarrow 2$  rotational transition, positive trace) with a simulation (negative trace) indicating the very good agreement for both the frequencies and the intensities of the quadrupole hyperfine transitions.

### 3.3 Commissioning and performance

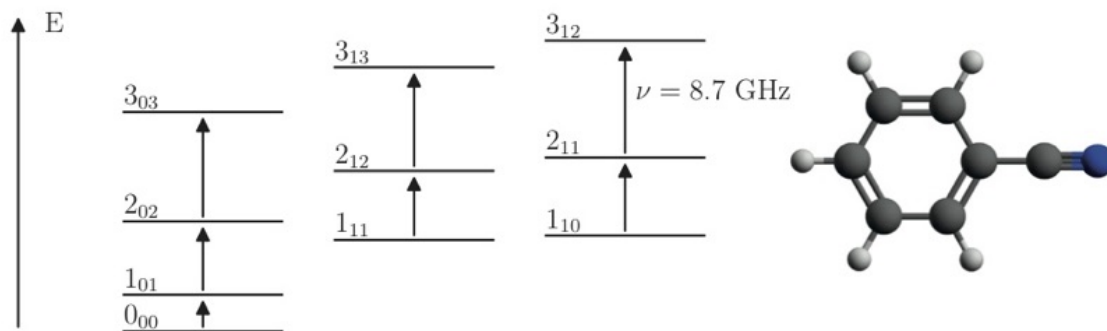
The commissioning of the spectrometer was performed with the molecules trifluoroiodo methane ( $\text{CF}_3\text{I}$ ) and benzonitrile ( $\text{C}_7\text{H}_5\text{N}$ ). These molecules were chosen because their rotational constants are known [60, 186] and their dipole moments are reasonable large, making them easier to detect with rotational spectroscopy. Furthermore at low rotational temperatures their most intense transitions are situated in the spectral bandwidth of the COMPACT spectrometer. Also both molecules exhibit nuclear quadrupole splitting, giving rise to distinct intensity patterns that serve as a good test of the intensity accuracy. Moreover,  $\text{CF}_3\text{I}$  is a gas, whereas benzonitrile is a liquid with a relatively high vapor pressure of about 1 mbar at standard conditions [187]. Hence, no further effort is required to seed a descent amount of molecules into the supersonic expansion.

Figure 3.10 shows the rotational spectrum in the spectral region of 2 – 8 GHz of the prolate

---

This section is partly based on the following publication:

- D. Schmitz, V. A. Shubert, T. Betz, and M. Schnell, *Multi-resonance effects within a single chirp in broadband rotational spectroscopy: The rapid adiabatic passage regime for benzonitrile*, J. Mol. Spec. **280**, 77-84 (2012). (key ideas: 50%, experimental: 40%, data analysis: 40%, writing up: 10%) [69]



**Figure 3.11:** Simplified energy level scheme of all relevant energy levels and transitions, neglecting quadrupole hyperfine splitting, of benzonitrile in the frequency bandwidth of the spectrometer. On the right, the molecular structure of benzonitrile is shown.

symmetric top CF<sub>3</sub>I, after 1, 10, 100, and 1000 FID acquisitions obtained with the COMPACT spectrometer using two simultaneously operated valves. CF<sub>3</sub>I (spectroscopic constants:  $B = 1523.27715(26)$  MHz,  $\chi_{aa} = -3217.424(12)$  MHz) was mixed with the carrier gas neon in a 3 : 100 pressure ratio and expanded into the chamber via supersonic expansion. The spectrum exhibits huge hyperfine splitting due to nuclear quadrupole coupling of the iodine nucleus with the total angular momentum. The resulting splitting pattern and its intensities are very characteristic and can facilitate the spectral assignments. The main features of the rotational spectrum are already seen after one FID acquisition. After 1000 acquisitions (about 9 minutes recording time), all of the spectral features are resolved with a good signal-to-noise ratio. Figure 3.10 displays a comparison of the experimental and the calculated rotational spectrum for the  $J \rightarrow J + 1 : 1 \rightarrow 2$  transition of CF<sub>3</sub>I. The experimental intensities of chirped-pulse FTMW spectroscopy, when working in the linear-fast passage regime, are accurate over the relevant frequency range and agree well with the calculated ones. Care must be taken at the limits of the frequency bandwidth of the spectrometer, where the power of the TWTA drops rapidly. Reliable intensity information is extremely useful for the assignment of new species, in determining relative dipole moment components, and in estimating the relative populations of different species, such as conformers, that contribute to the spectrum.

To obtain reliable intensity information, the spectrometer should be operated in the linear-fast passage (LFP) regime, which leaves the population distribution essentially unchanged. However, high power excitation in combination with large molecular dipole moments can drive the population out of equilibrium in the rapid adiabatic passage (RAP) regime. These strong perturbations of the populations together with broad bandwidth chirp excitation enable step-wise multi-resonance effects as explained in the following on the example of benzonitrile. The planar asymmetric-top molecule benzonitrile (rotational constants:  $A = 5656.01(17)$  MHz,  $B = 1546.8711(10)$  MHz,  $C = 1214.40331(83)$  MHz) has only one non-vanishing dipole moment component  $\mu_a = 4.5152(68)$  D, which gives rise to a purely  $a$ -type spectrum [186]. A simplified energy level scheme of all relevant energy levels and transitions is depicted in Figure 3.11, neglecting the quadrupole hyperfine splitting arising from the nitrogen nucleus quadrupole moment. Three progressive series of rotational transitions are located within the

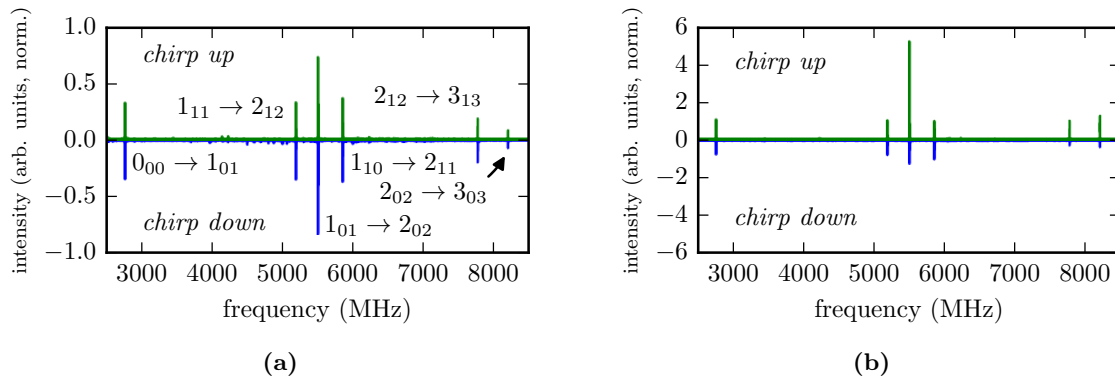


**Figure 3.12:** (a) Rotational spectrum of benzonitrile obtained by employing a low power excitation chirp with a positive (chirp-up) and a negative (chirp-down) chirp rate. The transition intensities of the two individual measurements are almost identical. (b) Same experimental procedure as in (a) but employing high power excitation chirps. The intensities of the chirp-up and chirp-down measurements differ significantly, suggesting population transfer in the RAP regime. The transition  $1_{10} \rightarrow 2_{11}$  was used to normalize the intensities in all experiments.

bandwidth of the spectrometer (compare Fig. 3.11). However, the transition  $2_{11} \rightarrow 3_{12}$  at 8.3 GHz cannot be accessed anymore and the populations of the rotational levels involved in the transition  $1_{10} \rightarrow 2_{11}$  at 5.3 GHz are not affected by any other transition in the frequency range of the spectrometer. Thus, the transition  $1_{10} \rightarrow 2_{11}$  was used to normalize the intensities in the following experiments.

Two sets of experiments were executed to study the effect of stepwise population transfer. Firstly, the molecules were probed with a microwave chirp with a positive chirp rate (chirp-up: 2 – 8.3 GHz, 1  $\mu$ s) and with a negative chirp rate (chirp-down: 8.3 – 2 GHz, 1  $\mu$ s) at low excitation power (gain of the TWTA was set to 50 %, corresponding to about 75 W output power), and secondly at high excitation power (gain of the TWTA was set to 100 %, corresponding to about 300 W output power). If the populations are affected by the excitation pulse via double-resonance excitation, the obtained intensities for the chirp up and the chirp down measurements should be different. The excitation chirp probes the population difference in various progressive series of transitions once starting from the low frequency, another time starting at the high frequency end.

Figure 3.12a presents the rotational spectra of benzonitrile in the 2 – 8.3 GHz frequency range obtained using a chirp-up pulse and a chirp-down pulse at low power setting on the TWTA. The individual rotational transitions are labeled using the  $J_{K_a K_c}$  quantum numbers. The relative intensities are nearly identical in both spectra (chirp-up and chirp-down). Thus, at low power the chirp has a negligible effect on the relative populations of the rotational states and the excitation can be described within the LFP regime. The situation is different for the high power measurement shown in Figure 3.12b. Two important points should be noted: (a) the relative intensities of the individual transitions clearly depend on the direction of the chirp, and (b) the relative intensities differ from those obtained in the low-power measurements for

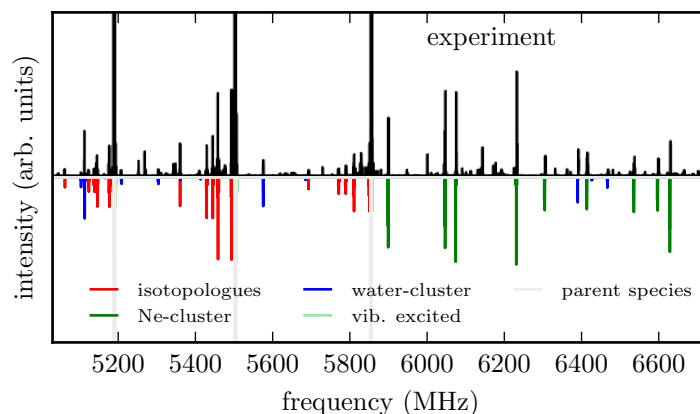


**Figure 3.13:** Rotational spectrum of benzonitrile obtained in the frequency region between 5 and 6.7 GHz. Transitions arising from the parent species, its isotopologues, one benzonitrile-water cluster, two benzonitrile-neon clusters, and a vibrationally excited state of benzonitrile are indicated.

which the linear fast passage regime is valid (see Fig. 3.12a). These findings can be explained with stepwise multi-resonance effects as described within the RAP regime, where population inversion is possible. As discussed in Section 2.4, the population of the respective energy levels can be significantly influenced by the chirp. For example, for the chirp-up measurement within the  $J_{0K_c=J}$  series (Fig. 3.12b), the population of the  $1_{01}$  energy level will be enriched in the course of the chirp via the  $0_{00} \rightarrow 1_{01}$  transition at 2.76 GHz. This change will then be probed by the same chirp when approaching resonance for the  $1_{01} \rightarrow 2_{02}$  transition at 5.5 GHz. As a result, the  $1_{01} \rightarrow 2_{02}$  transition is strongly enhanced compared to the  $0_{00} \rightarrow 1_{01}$  transition. This change in turn leads to an increase of the population of the  $2_{02}$  level, within the RAP regime, and thus to an enhancement of the  $2_{02} \rightarrow 3_{03}$  transition at 8.2 GHz.

In principle, tailored microwave chirps together with high power microwave sources allow the population transfer to a single rotational quantum state. However, complex rotational level schemes and the high number of populated levels might complicate this task. In atomic physics, complete population transfer was already achieved in a simple three-state ladder system of rubidium (5s, 5p, 5d states) using a chirped laser pulse in the RAP regime [188–191].

Finally, a measurement averaging 624 000 acquisitions of benzonitrile was performed to evaluate the sensitivity of the spectrometer. Many publications in high resolution spectroscopy exist that describe the spectra and report rotational constants of benzonitrile [186, 192], its isotopologues [193, 194], the benzonitrile dimer [195], the benzonitrile-water cluster [12], benzonitrile rare gas clusters [196], and dipole-bound complexes of benzonitrile with various other organic molecules [197]. A signal-to-noise ratio of about 10 000 for the strongest transitions of benzonitrile enabled the observation of all mono substituted isotopologues, one benzonitrile-water cluster, two benzonitrile-neon clusters, and a vibrationally excited state of benzonitrile.

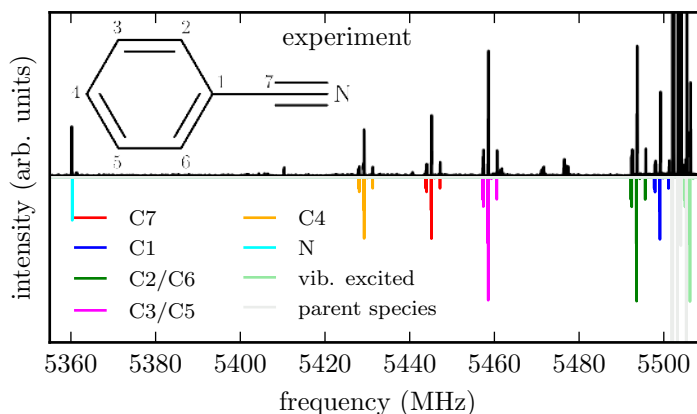


**Figure 3.14:** Zoom in of the spectrum to the rotational transition  $1_{01} \rightarrow 2_{02}$  of benzonitrile and its mono substituted isotopologues. The quadrupole splitting pattern is observed for all  $^{13}\text{C}$  isotopologues, but not for the  $^{15}\text{N}$  isotopologue due to its nuclear spin of  $1/2$ .

The benzonitrile dimer was not observed in the spectrum, because it has a vanishing permanent dipole moment [195]. The spectrum obtained in the frequency region between 5 and 6.7 GHz is presented in the upper trace of Figure 3.13. The lower trace shows the predicted spectra based on fitted rotational constants for the different species identified in the spectrum. The intensities for the parent species of benzonitrile are off the  $y$ -axis scale.

A zoom into the spectrum to distinguish the individual isotopologues is presented in Figure 3.14. Again the intensities of the parent species are cut off to provide a better visibility of the low intensity components in the spectrum. The intensities of the transitions originating from the  $^{13}\text{C}$  isotopologues reflect nicely their natural abundance of about 1 %. Because the structures of the C2 and the C6 isotopologues are equivalent, as well as the structures of the C3 and the C5 isotopologues, their transition intensities are doubled compared to the C1, C4, C7 isotopologues. The substitution of nitrogen  $^{14}\text{N}$  to  $^{15}\text{N}$  has the largest impact on the rotational constant because the nitrogen atom is furthest away from the center of mass of the molecule than any other atom. Due to the nuclear spin of  $1/2$  of  $^{15}\text{N}$ , this isotopologue exhibits no quadrupole hyperfine splitting and the population is not distributed over different hyperfine levels. Hence, the intensity of the transition originating from the  $^{15}\text{N}$  isotopologue is comparable to the transitions of the  $^{13}\text{C}$  isotopologues even though the natural abundance of  $^{15}\text{N}$  is only 0.4 %. The knowledge of the rotational constants of all singly substituted carbon and nitrogen isotopologues enables the determination of the heavy atom structure of benzonitrile employing Kraitchman equations [47]. The substitution structure of benzonitrile obtained by microwave spectroscopy was already determined by Rudolph et al. [194].

## Chapter 4

# Communication through the phenyl ring: internal rotation and nuclear quadrupole splitting in p-halotoluenes

### 4.1 Introduction

The effect of internal rotation in molecules, as well as the magnitude and origin of the forces that impede free internal rotation, has long interested chemists. Internal rotation is understood as the rotation of one or several parts of a molecule, such as a methyl group, about a bond relative to the remaining molecular structure. Molecules containing internal rotors play important roles in a variety of chemical environments and thus have been the subject of numerous previous studies [26, 31, 32]. Evidence of such complex molecules has been seen in astrochemical observations [199, 200]. Furthermore, the high-resolution data expected soon from next-generation array telescopes, such as the extended Very Large Array (eVLA) [201] and the Atacama Large Millimeter/submillimeter Array (ALMA) [33], will rely on high-quality terrestrial laboratory measurements in efforts to understand the spectra obtained from them.

Rotational spectroscopy and rotationally resolved ultraviolet (UV) spectroscopy have proven to be well-suited methods for exploring the properties of internal rotation [115, 202]. Herein, the COMPACT broadband chirped-pulse microwave spectrometer (Chap. 3) is used that allows for the quick recording of high-resolution rotational spectra over a wide frequency range. This capability, along with the rotational transition line intensities that it provides, makes it particularly suited for investigating the rotational spectra of complex molecules, i.e.

---

This chapter is completely based on the following publication:

- V. A. Shubert, D. Schmitz, and M. Schnell, *Communication through the phenyl ring: internal rotation and nuclear quadrupole splitting in p-halotoluenes*, Mol. Phys. **111**, 2189-97 (2013). (experimental: 33%, data analysis: 40%; writing up: 10%) [198]

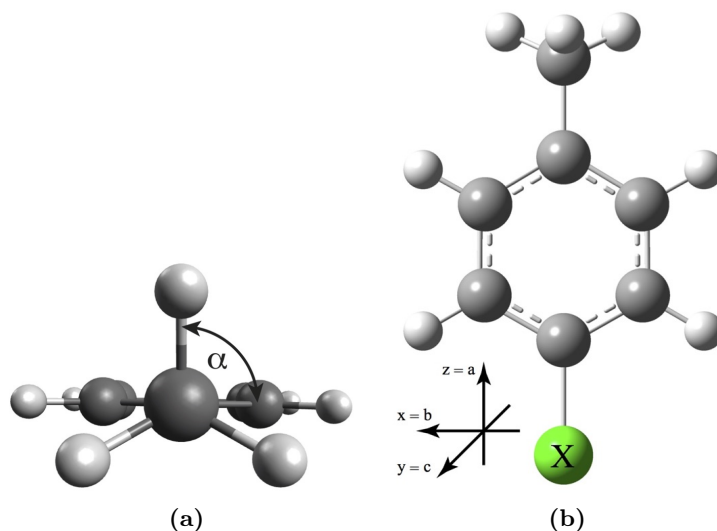


**Figure 4.1:** Scheme of the structure of a *p*-halotoluene. The halogen atom is labeled with an *X* (with  $X = \text{Cl}, \text{Br}, \text{I}$ ). The rotation angle of the methyl internal rotation is indicated in (a) as well as the principal axis system (b). Note, the principal axis system coincides with the principal axis system of the field gradient.

when the molecule is highly flexible and when rotational transitions are split by additional couplings, e.g. by the presence of quadrupolar nuclei.

The investigation of series of *p*-halotoluenes (with chlorine, bromine and iodine as the halogen substituent, see Scheme 4.1) was chosen to learn about the potential interactions of the quadrupolar nuclei with the internal rotation via the phenyl ring. Due to the symmetry of the molecule, the methyl group internal rotation with respect to the molecular frame is hindered by a sixfold barrier,  $V_6$ . It is discussed in the literature that internal rotation barriers can be influenced by substituents as far as 10 atoms away [203] and these effects can be transmitted through conjugated bond systems, such as phenyl rings [204]. The halogen substituents fluorine (investigated previously) [205], chlorine, bromine, and iodine (this work) differ in their electronic behavior. This difference is evidenced by their varying electronegativities and also their sizes, which in the case of the *p*-halotoluenes lead to differences in overlap of the valence *p*-orbitals of the halogens with the phenyl  $\pi$ -cloud.

The rotational spectra of the *p*-halotoluene series contain two sensitive probes for studying communication pathways via the phenyl ring. One is the interaction of the nuclear spin of the halogen substituents ( $I_{\text{Cl}} = 3/2$ ,  $I_{\text{Br}} = 3/2$ ,  $I_{\text{I}} = 5/2$ ) with the overall rotation of the molecule. This interaction leads to characteristic line splittings in the spectra that are sensitive to the chemical environment of the quadrupolar nucleus, e.g. the electron density around the atom and thus the character of the chemical bond (detailed in Sec. 2.2). The second probe is the barrier hindering the internal rotation of the methyl group, as it is sensitive to the character of the bond between the methyl carbon and the phenyl ring (Sec. 2.3). This bond character depends on the electronic structure of the phenyl ring that in turn depends on the other substituents on the ring.



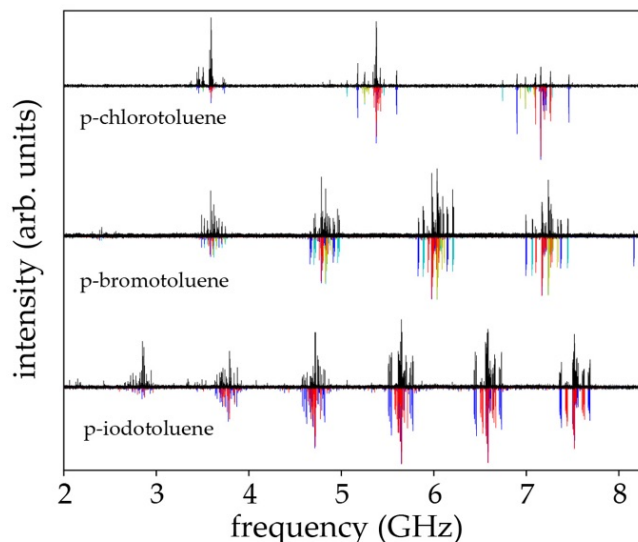


**Figure 4.2:** The experimental rotational spectra (black, positive traces) and simulated spectra (negative traces) of the p-halotoluenes measured in this work. The different colors of the simulated spectra correspond to the different isotopologues and  $m$  states of the transitions. Blue:  $m = 0$  for  $p^{35}\text{ClC}_7\text{H}_7$ ,  $p^{81}\text{BrC}_7\text{H}_7$  and  $p\text{IC}_7\text{H}_7$ . Red:  $m = 1$  for  $p^{35}\text{ClC}_7\text{H}_7$ ,  $p^{81}\text{BrC}_7\text{H}_7$  and  $p\text{IC}_7\text{H}_7$ . Teal:  $m = 0$  for  $p^{37}\text{ClC}_7\text{H}_7$  and  $p^{79}\text{BrC}_7\text{H}_7$ . Yellow:  $m = 1$  for  $p^{37}\text{ClC}_7\text{H}_7$  and  $p^{79}\text{BrC}_7\text{H}_7$ . For  $p\text{ClC}_7\text{H}_7$ , the groups of transitions correspond to  $J = 1 \rightarrow 2$ ,  $2 \rightarrow 3$  and  $3 \rightarrow 4$ . In  $p\text{BrC}_7\text{H}_7$ , the groups of transitions correspond to  $J = 1 \rightarrow 2$ ,  $2 \rightarrow 3$ ,  $3 \rightarrow 4$ ,  $4 \rightarrow 5$ ,  $5 \rightarrow 6$  and  $6 \rightarrow 7$ . For  $p\text{IC}_7\text{H}_7$ , the groups of transitions correspond to  $J = 1 \rightarrow 2$ ,  $2 \rightarrow 3$ ,  $3 \rightarrow 4$ ,  $4 \rightarrow 5$ ,  $5 \rightarrow 6$ ,  $6 \rightarrow 7$ ,  $7 \rightarrow 8$  in order of increasing frequency, respectively.

It is the aim of the present investigation to shed more light on the influence of the particular substituents and to study the ability of the phenyl ring to communicate information from one substituent to another. The range in values of both halogen electronegativities and quadrupolar coupling constants should yield information about the influence of both on the internal rotation barrier. Accompanied by electronic structure calculations, the capabilities and high resolution of the broadband chirped-pulse Fourier transform microwave (CP-FTMW) spectrometer presented in Chapter 3 are perfectly suited to such studies of intramolecular interactions. Spectra are anticipated that contain a larger number of transitions spread over a wide range due to the low-barrier  $V_6$  internal rotation tunneling and nuclear quadrupole coupling.

In the following, the experimental details (Sec. 4.2) and computational methods (Sec. 4.3) are introduced, followed by a section on the spectral details and fitting (Sec. 4.4). In the Results and Discussion section (Sec. 4.5), the interaction between the internal rotation of the methyl group and the nuclear spin of the halogen substituents is addressed. Finally, this chapter closes with a Summary and Conclusions section (Sec. 4.6).



## 4.2 Experimental

The CP-FTMW spectrometer was detailed in Chapter 3 and only a brief description is given here. The molecules of interest were introduced into the chamber via supersonic expansion from pulsed valves operating at 2 Hz. Two sets of experiments were performed. In the first, the sample holders were placed outside the vacuum and heated to 38 °C, 50 °C and 50 °C for *p*-chlorotoluene (pClC<sub>7</sub>H<sub>7</sub>), *p*-bromotoluene (pBrC<sub>7</sub>H<sub>7</sub>) and *p*-iodotoluene (pIC<sub>7</sub>H<sub>7</sub>), respectively. Neon was used as the carrier gas at an absolute backing pressure of 3.0 bar. In a second set of experiments employing argon as the buffer gas, the sample holders were placed inside the vacuum and heated to approximately 85 °C for all species at backing pressures between 1.3 and 2.8 bar.

After supersonic expansion into the chamber, the ensemble of molecules was polarized with a 1  $\mu$ s chirp spanning 2 – 8.5 GHz. For each spectrum, 50  $\mu$ s of the FID was recorded at a resolution of 10 ps, yielding a frequency resolution of 20 kHz in the Fourier transform (FT) and hence the rotational spectra obtained. Typically, 200 000 – 500 000 FIDs were co-added for each spectrum. Prior to performing the FT on pClC<sub>7</sub>H<sub>7</sub> and pBrC<sub>7</sub>H<sub>7</sub>, a Kaiser-Bessel window was applied for 69 dB sidelobe attenuation [58]. Background lines were present in the raw FT obtained from the FID and were removed by masking, as elaborated on in the supplementary material of Reference [198].

## 4.3 Computational Methods

Electronic structure calculations were performed with the Gaussian 03 [206] and Gaussian 09 [207] program suites. Structural optimizations were performed with both Møller-Plesset second-order perturbation theory (MP2) and density functional theory employing the Becke, three parameter, Lee-Yang-Parr (B3LYP) exchange-correlation functional (compare Sec. 2.6). The aug-cc-pVTZ basis set was used in both methods. For the pIC<sub>7</sub>H<sub>7</sub> calculations, a basis set [208] containing an effective core potential from the ESML basis set exchange was employed [166, 209]. To obtain reasonable quadrupole coupling constants for pIC<sub>7</sub>H<sub>7</sub>, B3LYP calculations were repeated using the 6-311G(d,p) basis set [210] from the ESML basis set exchange [166, 209]. B3LYP relaxed energy scans for the internal rotation of the methyl group were performed with both the cc-pVTZ and aug-cc-pVTZ basis sets. Relaxed energy MP2 scans were carried out only with the cc-pVTZ basis set.

## 4.4 Spectral details and fitting

The *p*-halotoluenes are asymmetric tops with only a single nonzero dipole moment component,  $\mu_a$ , that lies along the principal axis that passes through the halogen and methyl carbon. This configuration gives rise to *a*-type transitions, i.e.  $\Delta J = \pm 1$ ,  $\Delta K_a = 0$  and  $\Delta K_c = \pm 1$  (compare Table 2.2). Tunneling through the low sixfold barrier splits the rotational energy

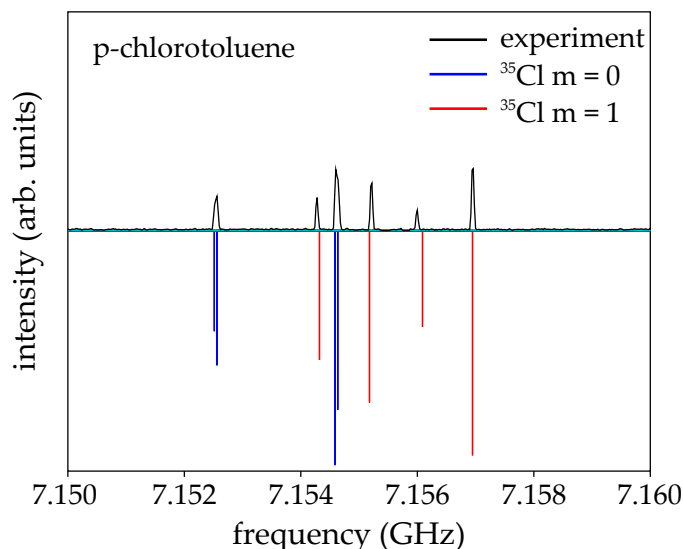


**Figure 4.3:** The experimental and simulated rotational spectra for the  $J_{K_a K_c}(m=0) = 3_{03} \rightarrow 4_{04}$  and the  $J_{K_a K_c}(m=1) = 3_{13} \rightarrow 4_{14}$  transitions of  $p\text{-}^{35}\text{ClC}_7\text{H}_7$  between 7.15 and 7.16 GHz. The inexact post-application of quadrupole splitting to the RAM36 simulations with a self-written program leads to greater disagreement between simulation and experiment for the  $m=1$  transitions. However, the relative intensities match very well.

levels, and an additional quantum number must be introduced. Herein, to characterize these internal rotation energy levels, the quantum number  $m$  of the free rotor states is used that is appropriate for low-barrier cases (Eqn. 2.63 and Eqn. 2.64). This quantum number can take values of  $m = 0, \pm 1, \pm 2, \pm 3, \dots$  and the  $m \neq 0$  free rotor states (i.e. in the limit of  $V_6 \rightarrow 0$ ) are doubly degenerate. For barriers of intermediate magnitude, some of these degeneracies are lifted. The selection rule for torsional transitions follows  $\Delta m = 0$ . The transitions associated with  $m = 0$  have the pattern of an ordinary asymmetric rotor and can be modeled using traditional effective asymmetric rotor Hamiltonians. These transitions may be conveniently used to determine the rotational constants. A detailed analysis of the  $m \neq 0$  levels requires modifications to the Hamiltonian. Common approaches are the principal axis method (PAM), rho axis method (RAM) [132], and internal axis method (detailed in Sec. 2.3). Only the transitions associated with  $|m| = 3$  are significantly affected by the barrier. They are largely split and allow for an accurate barrier determination. Due to cooling in the course of the supersonic expansion in the molecular beam used herein, only energy levels associated with  $m = 0$  and  $|m| = 1$  are significantly populated and these provide only limited information about the internal rotation barrier height.

Very low barriers to methyl-top internal rotation, such as in the  $V_6$  potential of the  $p$ -halotoluenes, are well known to be challenging to model and fit accurately. The method of performing separate fits for the  $m = 0$  and  $m = 1$  states is often used, although within the regime of low barriers, interpretation of the results is difficult. In the SPFIT/SPCAT program of Pickett [146], the  $m = 1$  states can be fit with an extra parameter,  $D_a$ , that is proportional to the barrier height (see Sec. 2.3). The  $D_a$  parameter appears in the Hamilto-

nian for coupling between internal and overall rotation in the term  $D_a \hat{J}_a$  and is given by the following equation:

$$D_a = F \rho_a W_{0\sigma}^{(1)} \quad (4.1)$$

$D_a$  is nonzero for the  $m = 1$  states, but is zero for the  $m = 0$  states [131]. In a high barrier case, the sum in Eqn. 2.70 converges quickly and all the non-vanishing perturbation coefficients  $W_{01}^{(1)}$ ,  $W_{00}^{(2)}$  and  $W_{01}^{(2)}$  can be derived from the two independent fits. Using the perturbation coefficients, the reduced barrier height (compare Sec. 2.3) and the orientation of the rotor relative to the principal axis system can be obtained as was shown for the molecule *o*-chlorotoluene [131]. However for low barriers, this strategy is more difficult to apply and gives unreliable results [130]. Even though the  $m = 1$  states can be fit using the parameter  $D_a$  to experimental accuracy, it is not possible to link  $D_a$  directly to a physical quantity. In both high- and low-barrier cases, ideally one would prefer a global fit of all the transitions simultaneously and to obtain a barrier directly from the output of the program. Towards this end, the RAM36 program by Ilyushin et al. was recently released and was successful in the analysis of the toluene internal  $V_6$  barrier [135].

An advantage of SPFIT/SPCAT is the treatment of nuclear quadrupole splitting that is not implemented in the current version of RAM36. Thus, the following strategy was used to fit and interpret the experimental data. The  $m = 0$  and  $m = 1$  states were assigned and fit separately using SPFIT/SPCAT. The rotational constants, nuclear quadrupole coupling constants ( $\chi_{aa}$  and  $\chi_{bb} - \chi_{cc}$ ), and the centrifugal distortion coefficient,  $D_J$ , were fit. The  $m = 1$  states were fit while allowing the  $D_a$  parameter to float. In the next step, the quadrupole constants were set to zero and the unperturbed ‘center frequencies’ predicted using the fitted constants for each molecule and isotopologue. These center frequencies were then used as input for RAM36. It is important to note that only the predictions for  $J_{K_a K_c} \rightarrow J'_{K'_a K'_c}$  transitions actually observed in the experimental spectra were used.

For pClC<sub>7</sub>H<sub>7</sub> in RAM36, the rotational constants, centrifugal distortion coefficient ( $D_J$ ), and internal rotor parameters ( $V_6$ ,  $F$ ,  $-2F\rho$ ) were fit. First, the rotational constants and  $D_J$  were obtained by fitting only the  $m = 0$  transitions. Once this step was converged, the  $m = 1$  states were added and the  $-2F\rho$  parameter was allowed to float while keeping the  $F$  and  $V_6$  parameters fixed at the toluene values [135]. It was found that the fits were most sensitive to the  $-2F\rho$  parameter, and thus it was fit before moving on to other parameters. Next,  $F$  was fit while keeping  $-2F\rho$  fixed to its optimized value. Several iterations of fitting  $F$  and  $-2F\rho$  were performed until both changed by less than 0.02% from the previous iteration. For pClC<sub>7</sub>H<sub>7</sub>, the positions of some low  $J$   $|m| = 3$  transitions near the range of the COMPACT spectrometer were previously published by Herberich [211], and these transitions were then added to the fit and  $V_6$  allowed to float while keeping all other parameters fixed. For pBrC<sub>7</sub>H<sub>7</sub> and pIC<sub>7</sub>H<sub>7</sub>, a similar approach as above was applied, but  $V_6$  was fixed at the fitted p<sup>35</sup>ClC<sub>7</sub>H<sub>7</sub> value. The approach of fixing certain parameters while allowing others to be fitted, and iterating through fitting the parameters, has been suggested previously so that the fits remain physically valid [132, 212]. In the final RAM36 simulations, a rotational temperature of 1 K was used for all

molecules.

It should be noted that the quantum numbers of the unperturbed center frequencies for the  $m \neq 0$  states predicted by SPCAT differ from those of RAM36. This difference is due to the fact that different methods are used to assign  $K_a$  and  $K_c$  quantum numbers within the PAM and RAM approaches. It is also because for the  $m = 1$  states, the  $K_a$  and  $K_c$  quantum numbers are no longer 'good'.

## 4.5 Results and discussion

The spectra of the *p*-halotoluenes are presented in the range from 2 to 8.3 GHz in the positive traces of Figure 4.2 along with the respective simulations, as negative traces, resulting from the spectral fits. For pClC<sub>7</sub>H<sub>7</sub> and pBrC<sub>7</sub>H<sub>7</sub>, two isotopologues are present in the molecular beam in natural abundance (p<sup>35</sup>ClC<sub>7</sub>H<sub>7</sub>, p<sup>37</sup>ClC<sub>7</sub>H<sub>7</sub>, p<sup>79</sup>BrC<sub>7</sub>H<sub>7</sub> and p<sup>81</sup>BrC<sub>7</sub>H<sub>7</sub>). Within this study, no lines associated with the <sup>13</sup>C-isotopologues were identified. As can be seen from Figure 4.2, with higher molecular mass and thus smaller *B* and *C* rotational constants, the spacing of the groups of rotational transitions becomes smaller, as expected. Individual subgroups arising from tunneling through the internal rotation barrier (denoted by  $m = 0$  and  $m = 1$ ) are further split due to nuclear quadrupole splitting and are color-coded in the simulation traces. The nuclear quadrupole splitting increases from pClC<sub>7</sub>H<sub>7</sub> to pBrC<sub>7</sub>H<sub>7</sub> to pIC<sub>7</sub>H<sub>7</sub> as expected from the magnitudes of their atomic nuclear quadrupole coupling values  $eQq_{n10}$  (summarized in Table 2.3).

Figure 4.3 displays the  $J_{K_a K_c}(m = 0) = 3_{03} \rightarrow 4_{04}$  and the  $J_{K_a K_c}(m = 1) = 3_{13} \rightarrow 4_{14}$  rotational transitions of p<sup>35</sup>ClC<sub>7</sub>H<sub>7</sub> in the range 7.15 – 7.16 GHz and demonstrates the resolving power of the COMPACT spectrometer. In both the transition frequencies and intensities, good agreement between the experimental and the simulated transition intensities is seen. The parameters for the fits are summarized in Tables 4.1-4.3 along with the standard deviation ( $\sigma$ ) and number of lines included in each fit ( $N^\circ$ ). In Figures 4.2 and 4.3, the simulated center transition frequencies (i.e. without quadrupole splitting) from RAM36 were taken and then each line was quadrupole split using a self-written MATLAB code employing the first-order perturbation theory for quadrupole coupling presented in Gordy and Cook [117, Chap. 9]. For the  $m = 1$  lines, small disagreements between the simulated spectra and experiment were seen that could be due to *K* mixing, as was reported for (CH<sub>3</sub>)<sub>3</sub>SnCl [124]. For the discussion on nuclear quadrupole interaction, the results from the SPFIT program are used. The full line lists and assignments are available in the supplementary material of Reference [198].

The initial fits with SPFIT typically gave  $\sigma$  values of 5 – 10 kHz, well below the experimental resolution. For both pClC<sub>7</sub>H<sub>7</sub> isotopologues (<sup>35</sup>Cl and <sup>37</sup>Cl), the rotational constants *B* and *C* of the  $m = 0$  states agree well with those previously reported by Herberich [211]. Furthermore, the *B* and *C* rotational constants from the global RAM36 fit also agree very well, although the *A* constant differs by about 1 MHz. The *A* rotational constant would require

**Table 4.1:** Rotational constants, quadrupole moment, and internal rotation parameters for two isotopologues of p-chlorotoluene. Note the errors given here for the measured values are standard errors.  $N^\circ$  is the number of lines included in the fit and  $\sigma$  is the standard deviation of the fit.

	<sup>35</sup> Cl isotopologue				<sup>37</sup> Cl isotopologue			
	Experiment	B3LYP <sup>a</sup>	MP2 <sup>a</sup>	Herberich [211]	Experiment	B3LYP <sup>b</sup>	MP2 <sup>b</sup>	Herberich [211]
$A_{eff} = A + F\rho^2$ (MHz)	5710.86 (50) <sup>c</sup>	5568.38	5535.80	5712.18 (66)	5710.77 (43) <sup>c</sup>	5568.38	5535.80	5713.1 (10)
$B$ (MHz)	968.24434 (99) <sup>c</sup>	964.13	970.01	968.246 (2)	943.9578 (14) <sup>c</sup>	939.83	945.65	943.953 (4)
$C$ (MHz)	827.92238 (99) <sup>c</sup>	826.04	829.64	827.920 (2)	810.1004 (14) <sup>c</sup>	808.14	811.75	810.099 (4)
$D_J$ (kHz)	0.031 (22) <sup>c</sup>				0.023 (30) <sup>c</sup>			
$\chi_{zz}$ (MHz) ( $m = 0$ )	-71.155 (5) <sup>d</sup>	-68.94	-67.15	-71.7 (7)	-56.069 (7) <sup>d</sup>	-54.15		-56.6 (13)
$\chi_{zz}$ (MHz) ( $m = 1$ )	-71.165 (7) <sup>d</sup>				-56.09 (2) <sup>d</sup>			
$\chi_{xx} - \chi_{yy}$ (MHz) ( $m = 0$ )	4.802 (13) <sup>d</sup>	6.97	3.64		3.749 (16) <sup>d</sup>	4.48		
$\chi_{xx} - \chi_{yy}$ (MHz) ( $m = 1$ )	4.7 (1) <sup>d</sup>				4.8 (2) <sup>d</sup>			
$\delta$ ( $m = 0$ )	0.02917 (8) <sup>c</sup>	0.042	0.022		0.0289 (1) <sup>c</sup>	0.034		
$\delta$ ( $m = 1$ )	0.0285 (6) <sup>c</sup>				0.037 (2) <sup>c</sup>			
$D_a$ (kHz)	-11312.3 (12) <sup>d</sup>				-11298.2 (17) <sup>d</sup>			
$V_6$ (GHz)	144.98 (88) <sup>c</sup>				145.02 (88) <sup>c</sup>			
$2\rho F$ (GHz)	11.34 (24) <sup>c</sup>			146.1 (4)	11.34 (24) <sup>c</sup>			146.1 (4)
$F$ (GHz)	164.6 (2) <sup>c</sup>				164.6 (2) <sup>c</sup>			
$I_\alpha$ (amu · Å <sup>2</sup> )	3.182 (33) <sup>c</sup>	3.23	3.24		3.182 (33) <sup>c</sup>	3.23	3.24	
	RAM36 / $m = 0$ / $m = 1$				RAM36 / $m = 0$ / $m = 1$			
$\sigma$ (kHz)	5.4 <sup>c</sup> / 6.0 <sup>d</sup> / 6.8 <sup>d</sup>				8.0 <sup>c</sup> / 5.9 <sup>d</sup> / 9.7 <sup>d</sup>			
$N^\circ$	34 <sup>c</sup> / 78 <sup>d</sup> / 67 <sup>d</sup>				31 <sup>c</sup> / 59 <sup>d</sup> / 46 <sup>d</sup>			
	17				17			

<sup>a</sup> Electronic structure calculation using an aug-cc-pVTZ basis set.

<sup>b</sup> Single point calculation on <sup>37</sup>Cl isotopologue using optimised structure of <sup>35</sup>Cl isotopologue.

<sup>c</sup> Parameter from global fit using RAM36.

<sup>d</sup> Parameter from local effective fits using SPFIT.

**Table 4.2:** Rotational constants, quadrupole moment, and internal rotation parameters for two isotopologues of p-bromotoluene. Note the errors given here for the measured values are standard errors.  $N^\circ$  is the number of lines included in the fit and  $\sigma$  is the standard deviation of the fit.

	<sup>79</sup> Br isotopologue			<sup>81</sup> Br isotopologue		
	Experiment	B3LYP <sup>a</sup>	MP2 <sup>a</sup>	Experiment	B3LYP <sup>b</sup>	MP2 <sup>b</sup>
$A_{eff} = A + F\rho^2$ (MHz)	5706.65 (32) <sup>c</sup>	5566.33	5534.61	5706.82 (37) <sup>c</sup>	5566.33	5534.61
$B$ (MHz)	636.97364 (24) <sup>c</sup>	632.67	640.32	630.55936 (27) <sup>c</sup>	626.27	633.87
$C$ (MHz)	573.02879 (27) <sup>c</sup>	570.10	575.97	567.83193 (30) <sup>c</sup>	564.91	570.75
$D_J$ (kHz)	0.0131 (23) <sup>c</sup>			0.0092 (25) <sup>c</sup>		
$\chi_{zz}$ (MHz) ( $m = 0$ )	555.618 (8) <sup>d</sup>	519.21	480.44	464.186 (10) <sup>d</sup>	434.66	
$\chi_{zz}$ (MHz) ( $m = 1$ )	555.65 (1) <sup>d</sup>			464.227 (6) <sup>d</sup>		
$\chi_{xx} - \chi_{yy}$ (MHz) ( $m = 0$ )	-26.311 (34) <sup>d</sup>	-25.88	-24.20	-22.055 (36) <sup>d</sup>	-21.91	
$\chi_{xx} - \chi_{yy}$ (MHz) ( $m = 1$ )	-26.21 (15) <sup>d</sup>			-22.284 (23) <sup>d</sup>		
$\delta$ ( $m = 0$ )	0.02279 (3) <sup>c</sup>	0.022	0.021	0.02286 (4) <sup>c</sup>	0.023	
$\delta$ ( $m = 1$ )	0.0227 (1) <sup>c</sup>			0.02310 (2) <sup>c</sup>		
$D_a$ (kHz)	-11314.8 (31) <sup>d</sup>			-11308.7 (8) <sup>d</sup>		
$V_6$ (GHz)	144.98			144.98		
$2\rho F$ (GHz)	11.326 (77) <sup>c</sup>			11.326 (84) <sup>c</sup>		
$F$ (GHz)	164.66 (55) <sup>c</sup>			163.01 (64) <sup>c</sup>		
$I_\alpha$ (amu · Å <sup>2</sup> )	3.240 (11) <sup>c</sup>	3.23	3.24	3.212 (13) <sup>c</sup>	3.23	3.24
$\sigma$ (kHz)	RAM36 / $m = 0$ / $m = 1$			RAM36 / $m = 0$ / $m = 1$		
	3.0 <sup>c</sup> / 5.8 <sup>d</sup> / 6.3 <sup>d</sup>			3.4 <sup>c</sup> / 7.3 <sup>d</sup> / 6.3 <sup>d</sup>		
$N$	47 <sup>c</sup> / 92 <sup>d</sup> / 81 <sup>d</sup>			50 <sup>c</sup> / 98 <sup>d</sup> / 81 <sup>d</sup>		

<sup>a</sup> Electronic structure calculation using an aug-cc-pVTZ basis set.

<sup>b</sup> Single point calculation on <sup>81</sup>Br isotopologue using optimised structure of <sup>79</sup>Br isotopologue.

<sup>c</sup> Parameter from global fit using RAM36.

<sup>d</sup> Parameter from local effective fits using SPFIT.

many more  $J$  levels than available within spectral range of the COMPACT spectrometer to be fit with the same accuracy as the  $B$  and  $C$  rotational constants. Furthermore,  $A$  is modified from the equilibrium structure value due to coupling with the internal rotation of the methyl group. From the RAM36 fit, the barrier height was determined to be 144.98(88) GHz and 145.02(88) GHz for the  $^{35}\text{Cl}$  and  $^{37}\text{Cl}$  isotopologues, respectively, slightly lower than the 146.1(4) GHz previously reported [211]. However, these barriers are within the uncertainty of that reported for  $p$ -fluorotoluene,  $V_6 = 144.79(19)$  GHz [205]. For  $p\text{ClC}_7\text{H}_7$ , the fitted parameters from the current data set yield predictions for the  $|m| = 3$  transitions that are improved over those predicted earlier [211]. The positions of the  $J = 4 \rightarrow 5$  and  $5 \rightarrow 6$ ,  $K_a = 1$ ,  $|m| = 3$  transitions reported by Herberich [211], for example, are now predicted within about 500 kHz for all but one transition. This result offers support for the self-consistent approach employed here to achieve this fit. The value of  $V_6$  for the  $p\text{BrC}_7\text{H}_7$  and  $p\text{IC}_7\text{H}_7$  fits was fixed to the  $V_6 = 144.98(88)$  GHz barrier height obtained from the  $p^{35}\text{ClC}_7\text{H}_7$  fit.

As noted in the Spectral Details and Fitting section, the fits were most sensitive to the  $-2F\rho$  parameter of RAM36. In each of the  $p$ -halotoluenes, this parameter was smaller than that for toluene. It contains information about the structure of the methyl top as it depends upon the moment of inertia of the methyl top,  $I_\alpha$ , about the molecule’s principal rotation axis that passes through the halogen atom. From the fitted constants  $I_\alpha \approx 3.2(1) \text{ amu} \cdot \text{\AA}^2$  is obtained, a value consistent with the  $3.194531(29) \text{ amu} \cdot \text{\AA}^2$  computed from the fitted constants for toluene [135]. Although the slightly larger average value is consistent with the theory that the halogen atom withdraws electron density from the methyl group through the phenyl ring, thus weakening the C-H bonds in the methyl group, the difference is too small to conclusively confirm this. The B3LYP optimizations predicted that  $I_\alpha \approx 3.2 \text{ amu} \cdot \text{\AA}^2$  for each  $p$ -halotoluene (including  $p$ -fluorotoluene) and toluene. These fitted and calculated values are larger than that previously calculated for  $p$ -fluorotoluene ( $3.11 \text{ amu} \cdot \text{\AA}^2$ ) and that from acetone ( $3.138 \text{ amu} \cdot \text{\AA}^2$ ) that was assumed also to be true for  $p$ -chlorotoluene [211].

The fits were not as sensitive to  $F$ , and values of approximately 163 GHz were found for each  $p$ -halotoluene. These values agree well with those reported for  $p$ -fluorotoluene ( $F = 163.60$  GHz) and toluene ( $F = 163.8952(15)$  GHz) [135]. The  $F$  values reported herein are consistent with previous observations and current electronic structure calculations. These calculations are summarized in Tables 4.1, 4.2 and 4.3 and a relaxed potential energy scan for the methyl group rotation in  $p^{35}\text{ClC}_7\text{H}_7$  is presented in Figure 4.4. The B3LYP and MP2 calculations predicted differences in the barrier heights depending upon the halogen substituent. However, experiments (i.e. with rotational temperatures  $> 50$  K according to the RAM36 simulations) observing transitions between  $|m| = 3$  levels of these molecules are required to better elucidate the effect of the halogen on the methyl group. However, the effect of the methyl group on the halogen atom can be better understood from the current data than vice versa. The quadrupole coupling constants obtained from the fits of the quadrupole splitting patterns are sensitive to the electronic structure around the halogen substituent. These fits were performed with SPFIT separately for the  $m = 0$  and  $m = 1$  transitions. For the  $p$ -halotoluenes and similar molecules in which a halogen substituent lies in the plane of the benzene ring, the size of the

**Table 4.3:** Rotational constants, quadrupole moment, and internal rotation parameters for p-iodotoluene. Note the errors given here for the measured values are standard errors.  $N^\circ$  is the number of lines included in the fit and  $\sigma$  is the standard deviation of the fit.

	Experiment	B3LYP	MP2 <sup>a</sup>
$A_{eff} = A + F\rho^2$ (MHz)	5707.01 (13) <sup>b</sup>	5568.30 <sup>a</sup>	5538.90
$B$ (MHz)	490.054574 (54) <sup>b</sup>	485.56 <sup>a</sup>	494.19
$C$ (MHz)	451.316364 (54) <sup>b</sup>	447.86 <sup>a</sup>	454.99
$D_J$ (kHz)	0.00571 (32) <sup>b</sup>		
$\chi_{zz}$ (MHz) ( $m = 0$ )	-1886.202 (12) <sup>d</sup>	-1848.35 <sup>c</sup>	
$\chi_{zz}$ (MHz) ( $m = 1$ )	-1886.204 (16) <sup>d</sup>		
$\chi_{xx} - \chi_{yy}$ (MHz) ( $m = 0$ )	58.380 (34) <sup>d</sup>	64.93 <sup>c</sup>	
$\chi_{xx} - \chi_{yy}$ (MHz) ( $m = 1$ )	58.22 (19) <sup>d</sup>		
$\delta$ ( $m = 0$ )	0.01698 (1) <sup>d</sup>	0.019 <sup>c</sup>	
$\delta$ ( $m = 1$ )	0.01693 (6) <sup>d</sup>		
$D_a$ (kHz)	-11325.6 (42) <sup>d</sup>		
$V_6$ (GHz)	144.98		
$2\rho F$ (GHz)	11.326 (17) <sup>b</sup>		
$F$ (GHz)	162.66 (66) <sup>b</sup>		
$I_\alpha$ (amu $\cdot$ Å <sup>2</sup> )	3.2191 (24) <sup>b</sup>	3.23	3.24
RAM36 / $m = 0$ / $m = 1$			
$\sigma$ (kHz)	8.7 <sup>b</sup> / 7.6 <sup>d</sup> / 8.5 <sup>d</sup>		
$N^\circ$	57 <sup>b</sup> / 210 <sup>d</sup> / 135 <sup>d</sup>		

<sup>a</sup> Electronic structure calculation employing an aug-cc-pVTZ basis set [208] containing an effective core potential from the ESML Basis Set Exchange [166, 209]

<sup>b</sup> Parameter from global fit using RAM36.

<sup>c</sup> Calculations using the 6-311G(d,p) basis set [210] from the ESML Basis Set Exchange [166, 209].

<sup>d</sup> Parameter from local effective fits using SPFIT.



quadrupole coupling constant component,  $\chi_{zz}$ , depends upon the electron density around the halogen atom. The ratios of  $\chi_{zz}$  between isotope pairs,  $\chi_{zz}(^{35}\text{Cl})/\chi_{zz}(^{37}\text{Cl}) = 1.2691$  and  $\chi_{zz}(^{79}\text{Br})/\chi_{zz}(^{81}\text{Br}) = 1.1970$  for the  $m = 0$  states agree well with those reported for BrCl, ( $\chi_{zz}(^{35}\text{Cl})/\chi_{zz}(^{37}\text{Cl}) = 1.26889$  and  $\chi_{zz}(^{79}\text{Br})/\chi_{zz}(^{81}\text{Br}) = 1.197048$ ) [213]. Tables 4.1-4.3 present the  $\chi_{zz}$  values obtained in this investigation. The values are in close agreement to those of the halobenzenes [64, 214], but magnitudes in the halobenzenes are slightly higher. This difference is explained by the small, positive inductive effect (+*I*) of the methyl group that injects electron density into the benzene ring, thus increasing the electron density available for the electron withdrawing halogen.

Of note is the quadrupole coupling constant for *p*-chlorotoluene. Since the initial study by Herberich in 1967 [211], no improvements to its value have been reported. In their study of *o*-chlorotoluene, Gerhard et al. showed that the value of the quadrupole coupling constant for several substituted benzenes could be rationalized by examining the other substituents and their positions relative to the chlorine on the benzene ring [131]. There are two electronic effects to consider: mesomeric (*M*) and inductive (*I*). A halogen substituent has a +*M* effect due to donation of electron density to the aromatic ring through partial overlap of the valence halogen p-orbitals with the  $\pi$ -cloud of the aromatic ring, but a −*I* effect from strongly extracting electrons from the ring through the  $\sigma$ -bond. A substituent that contributes electron density to the ring, then, would allow the halogen atom to extract more electron density, thus lowering the magnitude of the quadrupole coupling constant. The methyl group has a small +*I* effect. Thus, halotoluenes should have smaller quadrupole coupling constant magnitudes than the equivalent halobenzenes. However, the previously reported value for the quadrupole coupling constant of  $\text{p}^{35}\text{ClC}_7\text{H}_7$  ( $\chi_{zz} = -71.7(7)$  MHz) [211] is larger than for  $^{35}\text{chlorobenzene}$  ( $-71.241(7)$  MHz) [215]. The experimentally obtained values of the present study are  $\chi_{zz} = -71.155(5)$  MHz and  $\chi_{zz} = -71.165(7)$  MHz from the  $m = 0$  and  $m = 1$  fits, respectively. These improved values are less than that of chlorobenzene, now in line with the expected trend in quadrupole coupling constant with substituent. A similar trend is also seen for the bromo- and iodo-substituted benzenes and toluenes.

The Goldstein parameter,  $\delta = (2/3)(\chi_{xx} - \chi_{yy})/eQq_{n10}$ , is a good measure for the  $\pi$ -bonding nature in planar molecules with an in-plane halogen substituent, where  $eQq_{n10}$  is the quadrupole coupling constant for the nuclei due to one valence p-electron (see Eqn. 2.57 in Sec. 2.2). The *p*-halotoluenes are a prototypical example of this behavior, as the  $\delta$  values decrease with increasing halogen size. The overlap between the atomic valence p-orbital and aromatic  $\pi$ -cloud decreases as the halogen size increases, hence reducing the  $\pi$ -bonding character of the halogen-carbon bond.

For each quadrupolar halogen and isotopologue, the magnitude of the quadrupole coupling constant was slightly larger for the  $m = 1$  fit than the  $m = 0$  fit. A potential explanation for this is that in the  $m = 0$  state, the methyl rotor is perpendicular (staggered) relative to the aromatic ring, i.e.  $\alpha = 90.0^\circ$  (see Fig. 4.1). This configuration allows for optimum hyperconjugation between the HC  $\sigma$ -bond and the  $\pi$ -cloud of the ring. However, in an excited  $m = 1$  state, the average configuration is no longer perpendicular and thus reduces the

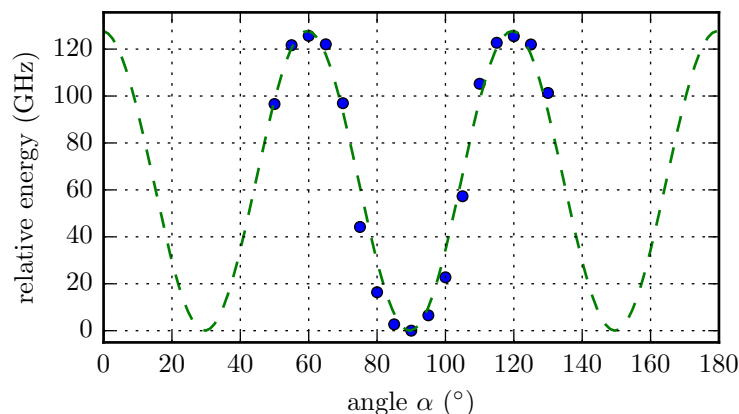


**Figure 4.4:** The results of the B3LYP/aug-cc-pVTZ relaxed potential energy scan for  $p^{35}\text{ClC}_7\text{H}_7$ . The calculated points are given as filled red circles and the dashed lines are a fit of the results to Equation 4.2. All points are relative to the global minimum. As discussed in the text, the barriers for all of the p-halotoluenes were found to be very similar experimentally, although the quantum chemical calculations predicted some differences.

hyperconjugation. If the hyperconjugation injects some electron density into the ring, then the quadrupole coupling constant should be smaller in the  $m = 0$  state than in the  $m = 1$  state, as observed.

Quantum chemical calculations on the p-halotoluenes of this study suggest a staggered configuration for the methyl group as the lowest energy structure, i.e.  $\alpha \approx 90^\circ$ . Pratt and Borst derived the same lowest energy configuration in the UV spectroscopy studies on toluene [216]. Furthermore, the calculated rotational constants for both methods (B3LYP and MP2) are in good agreement with the measured ones. Although the calculated quadrupole coupling constants are less accurate than the rotational constants, their agreement still provides a good measure for the quality of the structure.

The relaxed potential energy surface scans of the angle,  $\alpha$ , (see Fig. 4.1) for the rotation of the methyl group reproduce the  $V_6$  character of the potential, as depicted in Figure 4.4 for  $p^{35}\text{ClC}_7\text{H}_7$ . The potential energy curve was fit with

$$V(\alpha) = \frac{V_6}{2} (1 - \cos(6\alpha + \varphi)) \quad (4.2)$$

where  $\alpha$  is the rotation angle and  $\varphi$  is the phase of the rotation. The B3LYP/cc-pVTZ calculations slightly overestimate the barrier height, whereas the B3LYP/aug-cc-pVTZ calculations predict a barrier that is lower than that observed experimentally. The MP2 barrier height is almost three times higher than the other calculated or measured values. This effect was reported earlier [217, 218]. The overestimation of the barrier by MP2 methods is likely due to the overestimation of the interaction between the methyl hydrogens and phenyl  $\pi$ -cloud.

## 4.6 Summary and conclusions

The rotational spectra of the *p*-halotoluenes, (chloro-, bromo- and iodo-) were measured and the rotational constants were obtained, including the moment of inertia of the methyl group about its principal rotation axis, and quadrupole coupling constants. The barrier height was fit for  $\text{p}^{35}\text{ClC}_7\text{H}_7$  and  $\text{p}^{37}\text{ClC}_7\text{H}_7$  ( $V_6 = 144.98(88)$  GHz and  $145.02(88)$  GHz, respectively) by including the data reported by Herberich [211]. These barriers were slightly lower than those previously reported for *p*-chlorotoluene [211], but the same within the uncertainty as for *p*-fluorotoluene [205]. In the analysis of *p*-bromo- and *p*-iodotoluene, the barrier was fixed to that of  $\text{p}^{35}\text{ClC}_7\text{H}_7$ . The moment of inertia of the methyl group ( $I_\alpha \approx 3.2 \text{ amu} \cdot \text{\AA}^2$ , see Tables 4.1-4.3) determined from the fitted data for each molecule and isotopologue was larger than previously reported or assumed for these molecules, suggesting the methyl group hydrogens are less strongly bound to the methyl group than previously thought. The rotational constants agree well with those previously published for *p*-chlorotoluene, and the new rotational constants found for  $\text{pBrC}_7\text{H}_7$  and  $\text{pIC}_7\text{H}_7$  agree well with the electronic structure calculations (Tables 4.1-4.3).

The fits of the quadrupole-split transitions gave insight into the nature of the chemical bonds between the halogen and phenyl ring. The methyl group injects additional electron density into the phenyl  $\pi$ -cloud, thus providing more electron density for the halogen atom to extract from the phenyl ring. This effect makes the halogen-carbon bond more ionic than in the halobenzenes, an effect manifested by the decrease in the magnitude of the quadrupole coupling constant in the halotoluenes.

Unfortunately, the current data only yielded a limited view into the internal rotation barrier heights, although the electronic structure calculations suggested that some differences in the barriers should exist. Higher-level calculations would offer greater insight on this subject. Experimentally, measurement of the  $|m| = 3$  transitions would provide new data more sensitive to the barrier height. Such measurements were attempted in the apparatus employed herein, however, the rotational temperatures were still too low even when using argon at low backing pressures as the carrier gas and elevated sample temperatures. According to simulations from RAM36 [135], rotational temperatures of 45 – 50 K are necessary to measure these lines for *p*-chloro-, *p*-bromo- and *p*-iodotoluene.

---

The supplementary information of Reference [198] provides the linelists with the corresponding assignments.

## Chapter 5

# The broadband microwave spectra of the monoterpenoids thymol and carvacrol: Conformational landscape and internal dynamics

### 5.1 Introduction

Terpenes represent one of the largest classes of secondary metabolites in nature and are derived from adding substituents to their core building block, isoprene. They exhibit a huge assortment of structures and thus a variety of chemical and biological activities [220]. Furthermore, terpenoids account for the largest share of the emission of biogenic volatile organic compounds (BVOC) to the atmosphere [221–223]. BVOCs are subject to oxidation reactions in atmospheric chemistry impacting Earth’s climate [224]. Despite their importance, only a few high-resolution spectroscopic studies of terpenes have been reported. Nuygen and coworkers recently published the first microwave spectroscopic investigation of a linear monoterpene, linalool [225]. Of the monocyclic monoterpenes, only perillaldehyde [226], carvone, and limonene [227] have been investigated with high-resolution microwave spectroscopy. Kisiel et al. studied the structure and dipole moments of the bicyclic monoterpene camphor using microwave spectroscopy [228]. These studies are in line with previous work on medium-sized biologically relevant molecules (e. g. monosaccharides [16], amino acids [17–19], nucleobases [20, 21], neurotransmitters [22], and drugs [24–26]) that demonstrate the suitability of microwave spectroscopy for obtaining information about the molecular structure, conforma-

---

This chapter is completely based on the following publication:

- D. Schmitz, V. A. Shubert, B. M. Giuliano, and M. Schnell, *The broadband microwave spectra of the monoterpenoids thymol and carvacrol: Conformational landscape and internal dynamics*, J. Chem. Phys. **141**, 034304 (2014). (key ideas: D.S. 80%, experimental: 60%, data analysis: 80%, writing up: 80%) [219]

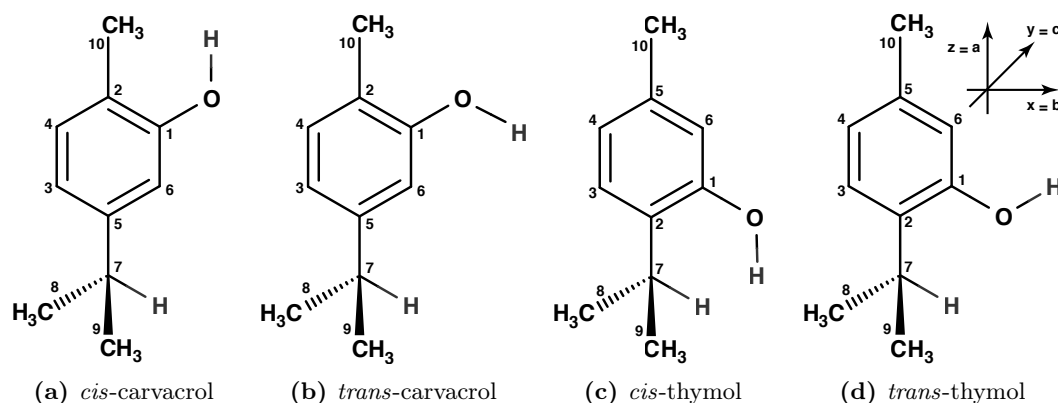


**Figure 5.1:** Schemes of the structures of the aromatic monoterpenoids thymol and carvacrol. They differ in the position of the hydroxyl substituent with respect to the isopropyl and the methyl groups. The coordinate system next to *trans*-thymol represents an approximation of the principal axes, which varies slightly between the different molecules and conformations. When discussing the orientation of the methyl rotor, the orientation of the axes with respect to the rest of the molecule becomes important.

tional preferences, and internal dynamics of this class of molecules.

In the present investigation, the vibrationally and rotationally cold gas-phase microwave spectra of the monocyclic monoterpenes and structural isomers, thymol, and carvacrol are reported. For both molecules, *cis*- and *trans*-conformational isomers can exist and the corresponding structures are depicted in Figure 5.1. Thymol and carvacrol differ in the position of the hydroxyl group, which impacts the flexibility of both the hydroxyl and the methyl groups. Due to their anti-bacterial [229–231], anti-inflammatory [232], and anti-fungal properties [233], thymol and carvacrol are particularly interesting for the pharmacological and foodstuff industries. They occur naturally as the main constituents in the essential oils of thyme, oregano, and satureja.

Spectroscopically interesting is the influence of the hydroxyl group on the ability of the methyl top to rotate internally. Microwave spectroscopy is well suited to observe the effects of large amplitude motion, e. g. internal rotation, and enables the determination of the corresponding rotational energy barrier. Since the chemical environment of the moving group differs between different molecules, and even between conformers of the same molecule, the derivation of a universal description of internal rotation is challenging. Recent improvements of the theoretical description of different barrier types show that development in this field is still highly active [26, 32, 135, 198]. Herein the influence is discussed of the hydroxyl group on the barrier to methyl group internal rotation, which can be expected to be largely different for thymol and carvacrol, and the results are compared to structurally similar molecules, such as *o*- and *m*-cresol [234, 235]. Furthermore, the influence is evaluated of the hydroxyl group on the configuration of the isopropyl group and hence the conformational preferences.

This chapter is organized as follows: The experimental setup and the quantum chemical calculations are briefly described (Sec. 5.2), followed by a presentation of the experimental and

computational results for each of the molecules under study (Sec. 5.3). The conformational space of the molecules and the barriers to internal rotation of the methyl tops are investigated. Subsequently, a discussion and a comparison of the results of thymol and carvacrol to each other and with literature data is presented. Finally, the findings are summarized and a short outlook is given (Sec. 5.5).

## 5.2 Experimental and computational methods

Thymol (2-isopropyl-5-methylphenol, 99.5 % purity) and carvacrol (5-isopropyl-2-methylphenol, 98 % purity) were purchased from Sigma-Aldrich Chemie GmbH, Steinheim, Germany and were used without further purification. Thymol is a white crystalline powder with a stated melting point of 48–51 °C and a boiling point of 232 °C. Carvacrol is a yellowish liquid with a stated melting point of 3–4 °C and a boiling point of 237 °C. The chemical structures of both molecules are depicted in Figure 5.1. The orientation of the OH-group is defined with respect to the C2 atom of the benzene ring and its rotation gives rise to *trans*- and *cis*-conformers for both molecules.

All rotational spectroscopy measurements were performed with the Hamburg COMPACT spectrometer which is detailed in Chapter 3 and thus only the experimental parameters are given here. After supersonic expansion into the vacuum chamber, the ensemble of molecules was polarized with a 1  $\mu$ s chirp spanning 2  $\rightarrow$  8.5 GHz. For each spectrum, 50  $\mu$ s of the FID were recorded at a resolution of 10 ps, yielding a frequency resolution of 20 kHz in the Fourier transform and hence the rotational spectra obtained. The molecules were seeded into a supersonic expansion using a pulsed nozzle (Parker General Valve, Series 9) operating at 2 Hz to create a cold molecular jet. The sample holders were placed directly prior to the nozzle and heated to 100 °C or 140 °C for thymol or carvacrol, respectively. A constant flow of neon at stagnation pressures of 3.0 bar transported the molecules to the nozzle. Note that the tubing between the reservoir and the valve, as well as the valve itself, were heated to avoid condensation. For carvacrol and thymol, 300 000 FIDs and 438 000 FIDs, respectively, were co-added for each spectrum. After performing the Fourier transformation, residual background lines were removed by masking, which means that the intensities in the spectrum at the frequencies identified as background lines were set to zero. Different approaches were used to identify background lines in the spectra: 1. by a comparison of the spectra obtained using only the first and last 20  $\mu$ s of the FID. In the last 20  $\mu$ s of the FID, the molecular signal is already significantly reduced; 2. by an individual background measurement with the valve switched off; 3. by a comparison of the two measurements of thymol and carvacrol.

One of the primary advantages of microwave spectroscopy is its ability to obtain information about the gas-phase structure of molecules to a high precision. However for a complete structure determination, rotational constants from numerous different isotopologues are required. Such an effort was recently reported for a comparatively large molecule, strawberry aldehyde (C<sub>12</sub>H<sub>14</sub>O<sub>3</sub>) [236]. However, this approach remains experimentally demanding and

time intensive. Another way to extract structural information from the experimental data is comparison with quantum chemical calculations (explained in Sec. 2.6). The assignment of an experimentally obtained spectrum (e.g. by comparison of rotational constants, barrier to internal rotation, dipole moments) to a quantum chemically optimized structure has given good results, even for larger molecules and complexes [170].

Herein, the experimental results were compared with electronic structure calculations performed with the Gaussian 03 [206] and Gaussian 09 [207] program suites. In order to determine the preferred orientations of the isopropyl groups, relaxed energy scans of the potential energy surface (PES) of the isopropyl group rotation were carried out. As starting structures for the energy scans, the *cis*- and *trans*-conformers of thymol and carvacrol were used as depicted in Figure 5.1. The Becke, three parameter, Lee-Yang-Parr (B3LYP) exchange-correlation functional was employed with the 6-311++G(d,p) basis set for these scans. Two unequal minima in the PES were found for each starting structure. To further refine the structures and verify the energy ordering of the individual conformations, optimizations and harmonic frequency calculations were carried out on all minima using several different basis sets and methods: B3LYP/6-311++G(d,p), B3LYP/aug-cc-pVTZ, MP2/6-311++G(d,p) (Møller–Plesset second-order perturbation theory), and M06-2X/6-311++G(d,p) (Minnesota functional). In order to get an overview of the internal dynamics, the *cis-trans* isomerization barrier was also computed, as well as the barrier to internal rotation for the different methyl tops. These calculations were performed at the B3LYP/6-311++G(d,p) level of theory for selected minima. Here, the barriers to internal rotation for the methyl tops at positions five and two of thymol and carvacrol, respectively, are particularly interesting because they are expected to be similar to that of *o*- and *m*-cresol [234, 235]. The barrier to internal rotation of those molecules is small enough that the corresponding splitting of the rotational energy levels into A and E species components should be observed in the spectra.

## 5.3 Results

### Carvacrol

The computational findings and their use to complement and interpret the experimental results are first presented. The relaxed PES of the isopropyl group rotation for the *cis*- and *trans*-conformers are depicted in Figure 5.2. The potential energy relative to the global minimum (denoted as *trans*-B) is plotted as a function of the dihedral angle, H-C7-C5-C6. The *trans*-carvacrol PES is lower in energy than that of the *cis*-isomer, with an offset of approximately 1.8 kJ/mol. Two minima exist on both the *cis*- and *trans*-conformer PESs, with dihedral angles H-C7-C5-C6 of exactly 0° and 180°. As illustrated in Figure 5.2, the methyl tops of the isopropyl (C8 and C9) are out-of-plane at the minima. For both the *cis* and the *trans* curves, the lowest minima coincide with a dihedral angle of 180°, where the hydrogen connected to C7 is opposite to the hydroxyl group. Those conformations are labeled with B and the second local minimum at a dihedral angle of 0° with A. Hence, in total four



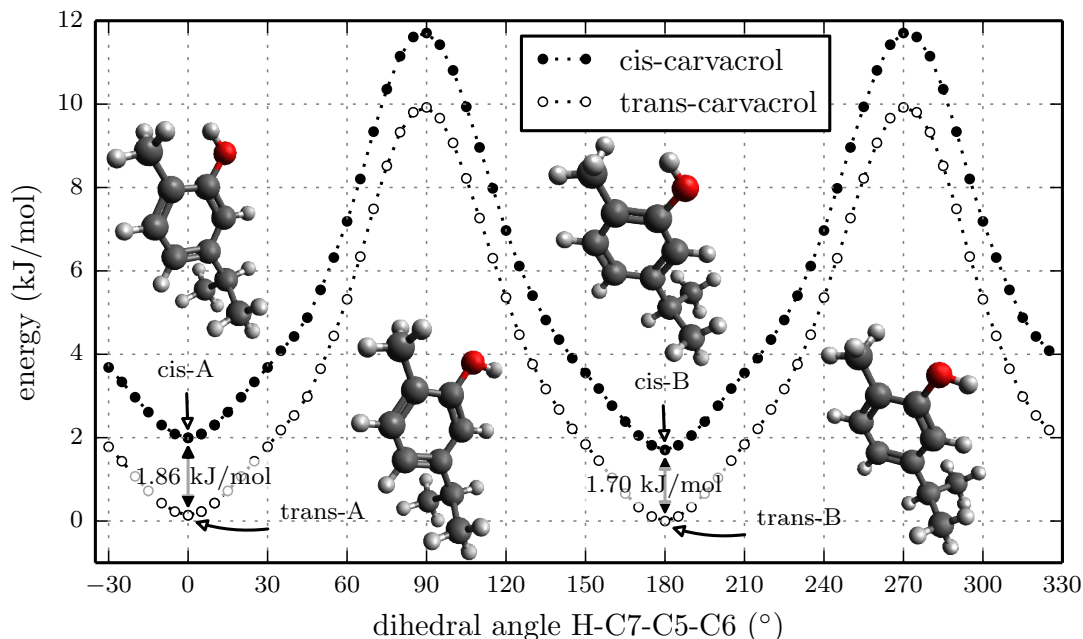


**Figure 5.2:** Scan of the potential energy surface calculated along the  $H-C7-C5-C6$  dihedral angle according to the labeling in Fig. 5.1 at the B3LYP/6-311++G(d,p) level of theory for *cis*- and *trans*-carvacrol. The position of the observed conformations (A, B) is indicated in the plot and illustrated with the corresponding structure.

conformations were found, two conformers each in the two conformational families of *cis*- and *trans*-carvacrol.

The isomerization barrier between the A and B rotamers that corresponds to rotation of the isopropyl group with respect to the rest of the molecule was determined to be approximately 10 kJ/mol for both *cis*- and *trans*-conformers. The barrier to *cis-trans* isomerization, corresponding to rotating the hydroxyl group around the C1-O bond, was computed to be 15 kJ/mol for both A and B rotamers. The computational results for the barrier to internal rotation of the methyl group bonded to the C2 carbon are listed in Tables 5.1 and 5.2. For the analysis of the hindered rotation, the Hamiltonian of the rigid rotor has to be extended to include the kinetic and potential energy terms of the internal rotor. In the case of a threefold symmetric top, the potential energy,  $V$ , can be described in terms of the internal rotation angle  $\alpha$  (compare Eqn. 2.62):

$$V(\alpha) = \frac{1}{2}V_3(1 - \cos(3\alpha)) + \frac{1}{2}V_6(1 - \cos(6\alpha)) + \dots \quad (5.1)$$

Depending on the symmetry of the molecular framework, higher order terms may also need to be included. Thus, to convert the computed barrier height into a quantity that can be compared with experimental results, the potential energy scans were fitted using Equation 5.1. For a methyl group in highly symmetric local environments, e.g. as a substituent on a phenyl ring with symmetric substitution in both *ortho* positions, such as in thymol (discussed in the



**Table 5.1:** Rotational constants, dipole moments, and barriers to internal rotation of the C2 methyl group for *cis*-carvacrol. Note the errors given here for the measured values are standard errors.  $N^\circ$  is the number of lines included in the fit and  $\sigma$  is the standard deviation of the fit.

	<i>cis</i> -carvacrol A			<i>cis</i> -carvacrol B		
	Experiment	B3LYP <sup>1</sup>	MP2 <sup>2</sup>	Experiment	B3LYP <sup>1</sup>	MP2 <sup>2</sup>
<i>A</i> (MHz)	2274.0616(37)	2281.04	2265.57	2152.8772(44)	2163.74	2142.48
<i>B</i> (MHz)	643.77212(46)	642.53	643.35	672.34073(50)	669.87	672.76
<i>C</i> (MHz)	564.76557(38)	564.32	563.77	578.22275(42)	577.29	577.62
$ \mu_a $ (D)	-	0.94	0.77	-	1.12	1.05
$ \mu_b $ (D)	-	0.94	1.30	-	0.80	1.14
$ \mu_c $ (D)	-	0.00	0.00	-	0.00	0.00
$V_3$ (kJ/mol)	-	5.61 <sup>3</sup>	-	-	5.90 <sup>3</sup>	-
$N^\circ$	15	-	-	27	-	-
$\sigma$ (kHz)	5.5	-	-	8.8	-	-

<sup>1</sup> aug-cc-pVTZ basis set

<sup>2</sup> 6-311++G(d,p) basis set

<sup>3</sup> B3LYP/6-311++G(d,p)

next section), the  $V_6$  contribution could be significant. For carvacrol, the single hydroxyl group substituted *ortho* to the methyl group breaks this symmetry so that truncation considering only the  $V_3$  term is sufficient. As expected, the barrier heights differ significantly between the *cis*- and *trans*-isomers.

As a test case, the internal rotation barrier of a methyl top within the isopropyl group for the *trans*-carvacrol A isomer was calculated to ensure that it is too high to have an observable effect on the spectra. The barrier for this motion and isomer should be the lowest of all of the isomers investigated here and was computed to be 13.2 kJ/mol.

For comparison with the experimentally obtained molecular constants, the geometries of the four minima were further optimized and frequency calculations were carried out at the B3LYP/6-311++G(d,p), B3LYP/aug-cc-pVTZ, M06-2X/6-311++G(d,p), and MP2/6-311++G(d,p) levels of theory. *Trans*-carvacrol B was confirmed to be the global minimum by all methods except MP2, which predicts the *trans*-carvacrol A conformer to be the global minimum. The B3LYP calculations predict just a 0.3 kJ/mol energy difference between the different *trans*-rotamers of carvacrol. The energy ordering of the *cis*- vs. the *trans*-conformers is, however, confirmed by all calculations. The calculated and fitted rotational constants are presented in Tables 5.1 and 5.2. The zero-point corrected energies are summarized in Table 5.3.

All four minimum structures discussed above were identified in the broadband microwave spectrum of carvacrol covering 2 – 8.5 GHz. Figure 5.3 shows a fraction of the spectrum from 3600 – 3615 MHz, in which transitions from all four conformations can be observed. They

**Table 5.2:** Rotational constants, dipole moments, and barriers to internal rotation of the C2 methyl group for *trans*-carvacrol. The errors given here for the measured values are standard errors.  $N^\circ$  is the number of lines included in the fit and  $\sigma$  is the standard deviation of the fit. Note that the angles ( $\delta$ ,  $\varepsilon$ ) and the rotational constant of the methyl top,  $F_0$ , are not fitted and their uncertainties are not considered in the fit. This omission mainly affects the  $V_3$  parameter, its error, and hence the resulting error of the  $V_3$  parameter is most likely underestimated. The direction cosines between the internal rotation axis ( $i$ ) and the principal axes ( $a$ ,  $b$ ,  $c$ ) are also given, employing the principal axis system orientation depicted in Figure 5.1d.

	<i>trans</i> -carvacrol A			<i>trans</i> -carvacrol B		
	Experiment	B3LYP <sup>1</sup>	MP2 <sup>2</sup>	Experiment	B3LYP <sup>1</sup>	MP2 <sup>2</sup>
$A$ (MHz)	2283.1750(15)	2288.58	2281.82	2159.0853(25)	2169.50	2153.85
$B$ (MHz)	642.240345(30)	641.17	641.27	670.84871(51)	668.31	670.63
$C$ (MHz)	564.09631(25)	563.68	563.13	577.52683(41)	576.48	576.84
$ \mu_a $ (D)	-	0.90	1.28	-	1.06	1.42
$ \mu_b $ (D)	-	0.90	0.81	-	0.60	0.45
$ \mu_c $ (D)	-	0.00	0.00	-	0.00	0.00
$\rho$	0.0138 <sup>3</sup>	0.0138	0.0140	0.0134 <sup>3</sup>	0.0134	0.0135
$F_0$ (GHz)	161.5 <sup>4</sup>	161.5	159.7	161.5 <sup>4</sup>	161.5	159.6
$\varepsilon$ (°)	180.0 <sup>4</sup>	180.0	180.0	180.0 <sup>4</sup>	180.0	178.4
$\delta$ (°)	13.0 <sup>4</sup>	13.0	12.9	1.02 <sup>4</sup>	1.02	0.35
$\angle(i,a)$ (°)	13.0 <sup>4</sup>	13.0	12.9	1.02 <sup>4</sup>	1.02	0.35
$\angle(i,b)$ (°)	103.0 <sup>4</sup>	103.0	102.9	91.0 <sup>4</sup>	91.0	90.4
$\angle(i,c)$ (°)	90.0 <sup>4</sup>	90.0	90.0	90.0 <sup>4</sup>	90.0	90.0
$V_3$ (kJ/mol)	4.0871(25)	3.7 <sup>5</sup>	-	4.4024(16)	3.9 <sup>5</sup>	-
$N^\circ$	49	-	-	42	-	-
$\sigma$ (kHz)	8.7	-	-	10.9	-	-

<sup>1</sup> aug-cc-pVTZ basis set

<sup>2</sup> 6-311++G(d,p) basis set

<sup>3</sup>  $\rho$  was not fitted but computed using the fitted rotational constants

<sup>4</sup> Values fixed to calculated values (B3LYP/aug-cc-pVTZ)

<sup>5</sup> B3LYP/6-311++G(d,p)

**Table 5.3:** Comparison of the zero-point corrected energies ( $\text{kJ/mol}$ ) and populations of the different structural isomers of thymol and carvacrol using different methods and basis sets.

	B3LYP <sup>1</sup>	B3LYP <sup>2</sup>	M06-2X <sup>1</sup>	MP2 <sup>1</sup>	population <sup>3</sup>
<b>thymol</b>					
<i>trans</i> A	0	0	0	0	0.48
<i>trans</i> B	1.06	1.62	2.56	0.75	0.28
<i>cis</i> A	3.38	3.10	1.99	3.58	0.18
<i>cis</i> B	6.00	6.06	6.72	8.28	0.07
<b>carvacrol</b>					
<i>trans</i> A	0.29	0.26	2.04	0	0.28
<i>trans</i> B	0	0	0	0.71	0.30
<i>cis</i> A	1.59	1.40	2.50	1.12	0.20
<i>cis</i> B	1.57	1.19	2.76	1.51	0.21

<sup>1</sup> 6-311++G(d,p)

<sup>2</sup> aug-cc-pVTZ

<sup>3</sup> B3LYP/aug-cc-pVTZ energies used for calculating the Boltzmann population, temperatures of  $T = 373.15\text{K}$  and  $T = 413.15\text{K}$  were used for thymol and carvacrol, respectively

all exhibit *a*-type spectra of near prolate asymmetric rotors and a few *b*-type transitions. Furthermore, some transitions are split into doublets, which are ascribed to internal rotation of the methyl group connected to the phenyl ring. These splittings were small ( $\approx 100\text{ kHz}$ ) and were observed only from the two conformations with the most intense spectra. These additional spectral features give us valuable information for spectral assignment. The spectra exhibiting no internal rotation splittings are fit to a rigid rotor model using Pickett's suite of programs, SPFIT [146]. The nature of the fitted transitions, at low  $J$ , did not permit the determination of the distortion constants from the fit. The rotational constants obtained and the lower line intensities suggest the assignment of the conformers without line splittings to the *cis*-isomers of carvacrol. These assignments are supported by the computed internal rotation barrier heights for the C2 methyl group in the *cis*-isomers (see Table 5.1). With barriers of  $5.6\text{ kJ/mol}$  and  $5.9\text{ kJ/mol}$ , they are 50 % higher than the barriers for the *trans*-isomers and thus should yield line splittings too narrow to be resolved in the experiments presented herein. The further assignment of the A- and B-rotamers of *cis*-carvacrol was straightforward because their rotational constants are sufficiently different and agree well with the calculated values. Table 5.1 shows the results of the spectral assignment of *cis*-carvacrol. The remaining lines in the spectrum, which were split due to internal rotation, could be assigned to the *trans*-isomers of carvacrol.

A more thorough analysis of the effect that internal rotation has on the observed spectra requires inclusion of the kinetic energy term of the internal rotor into the molecular Hamil-

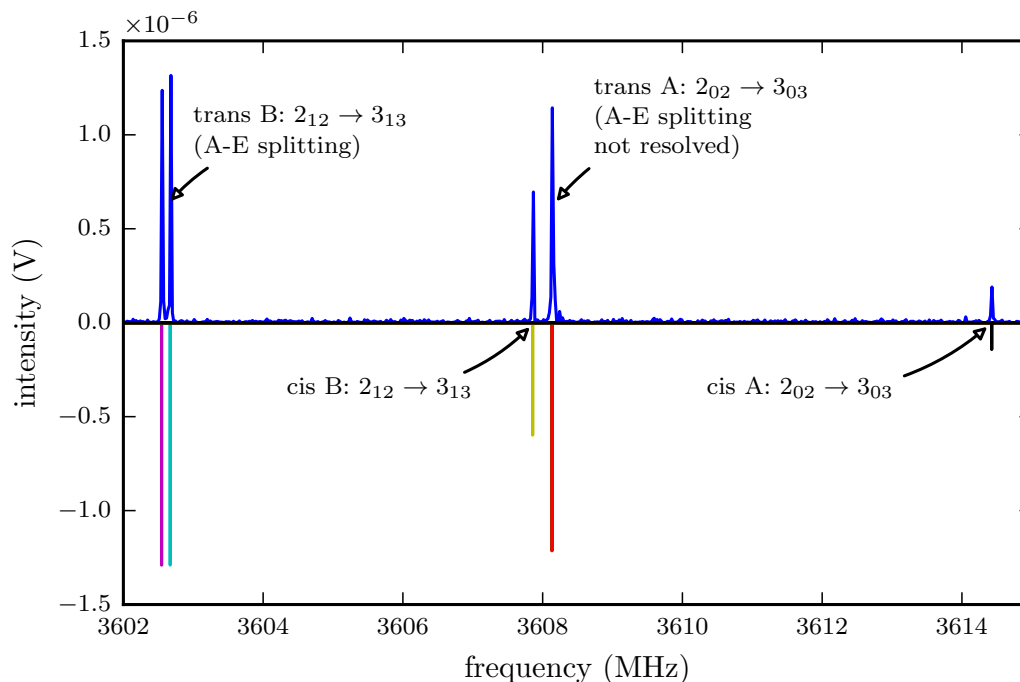


**Figure 5.3:** Part of the microwave spectrum of carvacrol in the region of 3600 – 3615 MHz. The upper trace shows the measured spectrum, the lower trace is a simulation based on fitted molecular parameters. The small line splitting due to internal rotation is apparent for the  $2_{12} \rightarrow 3_{13}$  transition of *trans*-carvacrol B. In comparison, the smaller line splitting of the transition  $2_{02} \rightarrow 3_{03}$  of *trans*-carvacrol A was not resolved. No line splitting was observed for the *cis*-conformers.

tonian (compare Eqn. 2.68 in Sec. 2.3). In principle this implementation is straightforward, but different coordinate transformations have been proposed for handling the problem efficiently [132, 139]. Herein, the combined axis method (CAM) developed by Woods [136, 137] and detailed in Section 2.3) is employed. Besides the barrier height,  $V_3$ , the analysis of the internal rotation also provides information about the orientation of the internal rotor within the molecular framework and its moment of inertia. A threefold barrier results in splittings of the energy levels into (non degenerate) A-states and doubly degenerate E-states which vary with the rotational quantum numbers and thus leads to splittings in the spectrum (see Fig. 2.6).

The program XIAM is chosen to perform a fit of the spectrum including transitions of both A and E symmetry. It is capable of treating up to three internal rotors with a  $V_3$  potential and applies the CAM method [138]. The orientation of the methyl rotor within the principal axis system is specified using the angles  $\delta$  and  $\varepsilon$ . In the case of a prolate asymmetric top using the  $I^r$ -representation,  $\delta$  describes the angle between the  $a$ -rotational axis of the molecule and the axis of internal rotation. The angle  $\varepsilon$  describes the angle between the  $b$ -rotational axis and the projection of the internal rotor axis onto the  $xy$ -plane of the principal axis system of the molecule.

The structure calculations for *trans*-carvacrol indicate that the internal rotation axis almost

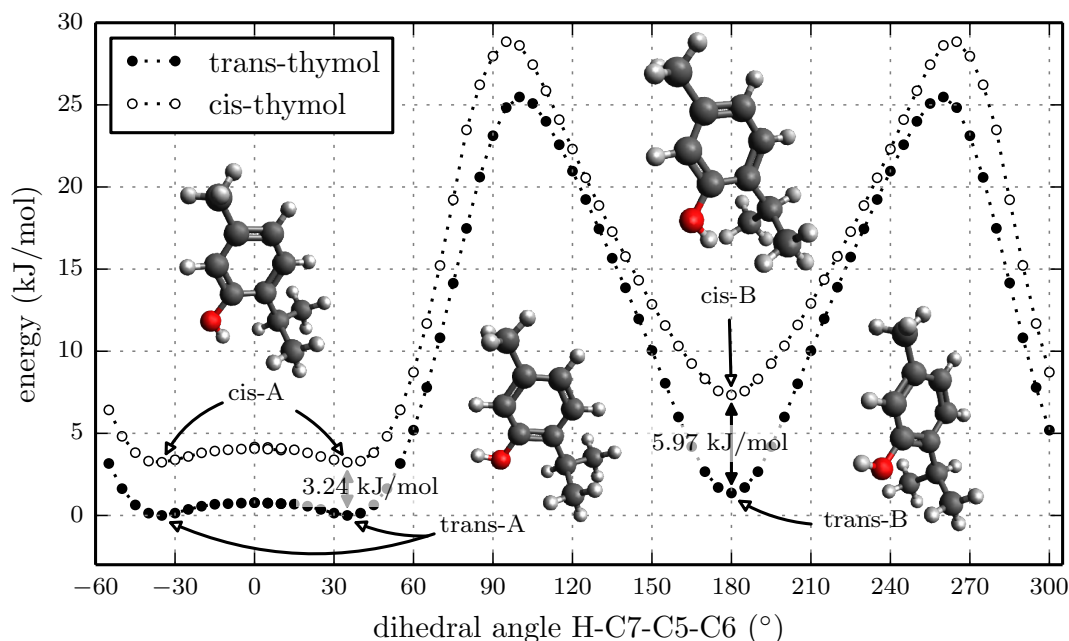


**Figure 5.4:** Scan of the potential energy surface calculated along the  $H-C7-C2-C1$  dihedral angle at the B3LYP/6-311++G(d,p) level of theory for cis- and trans-thymol. The two minima of cis-thymol A are equivalent, as are the two for trans-thymol A. The structure of trans-thymol A is most likely stabilized by a hydrogen bond.

coincides with the  $a$ -rotational axis. This result implies that  $\delta$  is close to  $0^\circ$  while  $\varepsilon$  is only poorly defined. Hence, fits of the data including these angles gave unphysical or diverging results. Therefore, the angles and the rotational constant of the methyl top ( $F_0 = \hbar/2I_\alpha$ ) were held fixed at the calculated values and only the rotational constants of the molecule and the barrier to internal rotation were allowed to float. The results of these fits are summarized in Table 5.2. As for the *cis*-rotamers, the assignment of the *trans*-rotamers to *trans*-carvacrol A or B was also unambiguous by comparison of the measured and the calculated rotational constants. In total 49 lines are assigned to *trans*-carvacrol A and 42 lines to *trans*-carvacrol B.

## Thymol

Due to their structural similarities, the same analysis protocol is followed for thymol as for carvacrol. Therefore, the main focus here is on the differences between the molecules rather than the analysis details. The relaxed potential energy scan of the internal rotation of the isopropyl group already reveals significant differences compared to carvacrol. As shown in Figure 5.4, the cuts through the potential energy surfaces exhibit three minima of *trans*- and *cis*-thymol instead of two as observed for carvacrol. For the A rotamers, the hydrogen at C7 is slightly out of plane, resulting in two equivalent minima. Compared to carvacrol, the energy difference between the *cis*- and the *trans*-conformational families of thymol is much

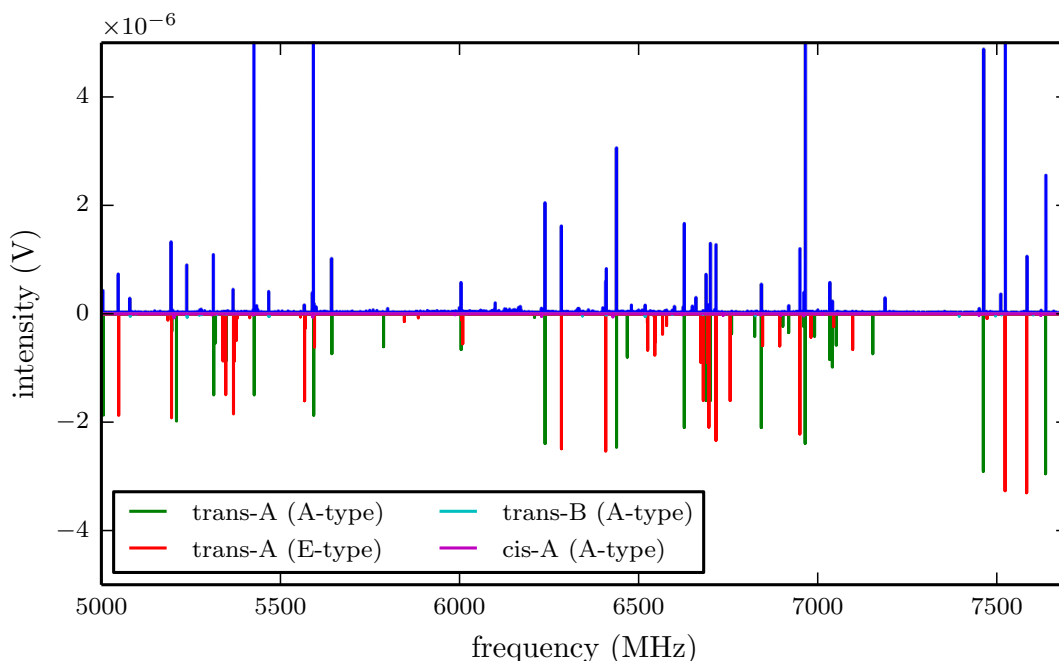


**Figure 5.5:** A part of the broadband microwave spectrum of thymol in the frequency region of 5.0–7.7 GHz. It is dominated by the A and E species components of *trans*-thymol A. The transitions of *trans*-thymol B and *cis*-thymol A are much weaker than those of *trans*-thymol A.

larger (approximately a factor of two and four larger for the A and B rotamers, respectively) because of the additional structural stabilization from the hydrogen bonds formed in the *trans*-thymol rotamers. The energy ordering of rotamers A and B is also reversed for thymol as compared to carvacrol at the B3LYP/6-311++G(d,p) level of calculation. Finally, the potential barrier between rotamers A and B was determined to be around 23 kJ/mol, 2.3-times higher than in carvacrol. These results are expected because the hydroxyl group in thymol is able to more strongly interact with the isopropyl group than in carvacrol. The barrier of the *cis-trans* interconversion by rotating the hydroxyl group around the C1-O bond was calculated to be 15.4 kJ/mol and 16.1 kJ/mol for the rotamers A and B, respectively.

The structure of thymol also suggests a lower barrier to internal rotation for the methyl group at the carbon 5. This hypothesis was confirmed by calculations on all four conformations, which yielded barrier heights between 0.04 kJ/mol (*cis*-thymol) and 0.3 kJ/mol (*trans*-thymol), values at least ten times smaller than for carvacrol. Therefore, an obvious effect of methyl group internal rotation on the microwave spectra of all conformations of thymol is expected. The calculated barriers were fit using Equation 5.1 and are summarized in Tables 5.4 and 5.5. Even though the  $V_6$  part of the potential is negligible for *trans*-thymol, it becomes significant for *cis*-thymol, and so both the  $V_3$  and  $V_6$  terms are included in Table 5.5. This result is an indication that the interaction of the hydroxyl group with the methyl group becomes weaker so that the local environment of the methyl rotor at carbon 5 approaches  $C_{2V}$  symmetry, as in toluene. To exclude possible effects on the spectra by the rotation of one of the isopropyl

**Table 5.4:** Rotational constants, dipole moments, and barriers to internal rotation of the C5 methyl group for *trans*-thymol. The errors given here for the measured values are standard errors.  $N^\circ$  is the number of lines included in the fit and  $\sigma$  is the standard deviation of the fit. The direction cosines between the internal rotation axis ( $i$ ) and the principal axes ( $a$ ,  $b$ ,  $c$ ) are also given, employing the principal axis system orientation depicted in Figure 5.1d.

	<i>trans</i> -thymol A			<i>trans</i> -thymol B		
	Experiment	B3LYP <sup>1</sup>	MP2 <sup>2</sup>	Experiment	B3LYP <sup>1</sup>	MP2 <sup>2</sup>
$A$ (MHz)	2034.068(71)	2039.45	2024.06	2261.070(62)	2237.63	2229.72
$B$ (MHz)	739.18202(35)	735.91	738.22	708.92030(45)	707.59	708.94
$C$ (MHz)	591.51673(30)	591.73	593.03	611.86246(50)	611.13	611.43
$ \mu_a $ (D)	-	1.12	1.43	-	1.15	1.50
$ \mu_b $ (D)	-	0.72	0.53	-	0.82	0.72
$ \mu_c $ (D)	-	0.10	0.07	-	0.00	0.04
$D_{p2J}$ (kHz)	2.44(23)	-	-	-	-	-
$\rho$	0.012990(42)	0.0126	0.0126	-	0.0137	0.0138
$F_0$ (GHz)	156.26(51)	161.7	160.1	-	161.7	160.1
$\varepsilon$ (°)	111.73(16)	112.4	105.2	-	0.0	7.1
$\delta$ (°)	3.8471(46)	3.5	4.6	-	8.3	8.8
$\angle(i,a)$ (°)	3.8471(46)	3.5	4.6	-	8.3	8.8
$\angle(i,b)$ (°)	91.423(12)	91.3	91.2	-	81.7	81.2
$\angle(i,c)$ (°)	86.4267(84)	86.8	85.5	-	90.0	88.9
$V_3$ (kJ/mol)	0.3699(11)	0.318 <sup>3</sup>	-	-	0.261 <sup>3</sup>	-
$N^\circ$	54	-	-	12	-	-
$\sigma$ (kHz)	11.6	-	-	4.0	-	-

<sup>1</sup> aug-cc-pVTZ basis set

<sup>2</sup> 6-311++G(d,p) basis set

<sup>3</sup> B3LYP/6-311++G(d,p)

methyl groups, a methyl group rotation for *trans*-thymol A was evaluated. It is very unlikely that the calculated barrier height of 13.7 kJ/mol will impact the spectrum in a measurable way.

The analysis of the spectrum revealed three conformers, with one having much higher intensity than the other two. The spectra are dominated by *a*-type transitions, which is not so apparent in the overview spectrum in Figure 5.5 due to widely split lines from internal rotation of the methyl group. We first concentrate on the analysis of the highest intensity conformer. For this species, transition splittings due to methyl group rotation could be identified and were successfully assigned. The smaller internal rotation barrier compared to carvacrol increased the line splitting up to 88 MHz. The assignment is made of 39 and 15 *a*-type lines of A and E symmetry, respectively. For the *b*-type lines, only those of A symmetry are observed. A global fit including all lines using XIAM was performed, in which the angles  $\delta$  and  $\varepsilon$  and the rotational constant of the methyl rotor,  $F_0$ , could be fit in addition to the rotational constants and barrier height. Only the  $V_3$  part of the potential was retained in the final fit, because, as stated before, the calculations suggest that the  $V_6$  term is negligible (less than 3 % compared to the  $V_3$  term). Furthermore, including  $V_6$  in the fit did not improve it and led to unphysical results for  $V_3$  and  $V_6$ . Moreover, also included is the internal rotation-overall rotation distortion operator,  $D_{pi2J}$ , which led to better fits, especially for lines with  $K_a > 1$ . This more complete assessment for thymol compared to carvacrol was possible due to the larger line splitting, so that more lines of E symmetry could be assigned. Even though the fit did not diverge, the resulting values of the internal rotor angles  $\delta$  and  $\varepsilon$  were dependent on the starting guess values of the fit. Therefore, the quantum chemically calculated angles are used as starting values and are assumed to be already close to the real values. The convergence of all other constants included in the fit was much more robust. Because of the structural similarities of the *cis*- and *trans*-isomers, an unambiguous assignment to the calculated structures based on only the rotational constants is not possible. However, the energy ordering of the different conformations (Table 5.3) and the barrier height to internal rotation provide sufficient information for a solid assignment. Taking this information into account, the highest intensity conformer must be the *trans*-thymol A conformer.

As already mentioned, the line intensities of the other two conformers were much weaker and sometimes even barely distinguishable from the noise (S/N ratio is around 2:1 for the lower intensity lines). Nevertheless, 10 lines were identified for one of the conformers and 12 lines for the other one. Only *a*-type transitions of A symmetry could be assigned for both of them. Even though there was evidence for line splitting as the calculated barrier to internal rotation predicts, it was not possible to clearly identify any E-symmetry lines. The comparison between the fitted and calculated rotational constants suggests that one of these conformations is *cis*-thymol A, while the calculated energy ordering (Table 5.3) suggests that the other one is *trans*-thymol B.



**Table 5.5:** Rotational constants and dipole moments for *cis*-thymol. Only *cis*-thymol A lines were identified in the spectra, and thus only experimental values for this *cis* conformation of thymol could be determined. The errors given here for the measured values are standard errors.  $N^\circ$  is the number of lines included in the fit and  $\sigma$  is the standard deviation of the fit.

	<i>cis</i> -thymol A			<i>cis</i> -thymol B	
	Experiment	B3LYP <sup>1</sup>	MP2 <sup>2</sup>	B3LYP <sup>1</sup>	MP2 <sup>2</sup>
$A$ (MHz)	2048.642(32)	2027.07	2009.27	2218.7704	2205.61
$B$ (MHz)	739.25463(50)	735.71	739.12	704.57	705.10
$C$ (MHz)	590.31448(44)	591.02	591.56	608.31	607.78
$ \mu_a $ (D)	-	1.25	1.15	1.11	0.96
$ \mu_b $ (D)	-	0.72	1.11	1.01	1.35
$ \mu_c $ (D)	-	0.04	0.14	0.03	0.36
$V_3$ ( $V_3, V_6$ ) (kJ/mol)	-	0.106 (0.069, 0.057) <sup>3</sup>	-	0.036 (0.025, 0.016) <sup>3</sup>	-
$N^\circ$	10	-	-	-	-
$\sigma$ (kHz)	4.4	-	-	-	-

<sup>1</sup> aug-cc-pVTZ basis set

<sup>2</sup> 6-311++G(d,p) basis set

<sup>3</sup> B3LYP/6-311++G(d,p)

## 5.4 Discussion

The measurements and calculations revealed that the energy differences among the conformers of thymol are larger than for carvacrol. This spread in energies explains the presence of four conformations in the supersonic expansion for carvacrol, compared to only three for thymol. The comparison of the zero-point corrected energies as well as the calculated populations of the different structural isomers given in Table 5.3 further elucidates this result. The calculated energy of the *cis*-thymol B conformer, which was not observed in the spectrum, is at least two times higher than the second highest energy conformer, *cis*-thymol A, for all methods and basis sets.

The influence of the substituents on the barrier to methyl rotation was investigated previously in various substituted toluenes [131, 135, 234, 235, 237, 239]. Some of the results are listed in Table 5.6 together with the thymol and carvacrol results. This list shows some clear trends for internal rotation barriers. The barrier heights of *trans*-carvacrol A and *anti*-*o*-cresol are very similar because the molecules only differ in that cresol does not contain an isopropyl substituent. The effects of the internal rotation for *cis*-carvacrol were not resolvable, but the barrier height can be expected to be similar to that of *syn*-*o*-cresol. A direct comparison of the barrier heights of *trans*-thymol A and *syn*-*m*-cresol was not possible, because Hellweg et al. also included the  $V_6$  term of the potential [235], which was excluded here because it resulted

**Table 5.6:** Comparison of the barriers to internal rotation of thymol, carvacrol, and similar molecules. The barrier heights are listed in increasing order.

	$V_3$ (kJ/mol)
toluene	$V_6 = 0.05787337(11)$ [135]
<i>anti-m</i> -cresol	0.038(2) ( $V_6 = -0.16(2)$ ) [235]
<i>syn-m</i> -cresol	0.2684(8) ( $V_6 = -0.13(1)$ ) [235]
<i>trans</i> -thymol A	0.3699(11) (this work)
<i>o</i> -tolunitrile	2.24538(4) [237]
<i>trans</i> -carvacrol A	4.0875(25) (this work)
<i>trans</i> -carvacrol B	4.4025(16) (this work)
<i>anti-o</i> -cresol	4.4256(14) [234]
<i>o</i> -chlorotoluene	5.527(10) [131]
memphenesin (conf. A)	5.736(18) [238]
<i>o</i> -xylene	6.23(21) [239]
<i>syn-o</i> -cresol	7.912(46) [234]

in unphysical results. However, the  $V_3$  contribution to the potential is of the same order of magnitude. In summary, the barrier height of the methyl rotor seems to depend mainly on steric effects, as also suggested by Gerhard and coworkers [131]. Hence, more extended substituents close to the rotating methyl group, such as another methyl group (e.g. as in xylene), result in higher barriers than more compact groups, such as a cyano group (e.g. as in *o*-tolunitrile). For a hydroxyl group, the barrier height very much depends on the orientation of the hydrogen, as expected.

## 5.5 Conclusion and outlook

The microwave spectra of two monoterpenoids, thymol and carvacrol, were presented. Four conformations of carvacrol were identified in the cold conditions of the molecular beam. In contrast, only three conformations of thymol were present. This difference can be explained by the higher energies of the group of *cis*-conformers of thymol relative to the global minimum *trans*-conformer compared with carvacrol, where the energy differences between the *cis*- and *trans*-conformer groups are smaller.

For thymol and carvacrol, internal rotation of the terminal methyl top was observed and a fitted barrier height that is consistent with measurements of similar molecules was obtained. The one order of magnitude difference in the barrier heights observed for these two molecules can be directly ascribed to the different positions of the hydroxyl substituent on the aromatic ring. In carvacrol, the hydroxyl group is substituted *ortho* to the methyl top and thus strong interactions arise, resulting in a high barrier to internal rotation. In thymol, the hydroxyl group is substituted *meta* to the methyl top and thus the larger distance between these groups results in weaker hindrance to methyl rotation and thus a lower internal rotation barrier.

---

The supplementary information of Reference [219] provides linelists with the corresponding assignments.

The results of the quantum chemical calculations agreed very well with the experiment. The rotational constants from both the MP2- and B3LYP-based methods are near to the values obtained experimentally, indicating that they are accurate enough to model the structures of the kinds of molecular systems investigated here.

In future work, extensions to studies of secondary interactions, i.e. hydrogen bonding by substitution of a second hydroxyl group onto the aromatic ring, will be interesting. In the next chapter the chiral monoterpenoid menthol and menthone are investigated. Menthol exhibits the same substituent patterns as thymol, but has a central cyclohexane ring instead of a phenyl ring. The additional structural flexibility of menthol influences the number of potential low-energy conformers and it will be intriguing to draw direct comparisons to planar thymol.

## Chapter 6

# Exploring the conformational landscape of menthol, menthone, and isomenthone: A microwave study

### 6.1 Introduction

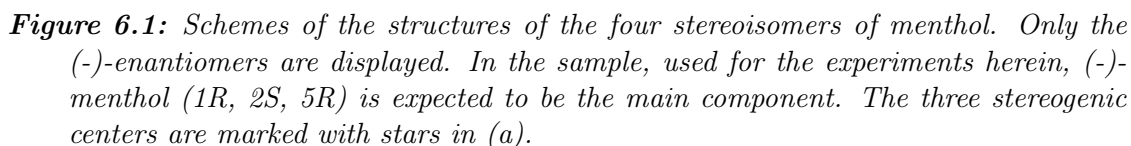
As detailed in the previous chapter, terpenoids represent a large and diverse class of organic molecules with varying chemical and biological activities [220], such as anti-bacterial [231, 241, 242], antioxidant, anti-inflammatory [232], and anti-fungal properties [233, 242]. To explain or even predict the molecular origin of a specific chemical or biological behavior, knowledge of the molecular structure, the potential energy surface (PES), the conformational flexibility, and the internal dynamics is required. In this Chapter, the gas-phase structures and conformational space of menthol, menthone, and isomenthone are investigated based on vibrationally and rotationally cold gas-phase microwave spectra and quantum chemical calculations. In contrast to thymol and carvacrol (previous chapter), the cyclohexane ring in menthol adds further flexibility and extends the conformational space.

Menthol is a monoterpene alcohol with several properties that make it a chemically and biologically interesting system. It is well-known for its minty smell and used as a flavoring agent in many different applications. Menthol is also famous for its cooling sensation when applied to skin or mucous membranes [243]. This property is exploited in its widespread use as a cooling-enhancing additive in cigarettes, cough medicines, and antipruritics [244, 245]. The three chiral centers of menthol result in eight different stereoisomers, of which the (-)-enantiomers are depicted in Figure 6.1. The stereoisomers, (-)-menthol (1R, 2S, 5R), and (-)-neomenthol (1R, 2R, 5S), are naturally occurring in the essential oil of *Mentha x piperita*

---

This chapter is completely based on the following publication:

- D. Schmitz, V. A. Shubert, T. Betz, and M. Schnell, *Exploring the conformational landscape of menthol, menthone, and isomenthone: A microwave study*, Front. Chem. **3**, 15 (2015). (key ideas: 80%, experimental: 80%, data analysis: 80%, writing up: 75%) [240]



Broadband microwave spectroscopy enables the simultaneous measurement of the rotational spectra of multiple conformations, providing a wide swath of the spectrum within the bandwidth of the instrument in a single measurement. This broad acquisition is beneficial for the

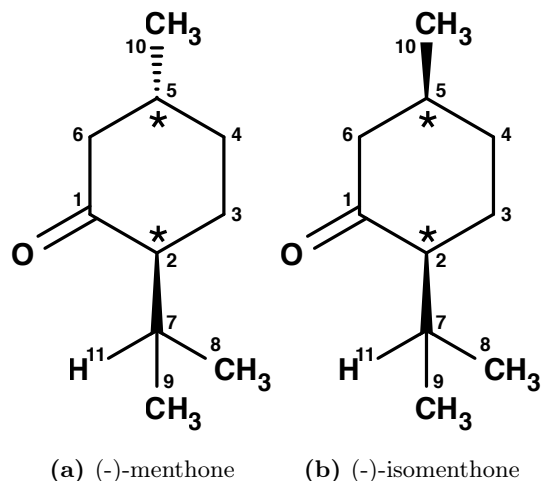


**Figure 6.2:** Schemes of the structures of the (-)-enantiomers of menthone. The two stereogenic centers are marked with stars.

assignment of the individual transitions within a spectrum because recurring patterns can be identified quickly and linked to a predicted spectrum. However, the presence of several species in the rotational spectrum can impede a straightforward assignment. Therefore a computer program was developed and used for the analysis of broadband microwave spectra in Section 6.3 and applied it to the mixture of menthone isomers (four different species). The program identifies and fits the different species within a spectrum using calculated *ab initio* rotational constants as initial input values.

## 6.2 Experimental and computational methods

Menthone (2-isopropyl-5-methylcyclohexanone, 97 % purity, mixture of isomers, i.e., potentially containing all four diastereomers ((+/-)-menthone and (+/-)-isomenthone)) and menthol (2-isopropyl-5-methylcyclohexanol, 99 % purity) were purchased from Sigma-Aldrich Chemie GmbH, Taufkirchen, Germany and were used without further purification. No further information was provided about the stereoisomeric composition of the menthol sample. Due to its synthetic origin, the stereoisomer (-)-menthol is expected to be the main component. Menthol is a white, flaky, and sticky hydrophilic crystalline solid with a stated melting point of 34 – 36 °C and a boiling point of 216 °C at standard conditions. The mixture of menthone isomers is a yellowish liquid with a stated boiling point of 85 °C. The schemes of the chemical structures of (-)-menthone, (-)-isomenthone, and (-)-menthol are depicted in Figures 6.1 and 6.2.

All rotational spectroscopy measurements were performed with the Hamburg COMPACT spectrometer which has been detailed elsewhere [69] and thus only a brief description is given here. The molecules were seeded into a supersonic expansion using a pulsed nozzle (Parker General Valve, Series 9) operating at 2 Hz. The sample holders were placed directly prior to

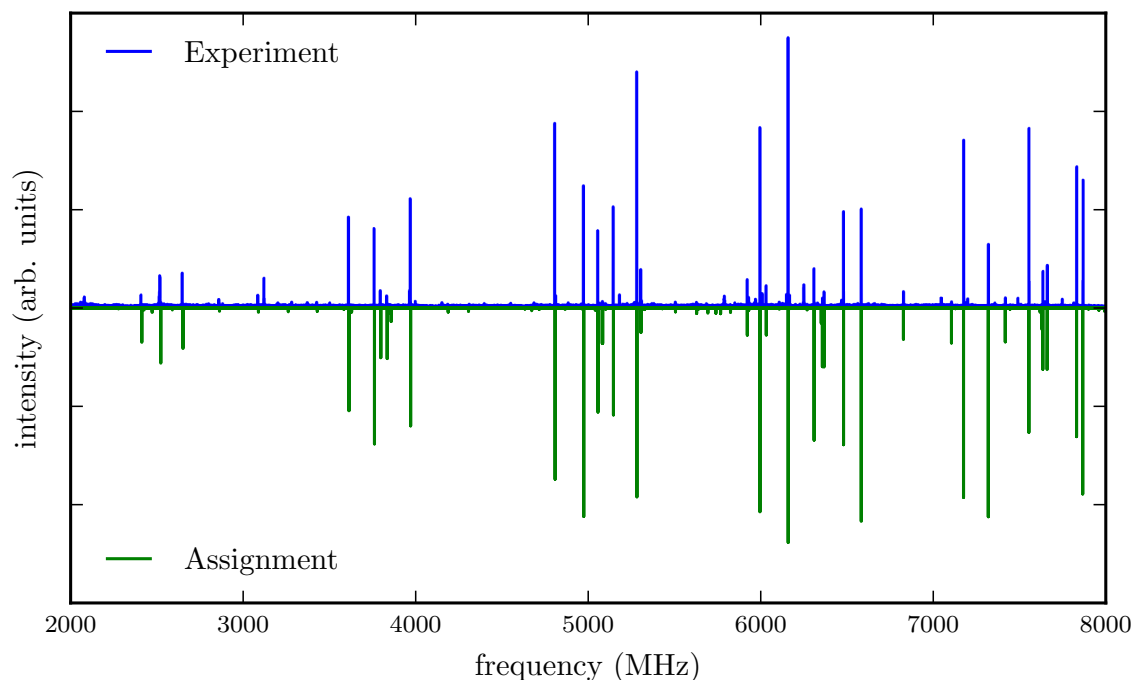


**Figure 6.3:** Microwave spectrum of menthol in the region of 2 – 8 GHz. The upper trace shows the experimental spectrum, the lower trace is a simulation based on fitted molecular parameters. The spectrum is dominated by *a*-type and *c*-type transitions. A rotational temperature of 0.5 K gives the best match between the simulated and the experimental intensities. A line splitting due to the internal rotation of any of the methyl groups is not observed in the spectrum.

the nozzle and heated to about 112 °C for both menthol and menthone. This temperature gave the best signal for both molecular samples. A constant flow of neon at a stagnation pressure of 3.0 bar transported the molecules to the nozzle. After supersonic expansion into vacuum, the ensemble of molecules was polarized with a 1  $\mu$ s chirp spanning 2  $\rightarrow$  8.5 GHz. The chirp was generated with an arbitrary waveform generator, amplified to 300 W with a traveling wave tube amplifier, and transmitted into the vacuum chamber with a horn antenna. Following excitation, the free induction decay (FID) of the macroscopic ensemble of polarized molecules was recorded. For each spectrum, 50  $\mu$ s of the FID were recorded at a resolution of 10 ps, yielding a frequency resolution of 20 kHz in the Fourier transform and hence the rotational spectra obtained. For menthol and menthone, 444 000 FIDs and 128 000 FIDs, respectively, were coadded for each spectrum. The resulting signal-to-noise ratio of (100:1) for the strongest transitions was sufficient to identify the parent isotopologue species of the different conformers. After performing the Fourier transformation, residual background lines were removed.

Herein, the experimental results were compared with electronic structure calculations performed with the Gaussian 09 [256] program suite. For menthol, in order to determine the preferred orientations of the hydroxyl group and the lowest energy orientation of the isopropyl group, relaxed energy scans of rotations for the hydroxyl and isopropyl groups with

**Table 6.1:** Experimentally obtained and calculated rotational constants and dipole moments for menthol. The errors given here are standard errors.  $N^\circ(a/b/c)$  gives the number of transitions included in the fit according to its type, and  $\sigma$  is the standard deviation of the fit. The computational results for conformer EQ1ext were obtained using three different combinations of calculation methods and basis sets and they are given in the following order: B3LYP/aug-cc-pVTZ / B3LYP/6-311++G(d,p) / MP2/6-311++G(d,p).

	Experiment	Conformer EQ1ext
$A$ (MHz)	1779.79549(38)	1776/1769/1795
$B$ (MHz)	692.62171(24)	686.1/683.0/699.7
$C$ (MHz)	573.34542(27)	569.8/567.6/574.5
$\Delta_J$ (kHz)	0.0166(31)	-
$\mu_a$ (D)	-	1.3/1.3/1.4
$\mu_b$ (D)	-	-0.1/-0.1/-0.1
$\mu_c$ (D)	-	0.8/0.9/0.8
$N^\circ$ (a/b/c)	53 (32/0/21)	-
$\sigma$ (kHz)	5.5	-

respect to the cyclohexane ring were performed. The Becke, three parameter, Lee-Yang-Parr (B3LYP) exchange-correlation functional with the 3-21G and the 6-311++G(d,p) basis sets were employed for these potential energy surface (PES) scans. To further refine the structures and verify the energy ordering of the individual conformers, optimizations and harmonic frequency calculations were carried out on all minima using several different basis sets and methods: B3LYP/6-311++G(d,p), B3LYP/aug-cc-pVTZ, and MP2/6-311++G(d,p) (Møller–Plesset second-order perturbation theory). Furthermore, the Minnesota functional M06-2X with the 6-311++G(d,p) basis set was used to optimize the structure of the conformers. The rotational constants and dipole moments agree well with the B3LYP and MP2 calculations, but the relative zero-point corrected energies differ by about 1 kJ/mol for some conformers. The results of the M06-2X calculations are compiled in the supplementary information of Reference [240], for which significant differences in the zero-point corrected energies are observed. In order to get an overview of the internal dynamics, the barrier to internal rotation for the different methyl tops was calculated at the B3LYP/6-311++G(d,p) level of theory.

## 6.3 Results and discussion

### Menthol

The experimental spectrum of menthol is presented in the positive trace of Figure 6.3. The spectrum is typical for a prolate asymmetric rotor with  $\mu_a$  as the largest dipole moment component. From the spectrum 32  $a$ -type and 21  $c$ -type lines were assigned and fitted, but no  $b$ -type lines were observed. The spectrum arises from only a single species, indicating that only one conformer of menthol is significantly populated in the supersonic expansion, in



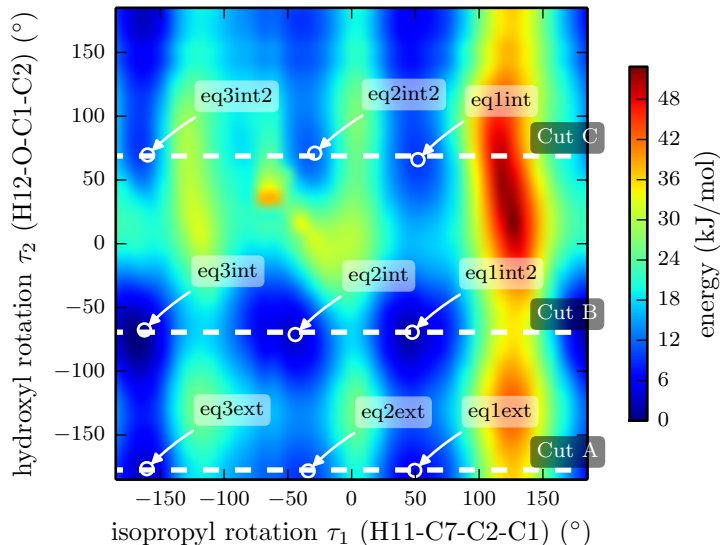


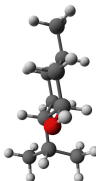
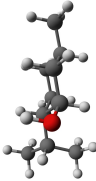
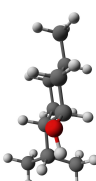
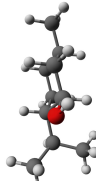
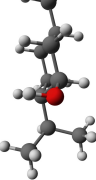
**Figure 6.4:** Plot of the potential energy landscape of (-)-menthol as a function of the isopropyl and the hydroxyl rotation angles. The data was extracted from a two-dimensional, relaxed potential energy scan using the B3LYP/3-21 functional. The dashed lines mark cuts through the 3D surface, which were evaluated using a higher level of theory (B3LYP/6-311++G(d,p)). The results of these three scans are depicted in Figure 6.5.

line with the findings of a recent FTIR study [251]. Furthermore, it confirms that menthol is indeed the main stereoisomer in the purchased sample, since isomenthol, neomenthol and neoisomenthol all have different rotational constants and thus can be easily differentiated by their rotational spectra. For fitting the spectrum, Pickett’s SPFIT/SPCAT program suite employing the  $I^r$  representation and the Watson A reduction was used [146]. Table 6.1 summarizes the results of the fit. Lines including rotational quantum numbers  $J = 1$  to  $J = 7$  and a maximum  $K_a$  of 4 were observed and assigned.

The conformational flexibility of menthol originates from the cyclohexane configuration and the orientations of the hydroxyl and isopropyl groups. Rotations of the different methyl groups do not contribute to the conformational space because they have  $C_{3V}$  local symmetry for which rotation gives rise to three equivalent minima. However, they could lead to characteristic tunneling splittings if the corresponding barriers are sufficiently low.

It was shown by NMR spectroscopy, gas-phase electron diffraction, and several quantum chemical computation studies that the chair conformation of cyclohexane is preferred in menthol [252, 253]. In order to get an overview of the potential energy surface, a relaxed two dimensional scan at the B3LYP/3-21G level of theory was performed by rotating the isopropyl and hydroxyl groups with all three substituents in equatorial positions. The rotation of the hydroxyl group with respect to the ring occurs around the dihedral angle  $\tau_2$  (H12-O-C1-C2), while the isopropyl orientation is described with the dihedral angle  $\tau_1$  (H11-C7-C2-C1) (compare Fig. 6.1). The resulting PES is shown in Figure 6.4 and reveals the existence of various stable rotamers. In this figure the nine lowest energy rotamers are marked using the labeling

**Table 6.2:** Calculated relative zero-point corrected energies, rotational constants, dipole moments, and torsional angles for the five lowest energy conformers of menthol. The labeling scheme introduced by Moreno et al. [254] is used. The results were obtained using three different combinations of calculation methods and basis sets and they are given in the following order: B3LYP/aug-cc-pVTZ / B3LYP/6-311++G(d,p) / MP2/6-311++G(d,p).

conformer	EQ1ext	EQ1int2	EQ1int	EQ3ext	EQ3int
$\Delta E$ (kJ/mol)	0.0/0.0/0.0	1.0/0.9/1.4	1.9/2.0/2.1	4.5/4.2/3.3	5.3/5.0/5.0
$A$ (MHz)	1776/1769/1795	1760/1753/1774	1762/1755/1777	1954/1948/1975	1939/1932/1960
$B$ (MHz)	686.1/683.0/699.7	685.0/682.1/698.0	687.2/684.6/699.1	668.2/665.7/674.7	668.4/665.9/674.1
$C$ (MHz)	569.8/567.6/574.5	589.0/566.8/573.5	568.6/566.1/573.1	575.6/573.6/582.7	574.4/572.2/581.5
$\tau_1$ ( $^\circ$ ) <sup>1</sup>	49.1/49.5/58.3	47.4/47.6/56.1	51.0/52.0/58.3	-160.5/-160.7/-158.7	-162.1/-162.5/-159.5
$\tau_2$ ( $^\circ$ ) <sup>1</sup>	-176.4/-177.8/-173.2	-69.7/-69.4/-66.6	66.0/65.9/62.3	-175.3/-176.6/-172.3	-67.1/-67.6/-67.7
$\mu_a$ (D) <sup>1</sup>	1.3/1.3/1.4	0.8/0.9/0.8	-0.8/-0.9/-0.9	1.5/1.5/1.6	1.0/1.1/1.1
$\mu_b$ (D) <sup>1</sup>	-0.1/-0.1/-0.1	-1.1/-1.2/-1.3	-1.2/-1.2/-1.3	-0.1/-0.1/-0.03	-1.0/-1.1/-1.0
$\mu_c$ (D) <sup>1</sup>	0.8/0.9/0.8	-0.7/-0.7/-0.7	0.9/0.9/0.9	0.8/0.9/0.8	-0.8/-0.9/-0.9
					

<sup>1</sup> Dihedral angle and dipole moment components are given for (-)-menthol.

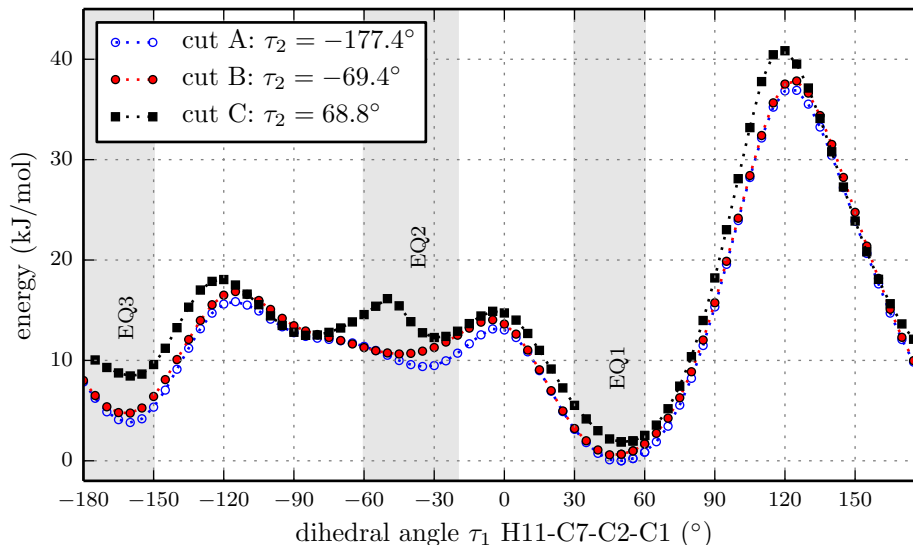


**Figure 6.5:** Relaxed potential energy scans for the rotation of the isopropyl group of (-)-menthol with fixed orientations of the hydroxyl group at dihedral angles  $\tau_2 = [-177.4, -69.4, 68.8]^\circ$  ( $H_{12}-O-C_1-C_2$ ) according to the marks in Figure 6.4, at the B3LYP/6-311++G(d,p) level of theory. All three traces have the same overall features, while cut A contains the lowest minima. The double minimum structure of cut C around EQ2 might be an artifact due to fixing dihedral angle  $\tau_2$ .

scheme introduced by Moreno et al. [254].

Three relaxed one-dimensional scans of the rotation of the isopropyl group were also performed with a larger basis set and the hydroxyl dihedral angle fixed at values of  $-177.4^\circ$ ,  $-69.4^\circ$  and  $68.8^\circ$ . These three cuts through the three-dimensional potential energy surface are indicated by the white dashed lines in Figure 6.4 and were carried out using the B3LYP functional and the 6-311++G(d,p) basis set. The results are presented in Figure 6.5. The slices go through the nine lowest energy structures and give a better understanding of the energy ordering. At the minima positions EQ1 and EQ3, the isopropyl group is out of plane with respect to the cyclohexane ring. At the minima positions EQ2, the isopropyl group is in plane but the hydrogen H11 is opposite to the hydrogen bonded to C2 (see Fig. 6.1). These structures are much higher in energy than those at the minima positions EQ1 and EQ3. The orientation of the hydroxyl group at an angle of  $\tau_2 = -177.4^\circ$  gives the lowest energy trace.

This relaxed potential energy scan revealed the energy ordering of the different conformers, and the five lowest energy conformers (EQ1ext, EQ1int2, EQ1int, EQ3ext and EQ3int) below 6 kJ/mol were chosen for further analysis at the B3LYP/aug-cc-pVTZ, B3LYP/6-311++G(d,p), and MP2/6-311++G(d,p) levels of theory. The zero-point corrected energies, rotational constants, and dipole moments from these calculations are listed in Table 6.2. EQ1ext is the lowest energy conformer at all three levels of theory, in agreement with the gas-phase electron diffraction data by Egawa et al. [253]. Relaxed potential energy scans were also carried out on conformer EQ1ext for the rotation of the methyl groups. The corresponding barrier heights

are around  $12\text{ kJ/mol}$ , too high to affect the observed rotational spectrum and in agreement with the observations presented herein.

The similarity of the rotational constants for the calculated structures EQ1ext, EQ1int2, and EQ1int complicate a straightforward assignment of the fitted constants of the single observed menthol conformation (Table 6.1) to one of the three lowest energy conformers compiled in Table 6.2. However, the energy ordering of the conformers, which is the same for all calculation methods and basis sets employed, suggests that the lowest energy conformer EQ1ext is the observed one. This observation is supported by the calculated dipole moment components of the menthol conformers. Conformer EQ1ext has a very weak dipole moment component along the  $b$ -axis and no  $b$ -type lines were observed in the spectrum. However, for the higher energy conformers, EQ1int2 and EQ1int,  $\mu_b$  is predicted to be the strongest dipole moment component. For the conformers EQ3ext and EQ3int, the calculated  $A$ -rotational constants differ by 200 MHz from the experimentally determined one. Hence, the observed menthol conformation is assigned to the lowest energy conformer, EQ1ext. It should be noted that the deviations of the rotational constants for the four different theoretical levels employed here are of the same order of magnitude as the deviations between the three EQ1 conformers (i.e., EQ1ext, EQ1int2, and EQ1int). The predictions of the dipole moment components, however, seem to be significantly more reliable and allow for the structural assignment of the observed menthol conformer, as stated above.

The observation of only a single menthol conformation can be explained by the potential energy surface. The three lowest energy conformers (EQ1ext, EQ1int, EQ1int2) differ in the rotation of the hydroxyl group. The barrier of this rotation between each conformer is around  $3\text{ kJ/mol}$  (B3LYP/6-311++G(d,p)). As this barrier height is small, it is expected that the supersonic expansion cools conformers EQ1int and EQ1int2 into EQ1ext. The sets of conformers EQ2 and EQ3 are much higher in energy by  $5 - 10\text{ kJ/mol}$  and, even though the populations in EQ3 might be frozen during supersonic expansion due to the higher isomerization barriers to EQ1 and EQ2, their populations remain too low to affect the spectrum. The observation of the conformer EQ1ext agrees with the gas electron diffraction study of Egawa et al. [253]. In comparison to the conformers EQ1int and EQ1int2, conformer EQ1ext might be stabilized by a weak non-conventional hydrogen bond between H11 and the hydroxyl O [251]. The signal-to-noise ratio of approximately 100:1 for the most intense lines did not permit the observation of lines originating from  $^{13}\text{C}$ - or  $^{18}\text{O}$ -isotopologues of menthol to enable more advanced structure determination.

## Menthone and isomenthone

The spectrum of the mixture of menthone isomers was recorded and is presented in the frequency range from 4700 to 5650 MHz in the positive trace of Figure 6.6. The high number and density of lines of molecular origin and various background lines complicated the assignment of the individual lines to the particular species. Therefore, a computer-aided assignment routine was developed to facilitate the assignment process. This routine is described in Section

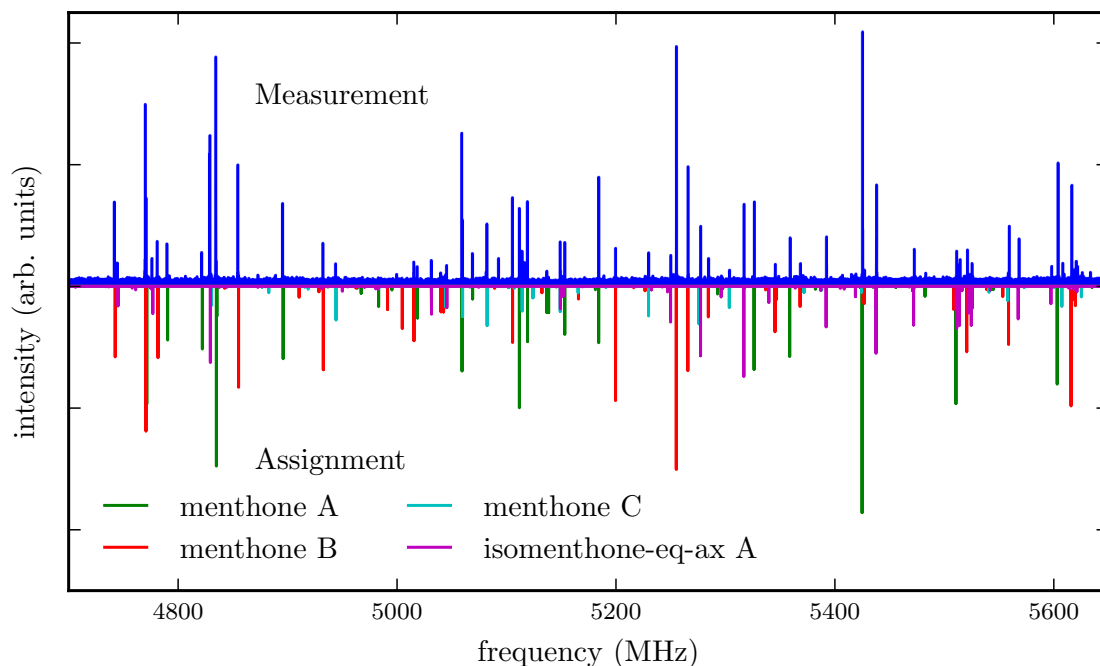


**Figure 6.6:** The upper trace is the spectrum of the mixture of the stereoisomers of menthone and isomenthone in the region of 4700 – 5650 MHz while the lower traces are simulations based on fitted molecular parameters. Three different conformers of menthone and one conformer of isomenthone were identified in the spectrum and successfully assigned. A rotational temperature of 1.5 K for all four species gives the best match between the simulated and the experimental intensities. A few residual lines with SNR ratios of about 3:1 remain unassigned, which might originate from contaminants, clusters, or instrument noise. Line splittings due to internal rotation of one of the methyl groups of menthone or isomenthone were not observed.

**6.3.** It was possible to assign most of the lines to four different species. For all species, most of the assigned transitions are *b*-type, with fewer *a*-type transitions and even fewer *c*-type transitions. This observation suggests that for all four species  $\mu_b > \mu_a > \mu_c$  applies. The final fits were executed employing the SPFIT/SPCAT suite of programs using the  $I^r$  representation and the Watson A reduction. The results are compiled in Table 6.3.

According to NMR measurements and quantum chemical calculations by Smith et al., the cyclohexane ring in menthone is in the chair configuration and both substituents, the isopropyl and the methyl groups, are in equatorial positions [255]. Hence the degrees of freedom of menthone are limited to the rotations of the isopropyl and methyl groups. The relaxed potential energy surface was calculated for the rotation of the isopropyl group (dihedral angle  $\tau_1$  (H11-C7-C2-C1)) at the B3LYP/6-311++G(d,p) level of theory. The result is displayed in Figure 6.7 and exhibits three different minima at orientations similar to those of (-)-menthol. These three structures were optimized at the B3LYP/aug-cc-pVTZ, B3LYP/6-311++G(d,p), and MP2/6-311++G(d,p) levels of theory. The results are summarized in Table 6.4. The zero-point corrected energies of the three menthone rotamers are within 3  $kJ/mol$  (B3LYP/aug-cc-pVTZ calculation) of each other.

**Table 6.3:** Experimentally determined rotational constants and quartic distortion constants of menthone and isomenthone. The errors given here are standard errors.  $N^\circ(a/b/c)$  is the number of lines included in the fit distributed for  $a$ -,  $b$ -, and  $c$ -type transitions, and  $\sigma$  is the standard deviation of the fit.

	menthone A	menthone B	menthone C	isomenthone eq-ax A
$A$ (MHz)	1953.43379(43)	2021.98637(36)	2109.38469(65)	1535.27577(48)
$B$ (MHz)	694.51551(19)	693.53686(16)	681.13604(27)	812.92526(33)
$C$ (MHz)	586.57758(19)	562.13636(16)	598.12413(25)	671.43466(33)
$\Delta_J$ (kHz)	0.0106(18)	0.0109(18)	0.0183(37)	0.0651(53)
$\Delta_{JK}$ (kHz)	0.0234(36)	0.0473(50)	0.097(11)	-0.1844(60)
$\Delta_K$ (kHz)	-	-	-	0.535(20)
$N^\circ$ (a/b/c)	92 (26/66/0)	112 (31/62/19)	57 (21/32/4)	76 (6/67/7)
$\sigma$ (kHz)	7.4	6.0	5.8	7.5

While all theoretical methods employed show comparable trends for both the rotational constants and the dipole moment components, some differences in the relative zero-point corrected energies for the individual conformers are found. For example, using MP2/6-311++G(d,p) calculations, menthone B is predicted to be the lowest-energy conformer by 0.8  $kJ/mol$ , while for all other approaches, menthone A is predicted to be the lowest-energy species (Table 6.4). An explanation of these results is not straightforward. The two menthone conformers A and B differ in the orientation of the isopropyl group with respect to the cyclohexanone ring. The minimum orientations are the result of an interplay between intramolecular interactions, such as van der Waals and dispersion interactions, potential hydrogen bonding to the ketone oxygen, or steric hindrance (repulsion of electron clouds). These different contributions to the final energy are considered differently in the various theoretical approaches (for example, the B3LYP approach does not account for dispersion that is empirically treated in the M06-2X approach and explicitly considered in MP2 calculations).

Thus, although it is possible to unambiguously assign structures to the three experimentally determined menthone conformers (Table 6.3), their exact energy ordering cannot be determined for this particular case with the available data.

For isomenthone (*cis*-configuration) the situation is different. Isomenthone may exist with the isopropyl and the methyl group substituent either equatorial or axial, which in turn influences the cyclohexane configuration. Intuitively, three different starting structures are feasible: the methyl group oriented equatorial and the isopropyl group axial to the cyclohexane ring (isomenthone eq-ax), the methyl group oriented axial and the isopropyl group equatorial to the cyclohexane ring (isomenthone ax-eq) and both substituents oriented equatorial to the ring (isomenthone eq-eq). The diaxial configuration always relaxes to one of the other conformers during the structural optimizations. It is destabilized by the high steric strain between the two substituents.

Again a relaxed potential energy scan was performed by rotating the isopropyl group around the dihedral angle  $\tau_1$  for the three different starting structures (-)-isomenthone eq-ax, (-)-

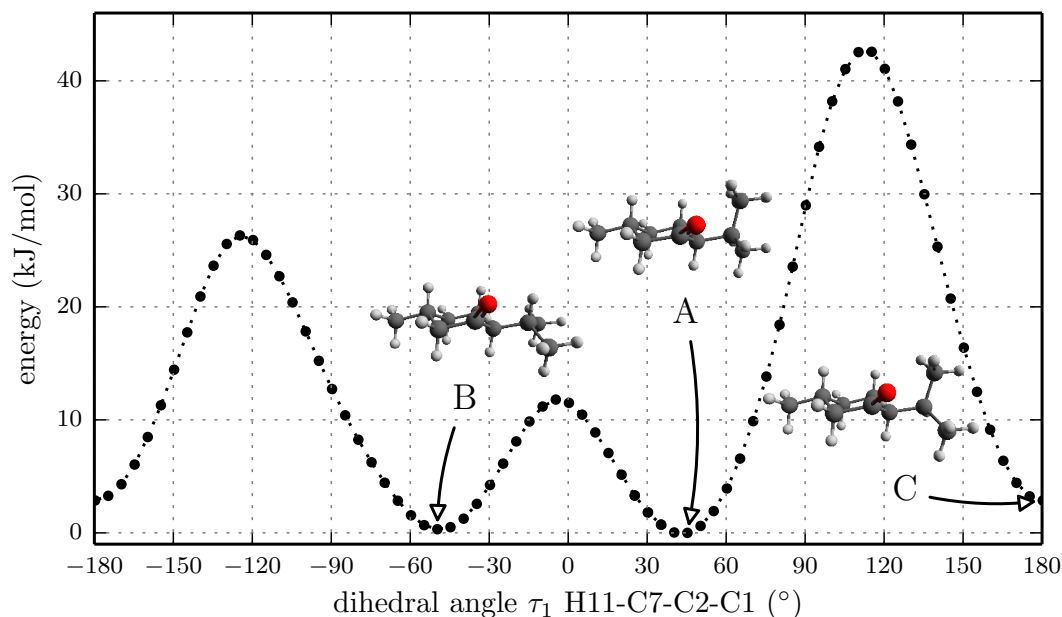


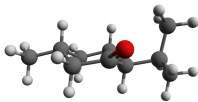
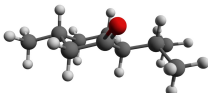
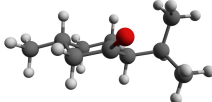
**Figure 6.7:** Scan of the potential energy surface calculated along the dihedral angle  $\tau_1$  H11-C7-C2-C1 according to the labeling in Fig. 6.2 at the B3LYP/6-311++G(d,p) level of theory for (-)-menthone. The position of the minimum conformations (A, B, C) is indicated in the plot and illustrated with the corresponding structure.

isomenthone ax-eq, and (-)-isomenthone eq-eq. Figure 6.8 shows the results for these relaxed potential energy scans. The global minimum was found for (-)-isomenthone eq-ax at about  $\tau_1 = -60^\circ$ . Therefore, the set of conformers with  $\tau_1$  being close to  $-60^\circ$  is labeled as A. The set of minimum structures at  $\tau_1 \approx -45^\circ$  is labeled as B, and the set at  $\tau_1 \approx -180^\circ$  is labeled as C. For all nine minimum structures, optimizations and frequency calculations were carried out using the B3LYP/aug-cc-pVTZ, B3LYP/6-311++G(d,p), and MP2/6-311++G(d,p) levels of theory. The results of these calculations for the three lowest energy structures (isomenthone eq-ax A, isomenthone ax-eq A, and isomenthone ax-eq B) are listed in Table 6.5. The dipole moment components and the dihedral angle of the isopropyl group are given for the (-)-enantiomers.

Considering only the three lowest energy conformers for menthone and isomenthone (Table 6.4 and Table 6.5) the assignment of the experimentally determined species to the calculated structures is straightforward. At least one of the experimentally determined rotational constants differs significantly from the calculated ones for isomenthone ax-eq A and isomenthone ax-eq B, so that three of the observed species are assigned to menthone A, menthone B, and menthone C and the fourth one to isomenthone eq-ax A. In addition to the rotational constants, the distortion constants  $\Delta_J$  and  $\Delta_{JK}$  were included in the fits for all conformers. Inclusion of the constant  $\Delta_K$  only improved the fitting results of conformer isomenthone eq-ax A. The axially aligned isopropyl group of isomenthone eq-ax seems to lead to a higher sensitivity regarding centrifugal distortion.



**Table 6.4:** Calculated relative zero-point corrected energies, Boltzmann populations, rotational constants, dipole moments, and torsional angles for the three lowest energy conformers of menthone. The results were obtained using three different combinations of theoretical methods and basis sets and they are stated in this order: B3LYP/aug-cc-pVTZ / B3LYP/6-311++G(d,p) / MP2/6-311++G(d,p).

	menthone A	menthone B	menthone C
	B3LYP <sup>2</sup> B3LYP <sup>3</sup> MP2 <sup>3</sup>	B3LYP <sup>2</sup> B3LYP <sup>3</sup> MP2 <sup>3</sup>	B3LYP <sup>2</sup> B3LYP <sup>3</sup> MP2 <sup>3</sup>
$\Delta E$ (kJ/mol)	0.0/0.0/0.84	0.19/0.29/0.0	3.0/2.9/3.9
Population (%) <sup>1</sup>	42.9/43.1/48.4	40.4/39.4/37.2	16.7/17.5/14.5
$A$ (MHz)	1950/1941/1965	2017/2009/2029	2105/2096.3/2117
$B$ (MHz)	688.7/686.1/694.1	689.3/686.4/695.2	675.7/673.1/684.5
$C$ (MHz)	582.4/579.9/590.0	558.7/556.2/566.3	593.3/591.0/601.7
$\mu_a$ (D) <sup>4</sup>	1.3/1.3/1.2	-1.3/-1.3/-1.2	1.8/1.8/-1.6
$\mu_b$ (D) <sup>4</sup>	-2.6/-2.7/-2.5	-2.4/-2.5/-2.2	-2.2/-2.3/2.0
$\mu_c$ (D) <sup>4</sup>	-0.5/-0.5/-0.53	1.1/1.2/1.2	-1.1/-1.1/-1.2
$\tau_1$ (°) <sup>4</sup>	42.6/42.9/41.9	-48.7/-48.8/-49.3	-179.8/-179.8/176.7
			

<sup>1</sup> Boltzmann distribution calculated at the sample reservoir temperature of 386 K.

<sup>2</sup> aug-cc-pVTZ basis set

<sup>3</sup> 6-311++G(d,p) basis set

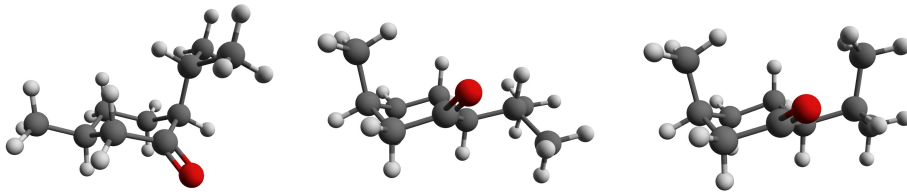
<sup>4</sup> Dipole moment components and dihedral angle are given for the (-)-enantiomer.

For the three lowest-energy conformers of isomenthone, the different theoretical approaches agree well with each other and the lowest-energy form eq-ax A matches the experimentally determined values for the rotational constants. The calculated relative zero-point corrected energies are also similar when comparing the B3LYP- and MP2-based approaches. However, for calculations employing the M06-2X density functional, significantly different energies are predicted (Tables 8-10 of the supplementary material of Ref. [240]). While a good agreement is again found for the rotational constants and dipole moment components, the three low-energy conformers given in Table 6.5 are predicted to be nearly isoenergetic using the M06-2X functional, a result for which an explanation is not yet understood and which is also not predicted by the other approaches.

The cyclohexane ring in all three observed menthone conformers is in a chair configuration and both substituents in equatorial orientations. Such a structural arrangement is expected due to steric effects. Hence, the conformational space of menthone is governed by the isopropyl rotation. The barriers separating the different menthone conformers are between 12 kJ/mol and 40 kJ/mol and should be high enough to freeze the population to that at the temperature of the sample reservoir during the cooling process of the supersonic expansion. The



**Table 6.5:** Calculated relative zero-point corrected energies, Boltzmann populations, rotational constants, dipole moments, and torsional angles for the three lowest energy conformers of isomenthone. The results were obtained using three different combinations of theoretical methods and basis sets and they are stated in this order: B3LYP/aug-cc-pVTZ / B3LYP/6-311++G(d,p) / MP2/6-311++G(d,p).

	isomenthone eq-ax A	isomenthone ax-eq A	isomenthone ax-eq B
	B3LYP <sup>2</sup> B3LYP <sup>3</sup> MP2 <sup>3</sup>	B3LYP <sup>2</sup> B3LYP <sup>3</sup> MP2 <sup>3</sup>	B3LYP <sup>2</sup> B3LYP <sup>3</sup> MP2 <sup>3</sup>
$\Delta E$ (kJ/mol)	0.0/0.0/0.0	2.7/2.5/3.7	2.7/2.5/4.4
Population (%) <sup>1</sup>	44.6/43.2/58.4	19.5/20.0/18.6	19.1/20.0/14.9
$A$ (MHz)	1538/1528/1516	1848/1839/1849	1731/1721/1741
$B$ (MHz)	804.5/802.2/824.6	765.3/762.6/781.4	771.0/768.8/788.6
$C$ (MHz)	662.3/660.2/680.6	624.8/622.5/641.0	674.1/672.0/693.4
$\mu_a$ (D) <sup>4</sup>	-0.7/-0.7/-0.6	-1.1/-1.1/-0.9	1.1/1.1/0.9
$\mu_b$ (D) <sup>4</sup>	-3.1/-3.1/-2.9	2.5/2.4/2.2	-2.7/-2.7/-2.5
$\mu_c$ (D) <sup>4</sup>	-1.0/-1.0/-1.0	-1.4/-1.4/-1.4	-0.7/-0.8/-0.7
$\tau_1$ (°) <sup>4</sup>	-64.5/-64.1/-64.0	-49.4/-49.4/-49.2	42.6/42.9/42.0
			

<sup>1</sup> Boltzmann distribution calculated at the sample reservoir temperature of 386 K.

<sup>2</sup> aug-cc-pVTZ basis set

<sup>3</sup> 6-311++G(d,p) basis set

<sup>4</sup> Dipole moment components and dihedral angle are given for the (-)-enantiomer.

situation is different for isomenthone. Both substituents are arranged *cis* to the cyclohexane ring. Hence, the equatorial orientation of both substituents forces the cyclohexane ring into the boat configuration, which is higher in energy compared to the chair configuration for unsubstituted cyclohexane. The diaxial orientation of the substituents is prevented by steric hindrance. Consequently, in the lowest energy conformers of isomenthone one substituent needs to be oriented equatorially and the other one axially. Likely due to the anomeric effect, the lowest energy conformer isomenthone eq-ax A having the isopropyl group oriented axially is stabilized. It is surprising that only one conformer of isomenthone was observed. Using the argument that the conformers are frozen out due to the barrier height, one would expect more conformers of the ax-eq kind. This absence might be explained by the fact that the fraction of isomenthone in the mixture is only 30 % (analysis by Sigmar-Aldrich), which is confirmed by weaker intensities of isomenthone (SNR of approximately 50:1 for the strongest transitions) compared to menthone A (SNR of approximately 100:1 for the strongest transitions). Thus the density of the additional conformations in the expansion is likely too low to allow them

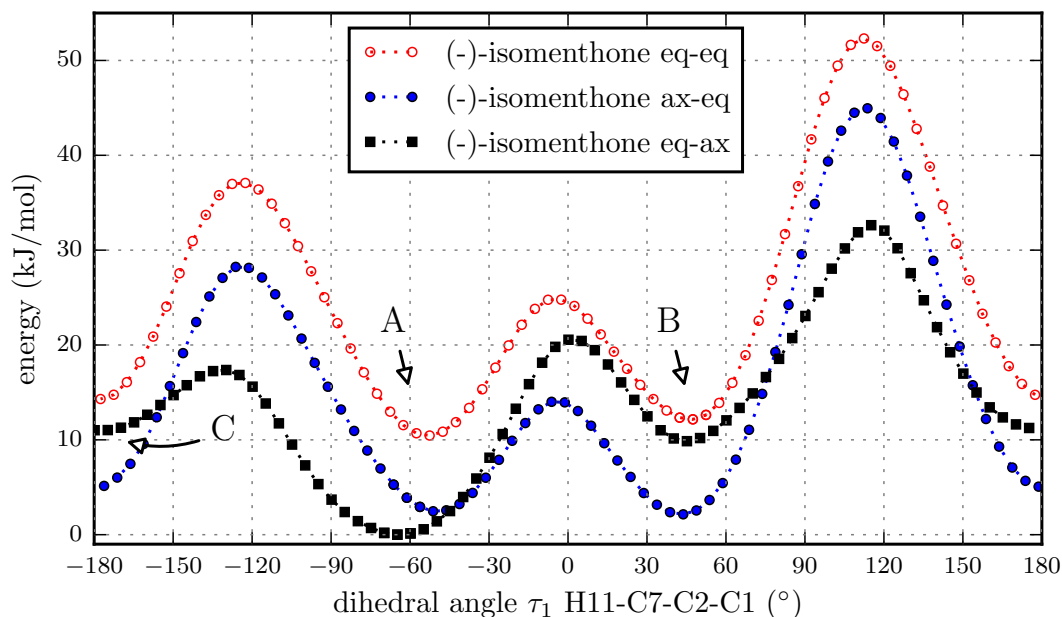


**Figure 6.8:** Scan of the potential energy surface calculated along the dihedral angle  $\tau_1$  H11-C7-C2-C1 according to the labeling in Fig. 6.2 at the B3LYP/6-311++G(d,p) level of theory for (-)-isomenthone eq-eq, (-)-isomenthone ax-eq and (-)-isomenthone eq-ax. The labels A, B, C are pointing to the corresponding minima. Only the conformation isomenthone eq-ax A was observed in the microwave spectrum.

to be observed with the signal-to-noise ratio of the spectrum presented here, i.e. with only 128000 single acquisitions coadded.

### Computer-aided assignment routine

The assignment of the spectrum from the menthone/isomenthone mixture was complicated by the overlap of different  $J$ -transitions that impeded a straightforward analysis. The presence of background lines led to further complications. Therefore a computer program was developed to facilitate the analysis. Earlier approaches to automate spectral assignment include a computer program based on a genetic algorithm to fit the details of a rotationally resolved UV spectrum and subsequently extract the molecular parameters of multiple mixture components [257]. This approach was implemented with a set of molecular parameters representing a chromosome and thus the molecular parameters of all molecules present in the mixture must be within the chromosome. The fitness of a solution was determined by a direct comparison of the measured and predicted spectrum.

Recently, Seifert and coworkers introduced another approach for an automated assignment routine called *Autofit* [258]. Their method is based on the assignment of three (linearly independent) lines, representing the minimum number of lines for fitting an asymmetric rotor spectrum including only rotational constants. Within a predefined bandwidth, the program

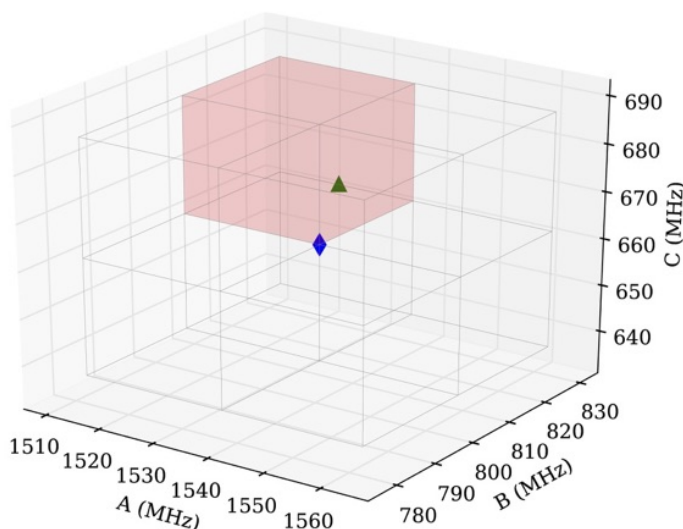


**Figure 6.9:** Scheme of the sampling volume of the rotational constants for the computer-aided assignment routine. The cubic sampling volume is divided into eight subcubes and the routine is carried out consecutively in each of the subcubes. Afterwards the results of the individual subcubes are compared. The blue diamond in the center indicates the position of the calculated rotational constants and the green triangle indicates the position of the experimentally obtained value for isomenthone eq-ax A. The red shaded area is used to display the results in Figure 6.10.

determines potential peaks for each transition, fits all possible combinations of the assignments, and uses the error of the fit to evaluate the solutions. The performance of this program was tested on multiple silicon-containing species and was capable of identifying not only the parent species, but also its carbon and silicon isotopologues [259].

Here another approach is presented for an automatic assignment and fitting procedure with the aim of determining the rotational constants to a high precision. In contrast to the *Autofit* program, which assigns and fits three different peaks directly, first the parameter space of rotational constants is scanned in order to evaluate the goodness of different parameter sets. Only the best parameter sets are used in all subsequent steps, which reduces the computation time drastically. In a second step, four transitions are assigned automatically depending primarily on the frequency and intensity overlap between the measured and predicted spectra. Three transitions are the absolute minimum to fit three rotational constants, but only when the effect of the rotational constants on the assigned transitions is sufficiently significant. Therefore four transitions are chosen to stabilize the fit and reduce the number of diverging results. Diverging and unphysical results are directly excluded and the quality of the fit is assessed by a comparison of the measured and predicted spectra. In the following, the algorithm is explained in detail using the example of isomenthone eq-ax A and the advantages and potential pitfalls are highlighted.

### Step 1: Definition and filling of the scan volume

As previously mentioned, we work in a three-dimensional parameter space of rotational constants with their values along the three axes. In the graphical presentation, the samples are

defined by  $(A, B, C)$ -triples plus a color-code describing their fitness. Two parameters are crucial to the performance of the routine: the volume size and the sample density. The volume should contain the rotational constants of the measured species. Hence the choice of the scan volume depends on the accuracy of the first guess, typically coming from quantum chemical calculations. As stated above, all theoretical approaches employed here give comparable rotational constants, which is a promising prerequisite for the computer-assisted fitting procedure.

A disadvantage to increasing the scan volume is the increased probability, that the routine converges to an artificial local minimum. To avoid this scenario, the initial volume is divided into smaller parts and the routine is run on each of them and the results are compared afterwards. In practice, a cubic volume with 50 MHz edge length centered at the calculated values (blue diamond in Fig. 6.9) is chosen subdivided into eight equally sized subcubes. This procedure is illustrated in Figure 6.9, where the blue diamond indicates the position of the calculated values and the green triangle is positioned on the manually fitted values.

The choice of the sample density is essential for the successful assignment, but also the most important factor on the computation time. The sample density is correlated with the density of transitions in the spectrum. A spectrum with a high density of transitions requires a higher sample density for successful performance. In the example presented here, each subcube was sampled with 2000 such points.

A prediction is made for each point and an intensity cutoff is applied for both the experimental ( $N = 561$ ) and the predicted data. Then both sets of transitions (experiment and prediction) are compared and an assignment is noted for each experimental peak within a predefined bandwidth of a predicted transition. If multiple experimental peaks are found within this bandwidth, only the closest peak is used for the assignment. The bandwidth for the assignment is closely related to the sample density. A higher sample density allows a smaller bandwidth, a low sample density requires a larger bandwidth. In the test case thus far examined, a bandwidth of 10 MHz gives good results.

Finally, the mean-square value of the assignments is calculated and used to judge the fitness of the prediction. The samples are ranked according to their fitness and only the most promising candidates (in this case, the best 10 %) are selected for the subsequent, computationally more demanding fitting procedure.

### **Step 2: Assignment and fitting of the samples within a sub-cube**

In this step, the best results of step one are used as starting point for the fitting procedure using SPFIT. Because only four transitions are used to fit the three rotational constants, the quality of these assignments is essential. Since the correct solution can only be obtained if the four transitions are assigned correctly in at least one trial, care must be taken in choosing the appropriate four transitions for fitting. As a selection criteria for choosing these transitions, the predicted intensities of the assigned transitions are used. To avoid errors in the predicted intensities from the use of incorrect simulation temperatures or dipole moments, the ten transitions with the highest predicted intensities are chosen. From these ten assignments, four

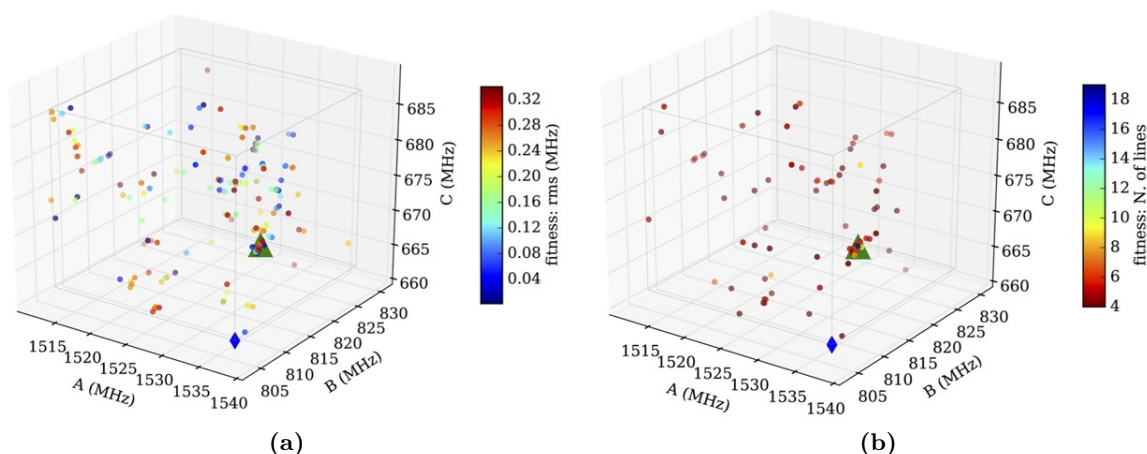


**Figure 6.10:** Results for the sub-cube shaded red in Figure 6.9. (a) Sample distribution after the fit employing SPFIT (step 2). The samples are color-coded using the value of the standard deviation provided by SPFIT. A subtle convergence towards the measured value (green triangle) is visible. (b) Sample distribution after evaluation of the fitting results (step 3). The samples are now color-coded using the number of assigned lines of the SPCAT prediction. The concentration of many samples at the measured rotational constants and the color-code of the samples indicates a correctly assigned spectrum (up to 18 assigned transitions). The comparison of (a) and (b) illustrates the necessity of the evaluation step 3. Good and bad fitting results are scattered throughout the volume in (a), but (b) reveals that the samples far away from real values predict spectra which have little overlap with the measured one.

at random are chosen to increase the diversity of transitions. Sometimes multiple experimental transition can be assigned to a predicted line. In such a case, as many as four consecutive fits are performed assigning the four most intense experimental peaks to a predicted line.

In summary, the best assignments from step one are fitted. Rules for choosing the proper transitions are mainly based on the intensities of the predicted and measured transitions. Diverging and unphysical fit results are directly eliminated, and only one sample is maintained for those which have converged to the same (A, B, C)-triple. The results are weighted using the root-mean-square error from the fit. The best fitting results within a sub-cube are plotted in Figure 6.10a.

### Step 3: Evaluation of the fitting results

In the final step, the fitting results from step two are reevaluated by a direct comparison of the predicted with the measured spectrum. This step is necessary, because the root-mean-square error is not a good check for the quality of a fit of three parameters including only four transitions. The overlap of the experimental transitions and the predicted transitions is assessed following the same prediction and assignment protocol as in step one, but with a much smaller tolerance (100 kHz in the test cases). The number of assigned transitions provides a reliable check of the quality of the assignment. Figure 6.10b shows the final result with a very good overlap of the automatically fitted samples and the manually fitted result (green triangle).

The assignment process depends heavily upon reliably measured and predicted intensities. In the case of untrustworthy experimental intensities, unavailable estimates of the dipole moments, or unknown rotational temperatures, it might be necessary to repeat the procedure employing different sets of dipole moment components and temperatures. In the present study, the routine was repeated three times, setting only one dipole moment component to be nonzero for the predictions in step one and two. However for the evaluation of the fit in step three, all types of rotational transitions were included.

All four isomers present in the menthone/isomenthone mixture were found using as initial input the rotational constants from the B3LYP/aug-cc-pVTZ calculations. The results are compiled in the supplementary material of Reference [240], listing the ten best hits for each of the predicted isomers. Furthermore, the routine was also tested on the spectra (2 – 8 GHz) of two other molecules of the monoterpene family: carvone (843 peaks) and carvomenthénol (204 peaks). For these molecules the different conformers (two for carvone and three for carvomenthénol) were identified without any preprocessing to remove background lines. The parameters of the routine (bandwidth, cubesize, number of samples) were identical to the ones used for isomenthone eq-ax A. The computation time heavily depends on the line density of the spectrum under study. For carvone, carvomenthénol, and menthone spectra, it took less than one hour to run the routine using a single core on an Intel quad-core i5 processor (2.3 GHz).

The computer program is still limited to molecular spectra that can be fit using a rigid rotor Hamiltonian, but the implementation of common rotational spectroscopy effects such as nuclear quadrupole coupling or internal rotation is in progress. It is always possible to extend the parameter space and include more than just the rotational constants into the fit. But with a growing number of included parameters, the set of starting samples increases exponentially if the same parameter space density is maintained. More lines would need to be included into the fit in order to get reliable results, as expected with an increasing number of assignment possibilities. Hence, the required computation time grows rapidly. To counteract the increasing computation time, the different fitting parameters can be classified according to their impact on the fit. As a consequence, the seed set would no longer be uniformly distributed along each parameter axis but denser along high impact parameters. Parameters with a very small effect on the fit, such as the  $A$ -rotational constant in  $a$ -type spectra, can be kept constant throughout the fit. This approach should be feasible for spectra including nuclear quadrupole coupling splitting or centrifugal distortion.

## 6.4 Conclusions

The microwave spectra of the structurally related monoterpenoids menthol, menthone, and isomenthone and an evaluation of their potential energy surfaces were presented. For menthol, a single conformation was observed under the conditions of the supersonic expansion. The

---

The supplementary information of Reference [240] provides the linelists with the corresponding assignments as well as the results of the automated fitting routine.

experimentally obtained rotational constants of the observed conformation agreed very well with those of the calculated lowest energy conformer.

In the broadband microwave spectrum of a mixture of the diastereomers menthone and isomenthone, three conformations of menthone and a single conformation of isomenthone were identified. Again, the comparison of the experimental rotational constants with the *ab initio* ones revealed a good match. The differences in the conformational landscape for menthone and isomenthone likely arise from the peculiar steric situation of the central cyclohexane ring, for which a chair configuration with sterically demanding substituents in the equatorial positions is preferred. Due to the arrangement of the stereogenic centers in isomenthone, one substituent, i.e., either the methyl or the isopropyl group, must be oriented axially, resulting in large shifts of the conformational landscape from menthone. Complications of assigning the dense microwave spectra manually led to a computer-aided assignment routine, which was capable of identifying and fitting all components in the menthone mixture with inputs from *ab initio* calculated rotational constants.



## Chapter 7

# Enantiomer differentiation by microwave three-wave mixing experiments

### 7.1 Introduction

Many molecules of biochemical relevance are chiral. The chemistry of life is built almost exclusively on left-handed amino acids and right-handed sugars, a phenomenon that is known as the 'homochirality of life'. Even though the physical properties of two enantiomers are almost identical, they might exhibit completely different biological effects, e.g. one may be beneficial to health while the opposite is toxic. In nature and as products of chemical syntheses, chiral molecules often exist in mixtures with other chiral molecules. The analysis of these complex mixtures to identify the molecular components, to determine which enantiomers are present, and to measure the enantiomeric excesses (ee) is still one of the challenging and very important tasks of analytical chemistry.

Established spectroscopic methods to identify enantiomers and determine the ee value rely on

---

This chapter is partly based on the following publications:

- V. A. Shubert, D. Schmitz, D. Patterson, J. M. Doyle and M. Schnell, *Identifying Enantiomers in Mixtures of Chiral Molecules with Broadband Microwave Spectroscopy*, Angew. Chem. Int. Ed. **52**, 1-5 (2013). (experimental: 40%, data analysis: 40%, writing up: 5%, D.P. 5%) [78]
- V. A. Shubert, D. Schmitz, and M. Schnell, *Enantiomer-sensitive spectroscopy and mixture analysis of chiral molecules containing two stereogenic centers – Microwave three-wave mixing of menthone*, J. Mol. Spec. **52**, 31-6 (2014). (key ideas: 20%, experimental: 50%, data analysis: 30%, writing up: 10%) [250]
- D. Schmitz, V. A. Shubert, D. Patterson, A. Krin, and M. Schnell, *Phase Dependence of Double-Resonance Experiments in Rotational Spectroscopy*, J. Phys. Chem. Lett. **6**, 1493-98 (2015) (key ideas: 20%; experimental: 40%, data analysis: 80%, writing up: D.S. 40%) [260]
- V. A. Shubert, D. Schmitz, C. Medcraft, A. Krin, D. Patterson, J. M. Doyle and M. Schnell, *Rotational spectroscopy and three-wave mixing of 4-carvomenthenol: A quickstart guide to measuring chirality in the microwave regime*, accepted at J. Chem. Phys. (experimental: 20%, data analysis: 10%; writing up: 5%)



the interaction of linearly or circularly polarized light with the target molecules. This interaction is relatively weak [261] and thus highly concentrated samples or intense light fields are required. These methods, such as circular dichroism, vibrational circular dichroism (VCD), and Raman optical activity spectroscopy, are commercially available and widely used. However, they are less useful for the analysis of molecular mixtures, in particular when more than one chiral species is present. Only one mixture analysis was reported so far, using Fourier transform VCD [262]. Recent developments in this area employ synchrotron radiation and femtosecond lasers to study femtosecond optical activity, photoionization with subsequent fragment detection in coincidence, and circular dichroism in the photoelectron angular distributions of chiral molecules [263–267].

In this chapter, the clear differentiation between enantiomers within a mixture of chiral molecules is demonstrated using broadband rotational spectroscopy. In addition, ee values of mixtures are measured and an outlook is given on how the absolute configuration of a chiral molecule can be determined. The experimental technique is based on a method, which was theoretically developed by Hirota [268] and experimentally demonstrated by Patterson et al. [269, 270]. The underlying physical mechanism arises from the Hamiltonian of an asymmetric top in a resonant electric field and is widely applicable to chiral molecules with nonzero dipole moment components  $\mu_a$ ,  $\mu_b$ ,  $\mu_c$ . In the framework of this thesis, the experimental method was adapted to a broadband excitation scheme, which allows the simultaneous measurement of different chiral components within a mixture.

## 7.2 Theoretical background

The differentiation between enantiomers becomes feasible by an excitation and detection scheme, which makes use of a closed cycle of transitions involving all three dipole moment components. The simplest case of a closed cycle includes three rotational states connected by three rotational transitions of *a*-type, *b*-type and *c*-type, which exclusively depend on  $\mu_a$ ,  $\mu_b$ , and  $\mu_c$ , respectively. Ignoring small differences due to the parity-violating potential arising from the weak interaction [271], the rotational constants and dipole moment component magnitudes ( $|\mu_a|$ ,  $|\mu_b|$ ,  $|\mu_c|$ ) are equal for enantiomeric pairs of any chiral molecule and thus give rise to identical rotational spectra. However, the scalar triple product of the permanent dipole moment components  $\mu_a \cdot (\mu_b \times \mu_c)$  flips sign between enantiomers since the dipole moments are mirrored. This fact is exploited to differentiate enantiomers in a polarization sensitive double-resonance experiment. Therein two transitions of a closed cycle are excited simultaneously or subsequently and the signal of the third transition is recorded, where the molecule itself is acting as a sum or difference frequency generator. The phase of the recorded signal changes by  $\pi$  radians between opposite enantiomers and allows for their differentiation. In the following, the Bloch equations describing these double-resonance experiments are introduced. Without loss of generality, the following theoretical description is restricted to one of the degenerate *M*-sublevels within the asymmetric-top energy levels to maintain a pure three-level quantum system. The density matrix formalism introduced in Section 2.4 for a two-level

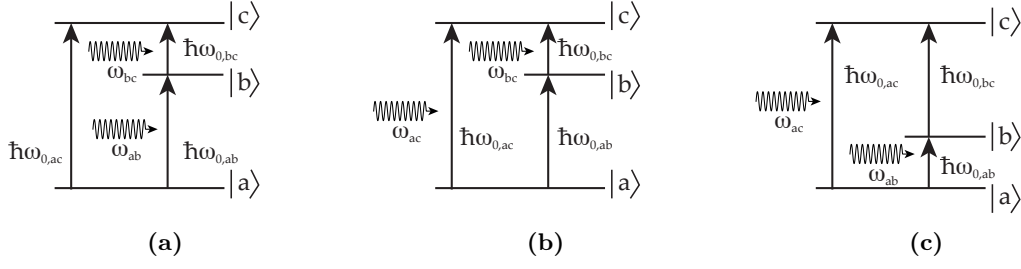


**Figure 7.1:** Schematics of energy level configurations for MW-RF double-resonance experiments: (a) progressive arrangement, (b) regressive arrangement with the RF transition  $\omega_{0,bc}$  connecting the upper two energy levels ( $\Lambda$ -type), and (c) regressive arrangement with the RF transition connecting the lower two energy levels ( $V$ -type). The resonance frequencies are  $\omega_{0,ab} = E_b - E_a/\hbar$ ,  $\omega_{0,bc} = E_c - E_b/\hbar$  and  $\omega_{0,ac} = E_c - E_a/\hbar$ , while  $\omega_{ab}$ ,  $\omega_{bc}$  and  $\omega_{ac}$  are the frequencies that are actually employed in the experiment.

system can easily be extended to a three-level system. Instead of a two-by-two density matrix for a two-level system, the density matrix for a three-level system has nine elements:

$$\hat{\rho} = \begin{pmatrix} \rho_{aa} & \rho_{ab} & \rho_{ac} \\ \rho_{ba} & \rho_{bb} & \rho_{bc} \\ \rho_{ca} & \rho_{cb} & \rho_{cc} \end{pmatrix} \quad (7.1)$$

The unperturbed Hamiltonian describing a three-level systems is given by:

$$\hat{\mathcal{H}}_0 = \begin{pmatrix} E_a & 0 & 0 \\ 0 & E_b & 0 \\ 0 & 0 & E_c \end{pmatrix} \quad (7.2)$$

with  $E_c > E_b > E_a$ . If all transitions of a three-level system are dipole allowed, three different combinations of driving two transitions are possible: the progressive regime ( $|a\rangle \rightarrow |b\rangle$  and  $|b\rangle \rightarrow |c\rangle$ ), Fig. 7.1a), the  $\Lambda$ -type regressive regime ( $|a\rangle \rightarrow |c\rangle$  and  $|b\rangle \rightarrow |c\rangle$ ), Fig. 7.1b) and the  $V$ -type regressive regime ( $|a\rangle \rightarrow |c\rangle$  and  $|a\rangle \rightarrow |b\rangle$ ), Fig. 7.1c). For the corresponding Hamiltonians including the interactions with the electromagnetic fields follows in the progressive regime  $\hat{\mathcal{H}}_{\text{pro}}$ :

$$\hat{\mathcal{H}}_{\text{pro}} = \begin{pmatrix} E_a & -\frac{1}{2}\mu_{ab}\mathcal{E}_{ab}(e^{i\omega_{ab}t} + e^{-i\omega_{ab}t}) & 0 \\ -\frac{1}{2}\mu_{ba}\mathcal{E}_{ba}(e^{i\omega_{ab}t} + e^{-i\omega_{ab}t}) & E_b & -\frac{1}{2}\mu_{bc}\mathcal{E}_{bc}(e^{i\omega_{bc}t} + e^{-i\omega_{bc}t}) \\ 0 & -\frac{1}{2}\mu_{cb}\mathcal{E}_{cb}(e^{i\omega_{bc}t} + e^{-i\omega_{bc}t}) & E_c \end{pmatrix} \quad (7.3)$$

in the  $\Lambda$ -type regressive regime  $\hat{\mathcal{H}}_{\text{reg},\Lambda}$ :

$$\hat{\mathcal{H}}_{\text{reg},\Lambda} = \begin{pmatrix} E_a & 0 & -\frac{1}{2}\mu_{ac}\mathcal{E}_{ac}(e^{i\omega_{ac}t} + e^{-i\omega_{ac}t}) \\ 0 & E_b & -\frac{1}{2}\mu_{bc}\mathcal{E}_{bc}(e^{i\omega_{bc}t} + e^{-i\omega_{bc}t}) \\ -\frac{1}{2}\mu_{ca}\mathcal{E}_{ca}(e^{i\omega_{ac}t} + e^{-i\omega_{ac}t}) & -\frac{1}{2}\mu_{cb}\mathcal{E}_{cb}(e^{i\omega_{bc}t} + e^{-i\omega_{bc}t}) & E_c \end{pmatrix} \quad (7.4)$$

and in the V-type regressive regime  $\hat{\mathcal{H}}_{\text{reg},V}$ :

$$\hat{\mathcal{H}}_{\text{reg},V} = \begin{pmatrix} E_a & -\frac{1}{2}\mu_{ab}\mathcal{E}_{ab}(e^{i\omega_{ab}t} + e^{-i\omega_{ab}t}) & -\frac{1}{2}\mu_{ac}\mathcal{E}_{ac}(e^{i\omega_{ac}t} + e^{-i\omega_{ac}t}) \\ -\frac{1}{2}\mu_{ba}\mathcal{E}_{ba}(e^{i\omega_{ab}t} + e^{-i\omega_{ab}t}) & E_b & 0 \\ -\frac{1}{2}\mu_{ca}\mathcal{E}_{ca}(e^{i\omega_{ac}t} + e^{-i\omega_{ac}t}) & 0 & E_c \end{pmatrix} \quad (7.5)$$

A few approximations are applied to reduce the complexity. First of all the assumption is made that the interaction volume is small compared to the wavelength by neglecting the dependence of the electromagnetic field on the wave vector  $\mathbf{k}$ . Also the initial phases of both incoming waves are set to zero. Furthermore, the assumption is made that each of the incoming fields only couples to one of the transition dipole moment components  $\mu_{ab}$ ,  $\mu_{bc}$  or  $\mu_{ac}$ . This assumption is valid for this work, because the transition frequencies are well separated, and the polarization directions of the two incoming waves are perpendicular to each other in the experimental setup (compare Fig. 7.2). The transition dipole moment components are complex quantities with  $\mu_{ij} = \mu_{ji}^*$  (with  $i \neq j = a, b, c$ ). For an  $a$ -type rotational transition between the initial rotational state  $|i\rangle$  and the final rotational state  $|j\rangle$  the transition dipole moment component  $\mu_{ij}$  can be written [41, Chap. 4]:

$$\mu_{ij,g} = \mu_a \langle i | \cos(\mathbf{a}, \mathbf{G}) | j \rangle = \mu_a \int \psi_i \cos(\mathbf{a}, \mathbf{G}) \psi_j^* d\tau \quad (7.6)$$

where  $\cos(\mathbf{a}, \mathbf{G})$  describes the direction cosine between the molecular  $a$ -axis and the space-fixed quantization axis  $G = X, Y, Z$  in the laboratory frame. The transition dipole moment components for  $b$ - or  $c$ -type transitions are similar, but with the direction cosine between the  $b$ - or  $c$ -axis and the space-fixed quantization axis. The selection rules for the different types of transitions are summarized in Table 2.2. They follow directly from the evaluation of the integral in Equation 7.6 or by symmetry considerations of the asymmetric-top wavefunctions.

The time dependence of the density matrix elements can be obtained by solving the Liouville equation 2.81:

$$i\hbar \frac{\partial \hat{\rho}(t)}{\partial t} = [\hat{\mathcal{H}}(t), \hat{\rho}(t)] \quad (7.7)$$

The resulting set of ordinary differential equations (ODE) for the three different regimes are compiled in Appendix A. After applying the rotating wave approximation and transformation to a rotating frame (described in Sec. 2.4 for a two-level system), the three-level Bloch equations are analytically solvable as shown in Reference [57]. In the present work, the full Bloch equations as given in Appendix A were solved numerically using the ODE solver 'zvode' of the Python package SciPy [272]. This solver enabled the use of not only single frequency

sinusoidal waveforms but also arbitrary waveforms as driving pulses, i.e. chirps, superpositions of sinusoidal pulses, or completely arbitrary driving pulses.

The expectation value of the measured polarization is identical to the one given in Equation 2.96:

$$\langle \hat{P} \rangle = N \cdot \text{Tr}(\hat{\rho} \hat{\mu}) \quad (7.8)$$

with:

$$\hat{\mu} = - \begin{pmatrix} 0 & \mu_{ab} & \mu_{ac} \\ \mu_{ba} & 0 & \mu_{bc} \\ \mu_{ca} & \mu_{cb} & 0 \end{pmatrix} \quad (7.9)$$

Prior to the three-wave mixing experiments, double-resonance experiments were performed to optimize the experimental conditions. The double-resonance experiments revealed an indirect observation of the Autler-Townes splitting mapped onto the phase of the recorded signal. The results of both types of experiments are fully characterized by the Bloch equation formalism, but the physical meaning is best described within the dressed-state picture for the double-resonance experiments [273]. After the introduction of the changes made to the experiment in the next section, the double-resonance experiments are presented and discussed in Section 7.4, followed by the results of the three-wave mixing experiments (enantiomer differentiation in Sec. 7.5 and ee determination in Sec. 7.6).

### 7.3 Experimental details

To enable double-resonance and three-wave mixing experiments, a few minor modifications are applied to the COMPACT spectrometer described in Chapter 3. A set of stainless steel electrodes is attached to the microwave horns isolated by a teflon spacer. As indicated in Figure 7.2, a radio frequency (RF) field is coupled to one of the electrodes and the second electrode is set to ground. The RF field and the microwave (MW) signal are generated by different channels of the same arbitrary waveform generator to ensure optimal phase stability. The RF field is then amplified by a 100 W power amplifier with a bandwidth of 30 – 550 MHz (KU PA BB 003055-100 A, Kuhne electronics) and coupled to the electrodes by a BNC feedthrough. Two valves separated by 3.5 cm (nozzle orifice separation) with different enantiomers or mixtures in their respective sample reservoirs can be used. These valves are operated such that only the pulse from one valve interacts with the MW and RF excitation pulses within an experimental cycle. A digital delay generator (Stanford Research, model DG645) is used to change which valve pulse interacted with the radiation.

Because the three-wave mixing technique makes use of the geometrical orientation of the three dipole moment components within a chiral molecule, the orthogonal orientation of the polarization of the excitation fields is important. The laboratory frame along the different fields are defined as indicated in Figure 7.2. The polarization direction of the microwave excitation pulse (called the *drive* pulse in the following) defines the *Z*-axis of the laboratory frame. The RF pulse (the so called *twist* pulse) is polarized orthogonally to the *drive* pulse

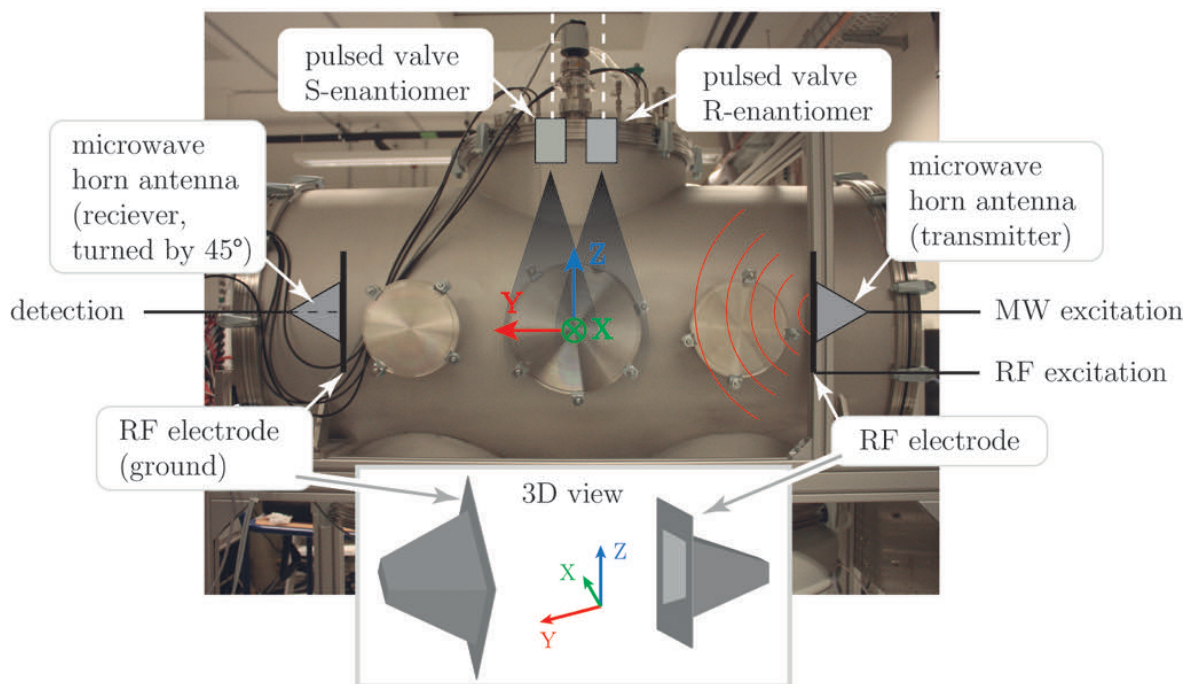


**Figure 7.2:** Scheme of the modified COMPACT spectrometer. Only the changes to the COMPACT spectrometer introduced in Chapter 3 (Fig. 3.1) are indicated. For introducing RF radiation, two electrodes are integrated into the setup. The polarization directions of the MW excitation ( $Z$ -direction) and the RF pump pulse ( $Y$ -direction) are perpendicular with respect to each other. The receiving horn on the left is turned by  $45^\circ$  to allow for the observation of the traditional FID signal (along the  $Z$ -direction) and the three-wave mixing signal (along the  $X$ -direction).

along the laboratory  $Y$ -axis. In a three-wave mixing experiment, the signal evolving from the third transition of the closed cycle (the so called *listen* transition) is then polarized mutually orthogonal to the *drive* and the *twist* pulse. For the three-wave mixing experiments, the receiving horn is turned by  $45^\circ$  to allow the observation of the traditional FID signal, which is polarized in  $Z$ -direction, as well as the three-wave mixing signal (polarized in  $X$ -direction). The receiving horn is not turned for the double-resonance experiments, performed in preparation of the three-wave mixing experiments and described in the next section.

## 7.4 Double-resonance experiments

Double-resonance experiments are well established in the microwave region of the electromagnetic spectrum and were mainly used to map the coherence transfer within the rotational energy level structure [55–57, 77]. The information about the coherence transfer are exploited to ascertain the energy level structure and hence guide the assignment of dense rotational spectra [63]. Furthermore, double-resonance experiments are employed to extend the detection bandwidth of a spectrometer. The effect of driving a transition that is otherwise invisible to the spectrometer (due to a limited detection bandwidth) can be observed on con-

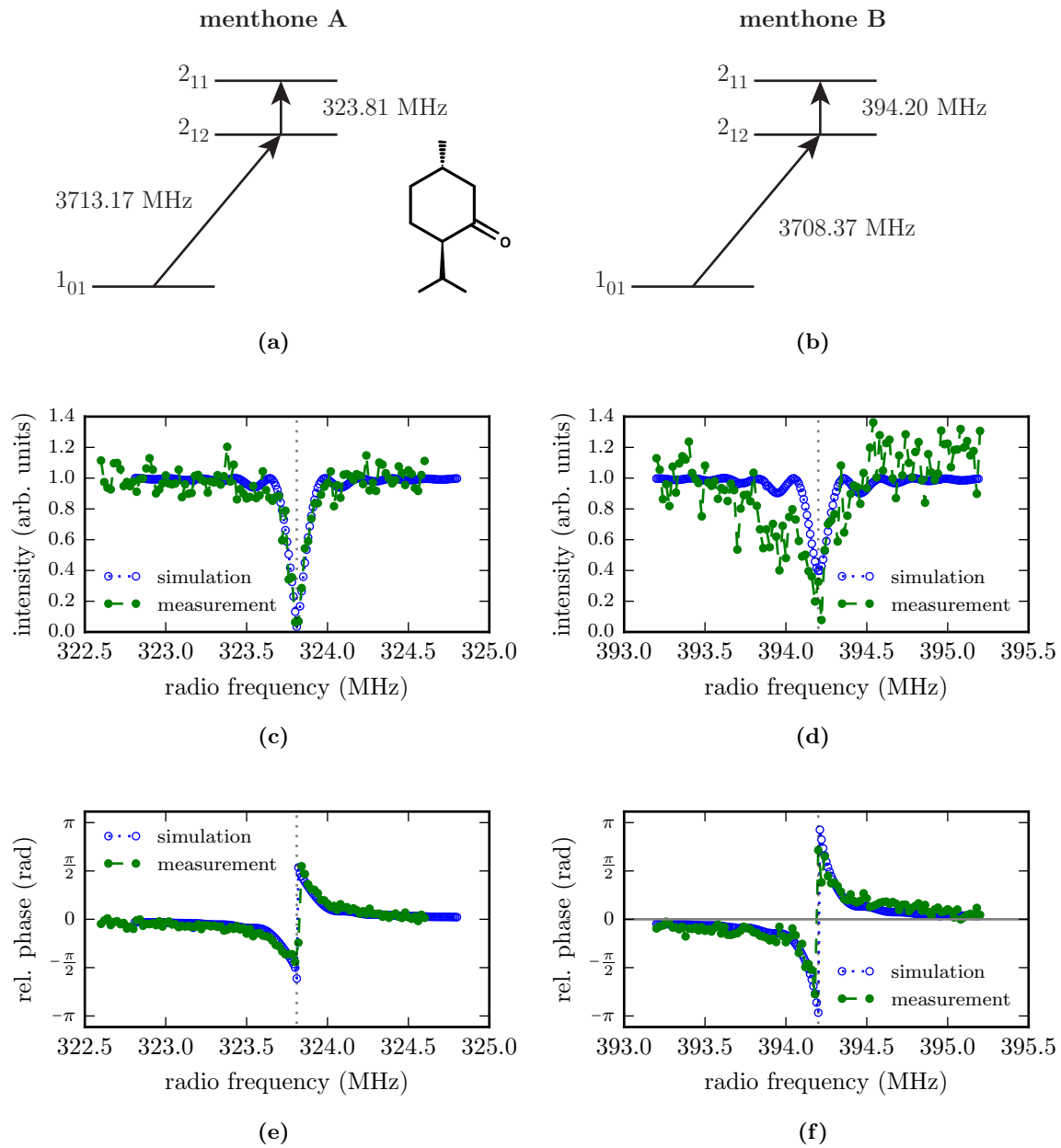


**Figure 7.3:** MW-RF double-resonance experiments for menthone A and menthone B (left and right columns). The simulations are based on the three-level optical Bloch equations. First row: Energy levels involved in the double-resonance experiments for (a) conformer A and (b) conformer B. Second row: Illustration of the amplitude dependences observed for the FID at the respective MW signal transition frequencies, that is, the  $1_{01} \rightarrow 2_{12}$  b-type transitions of the two menthone conformers, as a function of the RF pump frequency. The RF transition  $2_{12} \rightarrow 2_{11}$  is predicted at 323.81 MHz for conformer A (c) and at 394.20 MHz for conformer B (d) from the experimentally determined rotational constants. The amplitudes are normalized. Third row: Phase dependence of the FID at MW signal transition frequencies on the RF pump frequencies for (e) conformer A and (f) conformer B, illustrating the striking change at RF resonance. Both the amplitude and the phase dependence are extracted from the same experimental data.



nected transitions within the bandwidth of the spectrometer. This scheme is employed in the double-resonance experiments herein. The RF excitation pulse and its molecular response cannot be detected directly by the COMPACT spectrometer, but the effect on the amplitude and the phase of a connected microwave transition is indeed observable.

As mentioned before, MW-RF double-resonance experiments are carried out to determine the transition frequency in the RF regime and to adjust the pulse length for optimal coherence transfer. In the following, the double-resonance experiments are explained using the example of a progressive level scheme (compare Fig. 7.1a). For the regressive level schemes, the labels of the different energy levels need to be interchanged. A coherent superposition is created using a MW chirp coupling the states  $|a\rangle$  and  $|b\rangle$ . This superposition is then perturbed by a RF pulse transferring  $ab$ -coherence to  $ac$ -coherence. The coherence transfer is maximized in a two step approach: firstly a RF pulse slightly shorter than  $\pi$ -condition is scanned through resonance. Exactly at resonance best coherence transfer is achieved, which goes along with a maximum depletion of the  $ab$ -coherence. Secondly the RF-pulse length is optimized to hit exact  $\pi$ -condition.

Figure 7.3 and Figure 7.4 show the results for MW-RF double-resonance measurements for the molecules menthone (for the two different conformers menthone A and B) and isomenthone eq-ax (two different cycles), respectively. The same sample and experimental conditions were used as described in Section 6.2. All measurements reveal a strong depletion of the driving microwave transition at the RF transition resonance. Additionally, the relative phase of the microwave signal as observed in the FID changes rapidly when the RF pulse is tuned through resonance. The intensity decrease and the abrupt phase change of the microwave signal at resonance can be simulated using the three-level optical Bloch equations introduced in the previous section. For the simulations, the respective set of optical Bloch equations is employed in a two pulse scheme. The first pulse is a short and intense  $\frac{\pi}{2}$ -pulse at the resonance frequency of the MW transition ( $|a\rangle \rightarrow |b\rangle$  in the case of a progressive level scheme) to create maximum  $ab$ -coherence. This condition is in contrast to the experiments, where a chirp is used to excite both the  $|a\rangle \rightarrow |b\rangle$  and the  $|a\rangle \rightarrow |c\rangle$  transition. To consider only the excitation of the  $|a\rangle \rightarrow |b\rangle$  transition in the simulations is a valid approach to model the experiments in the case of menthone or isomenthone, because the  $|a\rangle \rightarrow |c\rangle$  transition is connected to the weaker dipole moment component ( $c$ -type transition for menthone A and B and  $a$ -type transition for isomenthone eq-ax). The second pulse used in the simulations is a  $5\mu\text{s}$  RF pulse with the corresponding detuning from resonance, which is in agreement with the experiment. In the simulations, the Rabi frequency of the RF transition  $\Omega_{bc}$  is adjusted to match the experimental results, i.e. the intensity and the phase behavior for different detunings. For the initial populations of the states, a Boltzmann distribution is assumed and the rotational energies computed by the SPCAT program [146] are employed.

Various methods can be used to retrieve the amplitude and the phase of a single frequency component within the FID. The Fast Fourier transform (FFT) algorithm provides the amplitudes of rotational spectra and also the phase information is encoded in the complex valued FFT. However, the manual evaluation of the Fourier series gave a much higher accuracy and

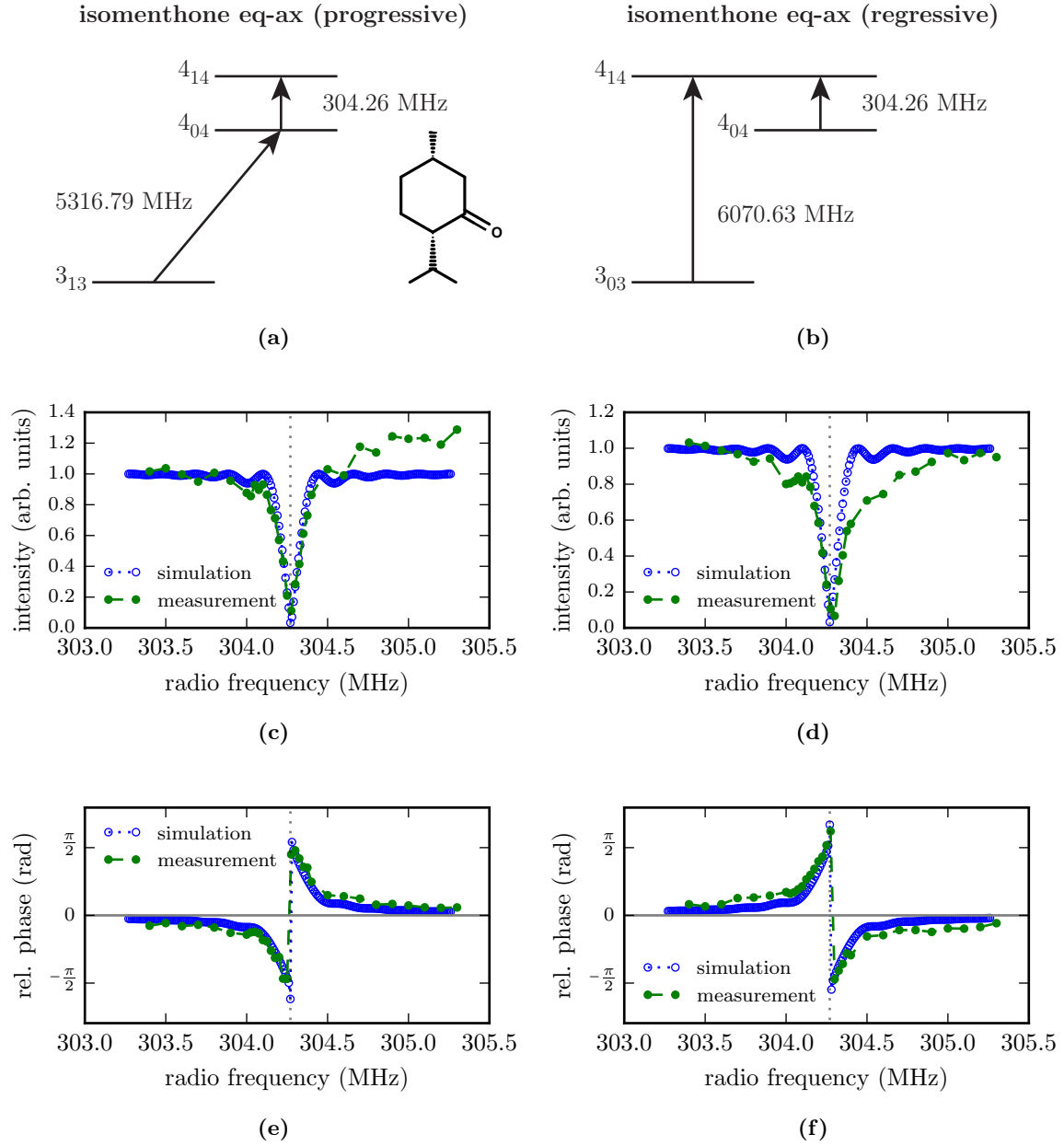


**Figure 7.4:** MW-RF double-resonance experiments for two different energy level combinations (left and right column) of isomenthone eq-ax. The simulations are based on the three-level optical Bloch equations. First row: energy level schemes visualizing the connectivity of energy levels and the two double-resonance schemes, progressive (a) and regressive ( $\Lambda$ -type) (b). Second row: Illustration of the amplitude dependence observed for the FID at the respective MW signal transition frequency, that is, the  $3_{13} \rightarrow 4_{04}$  b-type transition at 5316.79 MHz (c) and the  $3_{03} \rightarrow 4_{14}$  b-type transition at 6070.63 MHz (d), as a function of the RF pump frequency. The RF transition  $4_{04} \rightarrow 4_{14}$  connects the two b-type transitions. Third row: Phase dependence of the FID at MW signal transition frequencies on the RF pump frequency, illustrating the strong change close to RF resonance that is opposite for the two different energy level combinations (progressive (e) and regressive (f)).



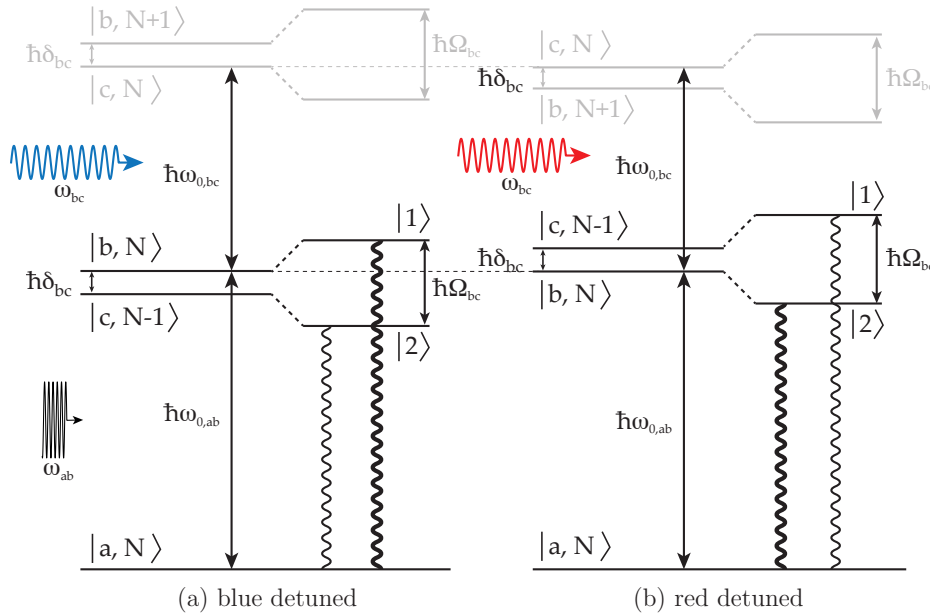


**Figure 7.5:** Dressed-state formalism describing the interaction of the RF pump field  $\omega_{bc}$  with the molecular energy levels  $|b\rangle$  and  $|c\rangle$  in a progressive scheme, for (a) blue and (b) red detuning of the RF field with respect to molecular resonance. The unperturbed states  $|b, N\rangle$  and  $|c, N-1\rangle$ , dressed with  $N$  and  $N-1$  photons, respectively (given on the left-hand side), are transformed into two dressed states,  $|1\rangle$  and  $|2\rangle$ , due to the interaction with the RF field and with each other (given on the right-hand side). For blue detuning (a), the unperturbed  $|b, N\rangle$  state is higher in energy than the  $|c, N-1\rangle$ . This situation is reversed for red detuning (b).

reliability for the amplitude and phase retrieval than the FFT algorithm itself. The mathematical description is summarized in Appendix B.

While the intensity depletion at resonance can be explained straightforwardly with maximum coherence transfer, the explanation for the sudden phase change at resonance is more complex. However, the dressed-state picture provides an accurate physical model, the AC Stark effect, for this typical phase behavior [273]. The AC Stark effect describes the interaction of a polar molecule with a time-dependent, external electromagnetic field. Note that the energy level arrangements involved in the MW-RF double-resonance experiments perfectly match the conditions for the Autler-Townes effect [273, 274]. The  $ab$ -coherence prepared by the MW chirp oscillates with the resonance frequency  $\omega_{0,ab}$  in the field free case. However, the RF field splits and shifts the energy levels  $|b\rangle$  and  $|c\rangle$  depending on the strength of the interaction (Rabi frequency  $\Omega_{bc}$ ) and the detuning from resonance. The sign of the detuning determines the energy ordering of the respective energy levels. Detailed explanations are given in the next paragraph together with a schematic to illustrate the energy level arrangement (Fig. 7.5).

Schematics for the red- and blue-detuned cases within the dressed-state picture are depicted in Figure 7.5 for the progressive energy level scheme. The states  $|b\rangle$  and  $|c\rangle$  are dressed with photons of the RF field of frequency  $\omega_{bc}$ . The unperturbed  $|b\rangle$  state dressed with  $N$  photons is described as the  $|b, N\rangle$  state. It interacts with the unperturbed  $|c, N-1\rangle$  state, i.e.,  $|c\rangle$  dressed

with  $N - 1$  photons. They are virtually separated by the detuning  $\delta_{bc}$  in the unperturbed case (left hand side of Fig. 7.5a and b). For blue detuning 7.5a, the  $|b, N\rangle$  state is higher in energy than the  $|c, N - 1\rangle$  state. As a consequence, the  $|b, N\rangle$  state will be shifted towards higher energies for the dressed state  $|1\rangle$  (right-hand side of Fig. 7.5a), while the  $|c, N - 1\rangle$  state will be shifted towards the lower energy state  $|2\rangle$ . The situation is reversed for the red-detuned case (Fig. 7.5b).

When probing these shifts by a transition to the third level  $|a\rangle$  with  $\hbar\omega_{0,ab}$ , which is far detuned from the dressing RF field, the  $ab$ -transition splits up into two components:  $|a, N\rangle \leftrightarrow |1\rangle$  with frequency  $\omega_{0,ab} + (\Omega_{bc} - \delta_{bc})/2$  and  $|a, N\rangle \leftrightarrow |2\rangle$  with frequency  $\omega_{0,ab} - (\Omega_{bc} + \delta_{bc})/2$ . Both transitions are dipole allowed because the mixed states  $|1\rangle$  and  $|2\rangle$  are both contaminated by the undressed state  $|b, N\rangle$ . This characteristic splitting was first observed by Autler and Townes in 1955 [274]. The difference between the two transitions corresponds to the generalized Rabi frequency  $\Omega_{bc} = \sqrt{\Omega'_{bc}{}^2 + \delta_{bc}^2}$ , where  $\Omega'_{bc}$  is the Rabi frequency  $\Omega'_{bc} = \mu_{bc}\mathcal{F}_{bc}/\hbar$  introduced in Section 2.4. As mentioned above, in the measurements and the simulations presented herein the probe  $ab$ -coherence is created prior to the perturbation due to the RF pulse. Employing this pulse scheme, the intensities of the two different frequency components of the  $ab$ -coherence (the Autler-Townes doublet) are simulated for the time the RF pulse is applied. Unfortunately, the experimental setup does not permit the direct observation of the Autler-Townes splitting because the CP-FTMW spectrometer is constructed to record the FID of weak molecular signals. The sensitive electronic components would be destroyed or at least saturated by any attempt to observe the molecular response during the RF pulse. Nonetheless, the simulations reveal an intensity ratio of:

$$\frac{I_{c,N-1}}{I_{b,N}} = \tan^2 \left[ \frac{1}{2} \cdot \arctan \left( -\frac{\Omega'_{bc}}{\delta_{bc}} \right) \right] \quad (7.10)$$

for the Autler-Townes doublet, where the transition between the dressed state evolving from the unperturbed state  $|b, N\rangle$  (dressed state  $|1\rangle$  or  $|2\rangle$  for blue or red detuned light, respectively) and  $|a, N\rangle$  is always stronger in intensity as indicated by the thickness of the wavy lines in Figure 7.5. The same intensity ratio can be derived using the dressed-state approach as demonstrated in Reference [273] for the reversed pulse scheme (lower transition is pumped and the upper transition is probed). The simulated intensities of the Autler-Townes splitting are visualized in a two-dimensional plot (Fig. 7.6a) for various detunings. To resolve the doublet structure, the simulations are performed with a  $50 \mu\text{s}$  long RF pulse. These simulations reveal an avoided crossing at zero detuning. This effect was experimentally observed before in a similar experiment on quantum dots [275].

Using the dressed-state approach, the phase shift of the  $ab$ -coherence for the different detunings is easily understood. Without any perturbation due to the RF pulse ( $\Omega'_{bc} = 0$ ), the relative measured phase is zero, but by disturbing the energy level scheme with the RF pulse the phase of the  $ab$ -coherence is shifted. Hence, depending on the detuning, the amplitudes and frequencies of the Autler-Townes doublet are mapped onto the relative phase of the  $ab$ -coherence, measured in a field free environment. In the next section the double-resonance

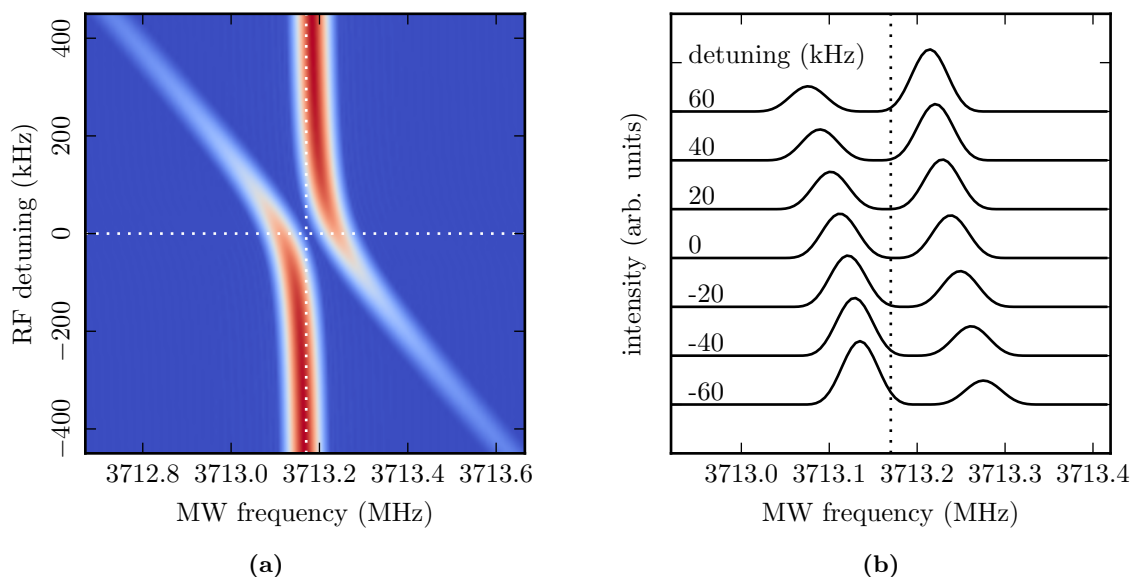


**Figure 7.6:** Illustration of the Autler-Townes doublet for different detunings. (a) Two-dimensional plot with the MW frequencies on the x-axis and the RF detuning on the y-axis. (b) Spectra of different detunings close to  $\delta_{bc} = 0$ . Note the intensities of the doublet are equal for zero detuning.

experiments are extended to differentiate between enantiomers of chiral molecules.

## 7.5 Enantiomer differentiation

As indicated in the previous sections the differentiation of enantiomers becomes feasible by a polarization sensitive double-resonance experiment. It exploits the fact that the scalar triple product of the permanent dipole moment components switches sign between enantiomers. The experimental procedure is very similar to the double-resonance experiments described in the previous section. In contrast to the double-resonance experiments not only a three-level scheme but a closed cycle involving all three types of dipole allowed transitions (*a*-type, *b*-type, *c*-type) is required. This prerequisite implies that all permanent dipole moment components ( $\mu_a$ ,  $\mu_b$ ,  $\mu_c$ ) need to be nonzero as already mentioned in the introduction. The technique itself is based on efficient coherence transfer, while the orthogonal polarization of the excitation pulses enables the mapping of the molecule-fixed axes onto the laboratory-fixed axes. The following description is based on Reference [276] and is worked out for clarity only for a progressive level scheme illustrated in Figure 7.7b. However, the theory itself is valid for any three-level system (i.e. regressive V- and  $\Lambda$ -type), but the labeling of the various levels is different then.

The experimental pulse scheme is depicted in Figure 7.7a together with the evolution of the *ab*-, *bc*- and *ac*-coherences. Firstly the *ab*-transition (*drive* transition) is excited resonantly employing a MW pulse polarized along the *Z*-direction converting population difference into

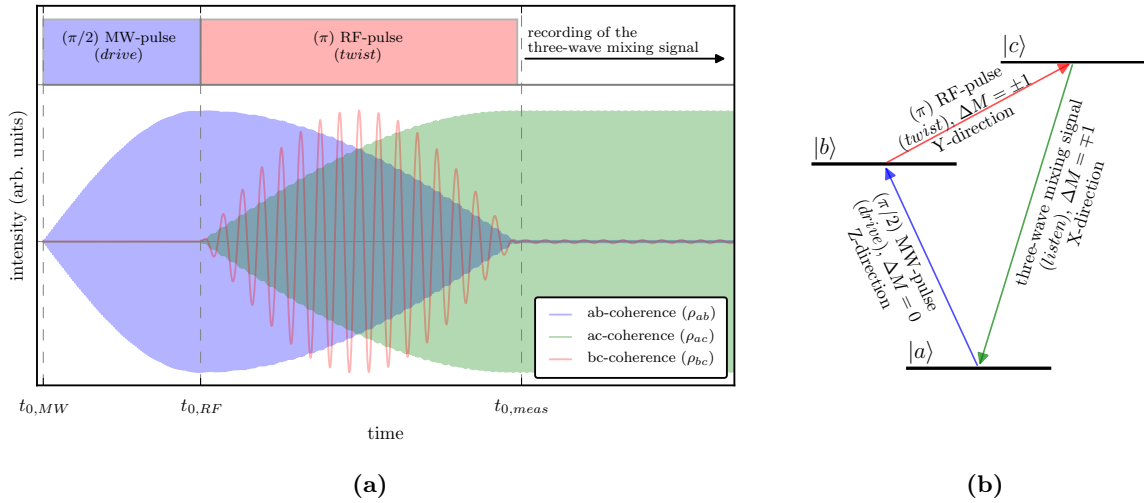


**Figure 7.7:** (a) Evolution of the  $ab$ -,  $bc$ - and  $ac$ -coherences in a prototype three-wave mixing experiment employing a drive and a twist pulse. Firstly, the drive pulse creates maximum coherence between the states  $|a\rangle$  and  $|b\rangle$ , when the pulse matches  $\frac{\pi}{2}$ -conditions. The second pulse is resonant to the  $bc$ -transition and transfers  $ab$ -coherence to  $ac$ -coherence. This transfer is maximized, when the pulse matches  $\pi$ -conditions. (b) Scheme of the energy levels and transitions involved in the three-wave mixing experiment. The selection rules for the  $M$  quantum number are also indicated.

coherence. Secondly, by applying the RF-pulse polarized along the  $Y$ -direction and exciting the  $bc$ -transition (*twist* transition),  $ab$ -coherence is transferred to  $ac$ -coherence. Finally, the polarization induced by the decaying  $ac$ -coherence is collected along the  $X$ -direction with the turned receiving horn antenna.

Analytic solutions of the three-level optical Bloch equations [276] as well as numerical calculations performed herein reveal that the *listen* signal is most intense by applying  $\frac{\pi}{2}$ - and  $\pi$ -conditions for the *drive* and the *twist* pulse, respectively. Due to the  $M$ -degeneracy of the rotational energy levels and the  $M$ -dependence of the transition dipole moment in Equation 7.6 only approximate  $\frac{\pi}{2}$ - and  $\pi$ -conditions are met for rotational transitions of a molecule. Of note is that the MW-pulse polarization defines the laboratory-fixed quantization. Consequently, the selection rule for the  $M$  quantum number is  $\Delta M = 0$  for the *drive* transition, because the MW-pulse is polarized parallel to the quantization axis. For the *twist* transition the selection rule  $\Delta M = \pm 1$  follows, because the *twist* pulse is polarized perpendicularly to the quantization axis [115]. Hence the *drive* and the *twist* pulse define the orientation of the coordinate system. With a transition cycle involving all three types of transitions, the polarization of the *listen* transition is mutually orthogonal to both *drive* and *twist* pulse. As mentioned before this coherence transfer scheme only works for closed cycles, which implies a selection rule  $\Delta M = \mp 1$  for the *listen* transition.

The coherence transfer scheme explained above is not limited to chiral molecules, but works for all molecules with nonzero dipole moment components  $\mu_a$ ,  $\mu_b$ ,  $\mu_c$ . However, by applying

the *drive* and the *twist* pulse polarized perpendicularly to each other and addressing different dipole moment components, the molecule-fixed coordinate system is projected onto the laboratory-fixed coordinate system. Hence, the sign of the scalar triple product  $\boldsymbol{\mu}_a \cdot (\boldsymbol{\mu}_b \times \boldsymbol{\mu}_c)$  is mapped onto the phase of the *listen* transition  $\varphi_{\text{listen}}$  in the following manner [276]:

$$\varphi_{\text{listen}, t_0} = \varphi_{\text{drive}, t_0} + \varphi_{\text{twist}, t_0} + \frac{\pi}{2} \cdot \frac{\boldsymbol{\mu}_a \cdot (\boldsymbol{\mu}_b \times \boldsymbol{\mu}_c)}{|\boldsymbol{\mu}_a| \cdot |\boldsymbol{\mu}_b| \cdot |\boldsymbol{\mu}_c|} \quad (7.11)$$

where  $\varphi_{\text{drive}, t_0}$  and  $\varphi_{\text{twist}, t_0}$  are the phases of the *drive* and *twist* excitation pulses at a specific time  $t_0$ , respectively. In consequence, the phase difference of  $\pi$  radians enables the definite differentiation between the two enantiomers of a chiral molecule. The sensitivity of the *listen* transition to the phases of the excitation pulses is used as an experimental control later in this chapter.

According to the selection rules of the quantum number  $J$  a closed cycle of transitions must include  $Q$ -,  $P$ - and  $R$ -type transitions. Possible cycles are chosen such that all three transition dipole moment components are maximized and the rotational energy levels involved are sufficiently populated for a given rotational temperature. All experiments presented herein were performed on enantiopure carvone (Sigma Aldrich, (R)-carvone (98 %) or (S)-carvone (96 %), IUPAC name: 2-Methyl-5-(1-methylethenyl)-2-cyclohexenone). The samples were used without further purification and heated to 120 °C. While R-carvone smells like spearmint, S-carvone smells like caraway, nicely demonstrating the different biological functionality of the enantiomers of chiral molecules. Under the cold conditions of a molecular jet, carvone exhibits three conformers, which are referred to as EQ1, EQ2 and EQ3, following the nomenclature of Moreno et al. [227]. The two lowest energy conformers EQ2 and EQ1 were used for the following three-wave mixing experiments and their structures are depicted in Figure 7.8a and 7.8b. The experimentally determined rotational constants of conformer EQ2 and EQ1 are  $A = 2237.20549(43)$  MHz,  $B = 656.278398(261)$  MHz,  $C = 579.641099(193)$  MHz and  $A = 2256.91206(88)$  MHz,  $B = 672.906930(241)$  MHz,  $C = 554.504807(172)$  MHz, respectively [227]. The ordering of the calculated permanent dipole moment components  $\mu_b > \mu_a > \mu_c$  is the same for both conformations as well as the sign of the scalar triple product  $\boldsymbol{\mu}_a \cdot (\boldsymbol{\mu}_b \times \boldsymbol{\mu}_c)$  for the corresponding enantiomer (+1 for R-carvone and -1 for S-carvone). Also both conformations have comparable magnitudes of the permanent dipole moment components with  $\mu_a \approx 2$  D,  $\mu_b \approx 3$  D, and  $\mu_c \approx 0.7$  D.

Usually the magnitudes of the permanent dipole moments  $\mu_a$ ,  $\mu_b$ ,  $\mu_c$  and hence the transition dipole moments of the rotational transitions included into a cycle differ. Various cycles for a given molecule are ranked based on the product of the intensities of the three individual transitions. Furthermore a transition along the smallest dipole moment component within the MW bandwidth is used for the *drive* excitation, because the MW amplifier delivers enough power for a short  $\frac{\pi}{2}$ -pulse even for weak transitions. For a strong three-wave mixing signal it is beneficial to choose the *listen* transition to be dependent on the largest dipole moment component. In consequence the RF-pulse excites the *twist* transition in the experimental setup. Apparently the bandwidth of the MW excitation and RF excitation needs to cover

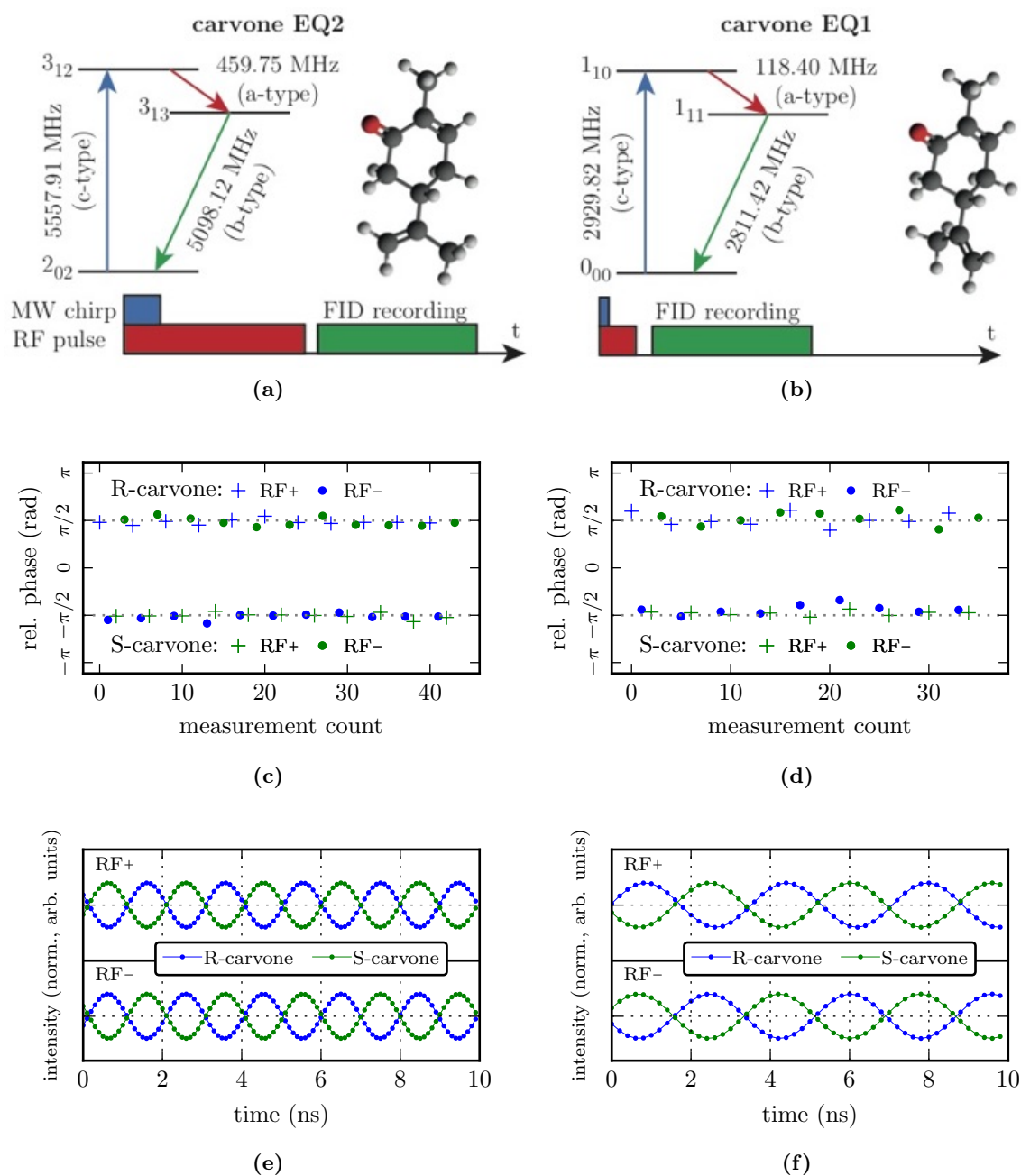


**Figure 7.8:** Results of three-wave mixing experiments performed on two different conformers of carvone. The left column shows the results for conformer EQ2 and the right column the results for conformer EQ1. First row: Energy levels and transitions involved in the three-wave mixing experiments for (a) conformer EQ2 and (b) conformer EQ1. The molecular structures were reproduced from Moreno et al. [227]. For both conformations a c-type transition and a b-type transition are used for the drive and twist excitation, respectively. In the second row the relative phases of the listen signal are plotted for experiments on the two different enantiomers and employing two different phases for the RF-excitation pulse (phase difference between RF+ and RF- is  $\pi$  radians). The results in (c) and (d) exhibit a stable phase difference of  $\pi$  radians between measurements of different enantiomers and between measurement using different RF-excitation phase on the same enantiomer. The plots (e) and (f) show a 10 ns portion of the FID for measurements on both enantiomers. The FID is filtered at the corresponding listen frequency (5098.12 MHz for EQ2 and 2811.42 MHz for EQ1). A phase difference of  $\pi$  radians is again apparent.



the frequencies of the *drive* and *twist* excitation pulse, respectively. Note, that the *drive* transition might not even be visible in a normal CP-FTMW experiment.

For the two conformers of carvone EQ2 and EQ1, potential three-wave mixing cycles were evaluated and the most promising cycle for each conformer was optimized for maximum coherence transfer. For EQ2 a cycle was used that involves the rotational states  $2_{02}$ ,  $3_{12}$  and  $3_{13}$  and the corresponding transitions  $2_{02} \rightarrow 3_{12}$  at 5557.91 MHz (*drive*, *c*-type),  $3_{12} \rightarrow 3_{13}$  at 495.75 MHz (*twist*, *a*-type) and  $2_{02} \rightarrow 3_{13}$  at 5098.12 MHz (*listen*, *b*-type). The *drive* transition was excited with a microwave chirp spanning the frequency range from 5.52 GHz to 5.58 GHz in 1  $\mu$ s. The chirp overlaps temporally with a single frequency *twist* pulse at 495.75 MHz and a total length of 5  $\mu$ s. The cycle for conformer EQ1 includes the transitions  $0_{00} \rightarrow 1_{10}$  at 2929.82 MHz (*drive*, *c*-type),  $1_{10} \rightarrow 1_{11}$  at 118.40 MHz (*twist*, *a*-type) and  $0_{00} \rightarrow 1_{11}$  at 2811.42 MHz (*listen*, *b*-type). Here, the microwave excitation chirp is just 250 ns long and spans 100 MHz at a center frequency of 2.95 GHz. The *twist* RF pulse is fixed at the frequency of the molecular resonance (118.40 MHz) with a length of 500 ns. Both cycles and the pulse sequence are depicted in Figure 7.8a and 7.8b. As mentioned earlier the initial phase of the RF excitation pulse ( $\varphi_{\text{twist}}$ ) is exploited as a control that the *listen* signal purely originates from the three-wave mixing excitation and not from any direct excitation. Hence, the experiments were carried out with an initial phase of  $\varphi_{\text{twist}} = \frac{\pi}{2}$  labeled as *RF+* and  $\varphi_{\text{twist}} = -\frac{\pi}{2}$  labeled as *RF-*.

Figure 7.8c and 7.8d present the measured phase of the *listen* transition of conformer EQ2 and EQ1 for a set of measurement, respectively. A phase shift of  $\pi$  radians between the two different enantiomers is apparent for both conformers and the same initial phase of the RF pulse (*RF+* or *RF-*). By switching the phase of the RF pulse from  $\frac{\pi}{2}$  to  $-\frac{\pi}{2}$ , the phase behavior is reversed as expected, indicating that the signal originates purely from three-wave mixing. Figure 7.8e and 7.8f show a portion of 10 ns of the measured and filtered FID. To extract the *listen* frequency component from the FID a Butterworth filter design was applied with a bandwidth of 500 kHz. Again the phase shift of  $\pi$  radians is apparent between the different enantiomers. In a final experiment both conformers were excited in the same experimental run by stacking the pulse sequence temporally beginning with the shorter pulses of conformer EQ1. The results are depicted in Figure 7.9. The traces for the different conformers of the same enantiomeric species were extracted from the same portion of the FID, but filtered with the corresponding *listen* frequencies.

## 7.6 Enantiomeric excess measurement

The enantiomeric excess (ee) measures the fraction of the excess enantiomer and is defined in the following way [277]:

$$ee = \left| \frac{m_R - m_S}{m_R + m_S} \right| \quad (7.12)$$

where  $m_R$  and  $m_S$  is the total mass of the R- and S-enantiomer in a mixture, respectively. The ee is a very important quantity for drug development to measure, control and optimize

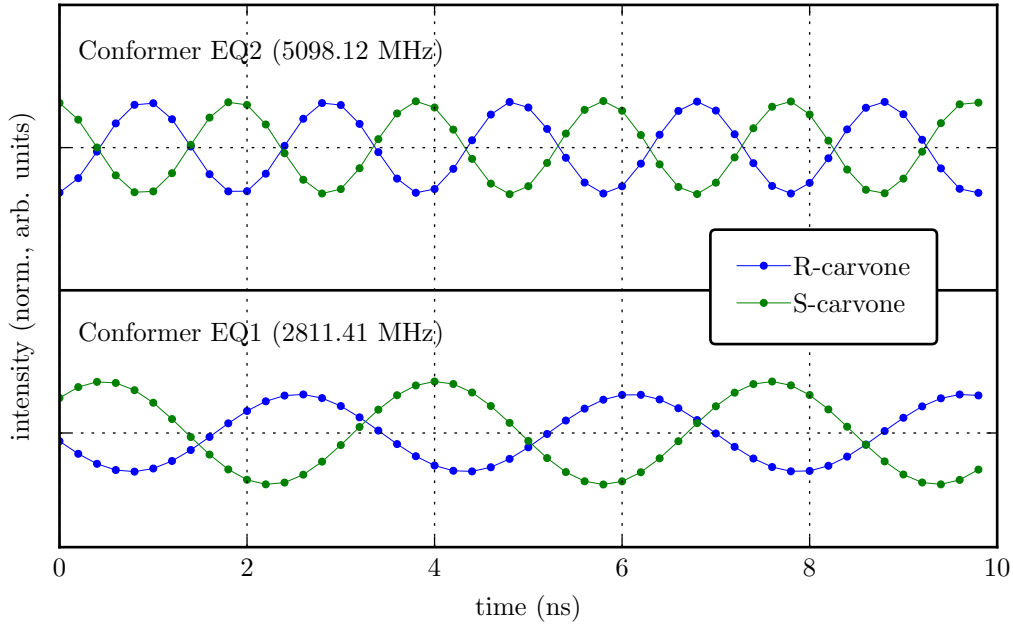


**Figure 7.9:** Portion of the FID trace of the listen signal of conformer EQ2 and conformer EQ1 excited in the same experiment employing a stacked excitation scheme. The two plots show the same portion of the FID for measurements on the R- and the S-enantiomer but filtered using the corresponding listen frequency (5098.12 MHz for EQ2 and 2811.42 MHz for EQ1). The phase difference of  $\pi$  radians is evident for both conformers.

the outcome of asymmetric synthesis routines. Current state-of-the-art measurement techniques include optical rotation determination or chiral gas chromatography [278]. Because the three-wave mixing signal is a superposition of the signal originating from the R- and the S-enantiomer, its intensity  $I$  is directly proportional to the ee:

$$\begin{aligned}
 I &= A(T, N) \cdot \left[ \frac{m_R}{m_R + m_S} \sin(\omega t) + \frac{m_S}{m_R + m_S} \sin(\omega t + \pi) \right] \\
 I &= A(T, N) \cdot \sin(\omega t) \cdot \left( \frac{m_R}{m_R + m_S} - \frac{m_S}{m_R + m_S} \right) \\
 I &\propto A(T, N) \cdot \frac{m_R - m_S}{m_R + m_S} \propto ee
 \end{aligned} \tag{7.13}$$

However, to determine the ee using this linear dependence of the signal intensity on the ee, the proportionality constant  $A(T, N)$  must be known. This implies that the intensity for a sample with known ee has to be determined first, but also that effects of the rotational temperature  $T$  and the number of molecules  $N$  on the proportionality constant  $A(T, N)$  need to be eliminated. Otherwise, slightly different experimental parameters, which are easily introduced by a varying performance of the pulsed nozzle, prevent the exact comparison of two different intensity measurements. To overcome this issue, the proportionality constant  $A(T, N)$  is normalized with the intensity of the *listen* transition obtained in a traditional



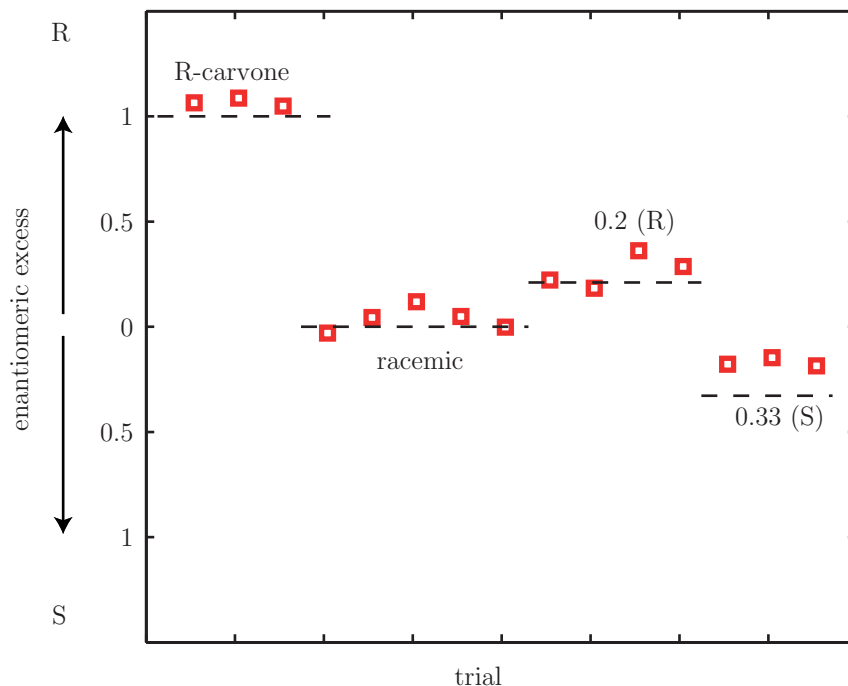


**Figure 7.10:** Repeated measurements of enantiomeric excess for carvone: enantiomerically pure *R*-carvone, the racemic mixture, and mixtures with a slight excess of *R*-carvone (0.2(*R*)) and of *S*-carvone (0.33(*S*)). At least 50 000 FIDs were averaged for each data point.

microwave spectroscopy fashion, where both enantiomers contribute to the signal intensity in the same manner.

Figure 7.10 shows the results of ee determination for four samples with different enantiomeric compositions. An enantiopure sample with a stated ee value of 1(*R*) was used for calibration. The agreement is satisfying for a proof-of-principle experiment, however it is still possible to further reduce the experimental error (about 10%). Different uncertainty sources were identified and can be eliminated in future measurements. First of all, the preparation of the mixture adds uncertainty to the corresponding ee. This uncertainty is easily reduced by high-precision lab equipment or by the preparation of large sample volumes. Furthermore, residual noise on the measured signal intensity induces uncertainty. A larger number of averages would reduce the residual noise. However with a longer measurement duration, the time between a three-wave mixing experiment is performed and the subsequent normalization measurement is increased. Fluctuation in the molecular density or the rotational temperature are then insufficiently monitored and their cancellation might not be complete. Nevertheless, a sophisticated alternating measurement scheme, where the three-wave mixing experiment and the normalization measurement are essentially performed at the same time (within a few seconds), would overcome this problem. Finally, the calibration standard also has a limited accuracy, which needs to be characterized.

## 7.7 Conclusion and outlook

The COMPACT spectrometer was extended to perform polarization sensitive broadband MW-RF double-resonance experiments. In a first step, these double-resonance experiments were exploited to study the AC Stark effect in an unconventional way by examining the phase of the transient FID. A characteristic phase change is observed when the RF pump frequency is scanned through resonance. This phase change can be attributed to the Autler-Townes effect because the RF field shifts the energy levels that are probed by the MW signal pulse. The Autler-Townes splitting is mapped onto the phase of the MW probe signal, causing the characteristic phase shift. The nature of the splitting changes with the magnitude and sign of the detuning, that is, it depends on the relative arrangement of the energy levels as either progressive or regressive. It can be described very well by simulations exploiting the three-level optical Bloch equations.

In a second step, the molecule-sensitive enantiomer differentiation of chiral molecules by microwave three-wave mixing was demonstrated. The intrinsically narrow lines in rotational spectroscopy and the characteristic phase of the three-wave mixing signal for the individual enantiomer allows the analysis of a mixture of chiral molecules. The technique was applied to characterize a mixture of conformational isomers of the monoterpene carvone. In addition, the ee values of enantiomeric mixtures of carvone were measured.

Future studies aim to determine the absolute configuration of a previously uncharacterized molecule. The permanent and the transition dipole moment components are required to determine the phase of the three-wave mixing signal. The former is obtained by quantum chemical calculations while the latter by evaluating the overlap integral (Eqn. 7.6). However, the determination of the phase relationship of the microwave pulse and the RF pulse in the interaction region remains challenging due to the different signal paths and the dispersion of the different microwave components. In addition, the time period from when the signal and when the measurement starts needs to be characterized precisely to derive the absolute phase of the three-wave mixing signal from the experimentally determined relative phase of a signal starting at  $t_{0, meas}$  (compare Fig. 7.7a).

## Chapter 8

# Summary and outlook

The chemical and biological functionality of a molecule is governed by its structural flexibility and internal dynamics while interacting with other molecules, electromagnetic radiation, or external forces. Hence, knowledge of the molecular structure and its internal dynamics is fundamental for strategic drug and advanced material design. Broadband microwave spectroscopy is a powerful technique to study the structure, the dynamics, and the chirality of small and medium sized molecules of biological relevance. This thesis provides an overview, starting with instrument design, construction, and commissioning through to the application of the technique to small molecules of biological interest. In that course, various experimental and theoretical approaches were developed and employed to shed light on the structure, dynamics, and chirality of molecules.

The construction and commissioning of the new chirped-pulse Fourier transform microwave spectrometer COMPACT is described in Chapter 3. The instrumental setup is closely related to the design proposed by Pate et al. [58], but adapted to the frequency range from 2 to 8 GHz (Fig. 3.1). This frequency range is well suited for studying medium sized molecules of biological interest due to their small rotational constants (Sec. 3.2). The purity of the signal sources and the traveling wavetube amplifier was evaluated and revealed the presence of higher harmonics (Fig. 3.2 and Fig. 3.3). The spectrometer is equipped with a pulsed valve to generate an ensemble of internally cold molecules. The valve creates a supersonic expansion and the molecules are probed in a collision free environment at rotational temperatures of less than 5 K. The virtually collision free environment and the low temperature dramatically reduces the line broadening. It was found that an acquisition time of 50  $\mu$ s provides a good tradeoff between measurement time, signal-to-noise ratio, and spectral resolution (25 kHz). The repetition rate of the experiment is limited by the data processing time for high-resolution measurements (about 2 Hz) and by the pumping speed for low-resolution measurements (up to 10 Hz).

The performance of the spectrometer was evaluated using the gas trifluoroiodo methane ( $\text{CF}_3\text{I}$ ) and the liquid benzonitrile ( $\text{C}_7\text{H}_5\text{N}$ ). The characteristic intensity pattern of the quadrupole splitting due to the iodine nucleus of  $\text{CF}_3\text{I}$  provides a reliable test case for a

comparison of the measured and simulated intensities. The agreement is good in the frequency range between 3 and 6 GHz (Fig. 3.10). The situation is different for benzonitrile. Due to benzonitrile’s large permanent dipole moment of 4.5152(68) D, the chirp alters the populations of the individual states significantly in a rapid passage manner, which leads to substantial changes of the transition intensities (Fig. 3.12). Finally, a deep averaged measurement of 624 000 acquisitions on benzonitrile was performed to evaluate the sensitivity of the spectrometer. This measurement revealed all  $^{13}\text{C}$ -isotopologues, the  $^{15}\text{N}$ -isotopologue, one benzonitrile-water cluster, two benzonitrile-neon clusters, and a vibrationally excited state of benzonitrile (Fig. 3.13 and Fig. 3.14). With the help of an additional delay generator, the experimental repetition rate can be further increased by obtaining more than one FID per gas pulse. Further improvements include a new nozzle design to allow for a better jet expansion adjustment under vacuum and the development of a monolithic application to control and further automate the measurement procedure.

In the framework of this thesis, the microwave spectra of related, previously uncharacterized small biomolecules were analyzed with increasing complexity: From a series of *p*-halotoluenes in Chapter 4 and the monoterpenoids thymol and carvacrol in Chapter 5 to the monoterpenoids menthol, menthone, and isomenthone in Chapter 6.

Even though the conformational flexibility is limited for the *p*-halotoluenes (*p*-chloro-, *p*-bromo- and *p*-iodotoluene), the low-barrier  $V_6$  internal rotation of the methyl group as well as the strong nuclear quadrupole coupling of the halogen atoms give rise to dense spectra. Despite the complicated analysis, the observed splitting pattern provides additional information about the barrier to internal rotation and the electronic structure (Fig. 4.2 and Fig. 4.3). The spectra were fit in a global manner employing the principle axis method and SPFIT to obtain the rotational constants, nuclear quadrupole coupling constants, and other spectroscopic constants (Table 4.1, Table 4.2, and Table 4.3). However, the important quantity of the barrier height to internal rotation  $V_6$  is not accessible using the principle axis method in a low barrier case. In the rho axis method, the barrier height can be extracted directly from the Hamiltonian, but its dependence on the barrier height is very weak for the lowest two *m*-states. Unfortunately, only transitions involving these two *m*-states were observed in the spectra obtained. However, with the help of previously published rotational transitions for higher *m*-states of *p*-chlorotoluene [211], the determination of the barrier height became possible and the  $V_6$  internal rotation barrier of the methyl group was found to be 0.058 kJ/mol for both *p*-chlorotoluene isotopologues. Another interesting result of this study is that the magnitudes of the quadrupole coupling constants are increased in the halotoluenes compared to the halobenzenes. This increase is explained by the +*I* inductive effect of the methyl group that injects additional electron density into the phenyl  $\pi$ -cloud, thus giving more electron density for the halogen atom to extract. This additional extraction makes the halogen-carbon bond more ionic than in the halobenzenes. Furthermore, the  $\pi$ -bonding character of the halogen-carbon bond decreases with increasing size of the halogen atom due to the reduced overlap of the valence p-orbital of the halogen and the aromatic  $\pi$ -cloud.

In comparison to the *p*-halotoluenes, the conformational space is more complex for thymol

and carvacrol, discussed in Chapter 5. These monoterpenoids may exist in *trans*- or *cis*-configurations of the hydroxyl group with respect to the isopropyl group. Furthermore, the rotation of the isopropyl group gives rise to two rotamers for each *cis*- and *trans*-isomer of thymol and carvacrol (Fig. 5.2 and Fig. 5.4). In the cold conditions of the molecular jet, four different conformations were identified for carvacrol, whereas three conformations were observed for thymol (Fig. 5.3 and Fig. 5.5). For both molecules, line splittings due to methyl group internal rotation were observed. Using the rho axis method and the program XIAM, the  $V_3$  barrier heights could be determined. The experimental barrier heights are 4.0863(25) kJ/mol for *trans*-carvacrol A, 4.4024(16) kJ/mol for *trans*-carvacrol B, and 0.3699(11) kJ/mol for *trans*-thymol A (Table 5.1, Table 5.2, Table 5.4, and Table 5.5). These results reflect the effect of the hydroxyl group on the barrier height. The impact of the substituent on the barrier height was also compared to similar molecules, e.g. toluene, cresol, and *o*-xylene (Table 5.6).

In Chapter 6, the rotational spectra and the experimentally obtained rotational constants of the monoterpenoids menthol, menthone, and isomenthone are reported. In contrast to thymol and carvacrol, the cyclohexane ring in menthol adds further flexibility and extends the conformational space (Fig. 6.4). Even though quantum chemical calculations predict five conformers below 5 kJ/mol (Table 6.2), only one conformer of menthol was observed in the spectrum (Fig. 6.3). This observation can be explained by the cooling behavior in the supersonic expansion and low isomerization barriers for these five conformers to the one observed. The comparison of the experimental rotational constants with the ab initio ones revealed a good match (Table 6.1). The calculations further predict that for the nine lowest energy conformers of menthol the chair configuration of the cyclohexane ring is preferred.

In the broadband microwave spectrum of a mixture of the diastereomers menthone and isomenthone, three conformations of menthone and a single conformation of isomenthone were identified (Fig. 6.6). Each set of rotational constants was unambiguously linked to a calculated structure (6.3). Again for menthone, a chair configuration with sterically demanding substituents in the equatorial positions is preferred (Table 6.4). However, the arrangement of the substituents in isomenthone forces the cyclohexane ring into a boat configuration with one of the substituents oriented axial to the cyclohexane ring for the lowest energy conformations (Table 6.5).

As the number of structural isomers present in the rotational spectrum increases, the manual assignment of the individual rotational transitions becomes complicated. The trend towards the study of larger molecules means this situation arises more often because, with an increasing size, molecules usually exhibit more conformations or stereoisomers. Another upcoming challenge is the assignment of dense high-resolution spectra obtained by radio astronomy. The complicated analysis of the overlapping spectra of the mixture of menthone isomers motivated the development of a new automated assignment program in Section 6.3. The computer program compares many predicted spectra with the experimental one in a systemic way, then picks and fits the best candidates. The automated routine was capable of identifying and fitting all components in the menthone mixture with ab initio calculated rotational constants as inputs.

Future work in the field of spectral analysis will focus on the theoretical description of internal dynamics, e.g. internal rotation or tunneling, in combination with other spectroscopic effects, e.g. quadrupole coupling. This approach will not necessarily require the development of a new rotational Hamiltonian, but rather an evaluation of the existing approaches and their combination in an unified framework. Furthermore, automated assignment and fitting of overlapping spectra will gain importance for conformationally rich biomolecules. Hence, future development faces two main challenges. Firstly, the ample conformational landscape needs to be evaluated in an accurate and time efficient way to provide high quality starting structures and rotational constants for the automated assignment routine. Secondly, the assignment and fitting algorithm needs to handle overlapping spectra of multiple species that likely also exhibit line splittings due to internal dynamics or quadrupole coupling.

Even though microwave spectroscopy provides access to most structural properties, the chirality of a molecule was always out of reach. Neglecting the small energy shift due to parity violation, the unperturbed rotational Hamiltonian does not provide any information about the configuration, because the rotational constants are identical. However, the scalar triple product of the permanent dipole moment components switches sign between enantiomers. In Chapter 7, this fact is exploited to uncover the molecular handedness in a three-wave mixing scheme. This three-wave mixing approach, proposed by Hirota [268], was successfully implemented in a cavity-based spectrometer by Patterson et al. [269, 270]. Within the framework of this thesis, the three-wave mixing scheme was adapted for the broadband regime. Therefore the COMPACT spectrometer was slightly modified and equipped with a radio frequency source polarized perpendicular to the microwave radiation (Fig. 7.2). By exciting two transitions of a closed triad of transitions, the phase of the third transition identifies the excess enantiomer. The experiments were performed on the monoterpene carvone determining not only which enantiomer is in excess ( Fig. 7.8 in Sec. 7.5), but also by how much (Fig. 7.10 in Sec. 7.6). The applicability of the three-wave mixing technique to mixtures of chiral molecules was demonstrated by the simultaneous measurement of two conformers of carvone (Fig. 7.9).

The determination of the absolute configuration without any a priori knowledge of the measured phase of the different enantiomers is the next step in continuing the three-wave mixing experiments. This task involves the accurate characterization of the experimental time delays and the dispersion of the individual high-frequency components as outlined in Section 7.7. Preliminary computations based on four-level optical Bloch equations show that by exciting all three transitions of a closed cycle, the population of a specific enantiomer in a defined state is enhanced. One application of this experimental technique would be the determination of the ee without the dependence on a known sample.

In preparation for the three-wave mixing experiments, double-resonance experiments were performed to determine the resonance frequency of the radio frequency transition and to optimize the duration of the microwave and the radio frequency pulses. Using the diastereomers menthone and isomenthone, the dependence of pumping a radio frequency transition on both the amplitude and phase of the coherence of a microwave transition with which it shares a common rotational level was investigated. The microwave signal intensity in the FID is sig-

nificantly depleted and a strong phase change is observed when scanning the radio frequency through molecular resonance (Fig. 7.3 and Fig. 7.4). The direction of the phase change depends on the energy level arrangement, that is, if it is progressive or regressive. The experimental results can be simulated using the three-level optical Bloch equations and are best described with the AC-Stark effect (Fig. 7.5), giving rise to an Autler-Townes splitting (Fig. 7.6). When measuring the rotational spectrum of complex molecules, the double-resonance technique can provide additional information to guide the assignment process. One can imagine even automated double-resonance experiments to fully determine the connectivity of the rotational levels involved, greatly simplifying the assignment.

# Bibliography

- [1] A. Yonath, "Polar bears, antibiotics, and the evolving ribosome (Nobel Lecture)," *Angew. Chem. Int. Ed.* **49**, 4340 (2010).
- [2] K. Wüthrich, "NMR studies of structure and function of biological macromolecules (Nobel Lecture)," *Angew. Chem. Int. Ed.* **42**, 3340 (2003).
- [3] R. R. Ernst, "Nuclear Magnetic Resonance Fourier Transform Spectroscopy (Nobel Lecture)," *Angew. Chem. Int. Ed.* **31**, 805 (1992).
- [4] R. Huber, "A structural basis of light energy and electron transfer in biology (Nobel lecture)," *Angew. Chem. Int. Ed.* **28**, 848 (1989).
- [5] J. Deisenhofer and H. Michel, "Nobel lecture. The photosynthetic reaction centre from the purple bacterium *Rhodospseudomonas viridis*," *Bioscience Rep.* **9**, 383 (1989).
- [6] H. Hauptman, "Direct Methods and Anomalous Dispersion (Nobel Lecture)," *Angew. Chem. Int. Ed.* **25**, 603 (1986).
- [7] J. Karle, "Recovering phase information from intensity data (Nobel Lecture)," *Angew. Chem. Int. Ed.* **25**, 614 (1986).
- [8] A. Klug, "From Macromolecules to Biological Assemblies (Nobel Lecture)," *Angew. Chem. Int. Ed.* **22**, 565 (1983).
- [9] D. C. Hodgkin, "The X-ray analysis of complicated molecules," *Nobel Lecture* (1964).
- [10] A. Lesarri, S. Mata, J. C. López, and J. L. Alonso, "A laser-ablation molecular-beam Fourier-transform microwave spectrometer: The rotational spectrum of organic solids," *Rev. Sci. Instrum.* **74**, 4799 (2003).
- [11] S. Melandri, M. E. Sanz, W. Caminati, P. G. Favero, and Z. Kisiel, "The hydrogen bond between water and aromatic bases of biological interest: An experimental and theoretical study of the 1:1 complex of pyrimidine with water," *J. Am. Chem. Soc.* **120**, 11504 (1998).
- [12] S. Melandri, D. Consalvo, W. Caminati, and P. G. Favero, "Hydrogen bonding , structure , and dynamics of benzonitrile-water," *Chem. Phys.* **111**, 3874 (1999).
- [13] S. Blanco, J. C. López, J. L. Alonso, P. Ottaviani, and W. Caminati, "Pure rotational spectrum and model calculations of indole-water," *J. Chem. Phys.* **119**, 880 (2003).
- [14] J. Thomas, O. Sukhorukov, W. Jäger, and Y. Xu, "Direct spectroscopic detection of the orientation of free OH groups in methyl lactate-(water)<sub>1,2</sub> clusters: Hydration of a chiral hydroxy ester," *Angew. Chem. Int. Ed.* **53**, 1156 (2014).
- [15] C. Pérez, J. L. Neill, M. T. Muckle, D. P. Zaleski, I. Peña, J. C. Lopez, J. L. Alonso, and B. H. Pate, "Water-Water and Water-Solute Interactions in Microsolvated Organic Complexes," *Angew. Chem. Int. Ed.* **53**, 993 (2014).
- [16] E. J. Cocinero, A. Lesarri, P. Écija, F. J. Basterretxea, J.-U. Grabow, J. A. Fernández, and F. Castaño, "Ribose Found in the Gas Phase," *Angew. Chem. Int. Ed.* **51**, 3119 (2012).
- [17] A. Lesarri, S. Mata, E. J. Cocinero, S. Blanco, J. C. López, and J. L. Alonso, "The structure of neutral proline," *Angew. Chem. Int. Ed.* **41**, 4673 (2002).
- [18] A. Lesarri, E. J. Cocinero, J. C. López, and J. L. Alonso, "The shape of neutral valine," *Angew. Chem. Int. Ed.* **43**, 605 (2004).
- [19] S. Blanco, A. Lesarri, J. C. López, and J. L. Alonso, "The gas-phase structure of alanine," *J. Am. Chem. Soc.* **126**, 11675 (2004).



- [20] J. L. Alonso, I. Peña, J. C. López, and V. Vaquero, "Rotational spectral signatures of four tautomers of guanine," *Angew. Chem. Int. Ed.* **48**, 6141 (2009).
- [21] J. L. Alonso, V. Vaquero, I. Peña, J. C. López, S. Mata, and W. Caminati, "All Five Forms of Cytosine Revealed in the Gas Phase," *Angew. Chem. Int. Ed.* **52**, 2331 (2013).
- [22] C. Cabezas, M. Varela, I. Peña, J. C. López, and J. L. Alonso, "The microwave spectrum of neurotransmitter serotonin," *Phys. Chem. Chem. Phys.* **14**, 13618 (2012).
- [23] C. Cabezas, J. L. Alonso, J. C. López, and S. Mata, "Unveiling the Shape of Aspirin in the Gas Phase," *Angew. Chem. Int. Ed.* **51**, 1375 (2012).
- [24] I. Peña, A. M. Daly, C. Cabezas, S. Mata, C. Bermúdez, A. Niño, J. C. López, J.-U. Grabow, et al., "Disentangling the Puzzle of Hydrogen Bonding in Vitamin C," *J. Phys. Chem. Lett.* **4**, 65 (2013).
- [25] M. Varela, C. Cabezas, J. C. López, and J. L. Alonso, "Rotational spectrum of paracetamol," *J. Phys. Chem. A* **117**, 13275 (2013).
- [26] N. A. Seifert, D. P. Zaleski, C. Pérez, J. L. Neill, B. H. Pate, M. Vallejo-López, A. Lesarri, E. J. Cocinero, et al., "Probing the C-H... $\pi$  Weak Hydrogen Bond in Anesthetic Binding: The Sevoflurane-Benzene Cluster," *Angew. Chem. Int. Ed.* **53**, 3210 (2014).
- [27] T. Betz, S. Zinn, and M. Schnell, "The shape of ibuprofen in the gas phase," *Phys. Chem. Chem. Phys.* **17**, 4538 (2015).
- [28] C. Pérez, M. T. Muckle, D. P. Zaleski, N. A. Seifert, B. Temelso, G. C. Shields, Z. Kisiel, and B. H. Pate, "Structures of Cage, Prism, and Book Isomers of Water Hexamers from Broadband Rotational Spectroscopy," *Science* **336**, 897 (2012).
- [29] C. Pérez, S. Lobsiger, N. A. Seifert, D. P. Zaleski, B. Temelso, G. C. Shields, Z. Kisiel, and B. H. Pate, "Broadband Fourier transform rotational spectroscopy for structure determination : The water heptamer," *Chem. Phys. Lett.* **571**, 1 (2013).
- [30] C. Pérez, D. P. Zaleski, N. A. Seifert, B. Temelso, G. C. Shields, Z. Kisiel, and B. H. Pate, "Hydrogen Bond Cooperativity and the Three-Dimensional Structures of Water Nonamers and Decamers," *Angew. Chem. Int. Ed.* **53**, 14368 (2014).
- [31] M. Schnell and J.-U. Grabow, "Multidimensional large-amplitude motion: revealing concurrent tunneling pathways in molecules with several internal rotors," *Angew. Chem. Int. Ed.* **45**, 3465 (2006).
- [32] M. Schnell, U. Erlekam, P. R. Bunker, G. von Helden, J.-U. Grabow, G. Meijer, and A. van der Avoird, "Structure of the Benzene Dimer-Governed by Dynamics," *Angew. Chem. Int. Ed.* **52**, 5180 (2013).
- [33] "European Southern Observatory - Atacama Large Millimeter/submillimeter Array." <http://www.eso.org/sci/facilities/alma.html> (2014).
- [34] "Herschel Space Observatory," <http://sci.esa.int/herschel/> (2014).
- [35] C. Qi, K. I. Öberg, D. J. Wilner, P. D'Alessio, E. Bergin, S. M. Andrews, G. A. Blake, M. R. Hogerheijde, et al., "Imaging of the CO snow line in a solar nebula analog," *Science* **341**, 630 (2013).
- [36] J. K. Jørgensen, R. Visser, N. Sakai, E. A. Bergin, C. Brinch, D. Harsono, J. E. Lindberg, E. F. van Dishoeck, et al., "A Recent Accretion Burst in the Low-Mass Protostar Iras 15398-3359: Alma Imaging of Its Related Chemistry," *Astrophys. J.* **779**, L22 (2013).
- [37] A. Belloche, R. T. Garrod, H. S. P. Müller, and K. M. Menten, "Detection of a branched alkyl molecule in the interstellar medium: *iso*-propyl cyanide," *Science* **233**, 232 (2014).
- [38] S. M. Fortman, J. P. McMillan, C. F. Neese, S. K. Randall, A. J. Remijan, T. Wilson, and F. C. De Lucia, "An analysis of a preliminary ALMA Orion KL spectrum via the use of complete experimental spectra from the laboratory," *J. Mol. Spec.* **280**, 11 (2012).
- [39] J. L. Neill, E. A. Bergin, D. C. Lis, T. G. Phillips, M. Emprechtinger, and P. Schilke, "Broadband analysis techniques for Herschel/HIFI spectral surveys of chemically rich star-forming regions," *J. Mol. Spec.* **280**, 150 (2012).
- [40] M. J. Travers, M. C. McCarthy, P. Kalmus, C. A. Gottlieb, and P. Thaddeus, "Laboratory Detection of the Linear Cyanopolyne HC<sub>11</sub>N," *Astrophys. J.* **469**, L65 (1996).
- [41] C. H. Townes and A. L. Schawlow, *Microwave spectroscopy*, 2nd ed. (Courier Dover Publications, Mineola, 1975).

- [42] C. H. Townes, "The Ammonia Spectrum and Line Shapes Near 1.25-cm Wave-Length," *Phys. Rev.* **70**, 665 (1946).
- [43] W. E. Good, "Inversion Spectrum of Ammonia," *Phys. Rev.* **70**, 213 (1946).
- [44] B. P. Dailey, R. L. Kyhl, M. W. P. Stranberg, J. H. van Vleck, and E. B. Wilson Jr, "The Hyperfine Structure of the Microwave Spectrum of Ammonia and the Existence of a Quadrupole Moment in  $^{14}\text{N}$ ," *Phys. Rev.* **70**, 984 (1946).
- [45] J. P. Gordon, H. J. Zeiger, and C. H. Townes, "Molecular Microwave Oscillator and New Structure in the Microwave Spectrum of  $\text{NH}_3$ ," *Phys. Rev.* **99**, 282 (1954).
- [46] J. P. Gordon, H. J. Zeiger, and C. H. Townes, "The Maser-New Type of Microwave Amplifier, Frequency Standard and Spectrometer," *Phys. Rev.* **99**, 1264 (1955).
- [47] J. Kraitchman, "Determination of Molecular Structure from Microwave Spectroscopic Data," *Am. J. Phys.* **21**, 17 (1953).
- [48] R. Dicke and R. Romer, "Pulse Techniques in Microwave Spectroscopy," *Rev. Sci. Instrum.* **26**, 915 (1955).
- [49] J. McGurk, T. Schmalz, and W. Flygare, "Fast passage in rotational spectroscopy: Theory and experiment," *J. Chem. Phys.* **60**, 4181 (1974).
- [50] J. C. McGurk, R. T. Hofmann, and W. H. Flygare, "Transient absorption and emission and the measurement of  $T_1$  and  $T_2$  in the  $J\ 0 \rightarrow 1$  rotational transition in OCS," *J. Chem. Phys.* **60**, 2922 (1974).
- [51] T. J. Balle and W. Flygare, "Fabry-Perot cavity pulsed Fourier transform microwave spectrometer with a pulsed nozzle particle source," *Rev. Sci. Instrum.* **52**, 33 (1981).
- [52] J.-U. Grabow, W. Stahl, and H. Dreizler, "A multioctave coaxially oriented beam-resonator arrangement Fourier-transform microwave spectrometer," *Rev. Sci. Instrum.* **67**, 4072 (1996).
- [53] F. Lewen, R. Gendriesch, I. Pak, D. G. Paveliev, M. Hepp, R. Schieder, and G. Winnewisser, "Phase locked backward wave oscillator pulsed beam spectrometer in the submillimeter wave range," *Rev. Sci. Instrum.* **69**, 32 (1998).
- [54] D. T. Petkie, T. M. Goyette, R. P. A. Bettens, S. P. Belov, S. Albert, P. Helminger, and F. C. De Lucia, "A fast scan submillimeter spectroscopic technique," *Rev. Sci. Instrum.* **68**, 1676 (1997).
- [55] B. Vogelsanger, M. Andrist, and A. Bauder, "Two-Dimensional Correlation Experiments in Microwave Fourier Transform Spectroscopy," *Chem. Phys. Lett.* **144**, 180 (1988).
- [56] B. Vogelsanger, A. Bauder, and H. Mäder, "Twodimensional experiments with collisioninduced transfer of populations in microwave Fourier transform spectroscopy," *J. Chem. Phys.* **91**, 2059 (1989).
- [57] B. Vogelsanger and A. Bauder, "Two-dimensional microwave Fourier transform spectroscopy," *J. Chem. Phys.* **92**, 4101 (1990).
- [58] G. G. Brown, B. C. Dian, K. O. Douglass, S. M. Geyer, S. T. Shipman, and B. H. Pate, "A broadband Fourier transform microwave spectrometer based on chirped pulse excitation," *Rev. Sci. Instrum.* **79**, 053103 (2008).
- [59] G. S. Grubbs, C. T. Dewberry, K. C. Etchison, K. E. Kerr, and S. A. Cooke, "A search accelerated correct intensity Fourier transform microwave spectrometer with pulsed laser ablation source," *Rev. Sci. Instrum.* **78**, 6 (2007).
- [60] S. L. Stephens and N. R. Walker, "Determination of nuclear spin-rotation coupling constants in  $\text{CF}_3\text{I}$  by chirped-pulse Fourier-transform microwave spectroscopy," *J. Mol. Spec.* **263**, 27 (2010).
- [61] D. A. Obenchain, A. A. Elliott, A. L. Steber, R. A. Peebles, S. A. Peebles, C. J. Wurrey, and G. A. Guirgis, "Rotational spectrum of three conformers of 3,3-difluoropentane: Construction of a 480 MHz bandwidth chirped-pulse Fourier-transform microwave spectrometer," *J. Mol. Spec.* **261**, 35 (2010).
- [62] A. J. Shirar, D. S. Wilcox, K. M. Hotopp, G. L. Storck, I. Kleiner, and B. C. Dian, "Impact of molecular conformation on barriers to internal methyl rotation: The rotational spectrum of m-methylbenzaldehyde," *J. Phys. Chem. A* **114**, 12187 (2010).
- [63] B. Reinhold, I. Finneran, and S. Shipman, "Room temperature chirped-pulse Fourier transform microwave spectroscopy of anisole," *J. Mol. Spec.* **270**, 89 (2011).

- [64] J. L. Neill, S. T. Shipman, L. Alvarez-Valtierra, A. Lesarri, Z. Kisiel, and B. H. Pate, "Rotational spectroscopy of iodobenzene and iodobenzene-neon with a direct digital 2-8 GHz chirped-pulse Fourier transform microwave spectrometer," *J. Mol. Spec.* **269**, 21 (2011).
- [65] K. Prozument, A. Colombo, Y. Zhou, G. Park, V. Petrović, S. Coy, and R. Field, "Chirped-Pulse Millimeter-Wave Spectroscopy of Rydberg-Rydberg Transitions," *Phys. Rev. Lett.* **107**, 1 (2011).
- [66] L. Evangelisti, G. Sedo, and J. Van Wijngaarden, "Rotational spectrum of 1,1,1-trifluoro-2-butanone using chirped-pulse Fourier transform microwave spectroscopy," *J. Phys. Chem. A* **115**, 685 (2011).
- [67] G. B. Park, A. H. Steeves, K. Kuyanov-Prozument, J. L. Neill, and R. W. Field, "Design and evaluation of a pulsed-jet chirped-pulse millimeter-wave spectrometer for the 70-102 GHz region," *J. Chem. Phys.* **135**, 024202 (2011).
- [68] M. K. Jahn, D. A. Dewald, D. Wachsmuth, J.-U. U. Grabow, and S. C. Mehrotra, "Rapid capture of large amplitude motions in 2,6-difluorophenol: High-resolution fast-passage FT-MW technique," *J. Mol. Spec.* **280**, 54 (2012).
- [69] D. Schmitz, V. A. Shubert, T. Betz, and M. Schnell, "Multi-resonance effects within a single chirp in broadband rotational spectroscopy: The rapid adiabatic passage regime for benzonitrile," *J. Mol. Spec.* **280**, 77 (2012).
- [70] A. L. Steber, B. J. Harris, J. L. Neill, and B. H. Pate, "An arbitrary waveform generator based chirped pulse Fourier transform spectrometer operating from 260 to 295 GHz," *J. Mol. Spec.* **280**, 3 (2012).
- [71] D. P. Zaleski, J. L. Neill, M. T. Muckle, N. A. Seifert, P. Brandon Carroll, S. L. Widicus Weaver, and B. H. Pate, "A  $K_a$ -band chirped-pulse Fourier transform microwave spectrometer," *J. Mol. Spec.* **280**, 68 (2012).
- [72] S. P. Dempster, O. Sukhorukov, Q.-Y. Lei, and W. Jäger, "Rotational spectroscopic study of hydrogen cyanide embedded in small 4He clusters Rotational spectroscopic study of hydrogen cyanide embedded in small 4 He clusters," *J. Chem. Phys.* **137**, 174303 (2012).
- [73] S. Mata, I. Peña, C. Cabezas, J. López, and J. Alonso, "A broadband Fourier-transform microwave spectrometer with laser ablation source: The rotational spectrum of nicotinic acid," *J. Mol. Spec.* **280**, 91 (2012).
- [74] K. Prozument, G. Barratt Park, R. G. Shaver, A. K. Vasiliou, J. M. Oldham, D. E. David, J. S. Muentner, J. F. Stanton, et al., "Chirped-pulse millimeter-wave spectroscopy for dynamics and kinetics studies of pyrolysis reactions," *Phys. Chem. Chem. Phys.* **16**, 15739 (2014).
- [75] B. C. Dian, G. G. Brown, K. O. Douglass, and B. H. Pate, "Measuring picosecond isomerization kinetics via broadband microwave spectroscopy," *Science* **320**, 924 (2008).
- [76] B. C. Dian, G. G. Brown, K. O. Douglass, F. S. Rees, J. E. Johns, P. Nair, R. D. Suenram, and B. H. Pate, "Conformational isomerization kinetics of pent-1-en-4-yne with 3,330  $cm^{-1}$  of internal energy measured by dynamic rotational spectroscopy," *P. Natl. Acad. Sci. USA* **105**, 12696 (2008).
- [77] D. S. Wilcox, K. M. Hotopp, and B. C. Dian, "Two-dimensional chirped-pulse Fourier transform microwave spectroscopy," *J. Phys. Chem.* **115**, 8895 (2011).
- [78] V. A. Shubert, D. Schmitz, D. Patterson, J. M. Doyle, and M. Schnell, "Identifying Enantiomers in Mixtures of Chiral Molecules with Broadband Microwave Spectroscopy," *Angew. Chem. Int. Ed.* **52**, 1 (2013).
- [79] S. Lobsiger, C. Perez, L. Evangelisti, K. K. Lehmann, and B. H. Pate, "Molecular Structure and Chirality Detection by Fourier Transform Microwave Spectroscopy," *J. Phys. Chem. Lett.* **6**, 196 (2015).
- [80] E. Gerecht, K. O. Douglass, and D. F. Plusquellic, "Chirped-pulse terahertz spectroscopy for broadband trace gas sensing," *Opt. Express* **19**, 8973 (2011).
- [81] J. L. Neill, B. J. Harris, A. L. Steber, K. O. Douglass, D. F. Plusquellic, and B. H. Pate, "Segmented chirped-pulse Fourier transform submillimeter spectroscopy for broadband gas analysis," *Opt. Express* **21**, 19743 (2013).
- [82] J. L. Neill, B. J. Harris, R. L. Pulliam, M. T. Muckle, R. Reynolds, D. McDaniel, and B. H. Pate, "Pure rotational spectrometers for trace-level VOC detection and chemical sensing," *Proc. SPIE* **9101**, 91010B (2014).

- [83] A. R. W. McKellar, "High-resolution infrared spectroscopy with synchrotron sources," *J. Mol. Spec.* **262**, 1 (2010).
- [84] M. Schmitt and W. L. Meerts, "Rotationally Resolved Electronic Spectroscopy and Automatic Assignment Techniques using Evolutionary Algorithms," in *Handbook of High-resolution Spectroscopy*, Vol. 2, edited by M. Quack and F. Merkt (John Wiley & Sons, Ltd, New York, 2011) pp. 1345–72.
- [85] D. W. Pratt, "Electronic Spectroscopy in the Gas Phase," in *Handbook of High-resolution Spectroscopy*, Vol. 2, edited by M. Quack and F. Merkt (John Wiley & Sons, Ltd, New York, 2011) pp. 1291–1320.
- [86] A. H. Zewail, "Femtochemistry: Atomic-Scale Dynamics of the Chemical Bond Using Ultrafast Lasers," *Angew. Chem. Int. Ed.* **39**, 2586 (2000).
- [87] C. Riehn, "High-resolution pump-probe rotational coherencespectroscopy - Rotational constants and structure of ground and electronically excited states of large molecular systems," *Chem. Phys.* **283**, 297 (2002).
- [88] C. Schröter, K. Kosma, and T. Schultz, "CRASY: mass- or electron-correlated rotational alignment spectroscopy," *Science* **333**, 1011 (2011).
- [89] K. Wüthrich, "The way of NMR structures of proteins," *Nat. Struct. Biol.* **8**, 923 (2001).
- [90] L. E. Kay, "NMR studies of protein structure and dynamics," *J. Magn. Reson.* **173**, 193 (2005).
- [91] H. M. Berman, J. Westbrook, Z. Feng, G. Gilliland, T. N. Bhat, H. Weissig, I. N. Shindyalov, and P. E. Bourne, "The Protein Data Bank," *Nucleic. Acids Res.* **28**, 235 (2000).
- [92] D. I. Svergun and M. H. J. Koch, "Small-angle scattering studies of biological macromolecules in solution," *Rep. Prog. Phys.* **66**, 1735 (2003).
- [93] D. I. Svergun, "Small-angle scattering studies of macromolecular solutions," *J. Appl. Crystallogr.* **40**, 10 (2007).
- [94] H. D. T. Mertens and D. I. Svergun, "Structural characterization of proteins and complexes using small-angle X-ray solution scattering," *J. Struct. Biol.* **172**, 128 (2010).
- [95] H. N. Chapman, P. Fromme, A. Barty, T. A. White, R. A. Kirian, A. Aquila, M. S. Hunter, J. Schulz, et al., "Femtosecond X-ray protein nanocrystallography," *Nature* **470**, 73 (2011).
- [96] L. Redecke, K. Nass, D. P. DePonte, T. A. White, D. Rehders, A. Barty, F. Stellato, M. Liang, et al., "Natively inhibited Trypanosoma brucei cathepsin B structure determined by using an X-ray laser," *Science* **339**, 227 (2013).
- [97] T. R. M. Barends, L. Foucar, S. Botha, R. B. Doak, R. L. Shoeman, K. Nass, J. E. Koglin, G. J. Williams, et al., "De novo protein crystal structure determination from X-ray free-electron laser data," *Nature* **505**, 244 (2014).
- [98] M. M. Seibert, T. Ekeberg, F. R. N. C. Maia, M. Svenda, J. Andreasson, O. Jönsson, D. Odić, B. Iwan, et al., "Single mimivirus particles intercepted and imaged with an X-ray laser," *Nature* **470**, 78 (2011).
- [99] T. Ekeberg, M. Svenda, C. Abergel, F. R. N. C. Maia, V. Seltzer, J.-M. Claverie, M. Hantke, O. Jönsson, et al., "Three-Dimensional Reconstruction of the Giant Mimivirus Particle with an X-Ray Free-Electron Laser," *Phys. Rev. Lett.* **114**, 1 (2015).
- [100] J. Küpper, S. Stern, L. Holmegaard, F. Filsinger, A. Rouzée, A. Rudenko, P. Johnsson, A. V. Martin, et al., "X-ray diffraction from isolated and strongly aligned gas-phase molecules with a free-electron laser," *Phys. Rev. Lett.* **112**, 1 (2014).
- [101] R. Neutze, R. Wouts, D. van der Spoel, E. Weckert, and J. Hajdu, "Potential for biomolecular imaging with femtosecond X-ray pulses," *Nature* **406**, 752 (2000).
- [102] H. N. Chapman, A. Barty, M. J. Bogan, S. Boutet, M. Frank, S. P. Hau-Riege, S. Marchesini, B. W. Woods, et al., "Femtosecond Diffractive Imaging with a Soft-X-ray Free-Electron Laser," *Nat. Phys.* **2**, 839 (2006).
- [103] A. Barty, J. Küpper, and H. N. Chapman, "Molecular Imaging Using X-Ray Free-Electron Lasers," *Annu. Rev. Phys. Chem.* **64**, 415 (2013).
- [104] M. Adrian, J. Dubochet, J. Lepault, and A. W. McDowell, "Cryo-electron microscopy of viruses," *Nature* **308**, 32 (1984).

- [105] C. Mueller, M. Harb, J. R. Dwyer, and R. J. D. Miller, "Nanofluidic cells with controlled pathlength and liquid flow for rapid, high-resolution in situ imaging with electrons," *J. Phys. Chem. Lett.* **4**, 2339 (2013).
- [106] C. J. Hensley, J. Yang, and M. Centurion, "Imaging of isolated molecules with ultrafast electron pulses," *Phys. Rev. Lett.* **109**, 1 (2012).
- [107] M. Gao, C. Lu, H. Jean-Ruel, L. C. Liu, A. Marx, K. Onda, S.-Y. Koshihara, Y. Nakano, et al., "Mapping molecular motions leading to charge delocalization with ultrabright electrons," *Nature* **496**, 343 (2013).
- [108] R. J. D. Miller, "Femtosecond Crystallography with Capturing Chemistry in Action," *Science* **343**, 1108 (2014).
- [109] J. Tenboer, S. Basu, N. Zatsepin, K. Pande, D. Milathianaki, M. Frank, M. Hunter, S. Boutet, et al., "Time-resolved serial crystallography captures high-resolution intermediates of photoactive yellow protein," *Science* **346**, 1242 (2014).
- [110] F. Merkt and M. Quack, "Molecular Quantum Mechanics and Molecular Spectra, Molecular Symmetry, and Interaction of Matter with Radiation," in *Handbook of High-resolution Spectroscopy*, Vol. 1, edited by M. Quack and F. Merkt (John Wiley & Sons, Ltd, New York, 2011) pp. 1–56.
- [111] M. Born and R. Oppenheimer, "Zur Quantentheorie der Molekeln," *Ann. Phys.* **84**, 457 (1927).
- [112] P. F. Bernath, "Rotational Spectroscopy," in *Spectra of Atoms and Molecules* (Oxford University Press, Oxford, 1995) Chap. 6.
- [113] R. N. Zare, *Angular Momentum: Understanding Spatial Aspects in Chemistry and Physics* (John Wiley & Sons, Inc., New York, 1988).
- [114] A. R. Edmonds, *Angular Momentum in Quantum Mechanics* (Princeton University Press, Princeton, 1996).
- [115] A. Bauder, "Fundamentals of Rotational Spectroscopy," in *Handbook of High-resolution Spectroscopy*, Vol. 1, edited by M. Quack and F. Merkt (John Wiley & Sons, Ltd, New York, 2011) pp. 57–116.
- [116] P. R. Bunker and P. Jensen, *Molecular symmetry and spectroscopy*, 2nd ed. (NRC Research Press, Ottawa, 1998).
- [117] W. Gordy and R. Cook, *Microwave Molecular Spectra* (John Wiley & Sons Inc., New York, 1964).
- [118] G. W. King, R. M. Hainer, and P. C. Cross, "The Asymmetric Rotor I. Calculation and Symmetry Classification of Energy Levels," *J. Chem. Phys.* **11**, 27 (1943).
- [119] J. K. G. Watson, "Indeterminacies of Fitting Parameters in Molecular Spectroscopy," in *Handbook of High-resolution Spectroscopy*, Vol. 1, edited by M. Quack and F. Merkt (John Wiley & Sons, Ltd, New York, 2011) pp. 587–606.
- [120] J. K. G. Watson, "Determination of Centrifugal Distortion Coefficients of Asymmetric Top Molecules," *J. Chem. Phys.* **46**, 1935 (1967).
- [121] H. H. Nielsen, "The Vibration-Rotation Energies of Molecules," *Rev. Mod. Phys.* **23**, 90 (1951).
- [122] N. R. Walker, S. G. Francis, S. L. Matthews, J. J. Rowlands, and A. C. Legon, "Microwave spectrum and structure of carbonyl gold iodide,  $\text{OCAuI}$ ," *Mol. Phys.* **104**, 3329 (2006).
- [123] C. Medcraft, R. Wolf, and M. Schnell, "High-resolution spectroscopy of the chiral metal complex  $[\text{CpRe}(\text{CH}_3)(\text{CO})(\text{NO})]$ : a potential candidate for probing parity violation," *Angew. Chem. Int. Ed.* **53**, 11656 (2014).
- [124] M. Schnell, J. Hougen, and J. Grabow, "Towards the complete analysis of the rotational spectrum of  $(\text{CH}_3)_3\text{SnCl}$ ," *J. Mol. Spec.* **251**, 38 (2008).
- [125] E. R. Cohen, T. Cvitas, J. G. Frey, B. Holmström, K. Kuchitsu, R. Marquardt, I. Mills, F. Pavese, et al., *Quantities, Units and Symbols in Physical Chemistry, IUPAC Green Book*, 3rd ed. (IUPAC & RSC Publishing, Cambridge, 2008).
- [126] C. P. Slichter, "Electric Quadrupole Effects," in *Principles of Magnetic Resonance* (Springer-Verlag, Berlin, 1996) 3rd ed., pp. 485–502.
- [127] H. P. Benz, A. Bauder, and H. H. Günthard, "Exact Quadrupole Interaction Energies in Rotational Spectra," *J. Mol. Spec.* **21**, 156 (1966).
- [128] J. H. Goldstein, "Quadrupole Coupling and Bond Character in the Vinyl Halides," *J. Chem. Phys.* **24**, 106 (1956).



- [129] C. H. Townes and B. P. Dailey, "Determination of Electronic Structure of Molecules from Nuclear Quadrupole Effects," *J. Chem. Phys.* **17**, 782 (1949).
- [130] D. R. Herschbach, "Calculation of Energy Levels for Internal Torsion and Over-All Rotation." *J. Chem. Phys.* **31**, 91 (1959).
- [131] D. Gerhard, A. Hellweg, I. Merke, W. Stahl, M. Baudelet, D. Petitprez, and G. Wlodarczak, "Internal rotation and chlorine nuclear quadrupole coupling of o-chlorotoluene studied by microwave spectroscopy and ab initio calculations," *J. Mol. Spec.* **220**, 234 (2003).
- [132] I. Kleiner, "Asymmetric-top molecules containing one methyl-like internal rotor: Methods and codes for fitting and predicting spectra," *J. Mol. Spec.* **260**, 1 (2010).
- [133] P. Groner, "Effective rotational Hamiltonian for molecules with two periodic large-amplitude motions," *J. Chem. Phys.* **107**, 4483 (1997).
- [134] H. M. Pickett, J. C. Pearson, and C. E. Miller, "Use of Euler series to fit spectra with application to water," *J. Mol. Spec.* **233**, 174 (2005).
- [135] V. V. Ilyushin, Z. Kisiel, L. Pszczółkowski, H. Mäder, and J. T. Hougen, "A new torsion-rotation fitting program for molecules with a sixfold barrier: Application to the microwave spectrum of toluene," *J. Mol. Spec.* **259**, 26 (2010).
- [136] R. C. Woods, "A General Program for the Calculation of Internal Rotation Splittings in Microwave Spectroscopy," *J. Mol. Spec.* **21**, 4 (1966).
- [137] R. C. Woods, "A General Program for the Calculation of Internal Rotation Splittings in Microwave Spectroscopy : Part II. The n-top problem," *J. Mol. Spec.* **22**, 49 (1967).
- [138] H. Hartwig and H. Dreizler, "The Microwave Spectrum of trans-2,3-Dimethyloxirane in Torsional Excited States." *Z. Naturforsch.* **51a**, 923 (1996).
- [139] C. C. Lin and J. D. Swalen, "Internal Rotation and Microwave Spectroscopy," *Rev. Mod. Phys.* **31**, 841 (1959).
- [140] M. O. Scully and M. S. Zubairy, "Atom-field interaction - semiclassical theory," in *Quantum Optics* (Cambridge University Press, Cambridge, 1997) Chap. 5, pp. 145–192.
- [141] J. von Neumann, *Mathematical Foundations of Quantum Mechanics* (Princeton University Press, Princeton, 1996).
- [142] K. Blum, *Density Matrix Theory and Applications*, 3rd ed. (Springer-Verlag, Berlin, 2011).
- [143] J.-U. Grabow, "Fourier Transform Microwave Spectroscopy Measurement and Instrumentation," in *Handbook of High-resolution Spectroscopy*, Vol. 2, edited by M. Quack and F. Merkt (John Wiley & Sons, Ltd, New York, 2011) pp. 723–800.
- [144] J. C. McGurk, T. G. Schmalz, and W. H. Flygare, "A density matrix, bloch equation description of infrared and microwave transient phenomena," in *Advances in Chemical Physics*, edited by S. A. Rice and I. Prigogine (John Wiley & Sons, Inc., Hoboken, 1975) 25th ed., Chap. 1, pp. 1–68.
- [145] Z. Kisiel, "PROSPE Website," <http://www.ifpan.edu.pl/~kisiel/prospe.htm> (2014).
- [146] H. M. Pickett, "The Fitting and Prediction of Vibration-Rotation Spectra with Spin Interactions," *J. Mol. Spec.* **148**, 371 (1991).
- [147] C. J. Cramer, *Essentials of Computational Chemistry*, 2nd ed. (John Wiley & Sons, Ltd, New York, 2004).
- [148] J. C. Slater, "The Theory of Complex Spectra," *Phys. Rev.* **34**, 1293 (1929).
- [149] D. R. Hartree, "The Wave Mechanics of an Atom with a Non-Coulomb Central Field. Part I. Theory and Methods," *Math. Proc. Cambridge* **24**, 89 (1928).
- [150] D. R. Hartree, "The Wave Mechanics of an Atom with a Non-Coulomb Central Field. Part II. Some Results and Discussion," *Math. Proc. Cambridge* **24**, 111 (1928).
- [151] V. Fock, "Näherungsmethode zur Lösung des quantenmechanischen Mehrkörperproblems," *Z. Phys.* **61**, 126 (1930).
- [152] C. Møller and M. S. Plesset, "Note on an Approximation Treatment for Many-Electron Systems," *Phys. Rev.* **46**, 618 (1934).

- [153] J. Cízek, "On the Correlation Problem in Atomic and Molecular Systems. Calculation of Wavefunction Components in Ursell-Type Expansion Using Quantum-Field Theoretical Methods," *J. Chem. Phys.* **45**, 4256 (1966).
- [154] R. G. Parr, "Density Functional Theory," *Annu. Rev. Phys. Chem.* **34**, 631 (1983).
- [155] P. Hohenberg and W. Kohn, "Inhomogeneous Electron Gas," *Phys. Rev.* **136**, 864 (1964).
- [156] W. Kohn and L. J. Sham, "Self-Consistent Equations Including Exchange and Correlation Effects," *Phys. Rev.* **140**, 1133 (1965).
- [157] A. D. Becke, "A new mixing of Hartree-Fock and local density-functional theories," *J. Chem. Phys.* **98**, 1372 (1993).
- [158] K. Kim and K. D. Jordan, "Comparison of Density Functional and MP2 Calculations on the Water Monomer and Dimer," *J. Phys. Chem.* **98**, 10089 (1994).
- [159] Y. Zhao and D. G. Truhlar, "The M06 suite of density functionals for main group thermochemistry, thermochemical kinetics, noncovalent interactions, excited states, and transition elements: two new functionals and systematic testing of four M06-class functionals and 12 other function," *Theor. Chem. Acc.* **120**, 215 (2008).
- [160] J. C. Slater, "Atomic Shielding Constants," *Phys. Rev.* **36**, 57 (1930).
- [161] S. F. Boys, "Electronic Wave Functions. I. A General Method of Calculation for the Stationary States of Any Molecular System," *P. Roy. Soc. A* **200**, 542 (1950).
- [162] W. J. Hehre, R. F. Stewart, and J. A. Pople, "Self-Consistent Molecular-Orbital Methods. I. Use of Gaussian Expansion of Slater-Type Atomic Orbitals," *J. Chem. Phys.* **51**, 2657 (1969).
- [163] R. Ditchfield, W. J. Hehre, and J. A. Pople, "Self-Consistent Molecular-Orbital Method. IX. An Extended Gaussian-Type Basis for Molecular-Orbital Studies of Organic Molecules," *J. Chem. Phys.* **54**, 724 (1971).
- [164] R. Krishnan, J. S. Binkley, R. Seeger, and J. A. Pople, "Self-consistent molecular orbital methods. XX. A basis set for correlated wave functions," *J. Chem. Phys.* **72**, 650 (1980).
- [165] T. H. Dunning Jr., "Gaussian basis sets for use in correlated molecular calculations. I. The atoms boron through neon and hydrogen," *J. Chem. Phys.* **90**, 1007 (1989).
- [166] D. Feller, "The role of databases in support of computational chemistry calculations," *J. Comput. Chem.* **17**, 1571 (1996).
- [167] C. Puzzarini, J. F. Stanton, and J. Gauss, "Quantum-chemical calculation of spectroscopic parameters for rotational spectroscopy," *Int. Rev. Phys. Chem.* **29**, 273 (2010).
- [168] C. Puzzarini, "Rotational spectroscopy meets theory," *Phys. Chem. Chem. Phys.*, 6595 (2013).
- [169] C. Puzzarini, "Extrapolation to the Complete Basis Set Limit of Structural Parameters : Comparison of Different Approaches," *J. Phys. Chem. A* **113**, 14530 (2009).
- [170] W. Caminati, "Microwave Spectroscopy of Large Molecules and Molecular Complexes," in *Handbook of High-resolution Spectroscopy*, Vol. 2, edited by M. Quack and F. Merkt (John Wiley & Sons, Ltd, New York, 2011) pp. 829–852.
- [171] K. L. Bak, J. Gauss, T. Helgaker, P. Jørgensen, and J. Olsen, "The accuracy of molecular dipole moments in standard electronic structure calculations," *Chem. Phys. Lett.* **319**, 563 (2000).
- [172] S. Stopkiewicz and J. Gauss, "Relativistic corrections to electrical first-order properties using direct perturbation theory," *J. Chem. Phys.* **129**, 164119 (2008).
- [173] W. C. Bailey, "DFT and HF-DFT calculations of  $^{14}\text{N}$  quadrupole coupling constants in molecules," *Chem. Phys.* **252**, 57 (2000).
- [174] J. Liévin, J. Demaison, M. Herman, a. Fayt, and C. Puzzarini, "Comparison of the experimental, semi-experimental and ab initio equilibrium structures of acetylene: influence of relativistic effects and of the diagonal Born-Oppenheimer corrections," *J. Chem. Phys.* **134**, 064119 (2011).
- [175] B. C. Dian, A. Longarte, and T. S. Zwier, "Conformational dynamics in a dipeptide after single-mode vibrational excitation," *Science* **296**, 2369 (2002).
- [176] S. G. Kukolich and L. C. Sarkozy, "Design, construction, and testing of a large-cavity, 1-10 GHz Flygare-Balle spectrometer," *Rev. Sci. Instrum.* **82**, 094103 (2011).
- [177] N. F. Ramsey, *Molecular Beams* (Oxford University Press, Oxford, 1985).

- [178] J. B. Fenn, "Electrospray wings for molecular elephants (Nobel lecture)," *Angew. Chem. Int. Ed.* **42**, 3871 (2003).
- [179] N. F. Ramsey, "Thermal Beam Sources," in *Experimental Methods in the Physical Sciences - Atomic, Molecular, and Optical Physics: Atoms and Molecules*, Vol. 29, edited by F. Dunning and R. G. Hulet (Academic Press, Waltham, 1996) Chap. 1, pp. 1–20.
- [180] W. Gerlach and Otto Stern, "Der experimentelle Nachweis der Richtungsquantelung im Magnetfeld," *Z. Phys.* **9**, 349 (1922).
- [181] W. Gerlach and O. Stern, "Das magnetische Moment des Silberatoms." *Z. Phys.* **9**, 353 (1922).
- [182] M. D. Morse, "Supersonic Beam Sources," in *Experimental Methods in the Physical Sciences - Atomic, Molecular, and Optical Physics: Atoms and Molecules*, Vol. 29, edited by F. Dunning and R. G. Hulet (Academic Press, Waltham, 1996) Chap. 2, pp. 21–47.
- [183] D. R. Miller, "Free Jet Sources," in *Atomic and Molecular Beam Methods*, Vol. 1, edited by G. Scoles (Oxford University Press, Oxford, 1988) Chap. 2, pp. 14–53.
- [184] D. H. Levy, "Laser Spectroscopy of Cold Gas-Phase Molecules," *Annu. Rev. Phys. Chem.* **31**, 197 (1980).
- [185] R. Jost, "The Cooling of Internal Degrees of Freedom of Polyatomic Molecules in Supersonic Free Jets," in *Low Temperature Molecular Spectroscopy*, edited by R. Fausto (Springer-Verlag, Berlin, 1996) pp. 249–70.
- [186] K. Wohlfart, M. Schnell, J.-U. Grabow, and J. Küpper, "Precise dipole moment and quadrupole coupling constants of benzonitrile," *J. Mol. Spec.* **247**, 119 (2008).
- [187] W. M. Hayes, D. R. Lide, and T. J. Bruno, eds., *CRC Handbook of Chemistry and Physics*, 95th ed. (Taylor & Francis Ltd., Oxford, 2014).
- [188] B. Broers, L. D. Noordam, and H. B. van Linden van den Heuvell, "Diffraction and focusing of spectral energy in multiphoton processes," *Phys. Rev. A* **46**, 2749 (1992).
- [189] B. Broers, H. B. van Linden van den Heuvell, and L. D. Noordam, "Efficient Population Transfer in a Three-Level Ladder System by Frequency-Swept Ultrashort Laser Pulses," *Phys. Rev. Lett.* **69**, 25 (1992).
- [190] P. Balling, D. J. Maas, and L. D. Noordam, "Interference in climbing a quantum ladder system with frequency-chirped laser pulses," *Phys. Rev. A* **50**, 4276 (1994).
- [191] D. Maas, C. Rella, P. Antoine, E. Toma, and L. Noordam, "Population transfer via adiabatic passage in the rubidium quantum ladder system," *Phys. Rev. A* **59**, 1374 (1999).
- [192] G. Włodarczak, J. Burie, J. Demaison, K. Vormann, and A. Császár, "The Rotational Spectrum of Benzonitrile : Experimental and Theoretical Determination of the Quartic Centrifugal Distortion Constants," *J. Mol. Spec.* **134**, 297 (1989).
- [193] J. Casado, L. Nygaard, and G. O. Sørensen, "Microwave spectra of isotopic benzonitriles. Refined molecular structure of benzonitrile." *J. Mol. Struct.* **8**, 211 (1970).
- [194] H. D. Rudolph, J. Demaison, and A. G. Császár, "Accurate determination of the deformation of the benzene ring upon substitution: equilibrium structures of benzonitrile and phenylacetylene." *J. Phys. Chem.* **117**, 12969 (2013).
- [195] M. Schmitt, M. Böhm, C. Ratzer, S. Siegert, M. V. Beek, and W. L. Meerts, "Electronic excitation in the benzonitrile dimer: The intermolecular structure in the  $S_0$  and  $S_1$  state determined by rotationally resolved electronic spectroscopy," *J. Mol. Struct.* **795**, 234 (2006).
- [196] W. L. Meerts, M. Schmitt, and G. C. Groenenboom, "New applications of the genetic algorithm for the interpretation of high-resolution spectra," *Can. J. Chemistry* **82**, 804 (2004).
- [197] D. R. Borst, D. W. Pratt, and M. Schäfer, "Molecular recognition in the gas phase. Dipole-bound complexes of benzonitrile with water, ammonia, methanol, acetonitrile, and benzonitrile itself," *Phys. Chem. Chem. Phys.* **9**, 4563 (2007).
- [198] V. A. Shubert, D. Schmitz, and M. Schnell, "Communication through the phenyl ring: internal rotation and nuclear quadrupole splitting in *p*-halotoluenes," *Mol. Phys.* **111**, 2189 (2013).
- [199] G. A. Blake, E. C. Sutton, C. R. Masson, and T. G. Phillips, "Molecular abundance in OMC-1: the chemical composition of interstellar molecular clouds and the influence of massive star formation," *Astrophys. J.* **315**, 621 (1987).



- [200] Y. Miao, D. M. Mehringer, Y.-J. Kuan, and L. E. Snyder, "Complex molecules in Sagittarius B2(N): the importance of grain chemistry," *Astrophys. J.* **445**, 59 (1995).
- [201] "The Karl G. Jansky Very Large Array," <https://science.nrao.edu/facilities/vla> (2014).
- [202] D. W. Pratt, "High-resolution Spectroscopy in the Gas Phase: Even Large Molecules Have Well-Defined Shapes," *Annu. Rev. Phys. Chem.* **49**, 481 (1998).
- [203] L. H. Spangler, "Structural Information from methyl internal rotation spectroscopy," *Annu. Rev. Phys. Chem.* **58**, 481 (1997).
- [204] L. B. Favero, J.-U. Grabow, and W. Caminati, "Morphing the Torsional Potential Energy Function from Local to Global Symmetry through a  $\pi$  Link: The Rotational Spectrum of  $\alpha,\alpha,\alpha$ -Trifluoro-p-tolualdehyde," *Chem. Eur. J.* **18**, 2468 (2012).
- [205] J. Rottstegge, H. Hartwig, and H. Dreizler, "The rotational spectrum, structure and barrier  $V_6$  to internal rotation of *p*-fluorotoluene," *J. Mol. Struct.* **478**, 37 (1999).
- [206] M. J. Frisch, G. W. Trucks, H. B. Schlegel, G. E. Scuseria, M. A. Robb, J. R. Cheeseman, J. A. Montgomery Jr., T. Vreven, et al., "Gaussian 03, Revision C.02," (2004).
- [207] M. J. Frisch, G. W. Trucks, H. B. Schlegel, G. E. Scuseria, M. A. Robb, J. R. Cheeseman, G. Scalmani, V. Barone, et al., "Gaussian 09, Revision A.1," (2009).
- [208] K. A. Peterson, B. C. Shepler, D. Figgen, and H. Stoll, "On the Spectroscopic and Thermochemical Properties of ClO, BrO, IO, and Their Anions," *J. Phys. Chem. A* **110**, 13877 (2006).
- [209] K. L. Schuchardt, B. T. Didier, T. Elsethagen, L. Sun, V. Gurumoorthi, J. Chase, J. Li, and T. L. Windus, "Basis Set Exchange: A Community Database for Computational Sciences," *J. Chem. Inf. Model.* **47**, 1045 (2007).
- [210] M. N. Glukhovtsev, A. Pross, M. P. McGrath, and L. Radom, "Extension of Gaussian-2 (G2) theory to bromine- and iodine-containing molecules: Use of effective core potentials," *J. Chem. Phys.* **103**, 1878 (1995).
- [211] G. E. Herberich, "Mikrowellenspektrum, Hinderungspotential der internen Rotation und teilweise  $r_0$ -Struktur des para-Chlorotoluols," *Z. Naturforsch.* **22a**, 761 (1967).
- [212] L.-H. Xu and J. T. Hougen, "Global Fit of Torsional-Rotational Transitions in the Ground and First Excited Torsional States of Methanol," *J. Mol. Spec.* **173**, 540 (1995).
- [213] A. Legon and J. Thorn, "Equilibrium nuclear quadrupole coupling constants from the rotational spectrum of BrCl: a source of the electric quadrupole moment ratios  $Q(^{79}\text{Br})/Q(^{81}\text{Br})$  and  $Q(^{35}\text{Cl})/Q(^{37}\text{Cl})$ ," *Chem. Phys. Lett.* **215**, 554 (1993).
- [214] S. A. Peebles and R. A. Peebles, "Determination of the heavy atom structure of bromobenzene by rotational spectroscopy," *J. Mol. Struct.* **657**, 107 (2003).
- [215] I. Merke, C. Keussen, H. Dreizler, and M. Onda, "Quadrupole Hyperfine Structure in the Rotational Spectra of 1,2- and 1,3-Dichlorobenzene," *Z. Naturforsch.* **45a**, 1273 (1990).
- [216] D. R. Borst and D. W. Pratt, "Toluene: Structure, dynamics, and barrier to methyl group rotation in its electronically excited state. A route to IVR," *J. Chem. Phys.* **113**, 3658 (2000).
- [217] P. C. Chen and C. W. Wu, "Ab Initio Molecular Orbital Study of Toluene and Its Derivatives," *J. Phys. Chem.* **99**, 15023 (1995).
- [218] K.-T. Lu, F. Weinhold, and J. C. Weisshaar, "Understanding barriers to internal rotation in substituted toluenes and their cations," *J. Chem. Phys.* **102**, 6787 (1995).
- [219] D. Schmitz, V. A. Shubert, B. M. Giuliano, and M. Schnell, "The broadband microwave spectra of the monoterpenoids thymol and carvacrol: Conformational landscape and internal dynamics," *J. Chem. Phys.* **141**, 034304 (2014).
- [220] K.-H. Wagner and I. Elmadfa, "Biological Relevance of Terpenoids," *Ann. Nutr. Metab.* **47**, 95 (2003).
- [221] M. Kanakidou, J. H. Seinfeld, S. N. Pandis, I. Barnes, F. J. Dentener, M. C. Facchini, R. Van Dingenen, B. Ervens, et al., "Organic aerosol and global climate modelling: a review," *Atmos. Chem. Phys.* **5**, 1053 (2005).
- [222] A. Guenther, C. N. Hewitt, D. Erickson, R. Fall, C. Geron, T. Graedel, P. Harley, L. Klinger, et al., "A global model of natural volatile organic compound emission," *J. Geophys. Res.* **100**, 8873 (1995).

- [223] A. P. Bateman, S. A. Nizkorodov, J. Laskin, and A. Laskin, "Photolytic processing of secondary organic aerosols dissolved in cloud droplets." *Phys. Chem. Chem. Phys.* **13**, 12199 (2011).
- [224] J. Lelieveld, T. M. Butler, J. N. Crowley, T. J. Dillon, H. Fischer, L. Ganzeveld, H. Harder, M. G. Lawrence, et al., "Atmospheric oxidation capacity sustained by a tropical forest." *Nature* **452**, 737 (2008).
- [225] H. V. L. Nguyen, H. Mouhib, S. Klahm, W. Stahl, and I. Kleiner, "A touch of lavender: gas-phase structure and dynamics of the monoterpene linalool validated by microwave spectroscopy." *Phys. Chem. Chem. Phys.* **15**, 10012 (2013).
- [226] J. R. Avilés Moreno, F. Partal Ureña, J. J. López González, and T. R. Huet, "Terpenes in the gas phase: The structural conformation of S-(-)-perillaldehyde investigated by microwave spectroscopy and quantum chemical calculations," *Chem. Phys. Lett.* **473**, 17 (2009).
- [227] J. R. Avilés Moreno, T. R. Huet, and J. J. López González, "Conformational relaxation of S-(+)-carvone and R-(+)-limonene studied by microwave Fourier transform spectroscopy and quantum chemical calculations," *Struct. Chem.* **24**, 1163 (2012).
- [228] Z. Kisiel, O. Desyatnyk, E. Bialkowska-Jaworska, and L. Pszczółkowski, "The structure and electric dipole moment of camphor determined by rotational spectroscopy," *Phys. Chem. Chem. Phys.* **5**, 820 (2003).
- [229] W.-X. Du, C. W. Olsen, R. J. Avena-Bustillos, T. H. McHugh, C. E. Levin, and M. Friedman, "Storage stability and antibacterial activity against Escherichia coli O157:H7 of carvacrol in edible apple films made by two different casting methods." *J. Agr. Food Chem.* **56**, 3082 (2008).
- [230] J. Xu, F. Zhou, B.-P. Ji, R.-S. Pei, and N. Xu, "The antibacterial mechanism of carvacrol and thymol against Escherichia coli." *Lett. Appl. Microbiol.* **47**, 174 (2008).
- [231] A. Ben Arfa, S. Combes, L. Preziosi-Belloy, N. Gontard, and P. Chalier, "Antimicrobial activity of carvacrol related to its chemical structure." *Lett. Appl. Microbiol.* **43**, 149 (2006).
- [232] P. C. Braga, M. Dal Sasso, M. Culici, T. Bianchi, L. Bordoni, and L. Marabini, "Anti-inflammatory activity of thymol: inhibitory effect on the release of human neutrophil elastase." *Pharmacology* **77**, 130 (2006).
- [233] M. A. Numpaque, L. A. Oviedo, J. H. Gil, C. M. García, and D. L. Durango, "Thymol and carvacrol : biotransformation and antifungal activity against the plant pathogenic fungi Colletotrichum acutatum and Botryodiplodia theobromae," *Trop. Plant Pathol.* **36**, 3 (2011).
- [234] A. Welzel, A. Hellweg, I. Merke, and W. Stahl, "Structural and Torsional Properties of *o*-Cresol and *o*-Cresol-OD as Obtained from Microwave Spectroscopy and ab Initio Calculations," *J. Mol. Spec.* **215**, 58 (2002).
- [235] A. Hellweg, C. Hättig, I. Merke, and W. Stahl, "Microwave and theoretical investigation of the internal rotation in *m*-cresol." *J. Chem. Phys.* **124**, 204305 (2006).
- [236] S. T. Shipman, J. L. Neill, R. D. Suenram, M. T. Muckle, and B. H. Pate, "Structure Determination of Strawberry Aldehyde by Broadband," *J. Phys. Chem. Lett.* **2**, 443 (2011).
- [237] N. Hansen, H. Mäder, and T. Bruhn, "A molecular beam Fourier transform microwave study of *o*-tolunitrile:  $^{14}\text{N}$  nuclear quadrupole coupling and methyl internal rotation effects," *Mol. Phys.* **97**, 587 (1999).
- [238] P. Écija, L. Evangelisti, M. Vallejo, F. J. Basterretxea, A. Lesarri, F. Castaño, W. Caminati, and E. J. Cocinero, "Conformational Flexibility of Mephenesin." *J. Phys. Chem. B* **118**, 5357 (2014).
- [239] H. Rudolph, K. Walzer, and I. Krutzig, "Microwave Spectrum, Barrier for Methyl Rotation, Methyl Conformation, and Dipole Moment of Ortho-Xylene," *J. Mol. Spec.* **47**, 314 (1973).
- [240] D. Schmitz, V. A. Shubert, T. Betz, and M. Schnell, "Exploring the conformational landscape of menthol menthone and isomenthone: A microwave study," *Front. Chem.* **3**, 1 (2014).
- [241] R. Kotan, S. Kordali, and A. Cakir, "Screening of antibacterial activities of twenty-one oxygenated monoterpenes." *Z. Naturforsch. C* **62**, 507 (2007).
- [242] D. L. McKay and J. B. Blumberg, "A Review of the Bioactivity and Potential Health Benefits of Peppermint Tea (*Mentha piperita* L.)," *Phytother. Res.* **20**, 619 (2006).

- [243] D. M. Bautista, J. Siemens, J. M. Glazer, P. R. Tsuruda, A. I. Basbaum, C. L. Stucky, S.-E. Jordt, and D. Julius, "The menthol receptor TRPM8 is the principal detector of environmental cold." *Nature* **448**, 204 (2007).
- [244] G. P. P. Kamatou, I. Vermaak, A. M. Viljoen, and B. M. Lawrence, "Menthol: a simple monoterpene with remarkable biological properties." *Phytochemistry* **96**, 15 (2013).
- [245] R. Eccles, "Menthol and related cooling compounds." *J. Pharm. Pharmacol.* **46**, 618 (1994).
- [246] R. S. Cahn, C. Ingold, and V. Prelog, "Spezifikation der molekularen Chiralität," *Angew. Chem.* **78**, 413 (1966).
- [247] T. Harada, Y. Kagamihara, S. Tanaka, K. Sakamoto, and A. Oku, "A Highly Convergent Asymmetric Synthesis of the C(19)-C(27) Segment of Rifamycin S: An Application of Enantiodifferentiating Acetalization with Menthone," *J. Org. Chem.* **57**, 1637 (1992).
- [248] K. R. Brain, D. M. Green, P. J. Dykes, R. Marks, and T. S. Bola, "The role of menthol in skin penetration from topical formulations of ibuprofen 5% in vivo." *Skin Pharmacol. Physiol.* **19**, 17 (2006).
- [249] K. Zhao, S. Singh, and J. Singh, "Effect of menthone on the in vitro percutaneous absorption of tamoxifen and skin reversibility." *Int. J. Pharm.* **219**, 177 (2001).
- [250] V. A. Shubert, D. Schmitz, and M. Schnell, "Enantiomer-sensitive spectroscopy and mixture analysis of chiral molecules containing two stereogenic centers - Microwave three-wave mixing of menthone," *J. Mol. Spec.* **300**, 31 (2014).
- [251] M. Albrecht, J. Will, and M. A. Suhm, "Chirality Recognition in Menthol and Neomenthol: Preference for Homoconfigurational Aggregation." *Angew. Chem. Int. Ed.* **49**, 6203 (2010).
- [252] J. Härtner and U. M. Reinscheid, "Conformational analysis of menthol diastereomers by NMR and DFT computation," *J. Mol. Struct.* **872**, 145 (2008).
- [253] T. Egawa, M. Sakamoto, H. Takeuchi, and S. Konaka, "Structural Determination of Menthol and Isomenthol, a Minty Compound and Its Nonminty Isomer, by Means of Gas Electron Diffraction Augmented by Theoretical Calculations," *J. Phys. Chem. A* **107**, 2757 (2003).
- [254] J. R. Avilés Moreno, F. Partal Ureña, and J. J. López González, "Hydrogen bonding network in a chiral alcohol: (1R,2S,5R)-(-)-menthol. Conformational preference studied by IR-Raman-VCD spectroscopies and quantum chemical calculations," *Struct. Chem.* **24**, 671 (2013).
- [255] W. B. Smith and C. Amezcua, "NMR versus molecular modelling : menthone and isomenthone," *Magn. Reson. Chem.* **36**, 3 (1998).
- [256] M. J. Frisch, G. W. Trucks, H. B. Schlegel, G. E. Scuseria, M. A. Robb, J. R. Cheeseman, G. Scalmani, V. Barone, et al., "Gaussian 09, Revision A.02," (2009).
- [257] W. L. Meerts and M. Schmitt, "A new automated assign and analysing method for high-resolution rotationally resolved spectra using genetic algorithms," *Phys. Scr.* **73**, C47 (2006).
- [258] N. A. Seifert, I. A. Finneran, C. Perez, D. P. Zaleski, J. L. Neill, A. L. Steber, Richard D. Suenram, A. Lesarri, et al., "Autofit, an Automated Fitting Tool for Broadband Rotational Spectra, and Applications to 1-Hexanal," *J. Mol. Spec.* **312**, 13 (2015).
- [259] N. A. Seifert, S. Lobsiger, B. H. Pate, G. A. Guirgis, J. S. Overby, and J. R. Durig, "Substitution Structures of Multiple Silicon-Containing Species by Chirped Pulse FTMW Spectroscopy," *Talk at the 68th International Symposium on Molecular Spectroscopy at Ohio State University* **RC12** (2013).
- [260] D. Schmitz, V. A. Shubert, D. Patterson, A. Krin, and M. Schnell, "Phase Dependence of Double-Resonance Experiments in Rotational Spectroscopy," *J. Phys. Chem. Lett.* **6**, 1493 (2015).
- [261] P. J. Stephens, "Theory of Vibrational Circular Dichroism," *J. Phys. Chem.* **89**, 748 (1985).
- [262] C. Guo, R. D. Shah, R. K. Dukor, X. Cao, T. B. Freedman, and L. A. Nafie, "Determination of enantiomeric excess in samples of chiral molecules using fourier transform vibrational circular dichroism spectroscopy: simulation of real-time reaction monitoring." *Anal. Chem.* **76**, 6956 (2004).
- [263] L. Nahon, G. A. Garcia, C. J. Harding, E. Mikajlo, and I. Powis, "Determination of chiral asymmetries in the valence photoionization of camphor enantiomers by photoelectron imaging using tunable circularly polarized light," *J. Chem. Phys.* **125**, 114309 (2006).
- [264] H. Rhee, J.-H. Choi, and M. Cho, "Infrared optical activity: electric field approaches in time domain." *Accounts of chemical research* **43**, 1527 (2010).

- [265] C. Lux, M. Wollenhaupt, T. Bolze, Q. Liang, J. Köhler, C. Sarpe, and T. Baumert, "Circular dichroism in the photoelectron angular distributions of camphor and fenchone from multiphoton ionization with femtosecond laser pulses," *Angew. Chem. Int. Ed.* **51**, 5001 (2012).
- [266] N. Bhargava Ram, C. S. Lehmann, and M. H. M. Janssen, "Probing chirality with a femtosecond reaction microscope," *EPJ Web of Conferences* **41**, 02029 (2013).
- [267] M. Pitzer, M. Kunitski, A. S. Johnson, T. Jahnke, H. Sann, F. Sturm, L. P. H. Schmidt, H. Schmidt-Böcking, et al., "Direct determination of absolute molecular stereochemistry in gas phase by Coulomb explosion imaging." *Science* **341**, 1096 (2013).
- [268] E. Hirota, "Triple resonance for a three-level system of a chiral molecule," *P. Jpn. Acad. B* **88**, 120 (2012).
- [269] D. Patterson, M. Schnell, and J. M. Doyle, "Enantiomer-specific detection of chiral molecules via microwave spectroscopy," *Nature* **497**, 475 (2013).
- [270] D. Patterson and J. M. Doyle, "Sensitive Chiral Analysis via Microwave Three-Wave Mixing," *Phys. Rev. Lett.* **111**, 023008 (2013).
- [271] M. Quack, J. Stohner, and M. Willeke, "High-resolution spectroscopic studies and theory of parity violation in chiral molecules." *Annu. Rev. Phys. Chem.* **59**, 741 (2008).
- [272] E. Jones, T. Oliphant, and P. Peterson, "SciPy: Open Source Scientific Tools for Python," *SciPy: Open Source Scientific Tools for Python* (2001).
- [273] C. Cohen-Tannoudji, J. Dupont-Roc, and G. Grynberg, "The Dressed Atom Approach," in *Atom-Photon Interactions Basic: Processes and Applications* (Wiley-VCH Verlag GmbH & Co. KGaA, Weinheim, 2004) Chap. 6, pp. 407–514.
- [274] S. H. Autler and C. H. Townes, "Stark Effect in Rapidly Varying Fields," *Phys. Rev.* **100**, 703 (1955).
- [275] B. D. Gerardot, D. Brunner, P. A. Dalgarno, K. Karrai, A. Badolato, P. M. Petroff, and R. J. Warburton, "Dressed excitonic states and quantum interference in a three-level quantum dot ladder system," *New J. Phys.* **11**, 013028 (2009).
- [276] J.-U. Grabow, "Fourier transform microwave spectroscopy: handedness caught by rotational coherence." *Angew. Chem. Int. Ed.* **52**, 11698 (2013).
- [277] A. D. McNaught and A. Wilkinson, *Compendium of Chemical Terminology - Gold Book* (Blackwell Science, Oxford, 1997).
- [278] W. Vetter and K. Bester, "Gas chromatographic enantioseparation of chiral pollutants-techniques and results," in *Chiral Analysis*, edited by K. Busch and M. Busch (Elsevier B.V., Amsterdam, 2006) Chap. 6, pp. 196–213.
- [279] I. Bronstein, K. Semendjaew, G. Grosche, V. Ziegler, and D. Ziegler, *Springer-Taschenbuch der Mathematik*, edited by E. Zeidler (Springer Fachmedien, Wiesbaden, 2013) p. 395.

# Acknowledgments

An dieser Stelle möchte ich mich bei allen bedanken, die das Zustandekommen dieser Arbeit unterstützt haben.

Mein besonderer Dank gilt meiner Betreuerin Melanie Schnell am Max-Planck-Institut für Struktur und Dynamik der Materie, die meine Arbeit geduldig und mit viel Hingabe begleitet hat. Ihre offene Art und ihr Vertrauen in mich haben es mir sehr leicht gemacht, selbstständig zu arbeiten und auch meine vielen Auslandsaufenthalte hätte ich ohne ihre Unterstützung nicht verwirklichen können. Vielen Dank für die kleinen und großen Korrekturen an meiner Arbeit. Es hat mir großen Spaß gemacht, in deiner Gruppe zu arbeiten.

I thank Dwayne Miller for co-supervising my thesis. Even though his schedule is extremely packed when he is in Hamburg, he found time for me to discuss the progress of my thesis, whenever it was needed.

I thank Alvin Shubert for sharing such a great time with me. You are the best team-mate one can hope for. You taught me how to perform the experiments, analyze the data, and write a publication. Thank you for all that and also for proof-reading my thesis with so much care.

I want to thank David Patterson for helping me with the experiments and the analysis of the double-resonance and three-wave mixing experiments. I thank Jens-Uwe Grabow for the interesting and helpful discussions about  $M$ -states,  $\pi$ -pulses, and trigger systems.

Ich danke Thomas Betz für seine Hilfe bei der Analyse des Mentholspektrums, Anna Krin für die Doppelresonanzmessungen von Isomenthon und Michela Giuliano für ihre Hilfe bei der Messung und der Analyse des Thymolspektrums.

Ich danke Sabrina Zinn and Simon Merz dafür, dass sie es so lange mit mir in einem Büro ausgehalten haben. Ihre humorvolle und hilfsbereite Art, der warme Kaffee am Morgen und die Schoko-Lade haben mir Tag für Tag die Arbeit versüßt.

I would like to thank the CoComol group, Chris Medcraft, Jack Graneek, Cristobal Perez, Amanda Steber, Anna Krin, Thomas Betz, and Sergios Domingos for providing such a nice working atmosphere. I will miss the senseless discussions about islands, warm beer, and croquet.

Many thanks to Wolfgang Jäger, Yunjie Xu, Steve Dempster, Christian Merten, and Javix Thomas that gave me a warm welcome, when I experienced the Canadian winter.

Meiner Freundin Julia und meinem Sohn Lasse danke ich für die Geduld und das Vertrauen, dass ich tatsächlich irgendwann fertig werde. Ihr seid meine Motivation und mein Ansporn. Diese Arbeit ist nur für Euch.

# Selbständigkeitserklärung

Ich versichere an Eides statt, dass ich die Inanspruchnahme fremder Hilfen aufgeführt habe, sowie, dass ich die wörtlich oder inhaltlich aus anderen Quellen entnommenen Stellen als solche kenntlich gemacht habe.

Hamburg, den

---

Unterschrift

## Appendix A

# Three-level optical Bloch equations

The three-level optical equations are derived by computing the commutator of the Liouville equation 7.7. The following set of ordinary differential equations is derived for the progressive regime (using the Hamiltonian in Eqn. 7.3):

$$\begin{aligned} i\hbar \frac{\partial \rho_{aa}}{\partial t} &= -\frac{\mathcal{E}_{ab}}{2} (\mu_{ab}\rho_{ba} - \mu_{ab}^*\rho_{ab}) (e^{i\omega_{ab}t} + e^{-i\omega_{ab}t}) \\ i\hbar \frac{\partial \rho_{bb}}{\partial t} &= \frac{\mathcal{E}_{ab}}{2} (\mu_{ab}^*\rho_{ab} - \mu_{ab}\rho_{ba}) (e^{i\omega_{ab}t} + e^{-i\omega_{ab}t}) + \frac{\mathcal{E}_{bc}}{2} (\mu_{bc}\rho_{cb} - \mu_{bc}^*\rho_{bc}) (e^{i\omega_{bc}t} + e^{-i\omega_{bc}t}) \\ i\hbar \frac{\partial \rho_{cc}}{\partial t} &= -\frac{\mathcal{E}_{bc}}{2} (\mu_{bc}^*\rho_{bc} - \mu_{bc}\rho_{cb}) (e^{i\omega_{bc}t} + e^{-i\omega_{bc}t}) \\ i\hbar \frac{\partial \rho_{ab}}{\partial t} &= -\hbar\omega_{ab,0}\rho_{ab} - \frac{\mathcal{E}_{ab}\mu_{ab}}{2} (\rho_{bb} - \rho_{aa}) (e^{i\omega_{ab}t} + e^{-i\omega_{ab}t}) + \frac{\mathcal{E}_{bc}\mu_{bc}^*}{2}\rho_{ac} (e^{i\omega_{bc}t} + e^{-i\omega_{bc}t}) \\ i\hbar \frac{\partial \rho_{ac}}{\partial t} &= -\hbar\omega_{ac,0}\rho_{ac} - \frac{\mathcal{E}_{ab}\mu_{ab}}{2}\rho_{bc} (e^{i\omega_{ab}t} + e^{-i\omega_{ab}t}) + \frac{\mathcal{E}_{bc}\mu_{bc}}{2}\rho_{ab} (e^{i\omega_{bc}t} + e^{-i\omega_{bc}t}) \\ i\hbar \frac{\partial \rho_{ba}}{\partial t} &= \hbar\omega_{ab,0}\rho_{ba} - \frac{\mathcal{E}_{ab}\mu_{ab}^*}{2} (\rho_{aa} - \rho_{bb}) (e^{i\omega_{ab}t} + e^{-i\omega_{ab}t}) - \frac{\mathcal{E}_{bc}\mu_{bc}}{2}\rho_{ca} (e^{i\omega_{bc}t} + e^{-i\omega_{bc}t}) \\ i\hbar \frac{\partial \rho_{bc}}{\partial t} &= -\hbar\omega_{bc,0}\rho_{bc} - \frac{\mathcal{E}_{ab}\mu_{ab}^*}{2}\rho_{ac} (e^{i\omega_{ab}t} + e^{-i\omega_{ab}t}) - \frac{\mathcal{E}_{bc}\mu_{bc}}{2} (\rho_{cc} - \rho_{bb}) (e^{i\omega_{bc}t} + e^{-i\omega_{bc}t}) \\ i\hbar \frac{\partial \rho_{ca}}{\partial t} &= \hbar\omega_{ac,0}\rho_{ca} + \frac{\mathcal{E}_{ab}\mu_{ab}^*}{2}\rho_{cb} (e^{i\omega_{ab}t} + e^{-i\omega_{ab}t}) - \frac{\mathcal{E}_{bc}\mu_{bc}^*}{2}\rho_{ba} (e^{i\omega_{bc}t} + e^{-i\omega_{bc}t}) \\ i\hbar \frac{\partial \rho_{cb}}{\partial t} &= \hbar\omega_{bc,0}\rho_{cb} + \frac{\mathcal{E}_{ab}\mu_{ab}}{2}\rho_{ca} (e^{i\omega_{ab}t} + e^{-i\omega_{ab}t}) - \frac{\mathcal{E}_{bc}\mu_{bc}^*}{2} (\rho_{bb} - \rho_{cc}) (e^{i\omega_{bc}t} + e^{-i\omega_{bc}t}) \end{aligned}$$

for the  $\Lambda$ -type regressive regime (using the Hamiltonian in Eqn. 7.4):

$$\begin{aligned}
i\hbar \frac{\partial \rho_{aa}}{\partial t} &= -\frac{\mathcal{E}_{ac}}{2} (\mu_{ac}\rho_{ca} - \mu_{ac}^*\rho_{ac}) (e^{i\omega_{ac}t} + e^{-i\omega_{ac}t}) \\
i\hbar \frac{\partial \rho_{bb}}{\partial t} &= -\frac{\mathcal{E}_{bc}}{2} (\mu_{bc}\rho_{cb} - \mu_{bc}^*\rho_{bc}) (e^{i\omega_{bc}t} + e^{-i\omega_{bc}t}) \\
i\hbar \frac{\partial \rho_{cc}}{\partial t} &= \frac{\mathcal{E}_{ac}}{2} (\mu_{ac}\rho_{ca} - \mu_{ac}^*\rho_{ac}) (e^{i\omega_{ac}t} + e^{-i\omega_{ac}t}) \frac{\mathcal{E}_{bc}}{2} (\mu_{bc}\rho_{cb} - \mu_{bc}^*\rho_{bc}) (e^{i\omega_{bc}t} + e^{-i\omega_{bc}t}) \\
i\hbar \frac{\partial \rho_{ab}}{\partial t} &= -\hbar\omega_{ab,0}\rho_{ab} - \frac{\mathcal{E}_{ac}\mu_{ac}}{2}\rho_{cb} (e^{i\omega_{ac}t} + e^{-i\omega_{ac}t}) + \frac{\mathcal{E}_{bc}\mu_{bc}^*}{2}\rho_{ac} (e^{i\omega_{bc}t} + e^{-i\omega_{bc}t}) \\
i\hbar \frac{\partial \rho_{ac}}{\partial t} &= -\hbar\omega_{ac,0}\rho_{ac} - \frac{\mathcal{E}_{ac}\mu_{ac}}{2} (\rho_{cc} - \rho_{aa}) (e^{i\omega_{ac}t} + e^{-i\omega_{ac}t}) + \frac{\mathcal{E}_{bc}\mu_{bc}}{2}\rho_{ab} (e^{i\omega_{bc}t} + e^{-i\omega_{bc}t}) \\
i\hbar \frac{\partial \rho_{ba}}{\partial t} &= \hbar\omega_{ab,0}\rho_{ba} + \frac{\mathcal{E}_{ac}\mu_{ac}^*}{2}\rho_{bc} (e^{i\omega_{ac}t} + e^{-i\omega_{ac}t}) - \frac{\mathcal{E}_{bc}\mu_{bc}}{2}\rho_{ca} (e^{i\omega_{bc}t} + e^{-i\omega_{bc}t}) \\
i\hbar \frac{\partial \rho_{bc}}{\partial t} &= -\hbar\omega_{bc,0}\rho_{bc} + \frac{\mathcal{E}_{ac}\mu_{ac}}{2}\rho_{ba} (e^{i\omega_{ac}t} + e^{-i\omega_{ac}t}) - \frac{\mathcal{E}_{bc}\mu_{bc}}{2} (\rho_{cc} - \rho_{bb}) (e^{i\omega_{bc}t} + e^{-i\omega_{bc}t}) \\
i\hbar \frac{\partial \rho_{ca}}{\partial t} &= \hbar\omega_{ac,0}\rho_{ca} + \frac{\mathcal{E}_{ac}\mu_{ac}^*}{2} (\rho_{cc} - \rho_{aa}) (e^{i\omega_{ac}t} + e^{-i\omega_{ac}t}) - \frac{\mathcal{E}_{bc}\mu_{bc}^*}{2}\rho_{ba} (e^{i\omega_{bc}t} + e^{-i\omega_{bc}t}) \\
i\hbar \frac{\partial \rho_{cb}}{\partial t} &= \hbar\omega_{bc,0}\rho_{cb} - \frac{\mathcal{E}_{ac}\mu_{ac}^*}{2}\rho_{ab} (e^{i\omega_{ac}t} + e^{-i\omega_{ac}t}) + \frac{\mathcal{E}_{bc}\mu_{bc}^*}{2} (\rho_{cc} - \rho_{bb}) (e^{i\omega_{bc}t} + e^{-i\omega_{bc}t})
\end{aligned}$$

and for the V-type regressive regime (using the Hamiltonian in Eqn. 7.5):

$$\begin{aligned}
i\hbar \frac{\partial \rho_{aa}}{\partial t} &= \frac{\mathcal{E}_{ab}}{2} (\mu_{ab}^*\rho_{ab} - \mu_{ab}\rho_{ba}) (e^{i\omega_{ab}t} + e^{-i\omega_{ab}t}) + \frac{\mathcal{E}_{ac}}{2} (\mu_{ac}^*\rho_{ac} - \mu_{ac}\rho_{ca}) (e^{i\omega_{ac}t} + e^{-i\omega_{ac}t}) \\
i\hbar \frac{\partial \rho_{bb}}{\partial t} &= -\frac{\mathcal{E}_{ab}}{2} (\mu_{ab}^*\rho_{ab} - \mu_{ab}\rho_{ba}) (e^{i\omega_{ab}t} + e^{-i\omega_{ab}t}) \\
i\hbar \frac{\partial \rho_{cc}}{\partial t} &= -\frac{\mathcal{E}_{ac}}{2} (\mu_{ac}^*\rho_{ac} - \mu_{ac}\rho_{ca}) (e^{i\omega_{ac}t} + e^{-i\omega_{ac}t}) \\
i\hbar \frac{\partial \rho_{ab}}{\partial t} &= -\hbar\omega_{ab,0}\rho_{ab} - \frac{\mathcal{E}_{ab}\mu_{ab}}{2} (\rho_{bb} - \rho_{aa}) (e^{i\omega_{ab}t} + e^{-i\omega_{ab}t}) - \frac{\mathcal{E}_{ac}\mu_{ac}}{2}\rho_{cb} (e^{i\omega_{ac}t} + e^{-i\omega_{ac}t}) \\
i\hbar \frac{\partial \rho_{ac}}{\partial t} &= -\hbar\omega_{ac,0}\rho_{ac} - \frac{\mathcal{E}_{ab}\mu_{ab}}{2}\rho_{bc} (e^{i\omega_{ab}t} + e^{-i\omega_{ab}t}) - \frac{\mathcal{E}_{ac}\mu_{ac}}{2} (\rho_{cc} - \rho_{aa}) (e^{i\omega_{ac}t} + e^{-i\omega_{ac}t}) \\
i\hbar \frac{\partial \rho_{ba}}{\partial t} &= \hbar\omega_{ab,0}\rho_{ba} - \frac{\mathcal{E}_{ab}\mu_{ab}^*}{2} (\rho_{aa} - \rho_{bb}) (e^{i\omega_{ab}t} + e^{-i\omega_{ab}t}) + \frac{\mathcal{E}_{ac}\mu_{ac}^*}{2}\rho_{bc} (e^{i\omega_{ac}t} + e^{-i\omega_{ac}t}) \\
i\hbar \frac{\partial \rho_{bc}}{\partial t} &= -\hbar\omega_{bc,0}\rho_{bc} - \frac{\mathcal{E}_{ab}\mu_{ab}^*}{2}\rho_{ac} (e^{i\omega_{ab}t} + e^{-i\omega_{ab}t}) + \frac{\mathcal{E}_{ac}\mu_{ac}}{2}\rho_{ba} (e^{i\omega_{ac}t} + e^{-i\omega_{ac}t}) \\
i\hbar \frac{\partial \rho_{ca}}{\partial t} &= \hbar\omega_{ac,0}\rho_{ca} + \frac{\mathcal{E}_{ab}\mu_{ab}^*}{2}\rho_{cb} (e^{i\omega_{ab}t} + e^{-i\omega_{ab}t}) - \frac{\mathcal{E}_{ac}\mu_{ac}^*}{2} (\rho_{aa} - \rho_{cc}) (e^{i\omega_{ac}t} + e^{-i\omega_{ac}t}) \\
i\hbar \frac{\partial \rho_{cb}}{\partial t} &= \hbar\omega_{bc,0}\rho_{cb} + \frac{\mathcal{E}_{ab}\mu_{ab}}{2}\rho_{ca} (e^{i\omega_{ab}t} + e^{-i\omega_{ab}t}) - \frac{\mathcal{E}_{ac}\mu_{ac}^*}{2}\rho_{ab} (e^{i\omega_{ac}t} + e^{-i\omega_{ac}t})
\end{aligned}$$



## Appendix B

### Fourier series

The FID  $f(t)$  can be described by a finite discrete Fourier series [279]:

$$f(t) = \frac{a_0}{2} + \sum_{n=0}^N (a_n \cos(\omega_n t) + b_n \sin(\omega_n t))$$

where  $a_0$  is the constant DC offset and  $a_n$  and  $b_n$  are the real valued Fourier coefficients. For the frequencies  $\omega_n$  follows:

$$\omega_n = \frac{2\pi n}{T}$$

where  $T$  is total length of the recorded FID. For a specific frequency  $\omega_n$  the Fourier coefficients are determined by the following integrals:

$$\begin{aligned} a_n &= \frac{2}{T} \int_0^T f(t) \cdot \sin(\omega_n t) \\ b_n &= \frac{2}{T} \int_0^T f(t) \cdot \cos(\omega_n t) \end{aligned}$$

For a specific frequency  $\omega_n$  one component of the series  $f(t)$  can be rewritten using an amplitude  $A_n$  and a phase  $\varphi_n$ :

$$f_n(t) = A_n \sin(\omega_n t + \varphi_n)$$

with

$$\begin{aligned} A_n &= \sqrt{a_n^2 + b_n^2} \\ \varphi_n &= \frac{\pi}{2} - \arctan2(b_n, a_n) \end{aligned}$$